ON THE INTERACTION OF LASER BEAMS WITH AIR

with specific reference to refraction and scattering

M. Kuppen

Submitted in partial fulfillment of the
requirements for the degree of
Doctor of Philosophy,
in the
Department of Physics,
University of Natal.

Durban
South Africa
April 1996

To my late mom, without whose faith and unwavering support,
this work would not have been possible.

Preface

The work described in this thesis was carried out at the University of Natal, Durban, from January 1992 to September 1995 under the supervision of Professor M. M. Michaelis. The thesis describes original work carried out by the author and where use is made of the results of others due acknowledgement has been given.

Acknowledgements

Many people have contributed towards the completion of this work. To give due credit to everyone involved would be impossible. For those persons who I fail to mention hereunder I extend my sincerest thanks.

I would firstly like to thank my supervisor Professor Max Michaelis for his guidance and support over the past three years. Max has been an inspirational force not only on a personal level but also on a scientific level as well and for this I am grateful.

I would also like to thank Willem de Beer and all other members of the Physics Workshop for their assistance in all the constructional work undertaken during the course of this study.

A special thanks must go out to Derick Davies who was responsible for the construction of the different colliding shock lenses as well as the pressure chamber. The translation of ideas on paper into working devices is not always easy. Derick nevertheless ensured that out of sometimes cryptic design specifications came working devices.

I would also like to thank Richard Buccelatto and Nicola Lisi for teaching me most of what I know concerning the operation of the colliding shock lens.

Dr. Erhard Mravlag who assisted me with the lidar system and provided important insight into the interpretation of the results deserves a special mention. Thanks Erhard for keeping me sane and focussed during those times when all else was falling apart around me.

Finally a very special word of thanks must go out to my mom whose faith and understanding enabled me to see this project through. Without her love and support this would not have been possible.

Abstract

The interaction of laser light with a parcel of air with a known density structure can result in one of three reactions. The simplest of these reactions is reflection. Depending on the nature of the density profile, that part of the light that is not reflected can be refracted or scattered. The extent of the refraction and scattering is determined by the density of the particles found in the air.

This thesis investigates two concepts that use the abovementioned interactions. The first, the colliding shock lens (CSL) was proposed by Buccellato, Lisi and Michaelis (1993). This device uses the graded index (GRIN) lens formed by the collision of symmetrically arranged shock waves to focus a laser beam. Unfortunately, the first reported colliding shock lenses had optical apertures of the order of millimeters. This is hardly useful in realistic laser systems whose beams typically have a diameter of 10mm.

The major part of this thesis involves the scaling up of the optical aperture of the CSL while simultaneously maintaining a fairly short focal length. We show how the behaviour of the CSL varies with factors such as input energy, electrical diameter, geometry and various other factors. By optimising the physical parameters a 1.5cm diameter lens is obtained having a focal length of 1.5m. We develop a simple scaling theory and run a simulation based on the fluid in cell (FLIC) method, and find good correlation in both cases between the experimentally obtained results and the theoretically predicted ones.

As a further development of the work on colliding shock lenses we introduce a cylindrical colliding shock lens. This device is shown to be able to line focus a laser beam of 1cm in diameter. At this stage the focus quality is still poor and suggestions are made for further improvements.

Lidar is an acronym for light detection and ranging. Such systems are based on the scattering of laser light incident on a parcel of air. We discuss the results of a campaign conducted during the period of June to November 1994 to study aerosol concentrations over Durban. Particular attention is paid to low level aerosols due to sugar cane burning over the Natal coast. These aerosols are known to influence local climate and since vertical profile

studies have never been carried out, this investigation gives some useful insight into the atmospheric dynamics. We find that in June (the begining of the burning campaign) the aerosol loading in the lower atmosphere is low. However, there are very stable aerosol layers at 3km and 5km. The density of the aerosols in these layers are decoupled. In September, the turbulent atmosphere over Durban is found to destroy structure in the aerosol layers. Nevertheless, the aerosol loading is high.

Scattering ratios and extinction coefficients are calculated to show the long and short term evolution of the aerosols. A new coefficient (the low altitude aerosol coefficent - LAAC) is defined as an indicator for aerosol loading in the lower atmosphere. This coefficient is compared with total column ozone values over Durban. An anti-correlatory behaviour is noticed.

We also report the detection of an extremely high aerosol layer (60km) over Durban. This layer is believed to be sodium. The profiles are compared to satellite data to verify the first ever detection of a constituent at these altitudes in Southern Africa.

Contents

List of Figures

Chapter 1

Introduction

The wave-particle duality in the behaviour of light has mystified scientists for centuries. Although the properties of light have been studied extensively since 1200 BC, the Greek philosophers (Aristotle, Plato, Pythagoras and others) were interested in the behaviour of light and not its properties. Various theories evolved but none giving clarity as to the exact nature of light.

Some of the earliest studies seemed to indicate that light only had a wave nature. In his deduction of Snell's law of refraction, Descartes used one of the first models of light. In this model, he conceived light as being a pressure transmitted by an elastic medium. Robert Hooke while studying interference effects due to thin films, proposed the idea that light was a rapid vibratory motion of the medium propagating at a very great speed. He further proposed that *"every pulse or vibration of the luminous body will generate a sphere."* This sounded the beginnings of the wave theory of light.

It was Newton who hinted at the dual nature of light. He maintained that light consisted of corpuscles that excited the aether into characteristic vibrations. These vibrations corresponded to different colours of the spectrum. Newton's work seemed at the time to encompass the wave and particle behaviour of light although not too clearly.

Huygens (1629-1695) later concluded that light slowed down on entering more dense media. He was able to derive the laws of reflection and refraction (to be proved later) by using his wave theory. Up to this point light was still believed to be either a stream of particles or a rapid undulation of aethereal

matter - the two properties being mutually exclusive.

The wave theory was furthered by Young (1773-1829) and Fresnel (1788-1827). In 1845, Michael Faraday established an interrelationship between electromagnetism and light when he found that the polarisation direction of a beam could be altered by the application of a strong magnetic field. It was Maxwell however, who concluded that *"light was an electromagnetic disturbance in the form of waves."*

The acceptance of the wave theory however, required the acceptance of the aether. If there were waves then one had to accept that there existed a medium in which they were supported. It was only in the 1900's, after extensive investigations, that doubt was cast on the existence of the aether. It was Poincare who in 1900 said *"Our aether, does it really exist?"* At the same time (1900), Max Planck introduced the theory of quantum mechanics. In 1905 Albert Einstein introduced his theory of special relativity and postulated that *"light is always propagated in empty space with a definite velocity c."* Expanding on Planck's "new" theory, Einstein proposed that light was quantised and that each such quantum of energy was proportional to its frequency in the following way :

$$E = h\nu \tag{1.1}$$

where E is the energy of the light, ν its frequency and h a constant known as Planck's constant.

By the early 1920's, with the acceptance of Quantum Mechanics, it became clear that light had a dual wave-particle nature. It can safely be described as a wave during propagation and as particles during most, if not all, interactions with different media.

1.1 Interaction of light

When a light ray strikes the interface separating two media having different refractive indices, part of the incident flux density will be diverted back as a reflected wave and the remainder will be transmitted across the boundary

as a refracted ray. Macroscopically, these phenomena can be explained using the wave nature of light. On a microscopic scale however, the atoms in the media scatter the light as if they were particles and the degree of scattering is determined by the size and distribution of the atoms in the medium. This distribution also determines the refractive index of the medium. The scattering gives rise to the resultant reflected and refracted waves.

As this thesis is concerned with the applications of the fundamental interactions of light with air, more detailed descriptions of these interactions (viz. reflection, refraction and scattering) will now be given.

1.1.1 Reflection

This interaction was known as early as 300 BC to Euclid. In 1690, Christiaan Huygens published his *"Traite de la Lumiere"* in which he described the wave nature of light. It was in this publication that he enunciated what is commonly known today as Huygens' Principle:

Every point on an arbitrary surface, as they are reached by the wave front, becomes the centres of secondary waves. The geometrical envelope of these waves at any given later time represents the instantaneous position of the wave front. The volume swept by the wave front thus defined determines the illumination region of space.

Using Huygens' principle we can derive the Law of Reflection.

Consider a plane wave impinging upon the plane surface of separation σ between two homogeneous media. Let medium 1 have a refractive index n_1 and medium 2 have refractive index n_2. Hence we can assume that the light travels in each of them with different velocities.

From Huygens' principle the points of the surface σ as they are reached by the incoming light wave, act as secondary sources of spherical wavelets. Since there is a discontinuity in the refractive index across the boundary, part of the wave is reflected and the rest is transmitted (or refracted). More will be said about the refracted part later.

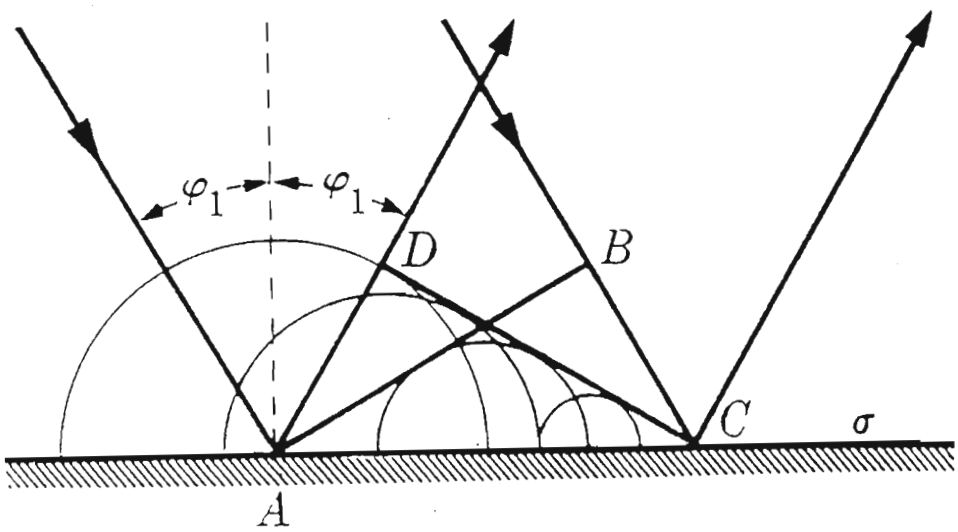

Figure 1.1: Law of reflection deduced from the Huygens construction - after Rossi (1965)

For the reflected part, the wavelets are propagated in the backward direction with a velocity equal to that of the incident wave. In fig 1.1, AB is the intersection of the incident wave front with a plane perpendicular to the wave front itself and to the reflecting surface σ. The figure (1.1) shows the instant when the wave front intersects the reflecting surface σ along a straight line perpendicular to the plane of the figure and passing through A. At this moment, the wave front is still a distance BC from the point C on σ. When the wave front reaches C, the wavelets originating from A and from other points on the straight line passing through A and perpendicular to the plane of the figure have radii equal to BC.

The wavelets originating from points intermediate between A and C have radii proportional to their distances from C. The envelope formed by these wavelets (the reflected wave) is a plane surface perpendicular to the plane of the figure and intersecting this plane along the line CD. The triangles ABC and CDA are congruent. Thus the angles ($B\hat{A}C$ and $D\hat{C}A$) which the incident and reflected rays form with the reflecting surface are equal.

The angle $B\hat{A}C$ is also equal to the angle between the incident ray and the normal to the reflecting surface (the angle of incidence). Similarly $D\hat{C}A$ represents the angle of reflection. We also see that the incident ray, reflected ray and normal all lie in the same plane.

1.1.2 Refraction

When light travels from a medium of refractive index n_1 into an adjacent medium of refractive index n_2 ($n_1 \neq n_2$), the light ray undergoes a change in direction due to a change in speed. This bending of the ray is referred to as **refraction**. In the 2nd century AD Ptolemy made measurements of the angles of incidence and refraction for waves in various media and tried to find a mathematical relationship between them. However, it was Snell in 1621 and later Descartes in 1637 who found that the ratio of the sines and cosines of these angles is constant. We refer to this law as the *Law of Refraction* or *Snells Law.*

$$\frac{sin\phi_1}{sin\phi_2} = constant \tag{1.2}$$

or

$$n_1 sin\phi_1 = n_2 sin\phi_2 \tag{1.3}$$

Using Huygens' principle we can also prove the Law of Refraction.

Consider a plane wave AB incident upon the plane surface of separation σ between two transparent media as before.

Construct the wavelets propagated from the points on σ into the second medium. See figure 1.3. Again assume that the media have different refractive indices and hence the speed of light is different in both media. Let n_1 and n_2 be the refractive indices of medium 1 and medium 2 respectively and let the velocity of light in the respective media be v_1 and v_2. At the moment the wave front reaches the refracting surface at A, it is a distance BC from point C. While the incident wave travels this distance, the point A and other points on the straight line passing through A perpendicular to the plane of the figure give rise to secondary wavelets having a radius AD'.

From the figure we can see that

$$\frac{\overline{AD'}}{\overline{BC}} = \frac{v_2}{v_1} \tag{1.4}$$

Wavelets originating from points intermediate between A and C have radii proportional to their distances from C. Thus the envelope formed by the secondary wavelets is the plane surface CD' perpendicular to the plane of the figure. It follows that the incident ray (perpendicular to the incident wave front AB) and the refracted ray (perpendicular to the refracted wave front CD') lie in a plane perpendicular to the refracting surface σ. Moreover, the angle of incidence ϕ_1 equals the angle $B\hat{A}C$, and that the angle of refraction

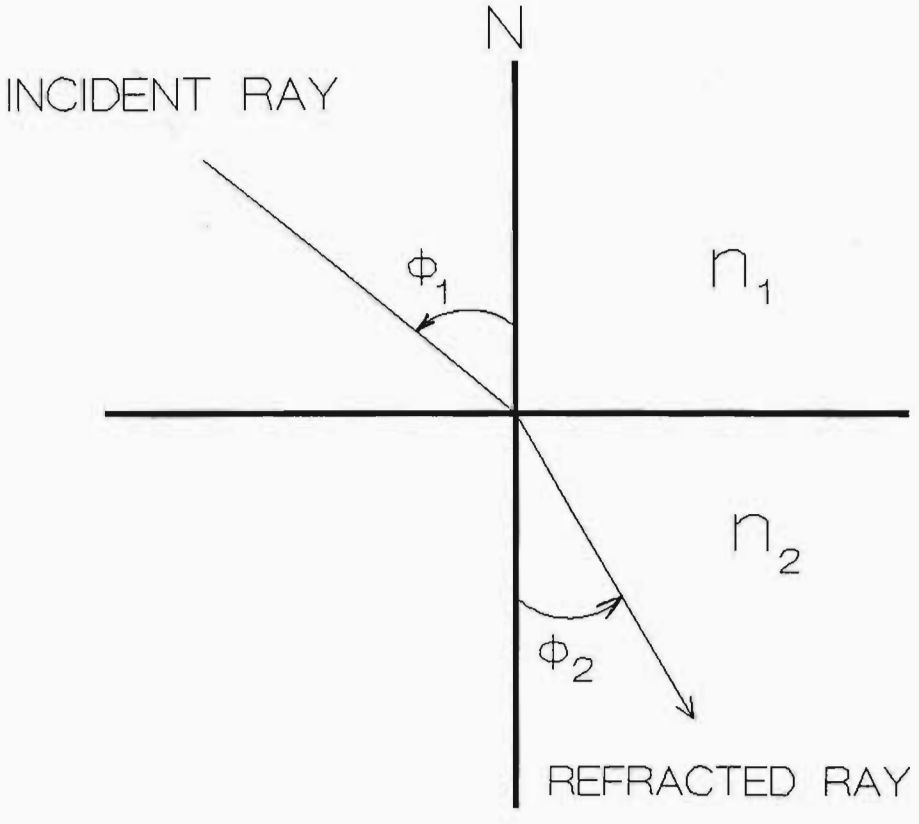

Figure 1.2: Figure showing angles of incidence and refraction

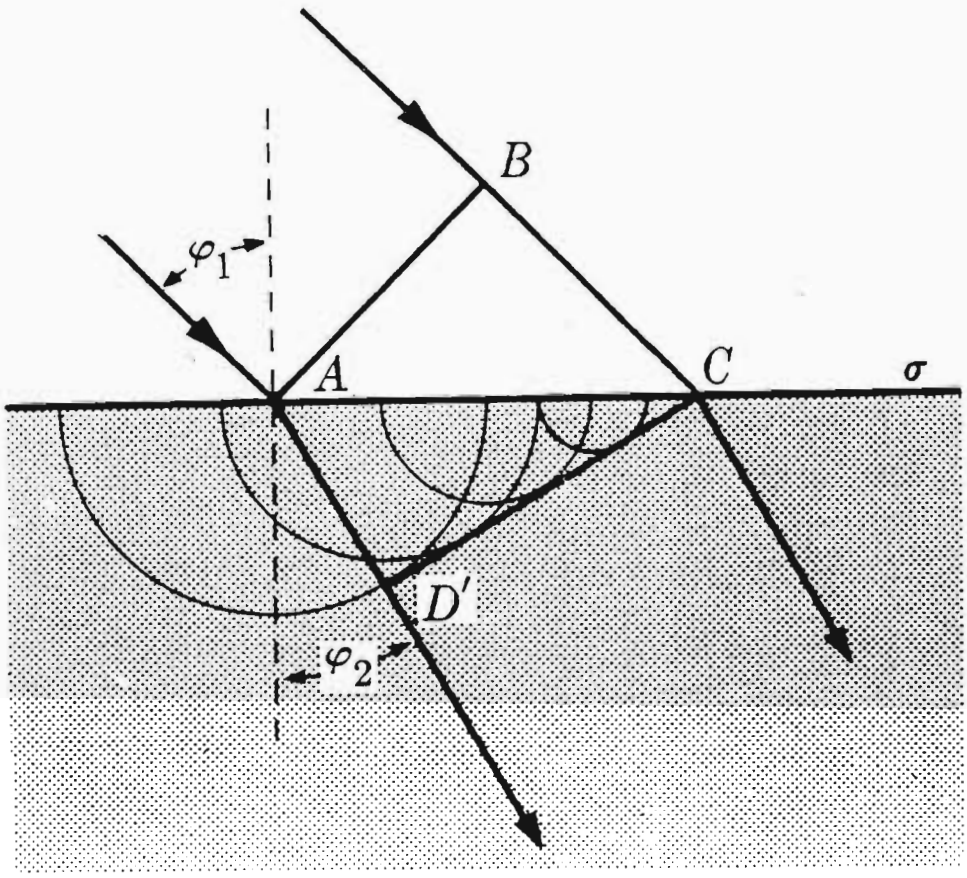

Figure 1.3: The law of refraction deduced from the Huygens construction - after Rossi (1965)

ϕ_2 equals the angle $A\hat{C}D'$. From the figure we see that :

$$\overline{BC} = \overline{AC} sin\phi_1 \tag{1.5}$$

and

$$\overline{AD'} = \overline{AC} sin\phi_2 \tag{1.6}$$

From the three preceding equations (1.4, 1.5 and 1.6) we derive

$$\frac{sin\phi_1}{sin\phi_2} = \frac{v_1}{v_2} \tag{1.7}$$

Hence we have proved that the ratio of the angle of incidence and the angle of refraction is constant. Furthermore, we can conclude:

$$\frac{n_2}{n_1} = \frac{v_1}{v_2} \tag{1.8}$$

We can also conclude that the incident ray, the refracted ray and the normal all lie in the same plane.

We have used Huygens principle to describe the refraction of a plane wave incident on a plane boundary between media of different refractive indices. Perhaps more interesting, is the situation where a light ray is incident on a thin lens.

Refraction by a Thin Lens

Using Snells law we can describe the refraction of a light ray due to a thin lens. A conventional spherical lens is bounded by two spherical surfaces (fig-

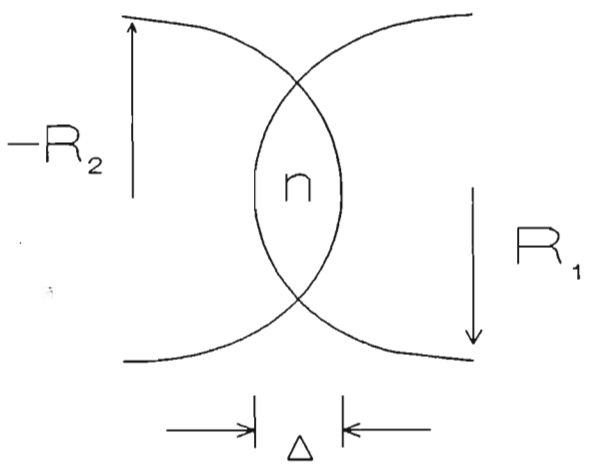

Figure 1.4: A biconvex spherical lens

ure 1.4). It is therefore completely defined by :

i) the radii R_1 and R_2 of its two surfaces,

ii) the thickness Δ of the lens and

iii) the refractive index n of the material.

A glass lens in air can be regarded as a combination of two spherical boundaries, air to glass and glass to air.

A ray crossing the first interface at an angle θ_a to the normal is refracted at this interface. See figure 1.5.

The relationship between the angle of incidence and refraction is once again given by Snells law :

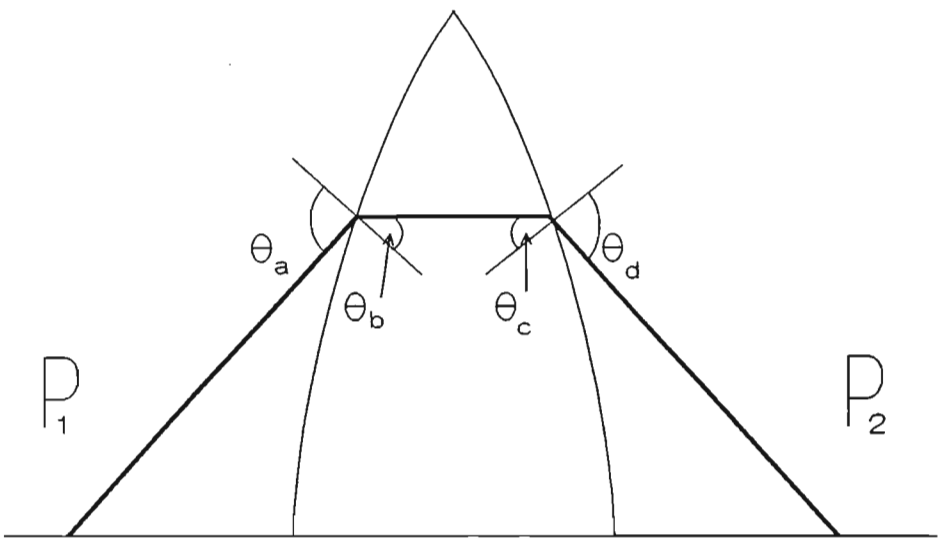

Figure 1.5: Refraction due to a spherical lens

$$n_1 sin\theta_a = n_2 sin\theta_b \tag{1.9}$$

where

n_1 : the refractive index of air,
θ_a : the angle of incidence,
n_2 : the refractive index of the lens and
θ_b : the angle of refraction.

We extend the refracted ray and apply Snells law again at the second interface to get :

$$n_2 sin\theta_c = n_1 sin\theta_d \tag{1.10}$$

In this case θ_c is the angle of incidence and θ_d the angle of refraction. The results for a thick lens are generally complicated. When the lens is thin, it can be assumed that the incident ray emerges from the lens at about the same height (say y) at which it enters. Under this assumption the following relations follow :

1. All rays originating from point $P_1 = (y_1, z_1)$ meet at point $P_2 = (y_2, z_2)$ (figure 1.6) where

$$\frac{1}{z_1} + \frac{1}{z_2} = \frac{1}{f} \tag{1.11}$$

and

$$y_2 = -\frac{z_2}{z_1} y_1 \tag{1.12}$$

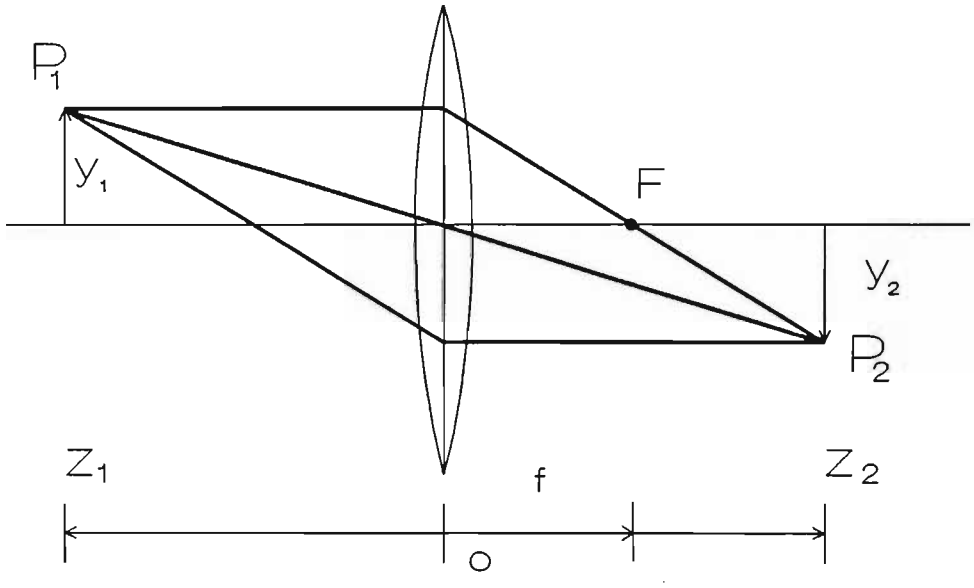

Figure 1.6: Image formation by a thin lens

The focal length f is given by the equation :

$$\frac{1}{f} = (n-1)\left(\frac{1}{R_1} - \frac{1}{R_2}\right) \tag{1.13}$$

after Hecht and Zajac (1974). For a complete derivation of the above equation, the reader is referred to section 5.2. of the aforementioned text.

2. Using figure 1.7 and the small angle approximation, the angles of the refracted and incident rays are related in the following way :

$$-\theta_2 = \frac{y}{z_2} \tag{1.14}$$

and

$$\theta_1 = \frac{y}{z_1} \tag{1.15}$$

Combining these two equations (1.14 and 1.15) we get :

$$\theta_2 = \theta_1 - y\left(\frac{1}{z_2} + \frac{1}{z_1}\right) \tag{1.16}$$

Hence from equation 1.11 we derive :

$$\theta_2 = \theta_1 - \frac{y}{f} \tag{1.17}$$

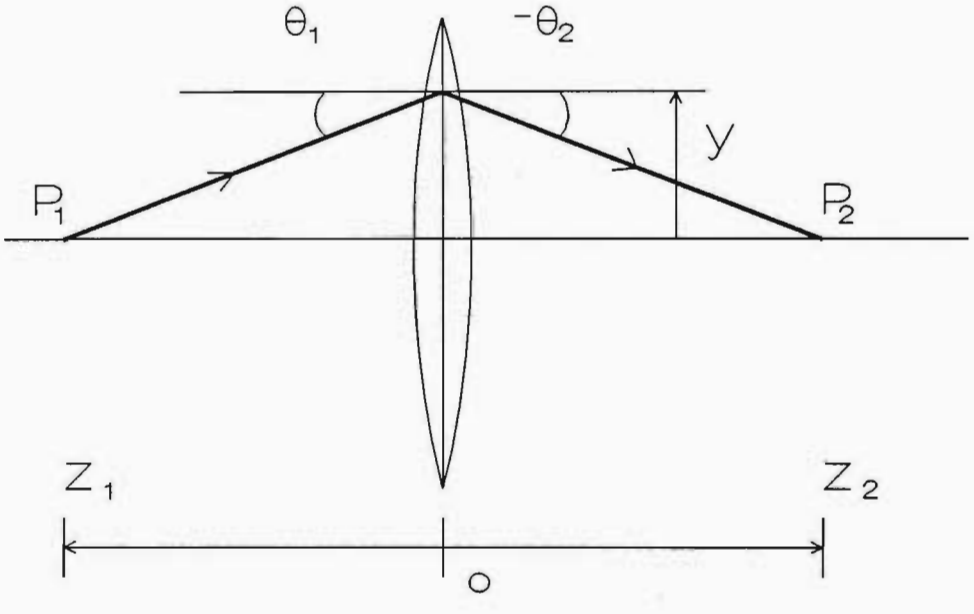

Figure 1.7: Ray bending by a thin lens

The above relationships hold for a thin spherical lens having a constant refractive index. Since the lens under investigation in this thesis does not have a constant refractive index across its active area, we need to look at this case as well.

Graded Index Optics

A graded index (GRIN) material has a refractive index that varies with position in accordance with a continuous function n(**r**). The optical rays in this medium follow curved trajectories instead of straight lines. By appropriate choice of n(**r**), a plate of GRIN material of finite thickness can have the same effect on light rays as a conventional lens. To determine the trajectories of light rays in an inhomogeneous medium with refractive index n(**r**), we use Fermat's principle,

$$\delta \int_A^B n(\mathbf{r}) ds = 0 \tag{1.18}$$

where ds is a differential length along the ray trajectory between A and B (figure 1.8).

If the trajectory is described by the functions $x(s)$, $y(s)$ and $z(s)$ where s is the length of the trajectory, then it can be shown (Weinstock (1974)) that $x(s)$, $y(s)$ and $z(s)$ must satisfy three partial differential equations :

$$\frac{d}{ds}\left(n\frac{dx}{ds}\right) = \frac{\partial n}{\partial x} \tag{1.19}$$

$$\frac{d}{ds}\left(n\frac{dy}{ds}\right) = \frac{\partial n}{\partial y} \tag{1.20}$$

$$\frac{d}{ds}\left(n\frac{dz}{ds}\right) = \frac{\partial n}{\partial z} \tag{1.21}$$

By defining the vector **r**(s) whose components are $x(s)$, $y(s)$ and $z(s)$, equations 1.19, 1.20 and 1.21 may be rewritten in the form

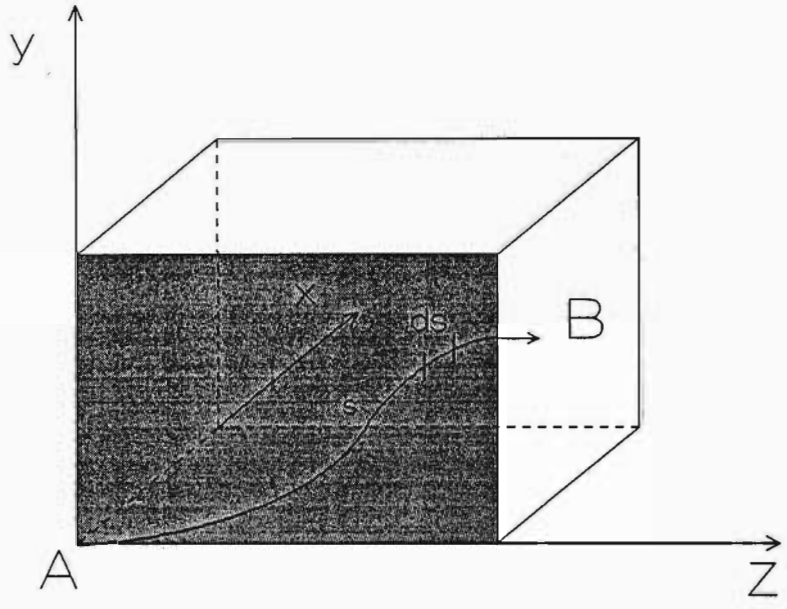

Figure 1.8: Ray trajectory in an inhomogeneous medium having refractive index n(**r**)

$$\frac{d}{ds}\left(n\frac{d\mathbf{r}}{ds}\right) = \nabla n \tag{1.22}$$

where ∇n (the gradient of **n**) is a vector with Cartesian components $\frac{\partial n}{\partial x}$, $\frac{\partial n}{\partial y}$ and $\frac{\partial n}{\partial z}$.

Equation 1.22 is known as the Ray equation. If we consider only ray trajectories almost parallel to the z axis then ds $\approx$ dz. The Ray equation then simplifies to

$$\frac{d}{dz}\left(n\frac{dx}{dz}\right) \approx \frac{\partial n}{\partial x} \tag{1.23}$$

and

$$\frac{d}{dz}\left(n\frac{dy}{dz}\right) \approx \frac{\partial n}{\partial y} \tag{1.24}$$

Consider now a slab of material whose refractive index n = n(y) is uniform in the x and z directions but varies continuously in the y direction (figure 1.9).

The trajectories of the paraxial rays in the y-z plane can be derived using Snells law in the following way.

Let $\theta(y) \approx \frac{dy}{dx}$ be the angle that the ray makes with the z axis at the position (y,z). After travelling through a layer of width Δy the ray changes its angle to $\theta(y + \Delta y)$. The two angles are related by Snells law

$$n(y)cos\theta(y) = n(y + \Delta y)cos\theta(y + \Delta y) \tag{1.25}$$

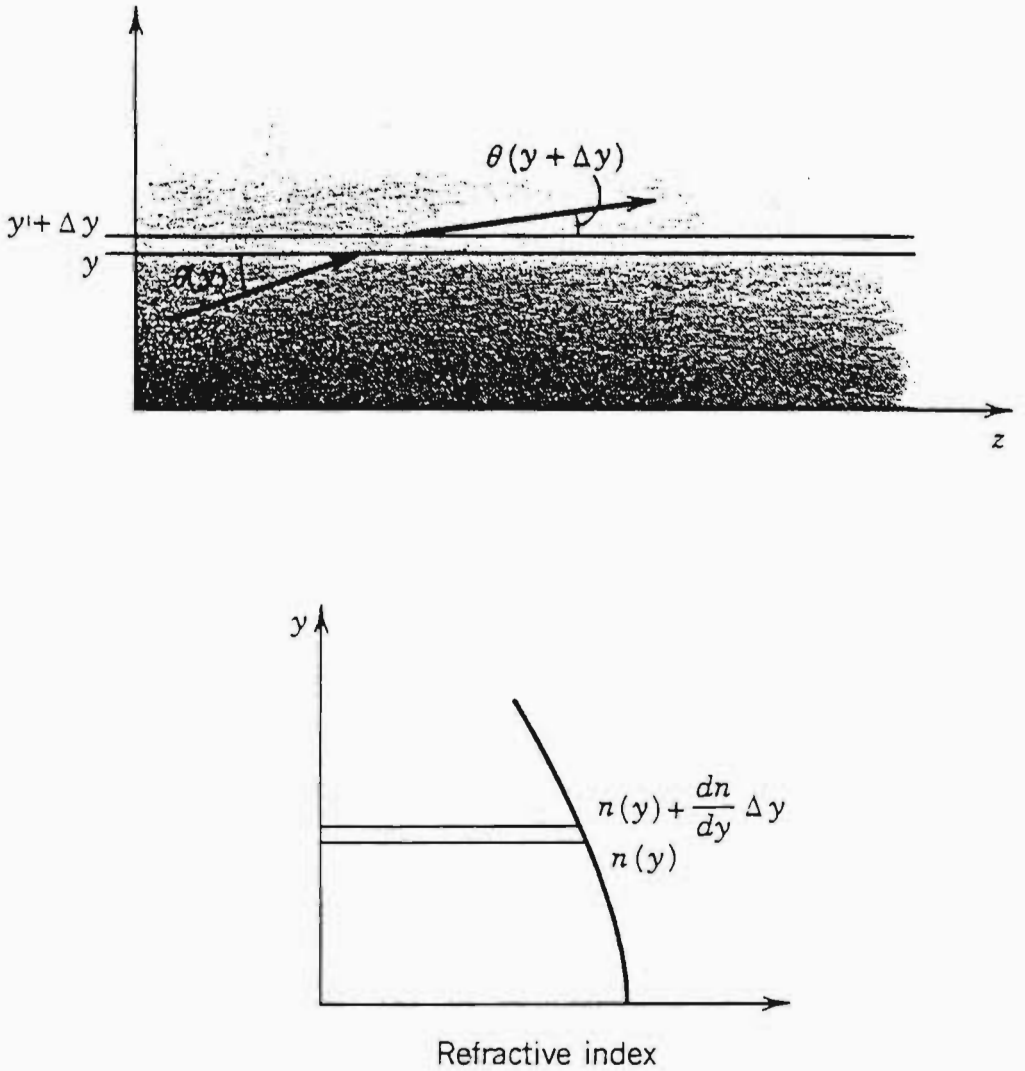

Figure 1.9: Refraction in a graded index slab

Using $f(y+\Delta y) = f(y) + \left(\frac{df}{dy}\right)\Delta y$ on the function $f(y) = cos\theta(y)$ and $f(y) = n(y)$, we get

$$n(y)cos\theta(y) = \left(n(y) + \frac{dn}{dy}\Delta y\right)\left(cos\theta(y) - \frac{d\theta}{dy}\Delta y sin\theta(y)\right) \tag{1.26}$$

In the limit Δy $\rightarrow$ 0 we obtain the differential equation

$$\frac{dn}{dy} = ntan\theta\frac{d\theta}{dy} \tag{1.27}$$

For paraxial rays, θ is very small so that $tan\theta \approx \theta$.
Substituting $\theta = \frac{dy}{dz}$ into 1.27 we get

$$\frac{d^2y}{dz^2} = \frac{1}{n}\frac{dn}{dy} \tag{1.28}$$

This equation (1.28) describes the ray trajectories in a slab of GRIN material. A graded index lens is analogous to the graded slab described above. In a graded index lens, the refractive index varies as a function of radial distance from its axis. In the paraxial approximation, the ray trajectories for a GRIN lens are once again governed by the paraxial ray equations 1.23 and 1.24.

1.1.3 Scattering

Reflection and refraction of light can best be described by the wave nature of light. However, scattering processes are best described by the particle nature of light.

The two broad categories of scattering are :

(1) Elastic scattering and

(2) Inelastic scattering.

For the purposes of relevance we will limit the discussion to elastic scattering.

Elastic scattering

This is a scattering process in which the wavelength of the scattered light is the same as that of the incident light.

Rayleigh scattering

Rayleigh scattering is an elastic scattering process. For particles (molecules) whose size is much smaller than the incident radiation wavelength, a photon of incident radiation ($h\omega_i$) interacts with the molecule. The molecule is excited by this photon. When the molecule relaxes to its original ground state, a second photon known as the photon of scattered radiation ($h\omega_s$) is emitted. The wavelength of this photon is the same as the wavelength of the incident photon (elastic scattering). Since two photons are involved in the scattering process, Rayleigh scattering can be considered a "two photon process."

Mie scattering

The elastic scattering process for which the size of the particle upon which a photon is incident, is comparable to the wavelength of the incident photon is termed Mie scattering. The emitted photon has the same wavelength as the incident photon. Since the cross section of the particle for Mie scattering can be large compared to Rayleigh scattering, the scattered signal for Mie scattering could completely swamp any Rayleigh component. This implies that quite low concentrations (a few ppm) of dust or aerosols can be detected using this technique.

Mie scattering like Rayleigh scattering is an elastic, two photon process (incident and scattered photon). The difference between the two is the fact that different sized particles are involved. These sizes can be quantified if we define a scattering size parameter α, where

$$\alpha = ka = \frac{2\pi a}{\lambda} \tag{1.29}$$

a : representative dimension of the particulate
λ : wavelength of the laser radiation

For particles with a scattering size parameter of α less than 0.5, the elastic scattering process is termed Rayleigh scattering. As the scatterers size increases beyond 0.5, the scattering process is Mie scattering. Figure 1.10 is a schematic for both Rayleigh and Mie scattering.

1.2 Outline of the thesis

Chapter 2 will serve as a general introduction into shock waves. A historical review of experiments performed using colliding shock and detonation waves will also be outlined.

In chapter 3 we will introduce the concept of the colliding shock lens (CSL). We will describe the very first CSL together with the early experiments and results of Buccellato et al. (1993). The major part of this chapter will deal with the scaling up of the effective optical aperture of the CSL. We will discuss the parameters changed, the different CSL's constructed during the course of the experiments and the results obtained.

Chapter 4 will outline the simulation of the colliding shock lens. A simple scaling theory will be proposed and comparisons with experimental data undertaken. A simulation based on the fluid in cell differencing method is detailed and results discussed.

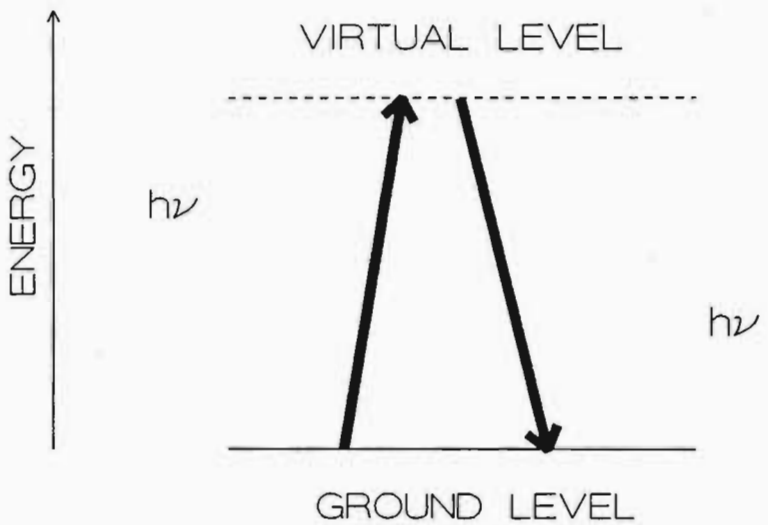

Figure 1.10: Rayleigh and Mie scattering

Chapter 5 introduces the new colliding shock lens, to be known from now on as the Cylindrical Colliding Shock Lens (CCSL). The geometry for this new lens will be described and preliminary results presented.

We will make conclusions (chapter 6) of the experimental and theoretical investigations of the colliding shock lens and the cylindrical colliding shock lens. Some applications of these devices will be discussed as well as future work to be undertaken.

The concept of lidar will be introduced in chapter 7 and the basic lidar theory outlined. The Durban lidar system will be discussed as well as the preliminary results obtained with the system in the period 1992 to 1993.

We will also present results of both high and low altitude aerosols detected over Durban in the period 1993 to 1995. In addition, this chapter contains discussions on the nature, behaviour and origin of these aerosols. We introduce a low altitude aerosol coefficient (LAAC) and attempt a comparison between these values and the total column ozone values over the station.

Finally in chapter 8 we will make general conclusions on the purpose of this study and outline the major results obtained during the course of the investigations carried out.

Chapter 2

Colliding Shock Waves

2.1 General theory on shock waves

Perhaps the first question to be answered is :

What is a shock wave and how do we describe it mathematically ?

Gas flows can be either supersonic or subsonic. One of the most distinctive features of supersonic flow is the occurrence of shock waves.

In gas flows, discontinuities of pressure, velocity and other variables of state sometimes occur. A discontinuity occurs over one or more surfaces. Pressure, velocity, density and other quantities describing the state of the gas change as we cross the discontinuity (called the surface of discontinuity). Certain boundary conditions must be satisfied on surfaces of discontinuity. The following treatment of boundary conditions follows that of Landau and Lifshitz (1959) :

Consider an element of the surface with a co-ordinate system fixed to this element; taking the x-axis to lie along the normal. See figure 2.1.

The following boundary conditions must be obeyed :

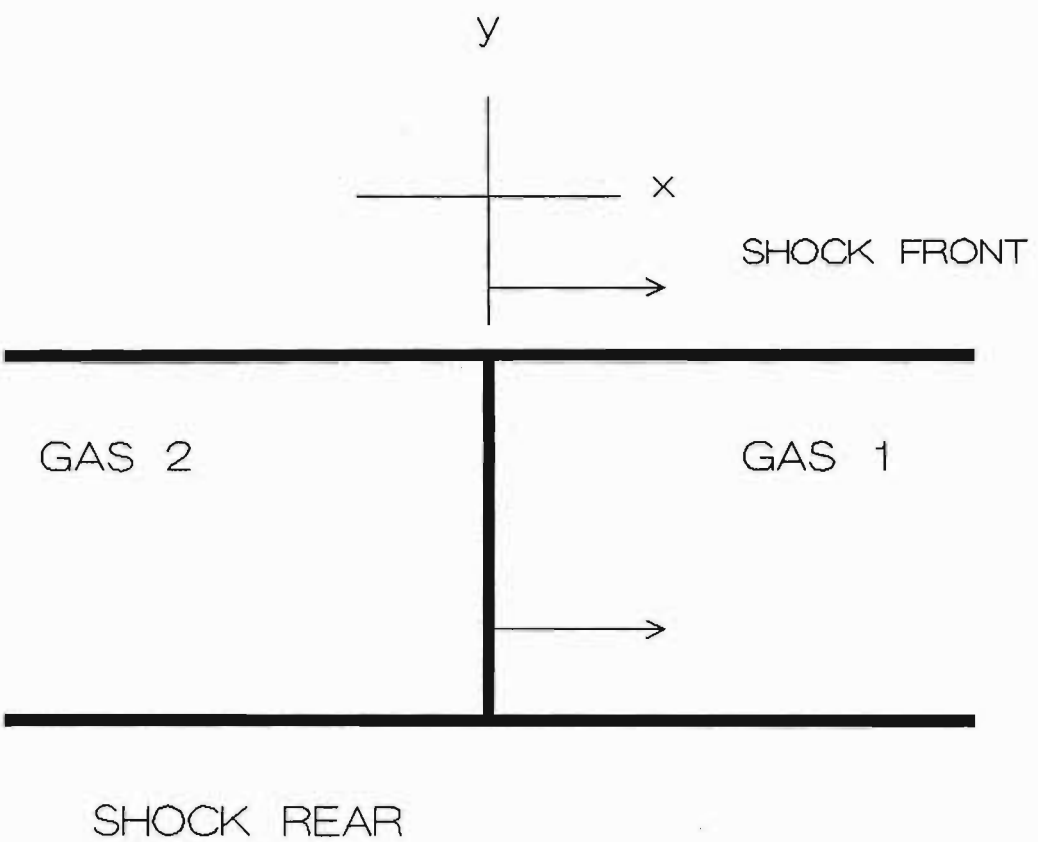

Figure 2.1: Schematic showing co-ordinate system and fluid element

1. **Mass flux must be continuous**

The mass of gas flowing from one side of the discontinuity must equal the mass flowing through and hence leaving the other side. If we let $\rho\ v_x$ be the mass flux per unit area; then we can say $\rho_1\ v_{1x} = \rho_2\ v_{2x}$ where 1 and 2 denote the two different sides of the discontinuity. From the notation of Landau and Lifshitz we can say $[\rho\ v_x] \equiv \rho_1\ v_{1x}$ - $\rho_2\ v_{2x}$.

Hence the first boundary condition can be written as :

$$[\rho v_x] = 0 \tag{2.1}$$

2. **Energy flux must be continuous**

$$[\rho v_x(\frac{1}{2}v^2 + w)] = 0 \tag{2.2}$$

where w is the heat function.

3. **Momentum flux must be continuous**

In other words, the forces exerted on each other by the gases on the two sides of the surface of discontinuity must be equal. The momentum flux per unit area is $pn_i + \rho v_i v_k n_k$. Since we have taken the x axis to lie along the normal vector **n**, the continuity of the x-component of the momentum flux can be represented as :

$$[p + \rho v_x^2] = 0 \tag{2.3}$$

The y and z components :

$$[\rho v_x v_y] = 0 \tag{2.4}$$

and

$$[\rho v_x v_z] = 0 \tag{2.5}$$

From equations 2.1 to 2.5 we see that there are two types of discontinuity.

a) The type for which there exists no mass flux through the surface and

b) The type for which the mass flux through the surface is non-zero.

A shock wave satisfies condition (**b**). For this case v_{1x} and $v_{2x} \neq 0$. Therefore from 2.1 to 2.5 $[v_y] = 0$, $[v_z] = 0$ i.e. the tangential velocity is continuous at the surface of discontinuity. The pressure, density, normal velocity and other thermodynamic quantities are discontinuous.

From equation 2.1 we can rewrite 2.2 as

$$[\frac{1}{2}v_x^2 + w] = 0 \tag{2.6}$$

since $[\rho v_x] = 0$ and we can replace v^2 by v_x^2 since v_y and v_z are continuous.

A discontinuity satisfying all three of the equations (2.1, 2.3 and 2.6) is therefore called a "shock wave".

We now derive expressions relating the velocity, pressure, temperature and density on the two sides of a shock wave. Again considering a co-ordinate system in which the surface element is at rest and the tangential component of the gas velocity is zero on both sides of the shock, we can rewrite v_x in equations 2.1, 2.3 and 2.6 as v.

Let us adopt the following convention :

We will call the gas into which the shock wave moves *gas 1* and the gas behind the shock *gas 2*. Therefore, the side of the shock towards *gas 1* we can call the "shock front" and that towards *gas 2* the "shock tail."

We can rewrite the boundary conditions as :

$$\rho_1 v_1 = \rho_2 v_2 = j \tag{2.7}$$

$$p_1 + \rho_1 v_1^2 = p_2 + \rho_2 v_2^2 \tag{2.8}$$

$$w_1 + \frac{1}{2} v_1^2 = w_2 + \frac{1}{2} v_2^2, \tag{2.9}$$

where j represents the mass flux density. We consider the gas to move from region 1 (*gas 1*) to region 2 (*gas 2*) hence j is positive. Using specific volumes : $V_1 = \frac{1}{\rho_1}$ and $V_2 = \frac{1}{\rho_2}$ we can write equation 2.7 as :

$$v_1 = jV_1 \quad and \quad v_2 = jV_2 \tag{2.10}$$

Substituting equation 2.10 into equation 2.8 we get :

$$p_1 + \rho_1 j^2 V_1^2 = p_2 + \rho_2 j^2 V_2^2 \tag{2.11}$$

or

$$j^2(\rho_1 V_1^2 - \rho_2 V_2^2) = (p_2 - p_1) \tag{2.12}$$

hence

$$j^2 = \frac{(p_2 - p_1)}{(\rho_1 V_1^2 - \rho_2 V_2^2)} \tag{2.13}$$

Substituting for ρ_1 and ρ_2 we have

$$j^2 = \frac{(p_2 - p_1)}{(V_1 - V_2)} \tag{2.14}$$

From equation 2.10 we can now relate the gas velocities in front of and behind the shock wave in the following manner :

$$v_1 - v_2 = j(V_1 - V_2) \tag{2.15}$$

Therefore substituting equation 2.14 we get :

$$v_1 - v_2 = \sqrt{(p_2 - p_1)(V_1 - V_2)} \tag{2.16}$$

Using equation 2.10 and substituting into the third boundary condition (equation 2.9) we have

$$w_1 + \frac{1}{2} j^2 V_1^2 = w_2 + \frac{1}{2} j^2 V_2^2 \tag{2.17}$$

Substituting now for j^2 :

$$w_1 + \frac{1}{2}\frac{(p_2 - p_1)}{(V_1 - V_2)}V_1^2 = w_2 + \frac{1}{2}\frac{(p_2 - p_1)}{(V_1 - V_2)}V_2^2 \tag{2.18}$$

Finally

$$w_1 - w_2 + \frac{1}{2}(p_2 - p_1)(V_1 + V_2) = 0 \tag{2.19}$$

Equations 2.16 and 2.19 now relate the velocities, pressures and volumes on both sides of the shock wave. Assuming we have a perfect gas (this is a safe assumption to the first approximation), the heat function is given by :

$$w = \frac{\gamma pV}{(\gamma - 1)} \tag{2.20}$$

Substituting into equation 2.19 we have

$$\frac{V_2}{V_1} = \frac{(\gamma + 1)p_1 + (\gamma - 1)p_2}{(\gamma - 1)p_1 + (\gamma + 1)p_2} \tag{2.21}$$

Using the Ideal Gas Law :

$$\frac{T_2}{T_1} = \frac{p_2 V_2}{p_1 V_1} \tag{2.22}$$

We are now in a position to rewrite equation 2.21 in terms of temperature.

$$\frac{T_2}{T_1} = \frac{p_2}{p_1}\frac{(\gamma + 1)p_1 + (\gamma - 1)p_2}{(\gamma - 1)p_1 + (\gamma + 1)p_2} \tag{2.23}$$

Combining equations 2.14 and 2.21 and after some simplification, the expression for the flux density j can be given as :

$$j^2 = \frac{[(\gamma-1)p_1 + (\gamma+1)p_2]}{2V_1} \tag{2.24}$$

The propagation velocities for the shock waves are now given as :

$$v_1^2 = \frac{[(\gamma-1)p_1 + (\gamma+1)p_2]V_1}{2} \tag{2.25}$$

and

$$v_2^2 = \frac{V_2[(\gamma+1)p_1 + (\gamma-1)p_2]^2}{2[(\gamma-1)p_1 + (\gamma+1)p_2]} \tag{2.26}$$

Using the above equations we can derive a set of expressions relating density, pressure and temperature in front of and behind the shock wave :

$$\frac{\rho_2}{\rho_1} = \frac{v_1}{v_2} = \frac{(\gamma+1)M_1^2}{[(\gamma-1)M_1^2+2]} \tag{2.27}$$

$$\frac{p_2}{p_1} = \frac{2\gamma M_1^2}{(\gamma+1)} - \frac{(\gamma-1)}{(\gamma+1)} \tag{2.28}$$

and

$$\frac{T_2}{T_1} = \frac{[2\gamma M_1^2 - (\gamma - 1)][(\gamma - 1)M_1^2 + 2]}{(\gamma + 1)^2 M_1} \tag{2.29}$$

where

$$M_1 = \frac{v_1}{c_1}$$

c_1 is defined as the velocity of sound in region 1.

For a more complete treatment of the above relationships, the reader is referred to Landau and Lifshitz (1959).

2.2 Review of experiments on colliding shocks

Converging shocks have been studied extensively from the 1940's primarily because of their ability to produce extremely high pressures and temperatures on convergence. It was this feature that made them very attractive for use in laser fusion schemes. The theoretical treatment by Guderley (1942) of a converging strong (cylindrical or spherical) shock wave, has served as the foundation for much of this work. Guderley assumes that a converging shock will approach the centre with the shock radius obeying some power law. This radius is given by :

$$r = at^n \tag{2.30}$$

where

a : some constant and
t : time before convergence.

Furthermore, n = 0.717 for spherical shocks and n = 0.834 for cylindrical shocks in order for the boundary conditions to be satisfied.

Some of the earliest experimental work on shock waves were performed by L.G. Smith (1949). He studied the interaction of plane shock waves and angled boundaries. Smith found a relationship between the angle of incidence and attenuation for shocks with Mach numbers ranging from 1 to 2.4. See figure 2.2.

The conclusion that Smith made was that there was considerable attenuation for low angles of incidence. When two shock waves collide at some angle, (or when a shock wave collides with a wall at an angle), depending on the angle between adjacent shocks the reflection can be regular or of the Mach type (as described in figure 2.3).

Perry and Kantrowitz (1951) showed how a Mach reflection is generated when a shock wave collides with a curved boundary. See figure 2.3. It was found that shock waves propagating in a shock tube tend to become perpendicular to the axis of the tube. At the point of intersection of the shock wave and the wall of the tube, the shock wave has an orientation which is normal to the wall. Perry and Kantrowitz (1951) postulated that equal amounts of positive and negative curvature must be distributed along the shock. For the shock to become flat, there must exist a smoothing mechanism which redistributes the curvature.

Earlier, Hertzberg and Kantrowitz (1950) reported an analogous phenomenon. Their experimental set-up consisted of a rectangular channel having one wall bent inwards (see figure 2.3). It was shown that the shock tends to a cylindrical shape in this arrangement. The curvature which was initially concentrated near the wall corner was uniformly distributed along the shock front.

In Mach reflection (figure 2.3), a portion of the curvature originally concentrated at the corner is spread along the shock, while the remainder remains at the triple point. The air velocity discontinuity across a shock (as we know) is normal to the shock, hence the curved Mach shock leaves the air moving in an intermediate direction with respect to the walls. The reflection produced when the Mach shock reaches the opposite wall is weaker than the

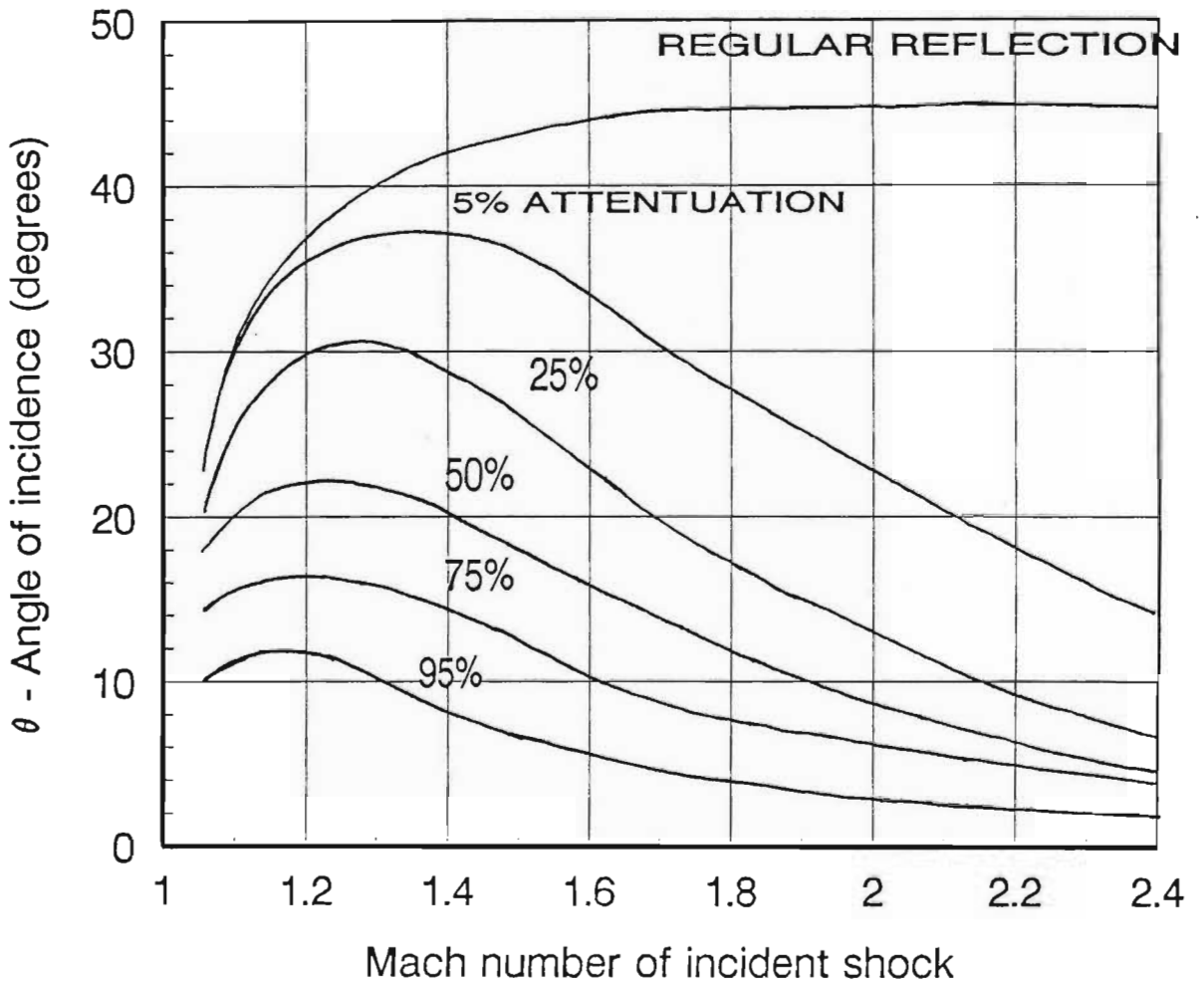

Figure 2.2: Attenuation as a function of angle of incidence and Mach number of the incident shock - from Smith (1949) - after Perry and Kantrowitz (1951)

original reflection. By repeated reflections, the original shock approaches a cylindrical form.

Since all cylindrical, spherical and plane shocks are characterised by uniform curvature, Mach reflection can result in smoothed converging shock waves even if the original shocks deviate slightly from the desired form. It should be pointed out at this stage that the very same argument used above for the case of a shock wave incident on a curved barrier can be used to describe the analogous situation of two shock waves colliding at some angle, where the included angle between the two waves is the same as the angle of incidence of the shock wave with the barrier above.

Following from the work of Smith, Perry and Kantrowitz (1951) studied the convergence of cylindrical shocks. The experimental set-up consisted of a cylindrical shock tube with a tear drop shaped centrebody (figure 2.4).

The shock tube itself consisted of two chambers. One chamber filled with He at high pressure and the other with air at low pressure. A needle pierced the diaphragm initiating a plane shock wave due to the release of the pressurised He. The tear drop forces the planar shock created in this way to implode in a cylindrical manner. Figure 2.5 shows the converging cylindrical shock waves generated with the abovementioned shock tube arrangement.

Perry and Kantrowtiz found that an increase in the initial shock strength causes a decrease in the stability of the converging cylindrical shock wave. Shocks of strength Mach 1.7 were found to converge in a stable manner.

Glass and Heuckroth (1959) adopted a different experimental scheme to study the head on collision of spherical shock waves. Glass spheres 2 inches in diameter with their centres located 9 inches apart were filled with air and He at high pressures (up to 500 psi). The two spheres were ruptured simultaneously to produce converging spherical shock waves with speeds of up to 1350 ft/sec. Spark shadowgrams, multi-spark schlieren photographs and wave-speed schlieren records of the radius time plane were performed. Figure 2.6 shows two such colliding spherical shock waves. The glass sphere on the left containing air at 400 psi and the one on the right containing He at 326 psi. The two shock waves with speeds of 1240ft/sec and 1350ft/sec (weak shock waves) collide and pass through each other unmodified (as expected).

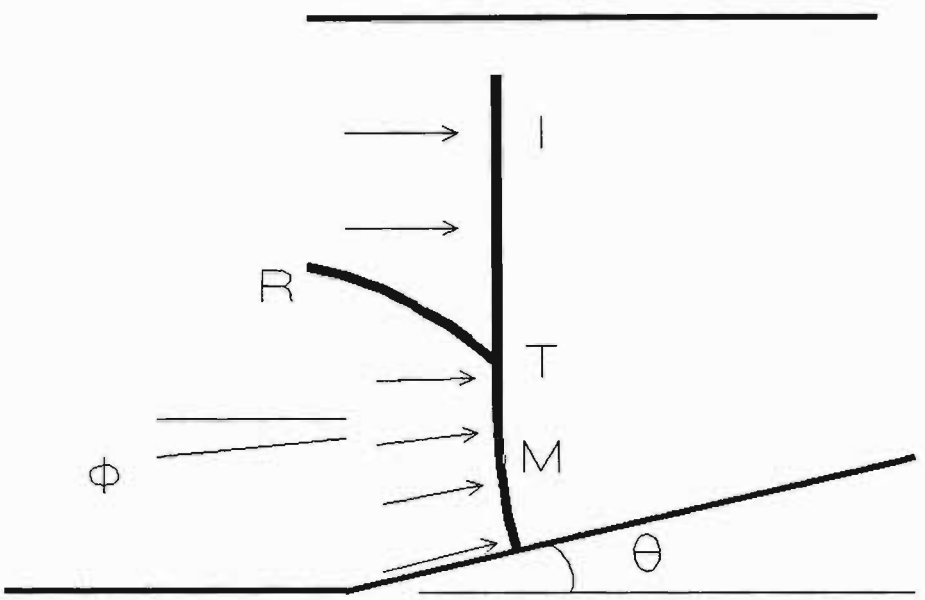

Figure 2.3: Sketch of Mach reflection configuration. I - incident shock. R - reflected shock. T - triple point - after Perry and Kantrowitz (1951)

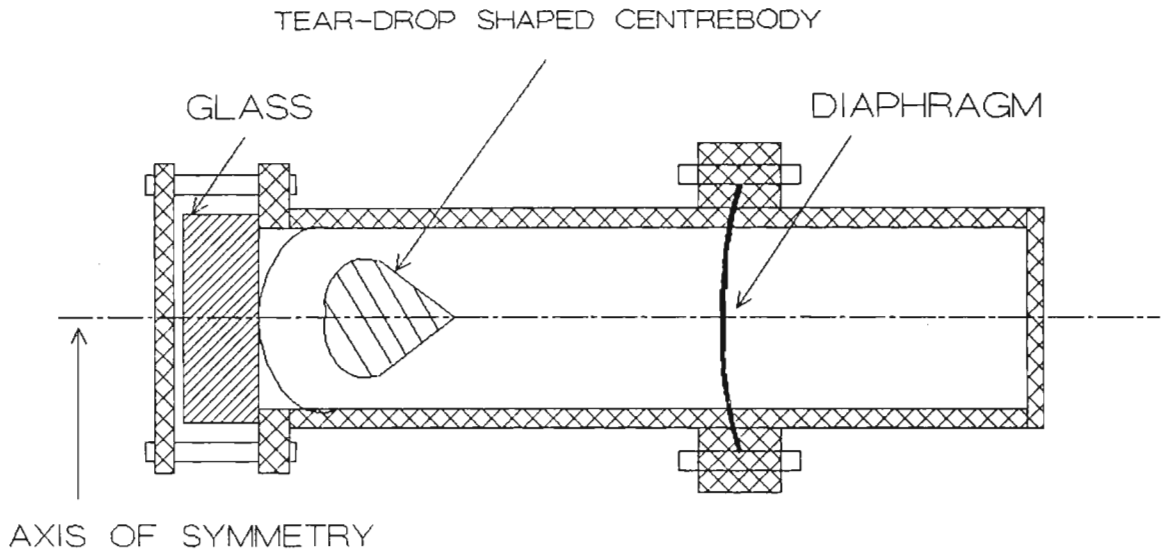

Figure 2.4: Schematic of shock tube used by Perry and Kantrowitz (1951)

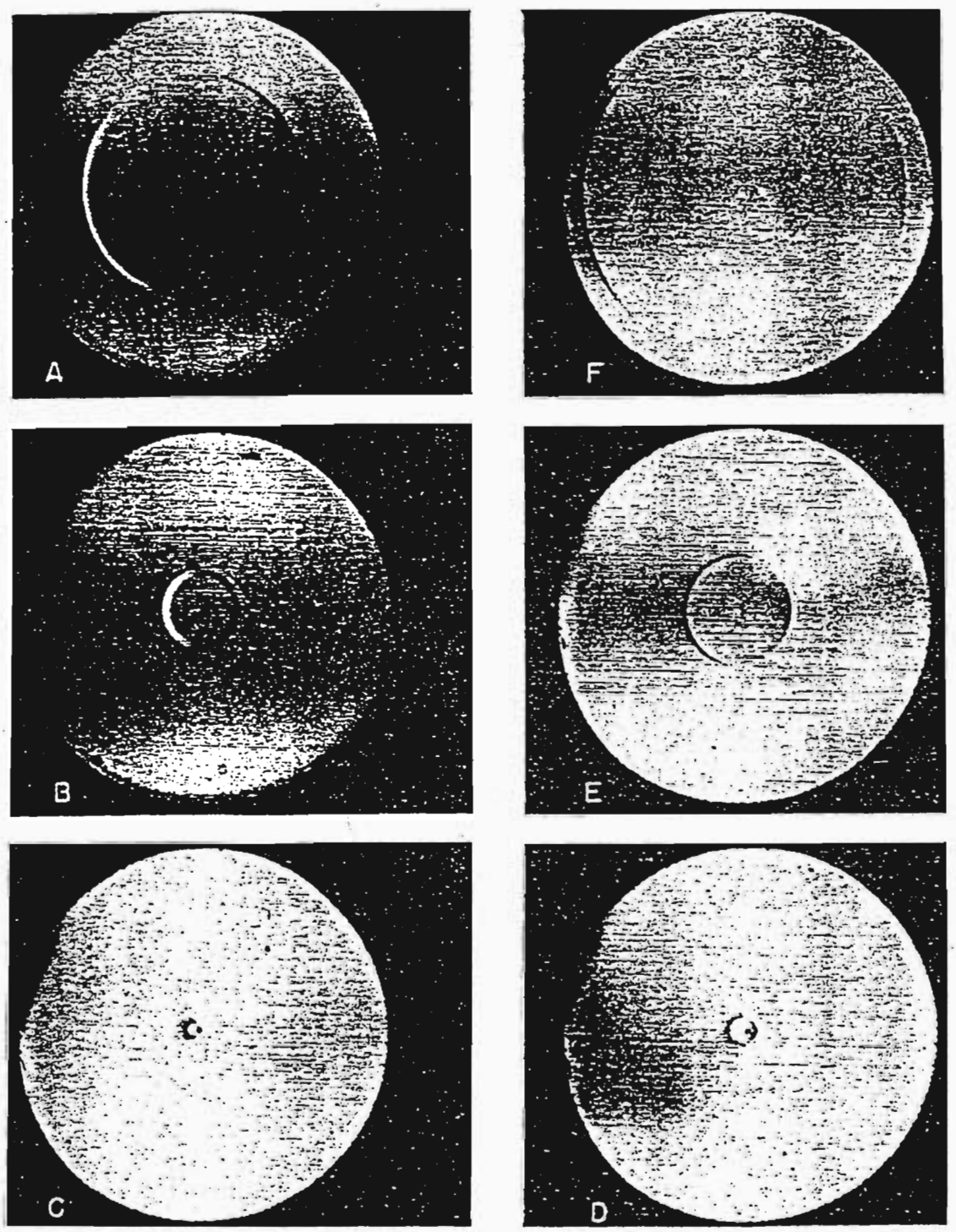

Figure 2.5: Schlieren photographs of converging shock waves in air (obtained from plane shock waves with M = 1.1). Taken from Perry and Kantrowitz (1951)

These experiments demonstrated that converging shocks could be studied with this experimental set-up.

Imploding detonation waves were used by Lee and Lee (1965) to produce imploding cylindrical shock waves. A schematic of the experimental set-up is shown in figure 2.7.

The cylindrical bomb as it was called, consisted of a stainless steel vessel separated into two chambers; the explosion chamber A and the implosion chamber B. The two chambers were separated by a steel centre plate 50cm in diameter and 1cm thick. The bomb is first evacuated and filled with an explosive mixture. A cylindrical diverging detonation wave is initiated in the explosion chamber A by an exploding wire or spark discharge. The centre plate prevents the ignition of the mixture in the implosion chamber B until the diverging wave reaches the annular opening connecting the explosion and implosion chambers. A detonation wave is thus initiated in chamber B. This detonation wave then implodes towards the centre. It was found that symmetrical cylindrical imploding detonation waves can be produced in equimolar acetylene-oxygen mixtures at initial pressures above 150 mmHg. Pressure measurements were carried out and the results demonstrated the self-amplifying characteristic of imploding detonation waves.

Knystautas, Lee and Lee (1969) also used detonation waves to produce converging cylindrical shock waves. However their scheme made use of the concept of Mach reflections. The experimental set-up (see figure 2.8) consisted of 30 equally spaced holes of diameter 1.3cm drilled around its periphery. The holes were joined to a series of equal length plexiglass tubes. A spark gap is placed at the end of each tube. The spark gaps were connected in series and were used to initiate the detonation waves at the ends of the tubes. These detonation waves emerge simultaneously into the cylindrical chamber.

It was found that where any two segments of the polygonal shaped detonation front collide at an angle, a reflected shock is generated. When more points of initiation are used, the polygonal shaped detonation front formed is such that adjacent segments generate Mach reflections. The minimum included angle between two adjacent detonation fronts had to be of the order

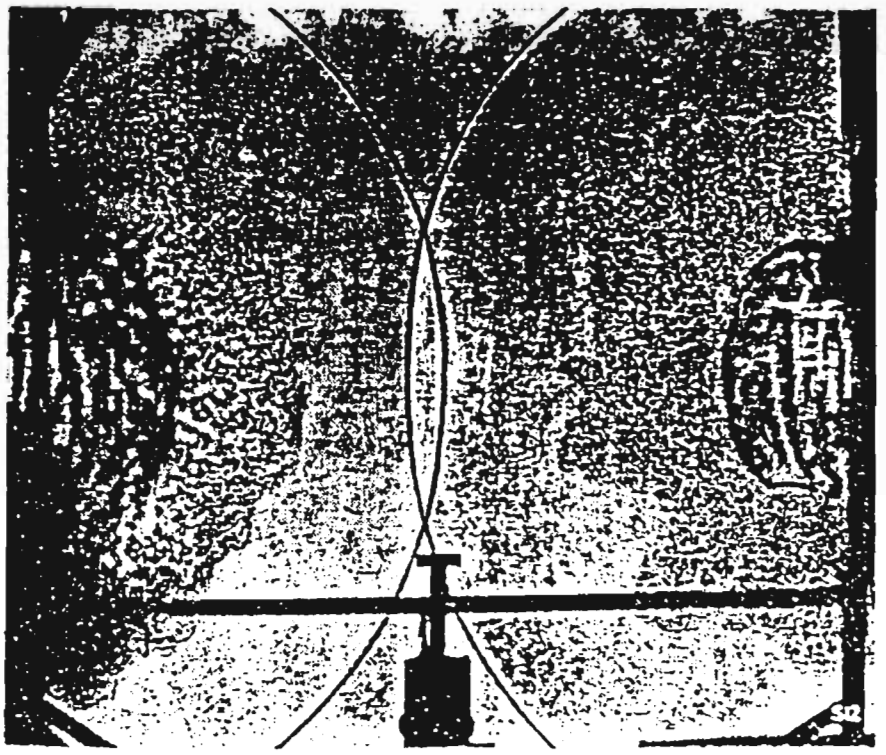

Figure 2.6: Shadowgram of colliding spherical shock waves taken from Glass and Heuckroth (1959)

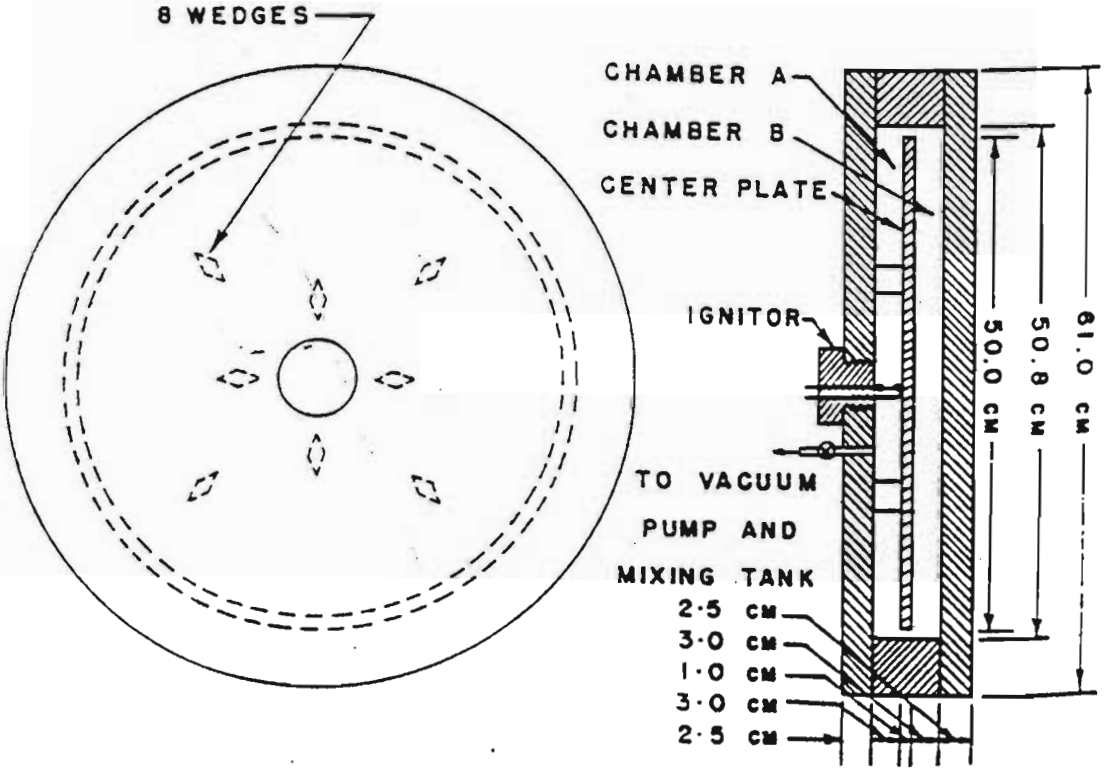

Figure 2.7: Schematic of experimental set-up of Lee and Lee

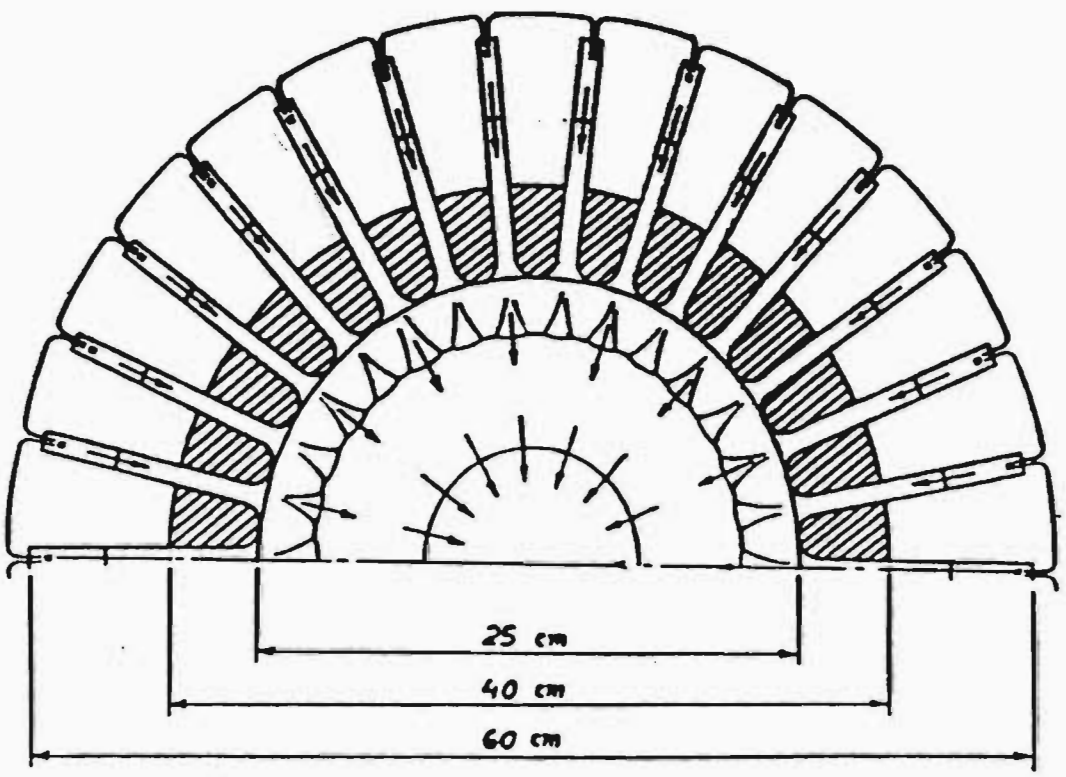

Figure 2.8: Experimental set-up of Knystautas et al. (1969)

of 100 degrees.

The approach to a smooth cylindrical form requires that the reflected shocks attenuate as they propagate in the tangential direction. This attenuation of the reflected shock is referred to as the curvature mechanism by Perry and Kantrowitz (1951). This experiment showed that due to Mach reflections, what started out as a polygonal shaped detonation front smooths itself out into a cylindrically converging detonation front (see figure 2.9).

The experiments described so far demonstrated that stable converging shock (or detonation) waves could be produced. An important aspect of the study to follow was the investigation of the temperatures and pressures on convergence.

Roig and Glass (1977) used converging detonation waves to study the extreme pressures and temperatures at the focus of implosion. The experimental set-up consisted of a hemispherical chamber (see figure 2.10) first described by Flagg and Glass (1968).

Flagg and Glass (1968) investigated the application of implosion wave dynamics to the generation of hypervelocities. Figure 2.11 shows the adaptation of the implosion wave generator (figure 2.10) to an implosion-driven hypervelocity launcher.

The proposed principle of operation was as follows. The implosion would take place in the hemispherical cavity. The launcher barrel was placed such that the bore was coincident with the origin of the hemisphere. The interior of the hemispherical surface was coated with a thin layer of solid explosive. A diaphragm and projectile were positioned at the entrance of the barrel and the rest of the volume was to be filled with a detonable mixture.

It was proposed that the gaseous mixture be ignited by an exploding wire. This would in turn generate an expanding spherical detonation wave (figure 2.11a). On collision with the boundary, an implosive driven imploding shock wave would be generated (figure 2.11b). As it implodes the shock wave would increase in strength. On reflection (figure 2.11c), the wave would leave a region of very high pressure and temperature. It was proposed that the gas in this region could be used as a driver for a hypervelocity launcher or a shock

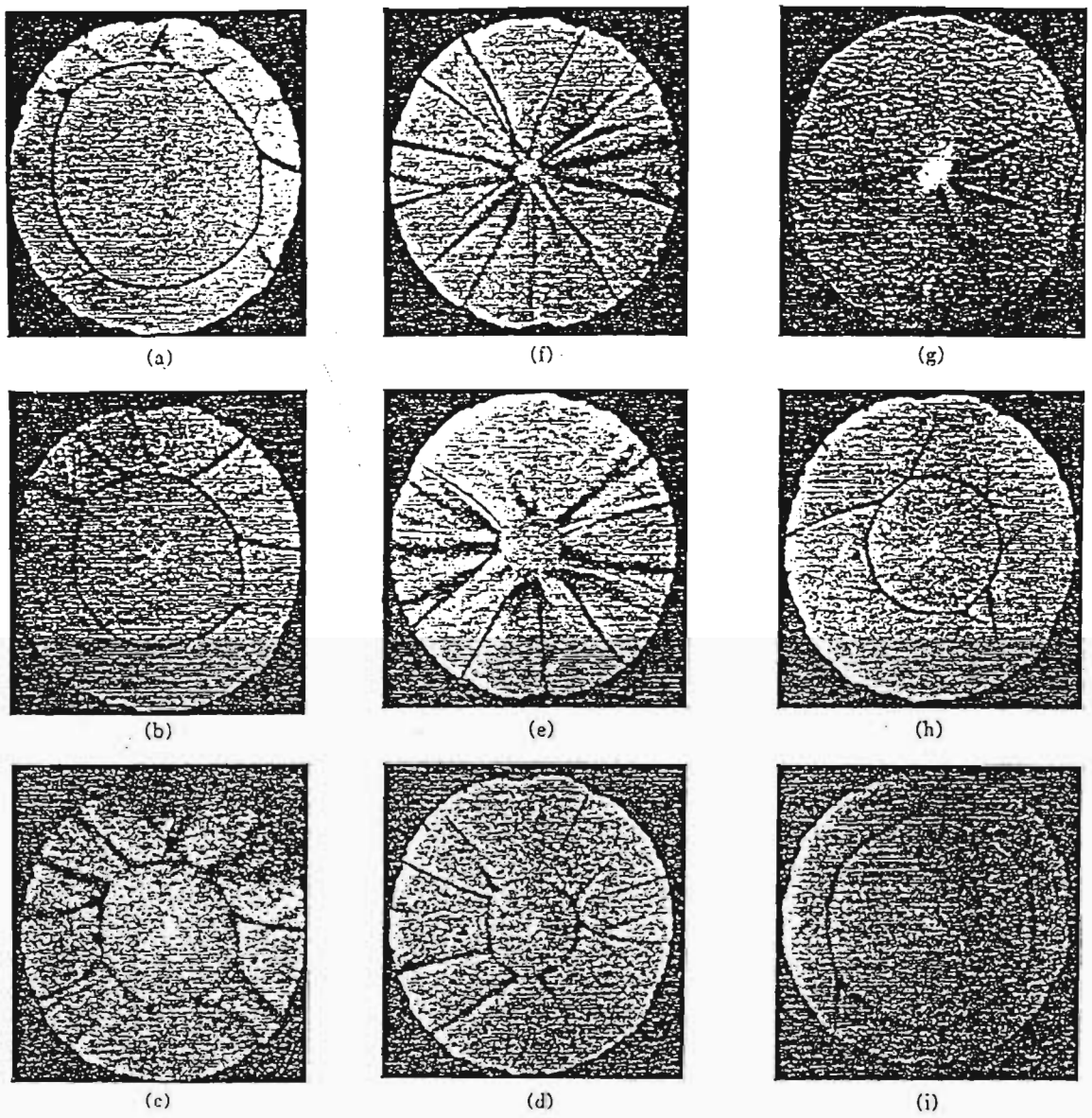

Figure 2.9: Schlieren photographs of an imploding cylindrical detonation wave taken from Kynstautas, Lee and Lee (1969)

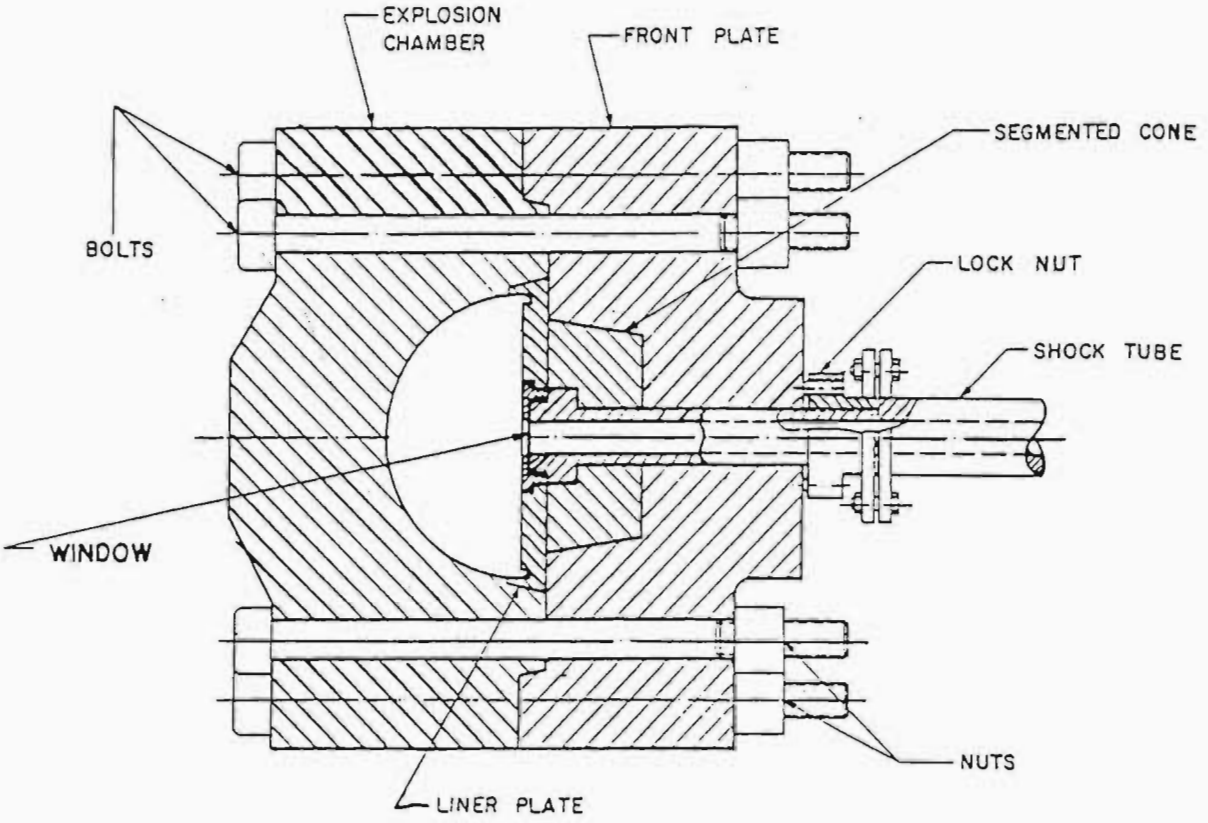

Figure 2.10: Schematic of implosion chamber used by Roig and Glass (1977)

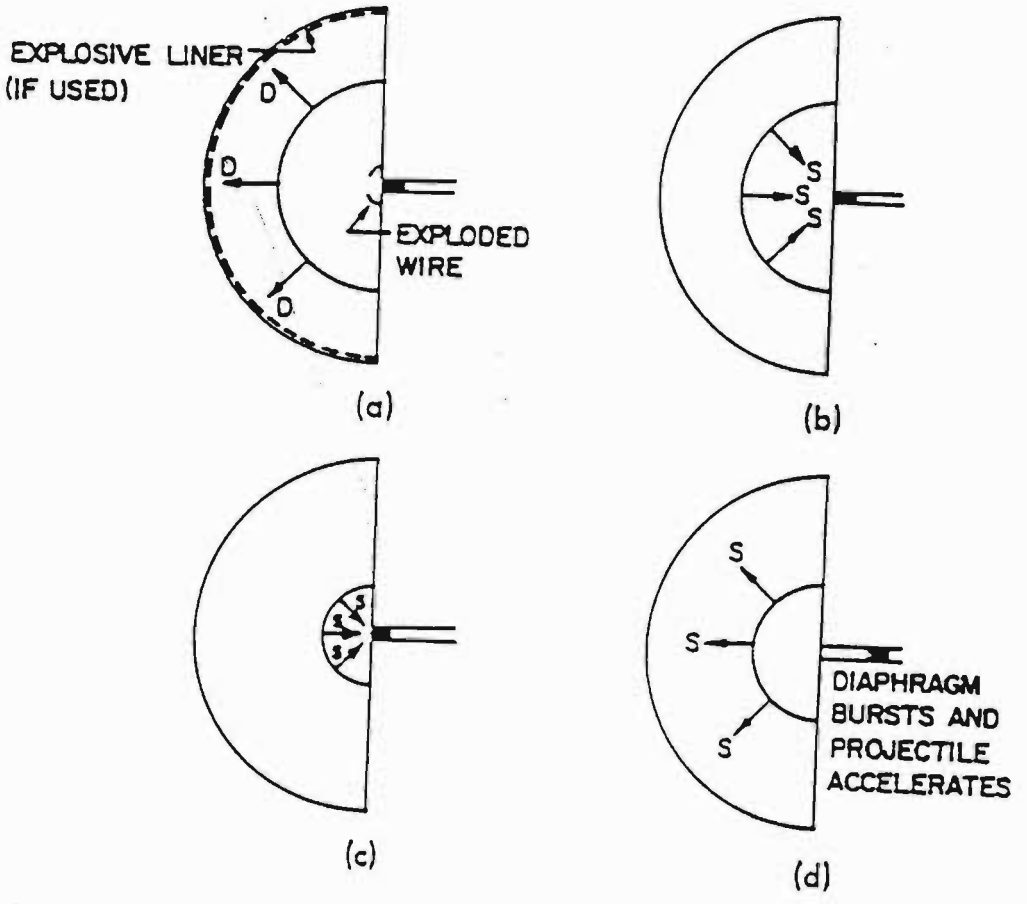

Figure 2.11: Schematic of implosion-generated hypervelocity launcher - after Flagg and Glass (1968)

tube. Flagg and Glass (1968) found that with this scheme they were able to drive plastic projectiles 7.9mm in diameter and 7.9mm long, weighing 356mg to velocities of 17600ft/s.

With the view to study the plasma conditions on implosion, Roig and Glass (1977) filled the hemispherical chamber with a mixture of 2 $H_2 + O_2$ at a pressure between 7 - 56 atmospheres. A thin (4mm) nickel wire located at the origin was exploded causing the gas to ignite. As in Flagg and Glass (1968), this ignition at the origin created a blast wave which decayed into an outward going detonation wave. On reflection from the hemispherical boundary, a converging shock wave resulted. This shock wave propagated into the combustion products at high temperature and pressure.

Time integrated spectra of the implosion region were taken. By monitoring 6 wavelength regimes simultaneously and fitting them to the blackbody curve, the average temperature on implosion was determined. A high pressure piezoelectric transducer located at the origin was used to determine the pressure. It was found experimentally that for an initial pressure of 7 atmospheres, the pressure on implosion was estimated to be 13×10^3 atm and the temperature between 4500 and 6000K.

Matsuo et al. (1980) recognised that although several experimental studies had been performed involving the production and measurement of imploding shock detonation waves, no attempts had been made to produce imploding shock waves in atmospheric air which were strong enough to be self luminous. Matsuo used an imploding chamber consisting of an annular explosive container with 2 end plates to study the behaviour of converging blast waves. See figure 2.12.

The container was made of two coaxial paper cylinders with rubber spacers to plug the top and bottom of the annular space between the two cylinders. In the space surrounded by the two cylinders and spacers, a highly sensitive explosive PETN (pentaerythritoltetranitrate) was loaded. Once detonated (by means of an exploding copper wire), the explosion of the PETN produced cylindrically converging blast waves. It was found that the shocks generated in this way were so strong that the fronts propagating through the air became luminous.

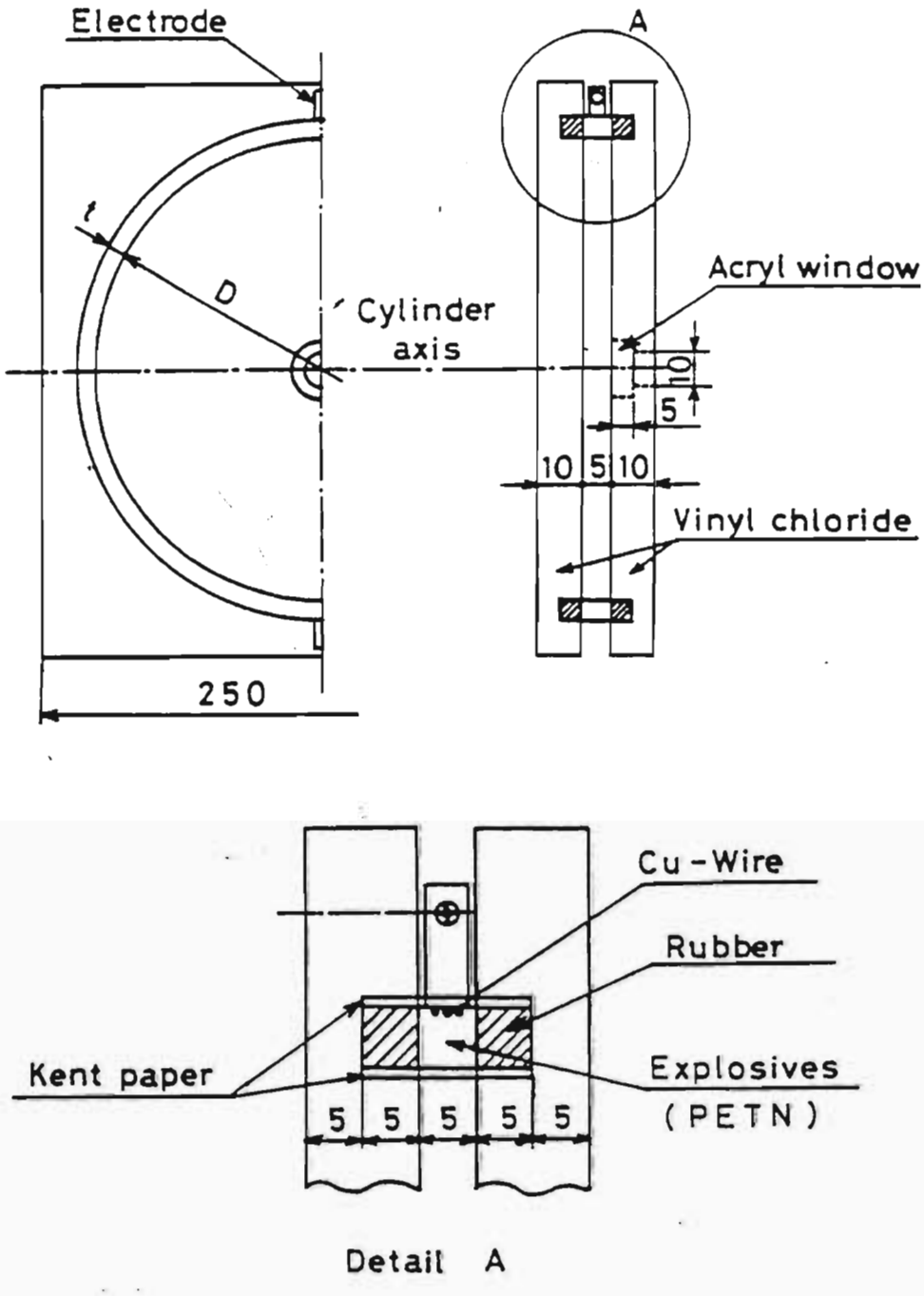

Figure 2.12: Schematic of implosion chamber used by Matsuo et al. (1980)

Using a framing camera, it was found that the luminosity of the shocks increased rapidly towards the axis. It was also shown that the time-space relation of the shock front was approximately represented by Guderleys formulas near the centre of implosion.

Matsuo and Nakamura (1981) using the apparatus described above found that by increasing the explosive thickness, the temperature and pressure at the point of implosion also increased. Experimental results showed that for an explosive thickness of 3mm, a pressure of 355 atm and a temperature of 16400K was obtained. Increasing the thickness to 8mm, the corresponding pressure and temperature were 689 atm and 31400K respectively. Cylindrically converging blast waves were produced in atmosphere by the detonation of PETN shells. The shocks were so strong that the shock fronts were observed to be luminous. A relationship was found between the amount of explosives and the strength of the shocks.

Matsuo et al. (1985), using the above apparatus found the maximum temperature on convergence to be of the order of 15000K with a maximum initial energy of 4.5J. The relationship between final temperature and initial temperature was found to be :

$$\frac{T}{T_o} = 4.93 W_o^{0.52}, \tag{2.31}$$

where T_o is the initial temperature and W_o (kJ/cm) is the initial energy per unit depth of the implosion chamber.

Chapter 3

Scaling up the Colliding Shock Lens

3.1 Historical development of the colliding shock lens

Since most of the work involving converging shocks was directed towards understanding and measuring the high temperature, pressure and density region created at the point of convergence, much attention was given to the implosion stage of the process. Consequently, very little attention was paid experimentally to the expanding stage.

Buccellato, Lisi and Michaelis (1993) proposed the idea of using the density gradient structure of the exploding stage as a graded index lens. Thus the idea of the colliding shock lens was born. This device will be discussed in more detail in the following section.

Up to this point, most experiments involving colliding shock waves used detonations to generate these waves. The colliding shock lens proposed by Buccellato et al. (1993) uses electric discharges to produce converging shock waves. Although much work was done on shocks generated by electric arcs in air (Muraoka et al. (1981), Michaelis et al. (1991a)), to the best of the author's knowledge, they have not been used before for the production of converging shock waves.

3.2 Description of the first colliding shock lens

It was noted by Buccellato et al. (1993) that when two spherical shocks collide, the nature of the interaction is dependent on their relative strengths. Four different conditions can be described.

1. When weak shock waves (low Mach number - M_o) collide, they pass through each other unmodified.

2. When shock waves of intermediate strength collide, it was noted that they also pass through each other but experience some temporal retardation.

3. When stronger spherical shock waves collide with each other, they merge to form a very high density region before moving apart, having lost all information about their pre-collision structure.

4. Finally, when very strong shocks collide, they produce a turbulent region at the point of impact.

Buccellato et al. used the fact that when several spherical shocks expand from points equidistant on a circumference, they generate a cylindrically symmetric converging shock front. This was experimentally verified in 1969 by Knystautas et al., who used multiple converging detonation waves to generate a symmetrically converging circular shock wave (as discussed previously).

Schwendeman and Witham (1987) later found (theoretically) that converging cylindrical shocks with regular polygonal shaped cross-sections are stable and tend towards a circular cross section.

It was also determined that after implosion (convergence), the spherical shock waves produce a stable axi-symmetric cigar shaped density structure. Buccellato et al. used this region as a graded index lens.

The very first CSL designed by Buccellato and Michaelis consisted of four pairs of opposing electrodes equi-spaced on the circumference of a circle 11mm in diameter. This was quickly replaced by eight pairs of electrodes

as described by Buccellato et al. (1993). These electrodes were mounted on two opposite plates of plexiglass with a circular hole of 7.5mm diameter in the centre for the probe beam to pass through. The electrodes in this prototype CSL consisted of sewing needles of diameter 0.85mm. An arc gap of 1mm was used between opposing electrodes and it was at this junction that the spherically expanding shock waves were generated. Figure 3.1 is a schematic representation of the colliding shock lens showing the laser beam, the effective lens (cigar shaped region) and the focussed spot.

Figure 3.2 is a schematic representation of the experimental set-up used by Buccellato et al. (1993). The gaps of the CSL were connected in series to a charging capacitor C. The value of this capacitor determines the input energy into the shocks. A spatially filtered nitrogen laser beam (FWHM 1ns) was directed through the centre of the CSL onto the face plate of a TV camera. The triggering of the CSL and the frame grabber was synchronised by a PC. A Rogowsky coil in the discharge circuit triggered the nitrogen laser via a variable delay box. A more complete description will be given in the sections to follow.

3.2.1 Results

Buccellato et al. investigated the properties of the prototype CSL. Figure 3.3 shows a time sequence for the colliding shocks imaged in the collision plane. Focusing is achieved in figs 3.3h and 3.3i.

It was also found that with this device, the laser beam could be focused down to a spot size of 100μm (FWHM) at a distance of 39cm. This FWHM spot diameter represents an energy of less than 40% of the energy encircled in the central lobe in the focal plane. Figure 3.4 shows the burn pattern at a distance of 39cm. Note that the size of the central lobe is of the order of 500μm. This lobe contains approximately 84% of the near field energy.

However, the effective lens diameter was found to be of the order of 1.5mm. A millimetric gas lens is useless. A centimetric CSL would have many industrial applications. A decimetric pulsed gas lens could serve as the final focusing element for a laser fusion reactor (Michaelis et al. (1991)). Much of the work to follow has been an attempt to scale up the CSL.

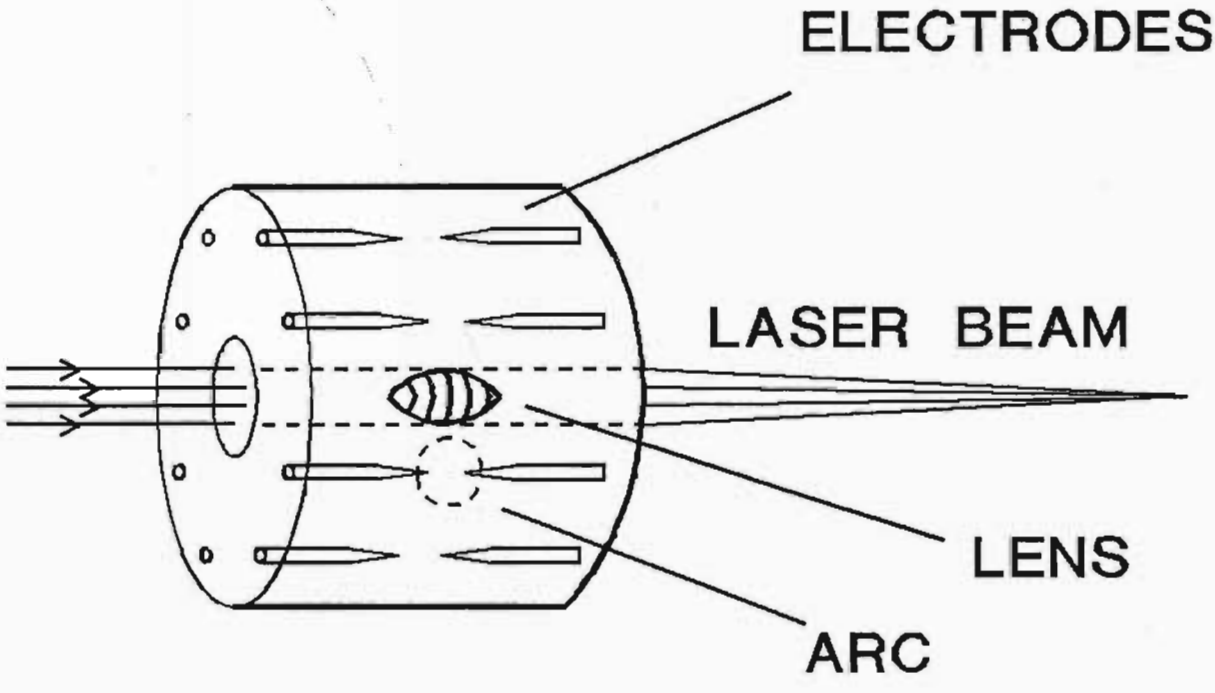

Figure 3.1: Schematic of first CSL

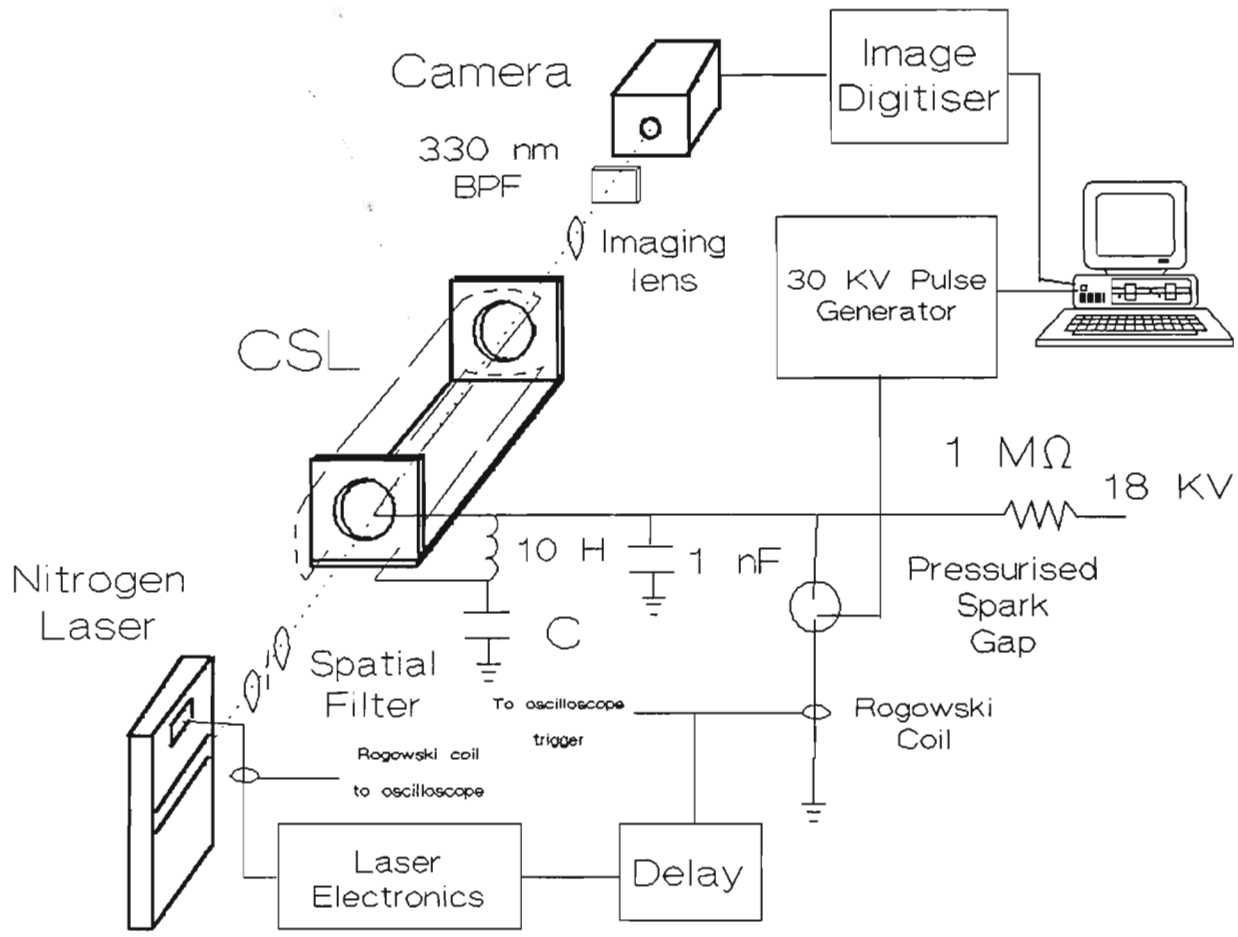

Figure 3.2: Schematic representation of colliding shock lens (CSL) experimental set-up from Buccellato et al. (1993)

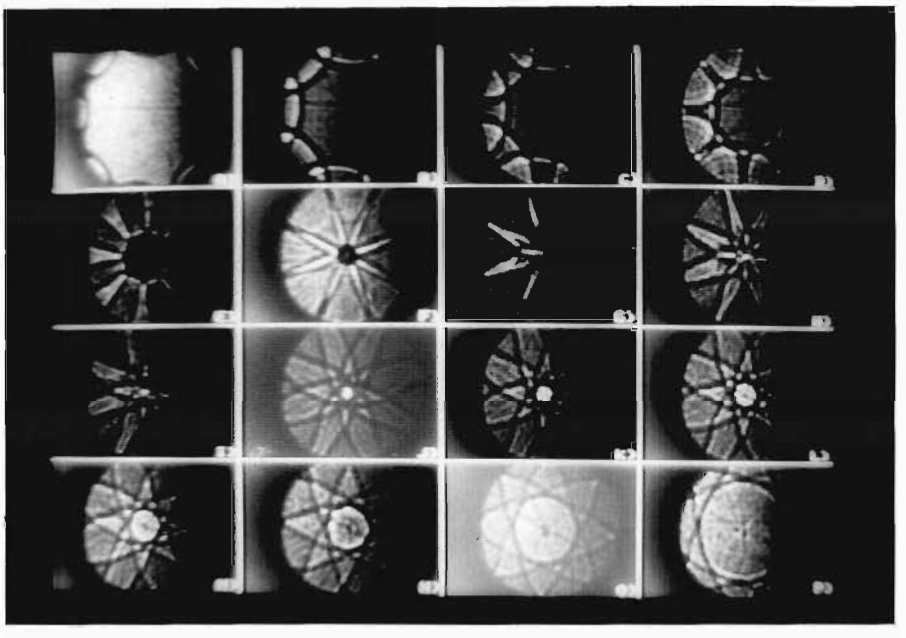

Figure 3.3: Time sequence of the eight arc CSL from Buccellato et al. (1993)

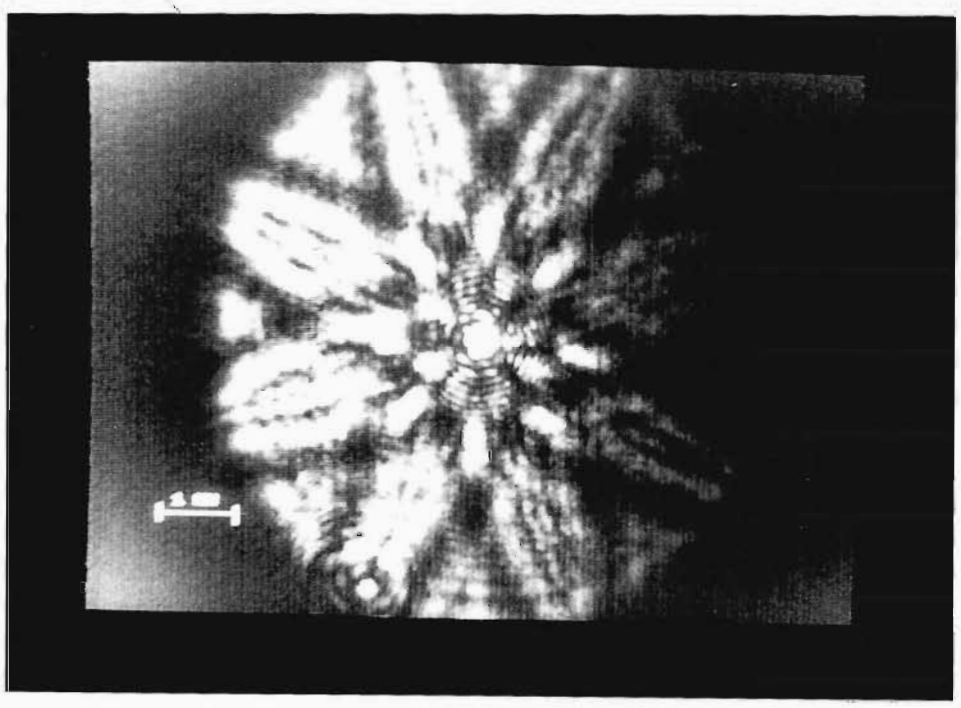

Figure 3.4: Eight arc CSL focal spot (focal length 39cm, delay 11.8μs) from Buccellato et al. (1993)

3.3 Scaling up the colliding shock lens

As mentioned above, the first CSL had too small an aperture to be useful, although its optical quality seemed promising. But it did serve to pose the question: could the CSL be scaled up ? Two contradictory arguments were put forward.

According to the pessimistic view, refraction towards the focus is caused only by the narrow shock front gradient. This view is supported by the refractive fringe study of shocks by Bacon et al. (1989) and Michaelis et al. (1991b) and is illustrated by fig. 3.5 in which the weak shocks have passed through each other, virtually undisturbed. According to this view, the lens would only work so long as the separating shock fronts are not too far apart, which could explain why the first lens has a millimetric aperture. The aperture of the CSL would not scale up beyond a small geometric factor times the shock front thickness.

The optimistic counter-argument runs as follows. The central collision of converging shocks produces a region of high density in which all "memory" of the early shocks is erased by non-linear effects. This view is supported by the post collision frames of figure 3.3 which show a circular rather than polygonal expansion front. This front may have a weaker gradient than the initial shocks and is therefore broader. The angular deflection of a ray being low, it is permissible to integrate the density along the ray, assuming that the ray's radial position doesn't change inside the lens. Integration of the hollow cigar gives the familiar lenticular shape (figures 3.6 and 3.14).

Although it is true that only the front refracts light "inwards", the gradient of the shock rear is not strong enough to cancel the effect of the front. Gas inside the cigar plays a compensatory role which cannot be forgotten as in the first argument.

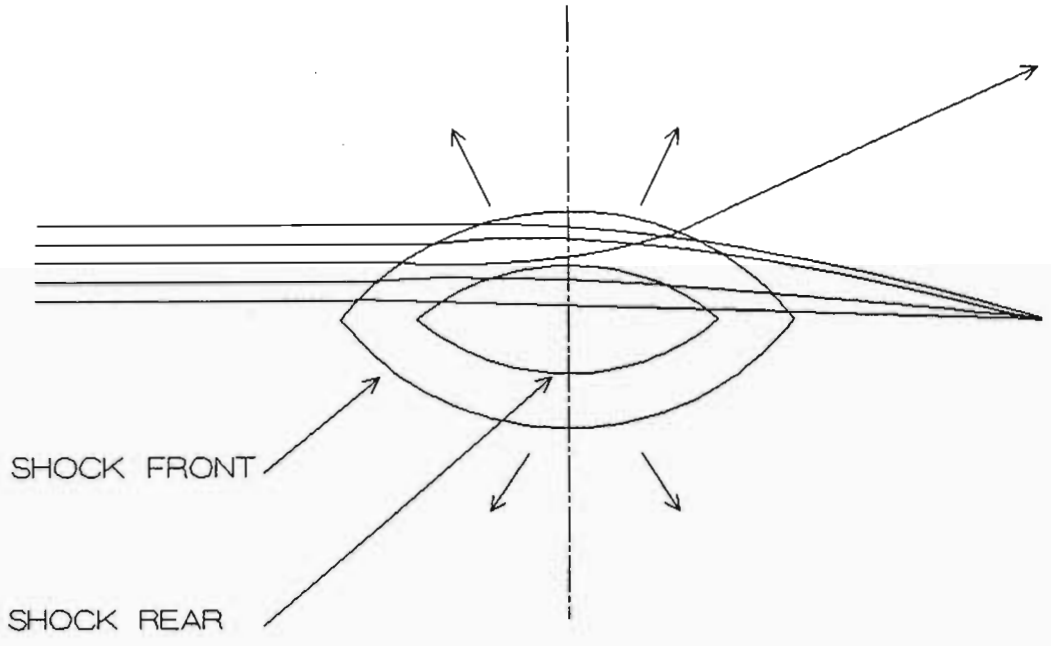

Figure 3.5: Schematic showing lensing properties of shocks which have passed through each other undisturbed - after collision.

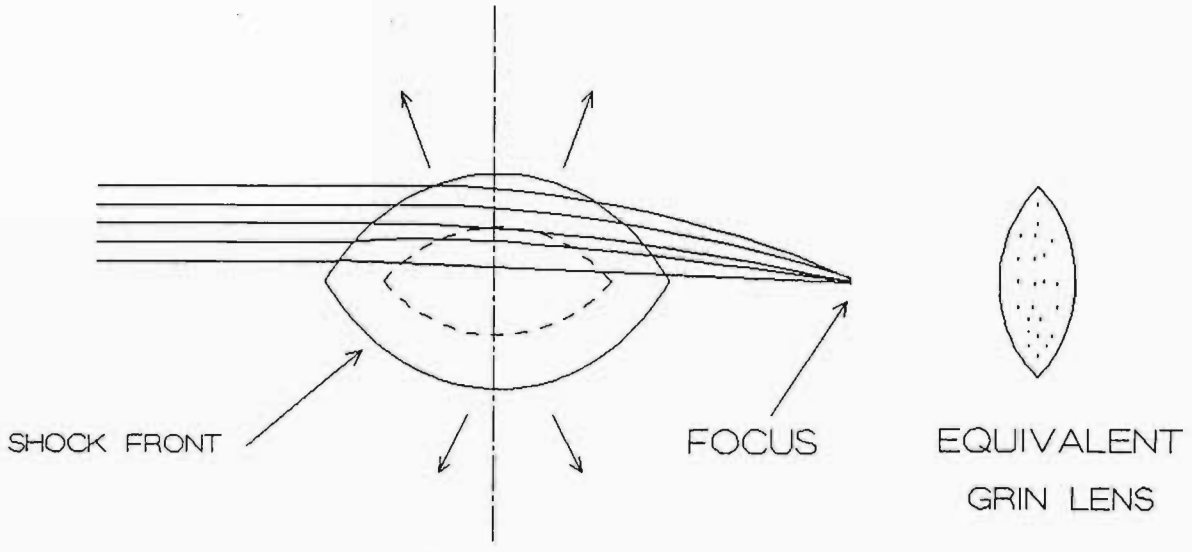

Figure 3.6: Schematic showing lensing properties of shocks after collision where the shocks have lost all "memory".

3.3.1 Experimental apparatus

The experimental apparatus used for the following set of experiments was the same as that used by Buccellato et al. (1993). Figure 3.2 is a schematic representation of the circuit in which C refers to the charging capacitor which is discharged through the electrodes of the CSL. The CSL consists of two 5mm thick plexiglass plates which support eight or sixteen pairs of opposing electrodes. (The plates can be either square as in fig. 3.2, or circular as in fig. 3.1). The separation between the plates can be adjusted from 1cm to 4cm.

The electrodes used in this experiment are constructed from 0.5, 1 or 2mm diameter stainless steel pins depending on the maximum energy to be stored in the capacitor. The electrode separation was always set at 0.5mm. The electrodes are connected in series to ensure that the gaps break down simultaneously. A circular window is cut out of each of the plexiglass plates to allow a nitrogen laser beam (337nm) to be shone through. It is with this beam that the properties of the CSL are studied.

The charging capacitor (C) is initially charged to 18kV through a 10H inductor by means of a high voltage dc power supply. A 5V computer signal triggers the pulse generator resulting in a 30kV pulse of 1μs duration being sent to the extra electrode of the pressurised spark gap. This causes the spark gap to break down pulling one side of the CSL to ground. The 1nF capacitor provides the initial energy to break down the spark gap. The potential difference across the CSL produces the ring of simultaneous arc discharges. Each of these arcs generates an expanding spherical shock wave. The expanding shock waves collide at the centre of the CSL and a high pressure, temperature and density region is created. We call this the "implosion stage". A short time (of the order of microseconds) after collision, the expansion of this high density region results in the axi-symmetric "cigar" shaped density distribution which forms the graded index lens.

The detection circuit for this experiment is capable of detecting either the shock structure at various times or the focal spot for different focal lengths. This is accomplished in the following way :

A Rogowsky coil in the CSL discharge circuit sends a signal to a delay

box when the CSL "fires". This signal is then delayed and used to trigger the spatially filtered and expanded nitrogen laser beam. The beam then passes through the windows of the CSL before falling on the face plate of a CCD camera and is digitised by means of an Oculus 200 frame grabber. A 330nm interference filter with a bandwidth of 10nm is placed in front of the camera to select out the nitrogen beam from the light generated by the arcs. To study the behaviour of the shock waves, a convex lens is used to image in the shock plane (fig. 3.2). By varying the delay of the nitrogen laser one obtains a sequence of shadowgrams for the shock waves, from convergence through to collision and finally divergence. This enables us to calculate the size of the lensing region formed by the cigar.

By removing the imaging lens and allowing the laser beam to fall directly on the face plate of the camera, the quality and size of the focal spot can be evaluated for different focal lengths. The experimental spot size is calculated by measuring the horizontal diameter of the central lobe of the focused pattern in the focal plane. This diameter corresponds to the extent of the Airy disk. In some cases, the focal spot diameter is also quoted as a full width at half maximum (FWHM) value.

To avoid confusion in the terminology, we henceforth refer to the maximum diameter of the cigar shaped lensing region as the *optical aperture* of the lens, to the plexiglass structure incorporating the electrodes as the CSL, and to the diameter of the circle of electrodes as the *electrical diameter*.

To characterise the CSL one must determine the extent to which the various parameters (energy, electrical diameter, number of electrodes, wall geometry) affect the optical aperture, the focal length and the quality of the focus. To this end the following parameters were varied :

A. Shock strength

The first question that needs to be answered is how the shock strength affects the lensing region. In our experiments, the shock strength can be varied in one of two ways :

i) Either by changing the charging voltage applied to the charging capacitor or

ii) By changing the capacitance of the charging capacitor whilst keeping the charging voltage constant.

Changing the charge voltage would have allowed a greater range of energies ($E=1/2\ CV^2$). However, since it is imperative that the energy remains constant on a shot to shot basis, it was found that given the experimental apparatus at our disposal, changing the capacitance allowed better control over the input energy.

B. Electrical diameter

Like the shock strength, changing (increasing) the electrical diameter is an obvious change to effect in order to achieve a larger effective lens diameter. The relationship between the electrical diameter, shock strength and other parameters with the optical aperture needed to be determined. The electrical diameter in this experiment is increased by using different CSLs. Four CSLs were constructed. Including the CSL used by Buccellato et al. (1993), we therefore had five CSLs at our disposal. The electrical diameters ranged from 11mm for the smallest one to 160mm for the largest device.

C. Number of electrodes

Knystautas, Lee and Lee (1969) showed that due to Mach addition, a polygonal detonation structure would approach a smooth cylindrical converging detonation wave (see chapter 2). We have also seen that in order for Mach reflections to be generated, the minimum included angle between any two colliding fronts must be of the order of 100 degrees. Hence for different CSLs having different electrical diameters, it was recognised that it might be necessary to change the number of electrodes (either increase or decrease) in order to satisfy the Mach reflection criterion and hence maintain a smooth cylindrical convergence.

D. Enclosure

We were initially unsure whether confining the shocks in some way would affect the quality of lensing. The first CSL (Buccellato et al. 1993) consisted of "side walls" (as we have already seen). The sole purpose of these walls were to hold the electrodes in place. The shocks in this device could be seen to be largely "unconfined". In this respect we experimented with **enclosed** and **unenclosed** CSLs. The term **unenclosed** is used to describe a CSL

of the Buccellato type. The **enclosed** CSL was constructed by encasing the unenclosed one in a perspex tube. In some cases the wall separation is reduced.

E. Pressure and Gases

Intuitively, one would expect that by raising the ambient operating pressure of the CSL, one could achieve an increase in density of the shock front as compared to a lower ambient pressure (atmospheric in this case) for the same input energy. This increase in density would cause the same CSL to have a shorter focal length hence better lens quality.

During the course of this work the terms *lens quality* and *f number* will be interchanged. This is based on the assumption that for the purposes of scaling, a low f number is what is sought.

Since the colliding shock lenses have up to this point only been operated at atmospheric pressure, by virtue of their construction, they are not equipped to facilitate a change in ambient pressure. A pressure chamber was constructed (see figure 3.7) to effect this change. The chamber is 250mm in diameter and 390mm long. Two quartz end windows 130mm in diameter were fitted at either end to allow the Nitrogen laser beam through. An observation window was installed at the top to check on the alignment of the CSL. The CSL to be studied is simply placed inside the chamber which is then placed on the optical rail in line with the probe laser beam and diagnostic optics. The two inlet/outlet valves allow for the input of gases at varying pressure.

The chamber itself (with aluminium blanks fitted where the windows now reside) was tested to a pressure of 10 bar above atmosphere. The quartz windows however are designed to handle a maximum of 5 bar. We therefore varied the pressure up to a maximum of 2 bar relative (3 bar absolute). Using the same apparatus we were in a position to study the behaviour of the CSL using different gases. The gases used were air, CO_2 and Ar. An attempt was made to operate the CSL using He as well. This will be discussed later.

It should be pointed out that the size of the chamber was based on our best CSL at the time of construction (CSL3). Since subsequent CSLs have performed better (to be discussed later), CSL3 was used to demonstrate the

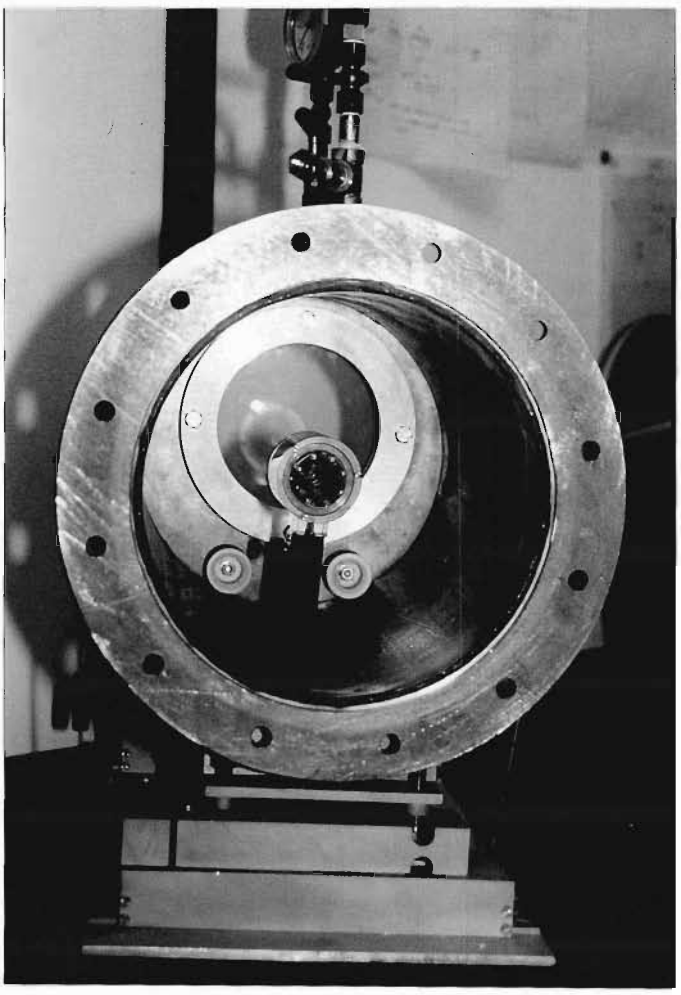

Figure 3.7: Photograph showing the chamber constructed for CSL pressure and gas studies.

effect of changes in pressure in gases. These principles can then quite safely be translated to the better devices.

We now present a summary of the physical characteristics of the five CSL's used to test the abovementioned concepts. The CSL's will be labelled CSL1-5.

CSL1 : This is the original CSL (see Buccellato et al. (1993)). It has 8 pairs of electrodes arranged on a circle of diameter 11mm. The diameter of the windows is 7.5mm. CSL1 is unenclosed. See figure 3.8.

CSL2 : This CSL (figure 3.9) has an electrical diameter of 33.5mm and the window diameter is 11mm. This second unenclosed CSL, has 8 pairs of electrodes. The wall separation was variable from 40mm to 10mm. A separation of 40mm was used when comparisons with CSL1 were made and a separation of 10mm was used when comparisons with CSL3 were made.

CSL3 : To see how enclosing the CSL would affect its lensing properties, we constructed a CSL with the same electrical diameter and windows as the preceding one, but enclosed in a plexiglass cylinder of diameter 40mm. This CSL (figure 3.10), like the preceding two is also fitted with 8 pairs of electrodes. The wall separation was reduced from 40mm to 10mm.

CSL4 : This CSL (figure 3.11) has an electrical aperture of 80mm and a window diameter of 50mm. The distance between the endplates is 21.5mm and the diameter of the plexiglass tube is 120mm. This lens can be fitted with either 8 or 16 pairs of electrodes.

CSL5 : This final CSL (see figure 3.12) was constructed in an attempt to obtain a really large lens diameter. The electrical aperture is 160mm. The wall separation is 65mm and the optical window is 110mm in diameter. The electrodes used in this lens are constructed from 8mm diameter steel bolts.

3.3.2 Results and discussion

In order to better understand the scaling results we first briefly re-examine the process of graded index lens formation.

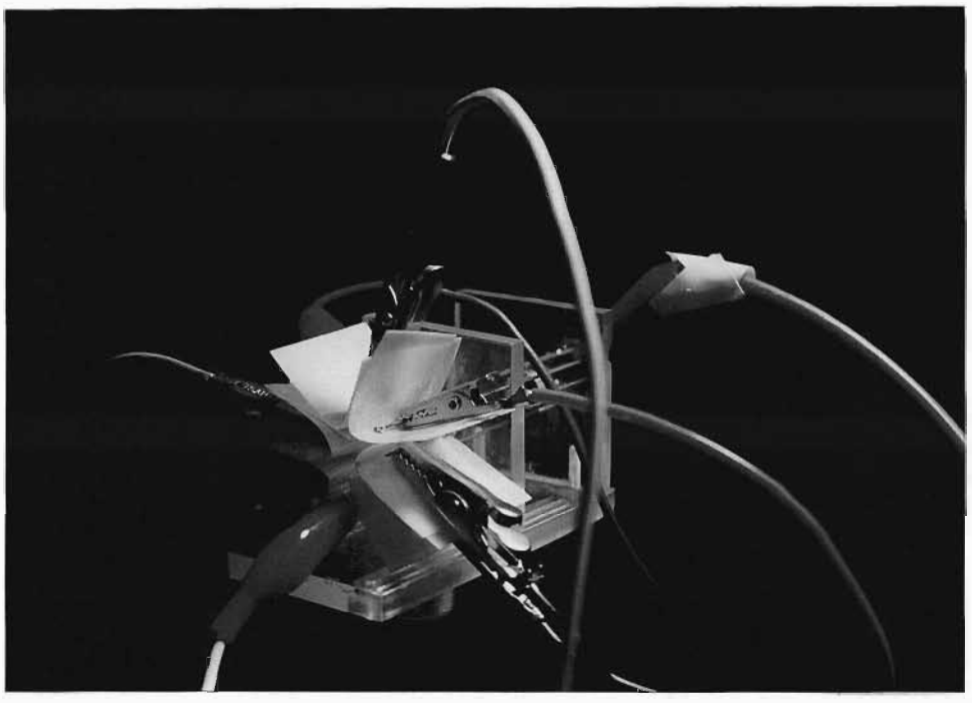

Figure 3.8: Photograph of CSL1

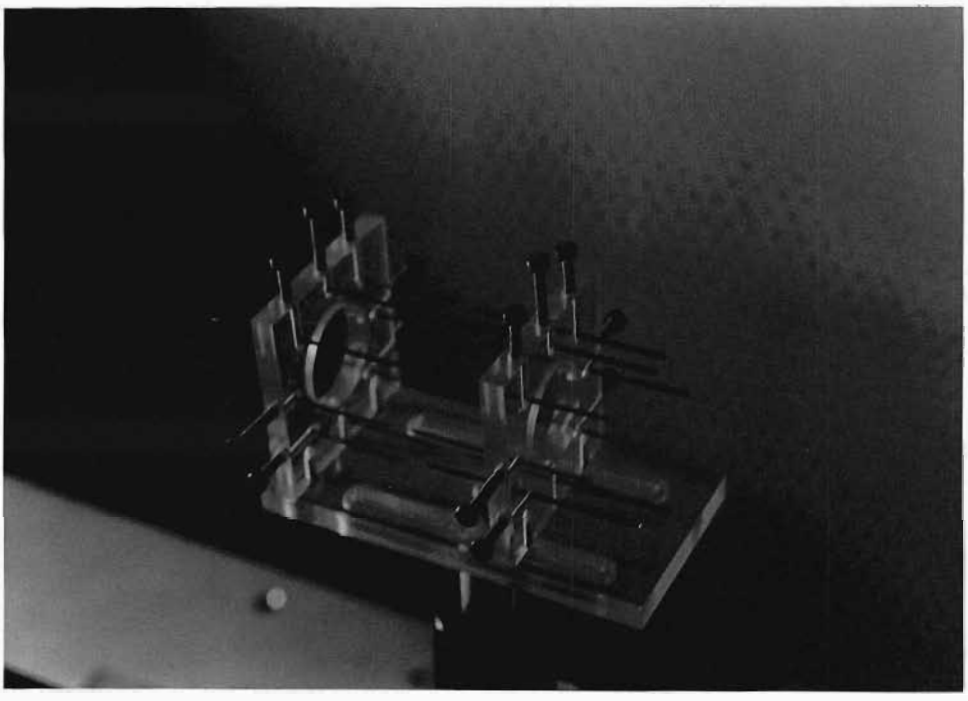

Figure 3.9: Photograph of CSL2

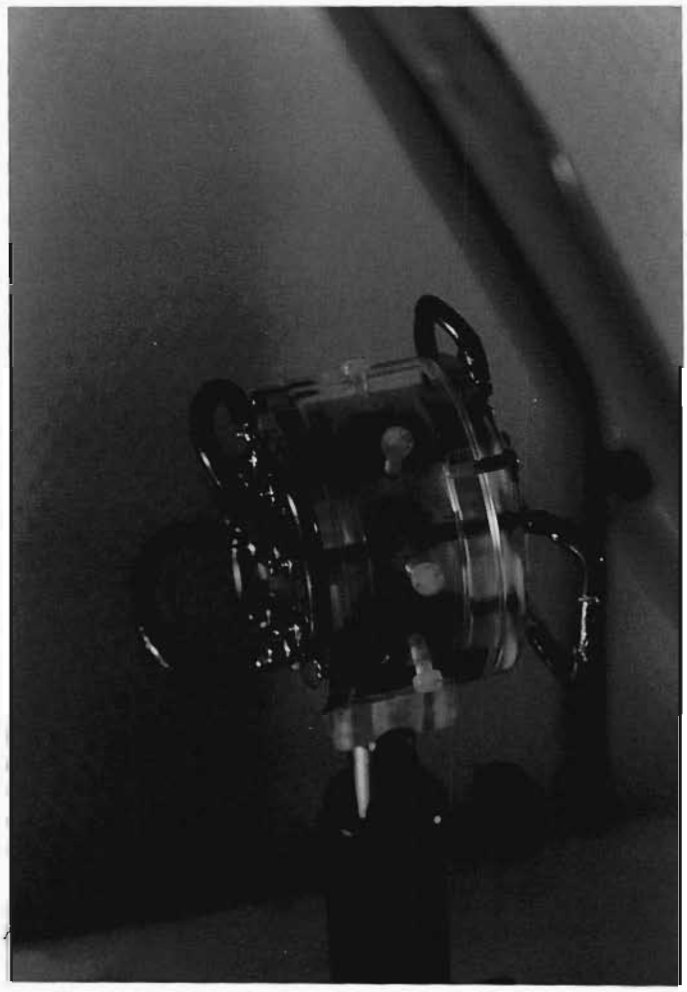

Figure 3.10: Photograph of CSL3

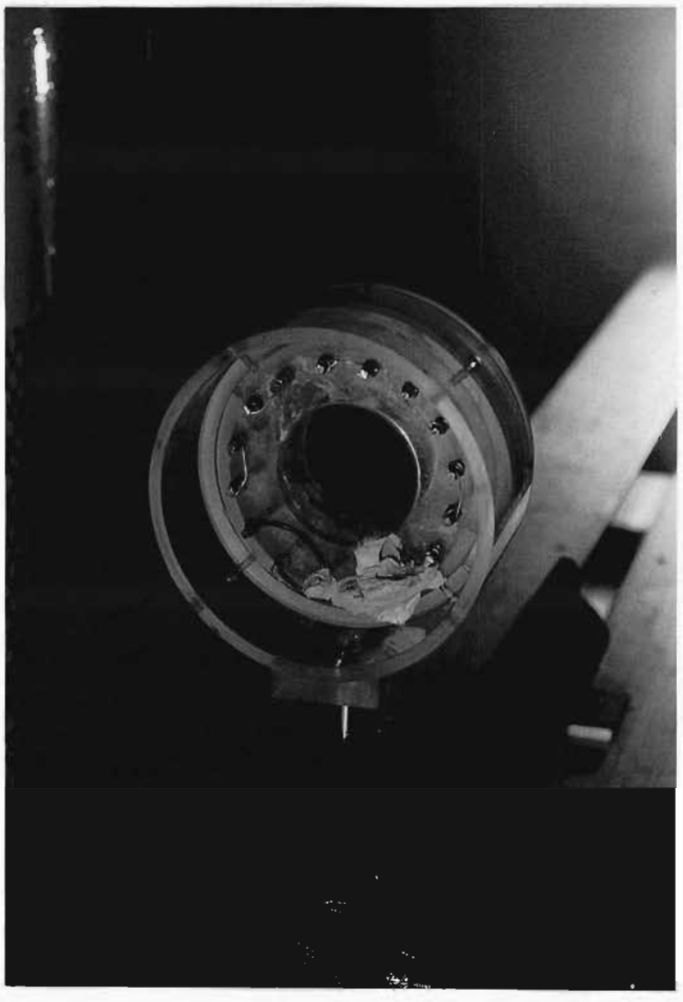

Figure 3.11: Photograph of CSL4

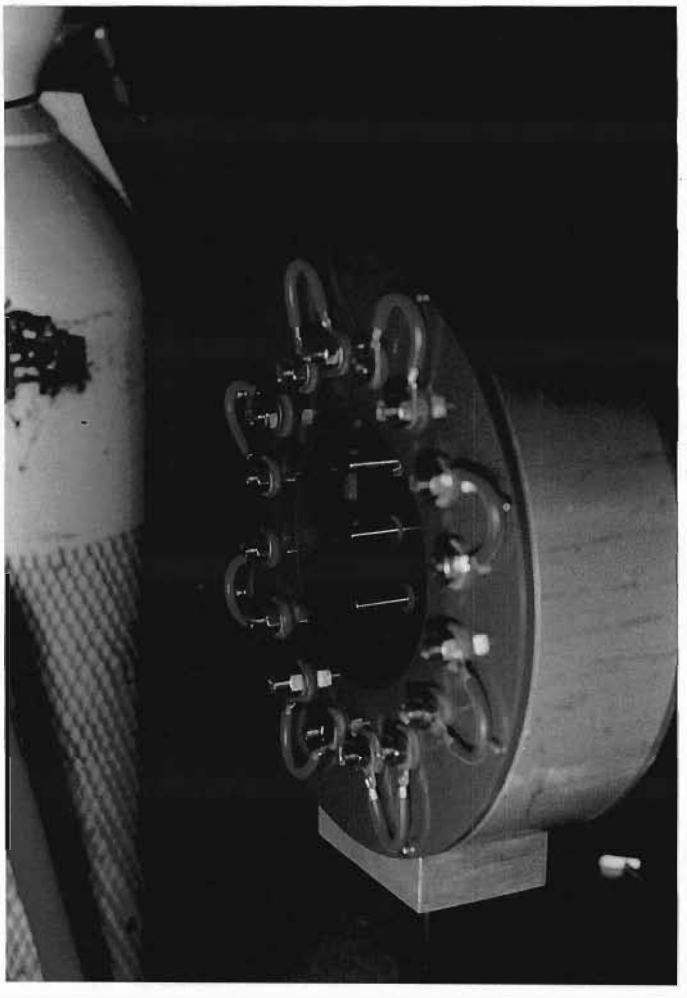

Figure 3.12: Photograph of CSL5

When the pressurised spark gap in the CSL power supply breaks down, the electrical discharges between opposing pairs of electrodes in the CSL act as point sources for spherically expanding shock waves. As mentioned before, these shock waves collide at the centre of the CSL. On collision of two or more shock waves, a high density, pressure and temperature region forms. In our experiments where M $\approx$ 1.5, we do not expect the region to become turbulent, except for higher energies, as explained below. This region then expands to form the cigar shaped region already described. Fig. 3.13 is a computed density profile (from Buccellato (1994)) that results during the expansion phase. Only half the lensing region or "cigar" is shown. The refractive index increases sharply near the edges of the "cigar" and a depression is visible in the centre.

Although this profile looks extraordinarily complicated, its computation allows one to verify the following statement, which simplifies the ray optics. There are virtually no radial deviations within the lens. This is because the refractive index differs from unity by less than one percent and the refractive index gradients and the angular deflections are small (less than 5 degrees). To calculate the latter, it suffices to integrate the density along the path of each fixed radius paraxial ray. The complicated profile then reduces to the familiar lenticular shape (fig. 3.14). The central "hole" may be computational.

We now compare the performance of various lenses.

Typical parameters reported for the first eight arc colliding shock lens (1) were an optical aperture of 1.5mm for a focal length of 39cm and 2mm for a focal length of 52cm. The input electrical energy was 0.8J. (C = 5nF). Figure 3.15) (after Buccellato et al. (1993)) shows the FWHM spot diameters as a function of time for the first CSL.

The following presentation of results will follow the chronological development of the various CSLs.

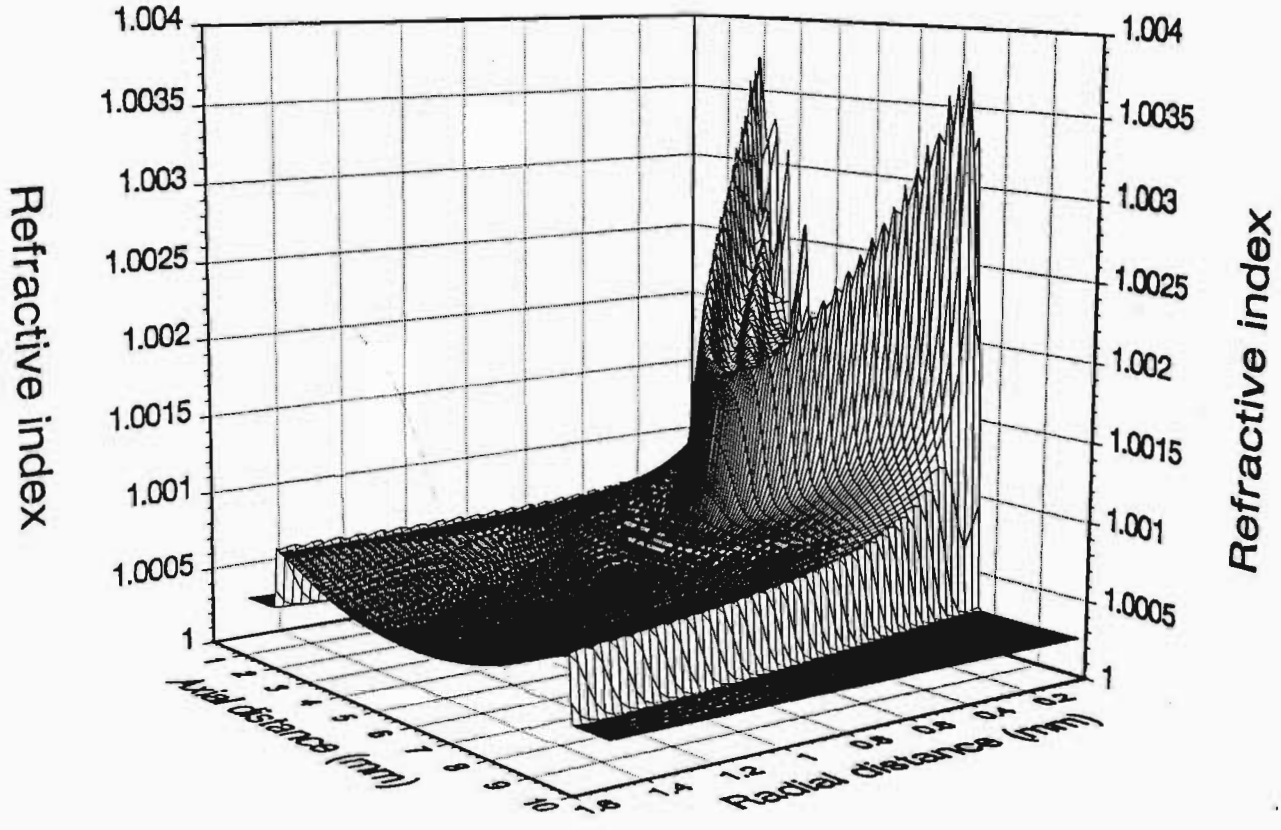

Figure 3.13: Computed refractive index field of the CSL $1\mu s$ after initial shock wave reflection.

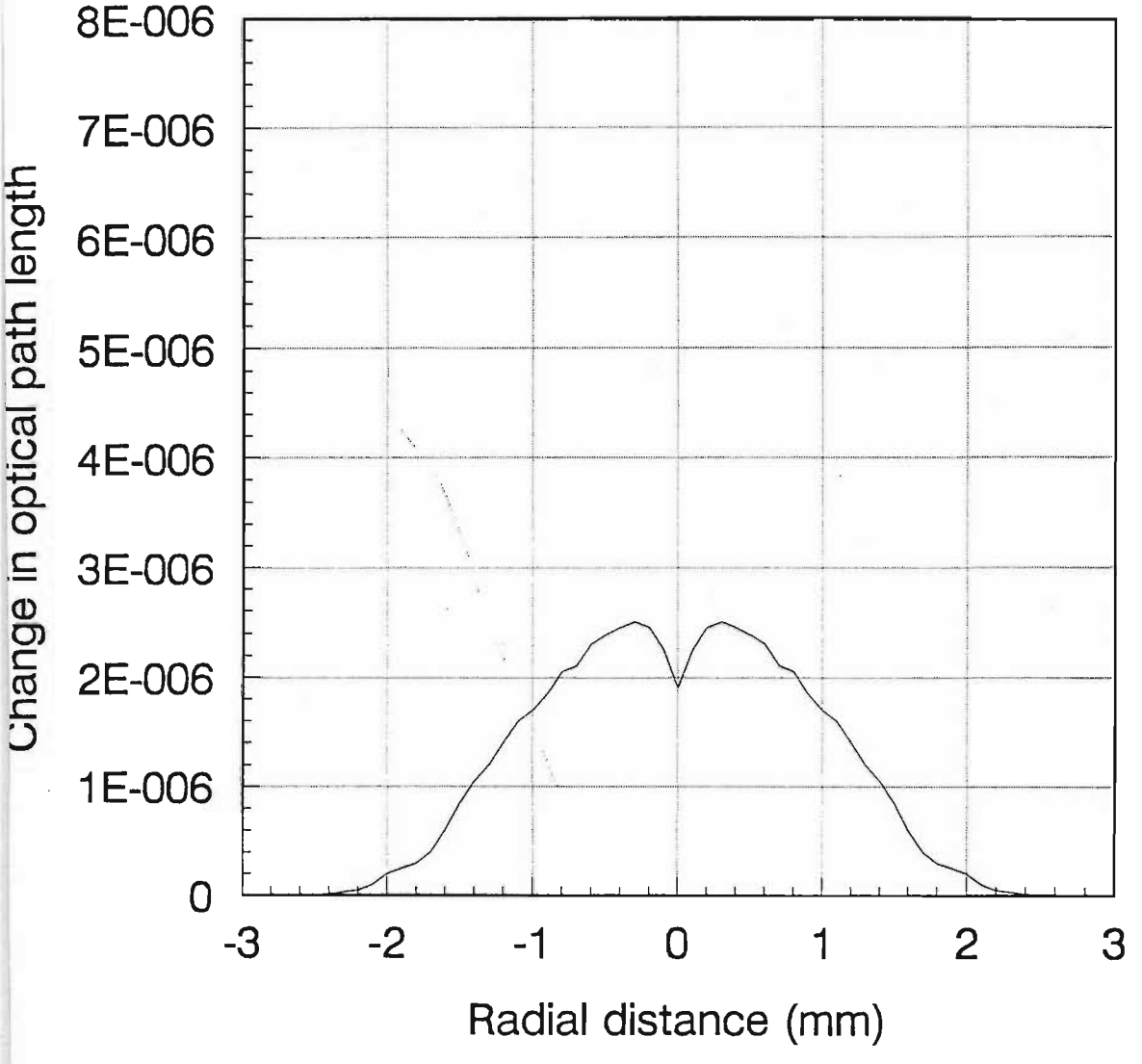

Figure 3.14: Integrated optical path difference obtained using figure 3.13

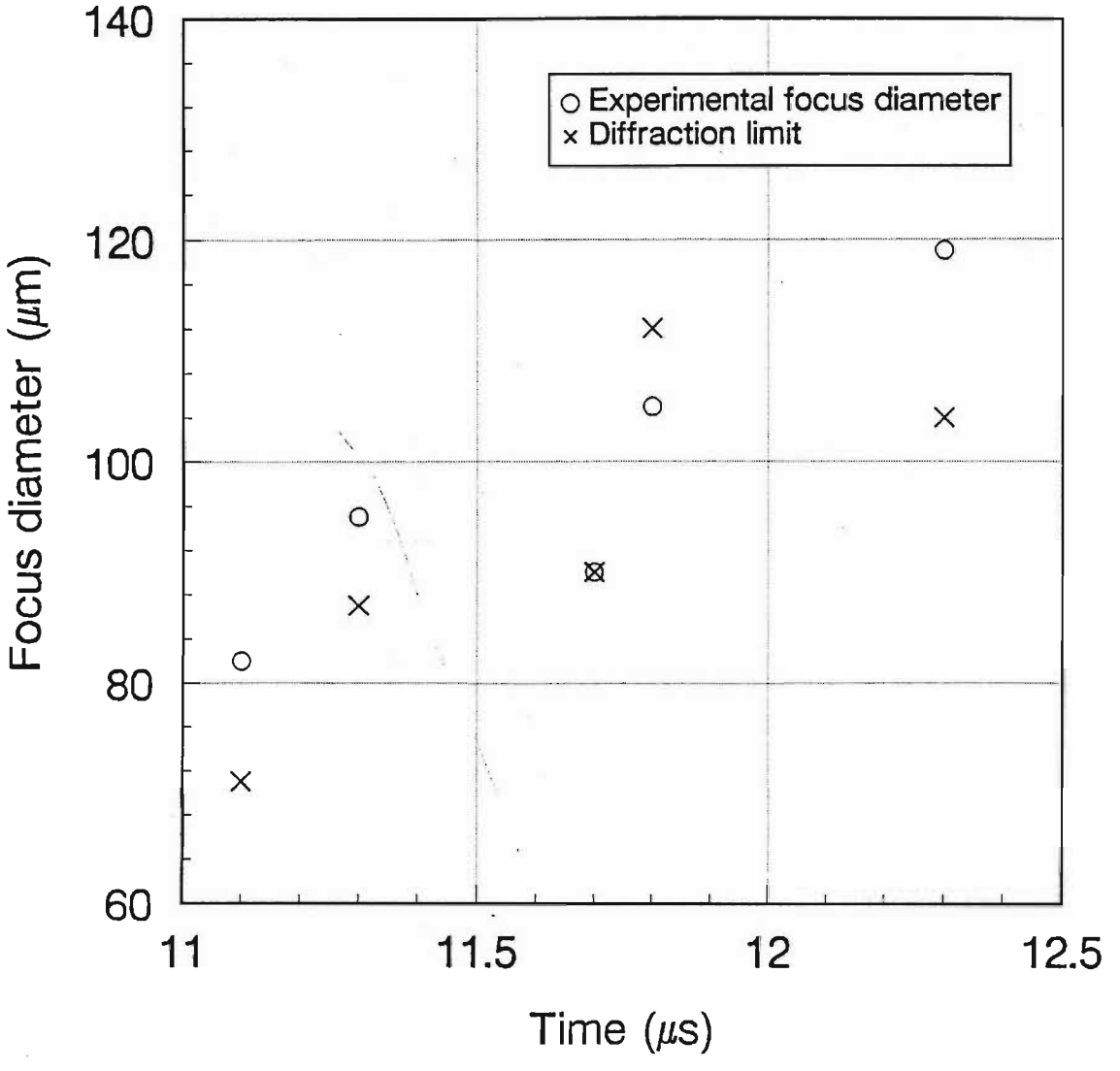

Figure 3.15: Comparison of focus diameters from Buccellato et al. (1993) : ○ : experimental focus diameter; X : diffraction limit

Increasing the electrical aperture (unenclosed CSL)

For the first investigation, we compare the performance of CSL1 and CSL2. By using CSL2 with a wall separation of 40mm and keeping the same charging capacitor as that used by Buccellato (1993) (5nF), we are able to determine the effect an increase in electrical diameter has on the focal length and optical aperture for the unenclosed CSLs. We would expect that since the energy falls off with shock radius R, the larger CSL (CSL2) should produce a weaker converging shock wave, since the shocks travel a greater distance before colliding. The larger CSL would also create a longer cigar shaped structure. See figure 3.16. This combination of greater cigar length and weaker density gradient would result in a longer focal length.

Hence, CSL1 should have a shorter focal length than CSL2 for the same optical aperture (or conversely a larger optical aperture for the same focal length).

Figure 3.17 shows a plot of optical aperture vs time after collision for CSL2. This is obtained by imaging in the shock plane of the CSL. We can see that the optical aperture increases with time. The focal length also shows the same trend (figure 3.18). Combining these two results, we obtain a plot of focal length vs optical aperture (figure 3.19). To compare CSL2 with CSL1, we read off the optical aperture for a known focal length i.e. 52cm.

The optical aperture for this focal length is 0.5mm (2mm for CSL1). It is clear that the strength of the shocks on implosion is greater for CSL1 than for CSL2. For the same optical aperture, CSL1 has a shorter focal length than CSL2.

We can conclude that for the unenclosed case, increasing the electrical aperture must be accompanied by a corresponding increase in input energy to maintain and in fact improve the performance of the CSL. This in itself would seem to be an obvious result.

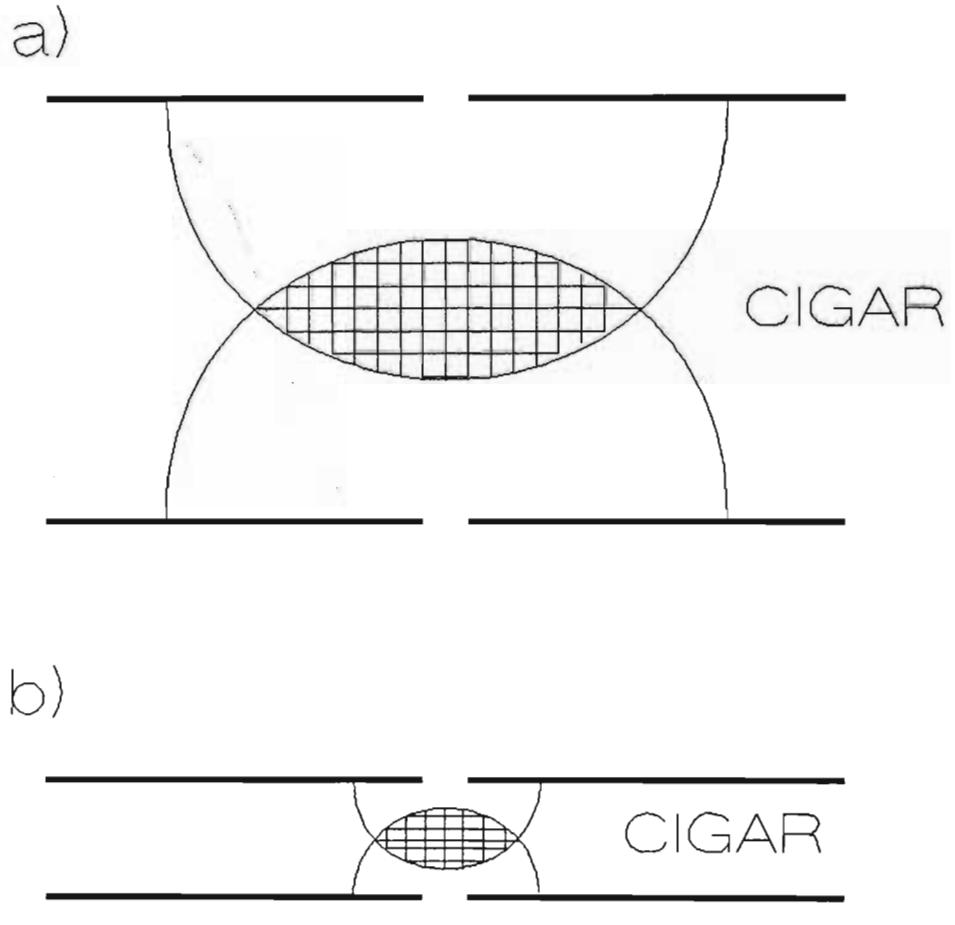

Figure 3.16: Schematic showing the cigar formed by a CSL with a larger (a) and smaller electrical diameter (b)

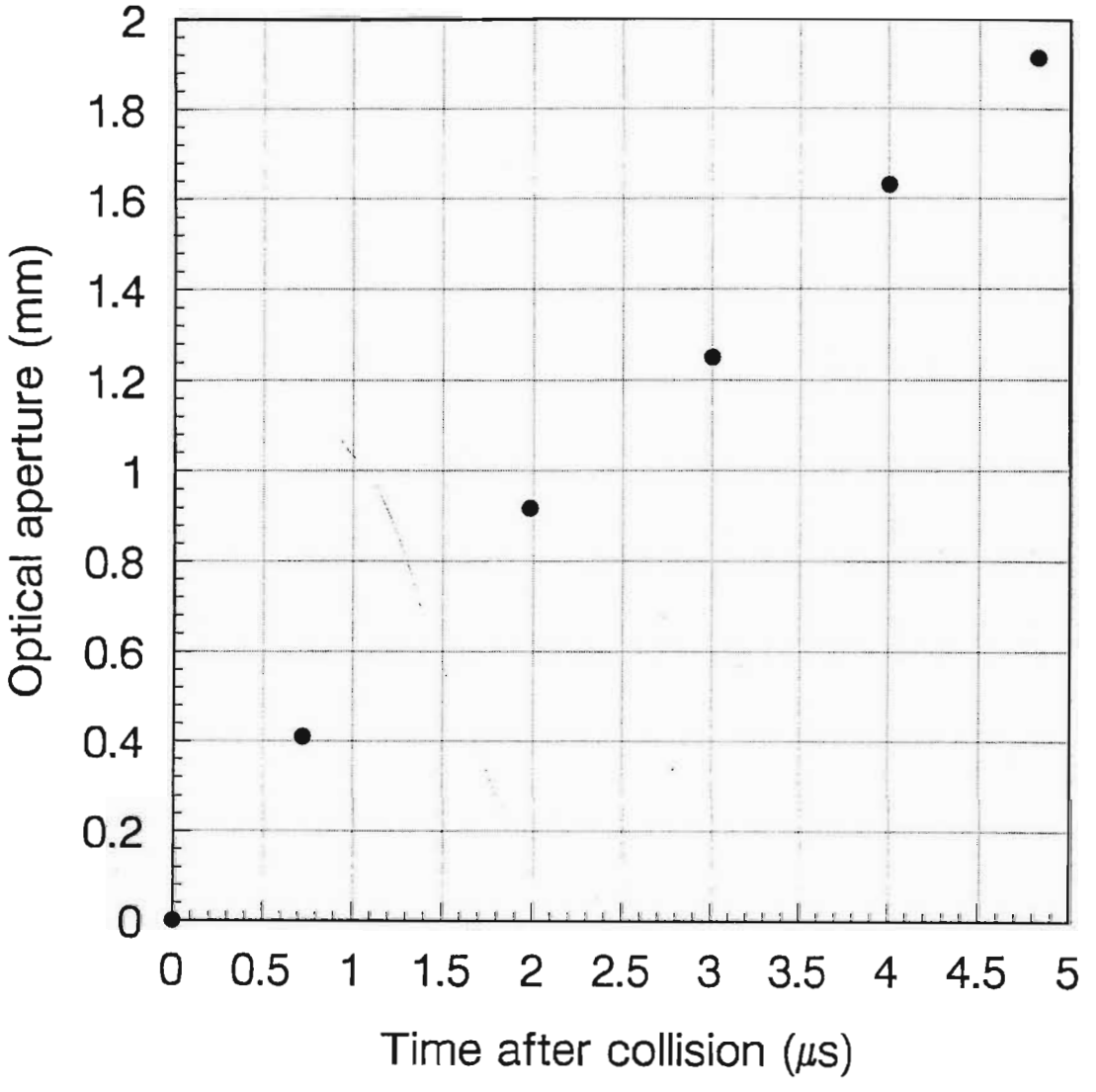

Figure 3.17: Plot of optical aperture versus time after collision for CSL2 using a 5nF charging capacitor

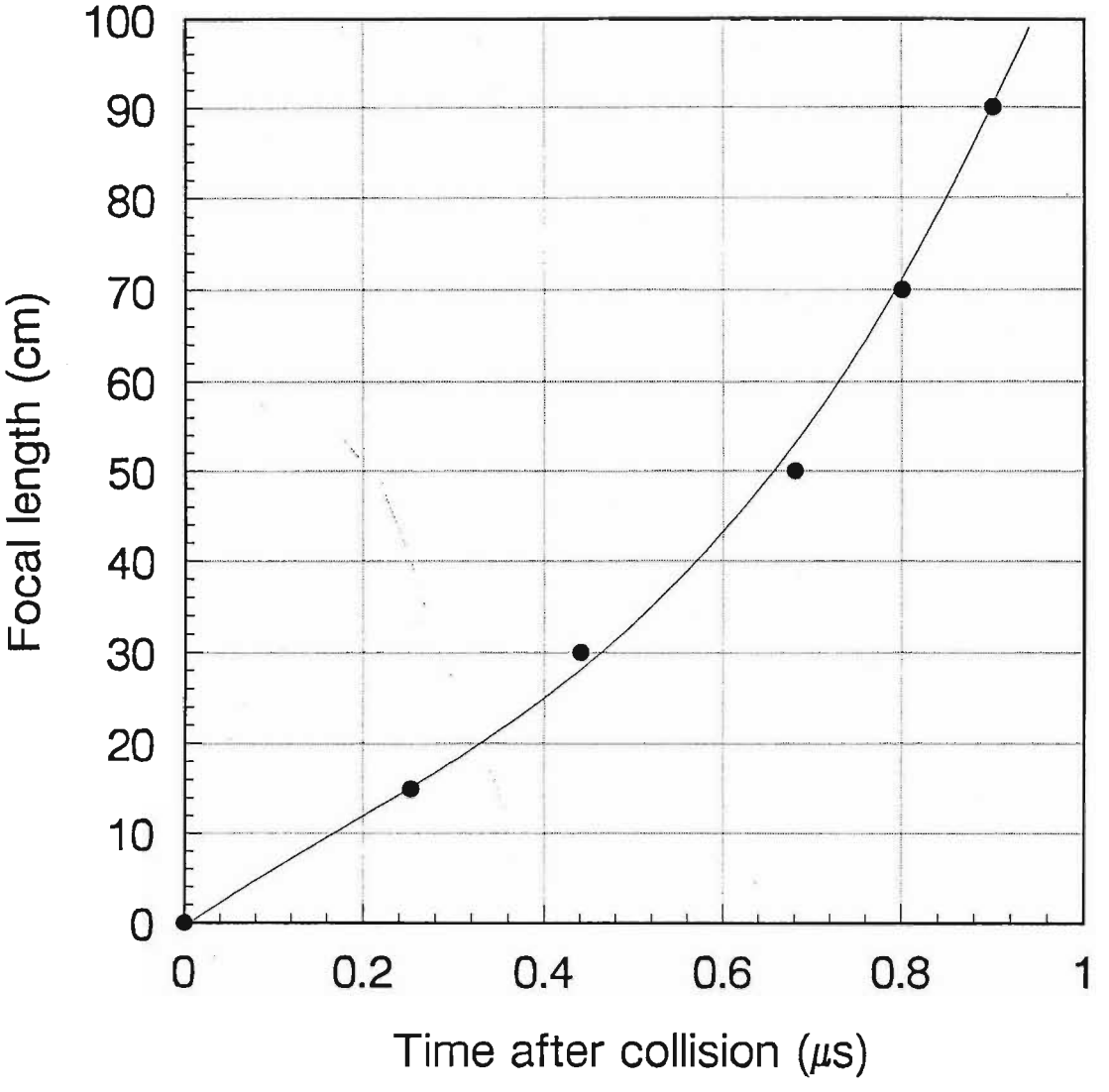

Figure 3.18: Focal length versus time after collision for CSL2 - 5nF charging capacitor

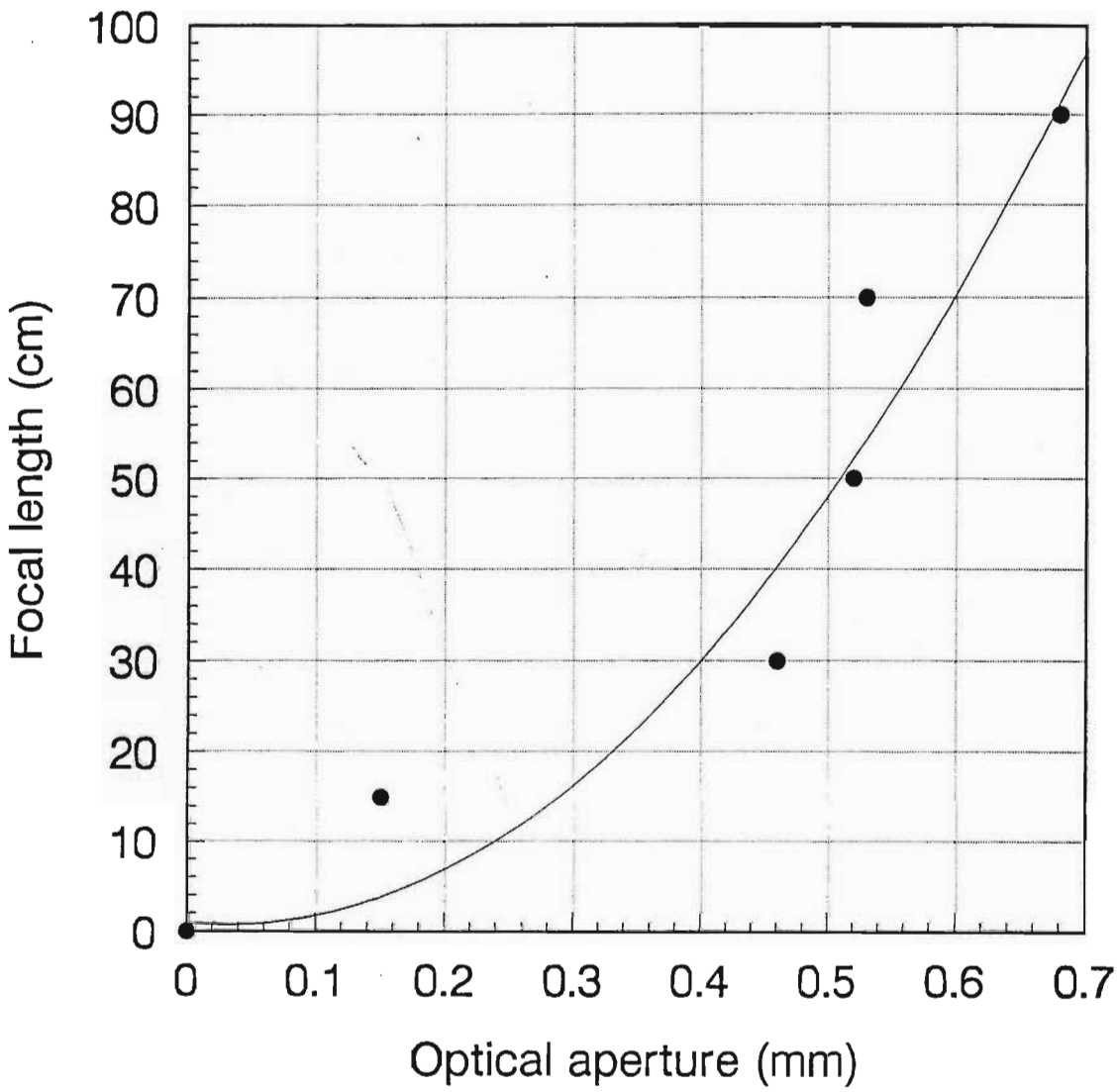

Figure 3.19: Focal length versus optical aperture for CSL2 - 5nF charging capacitor

Enclosing the CSL

Intuitively it would seem that by enclosing a CSL, reducing the loss of energy and confining the shock waves to two dimensions rather than three, we should be able to produce stronger shock waves and hence better focusing (i.e. shorter focal lengths and larger optical apertures than with the unenclosed lens). We therefore constructed CSL3 which is an enclosed version of CSL2 (when the wall separation is set to 10mm). For the following comparison, the wall separation of CSL2 was fixed at 10mm so that only the contributions due to the enclosure were different in both lenses.

Figure 3.20 shows the focal length vs optical aperture for CSL2 and CSL3. The capacitor used was the same for both (5nF), hence the input energy was the same as well (0.81J). We also plot f number vs focal length for CSL2 and CSL3 (figure 3.21).

The difference in the behaviour of the two CSLs is striking. CSL3 has an optical aperture of 2.2mm at 0.9m focal length while CSL2 has an aperture of 0.7mm for the same focal length. Perhaps more correctly, for an optical aperture of 0.7mm, CSL2 has a focal length of 0.9m while CSL3 has a focal length of 0.08m. This indicates that the shock densities are stronger in CSL3. The f number of CSL3 is better than that of CSL2 by a factor of ≈ 3.

Clearly, enclosing the colliding shock lens has resulted in a more efficient transfer of electrical energy to shock energy. Exactly how this takes place is still largely unclear. Figures 3.22 and 3.23 show schematics of an unenclosed and enclosed CSL and the associated shock behaviour as a function of time.

We see from figure 3.22 that only the inward moving hemisphere of the spherical shock wave created at the electrode contributes towards the formation of the cigar shaped lensing region after collision. The outward moving part is lost. The interaction of the inward moving shock with the side walls will result in a reflected wave as shown.

In the enclosed CSL (figure 3.23), the outward moving part of the shock wave is reflected off the boundary wall and propagates inward. At a first glance it would seem as if the reflected shock wave contributes towards the strengthening of the inward moving wave resulting in a higher density. This

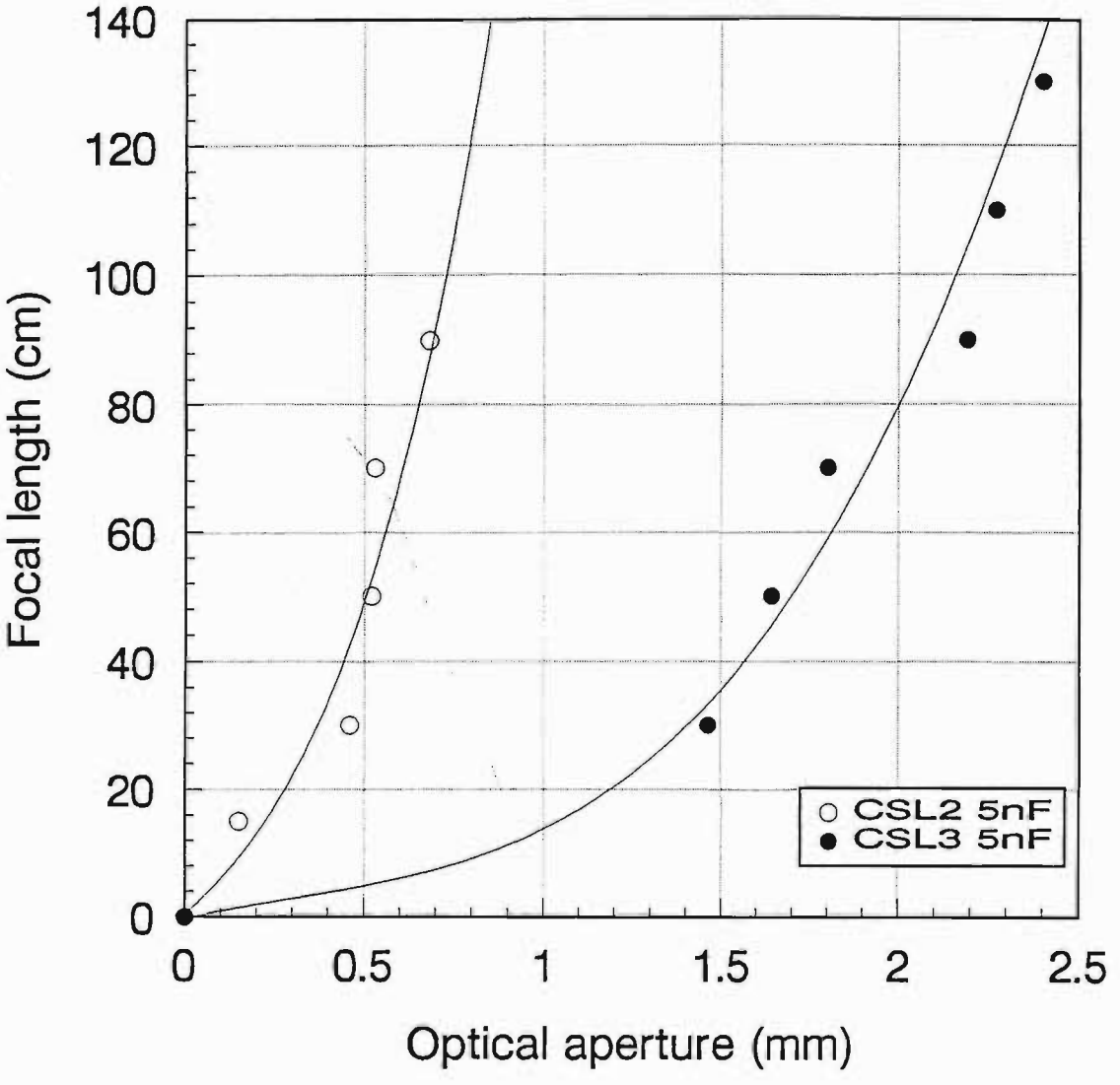

Figure 3.20: Comparative focal length versus optical aperture for CSL2 and CSL3 - 5nF charging capacitor

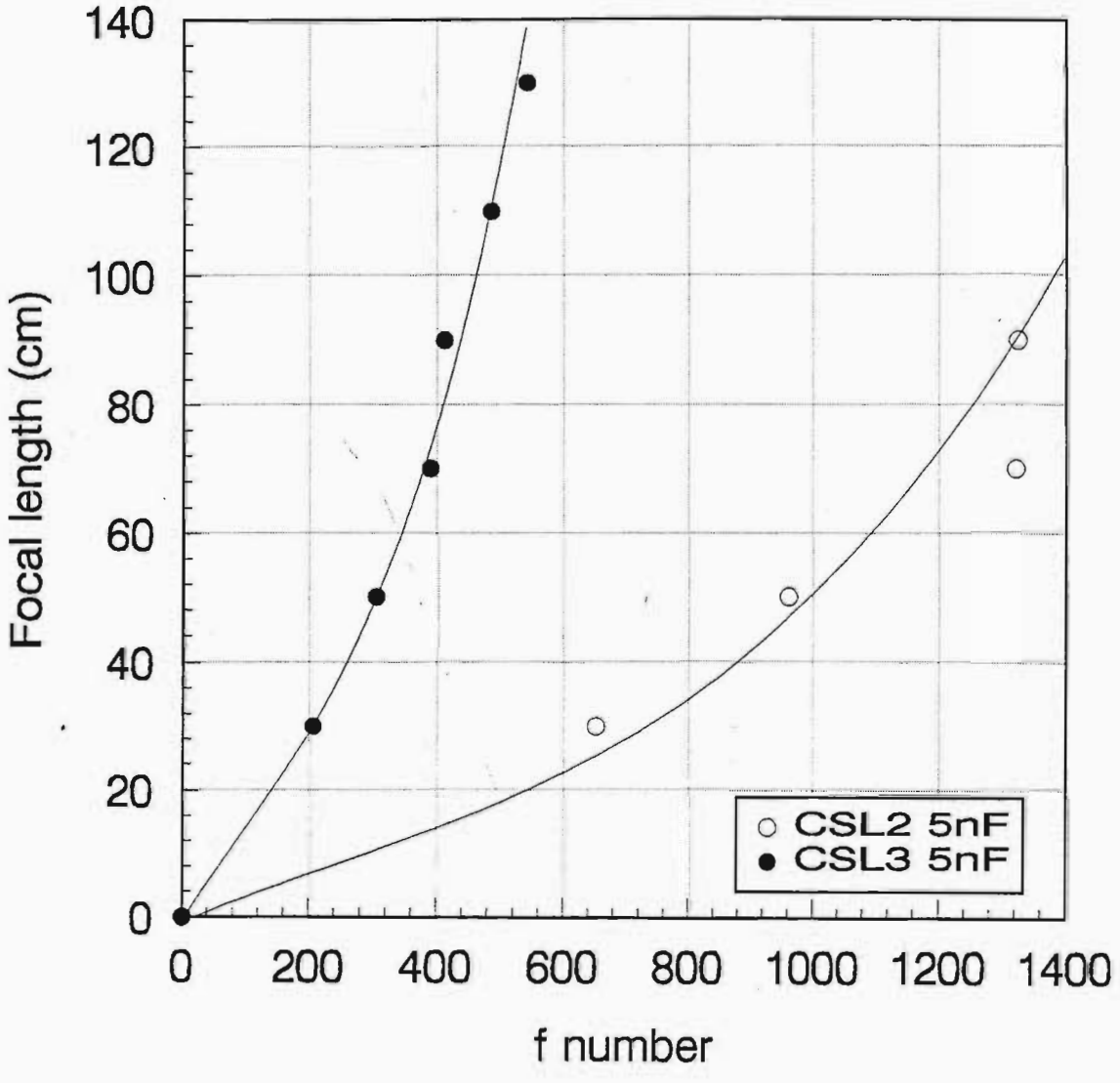

Figure 3.21: f number versus focal length for CSL2 and CSL3 - 5nF charging capacitor

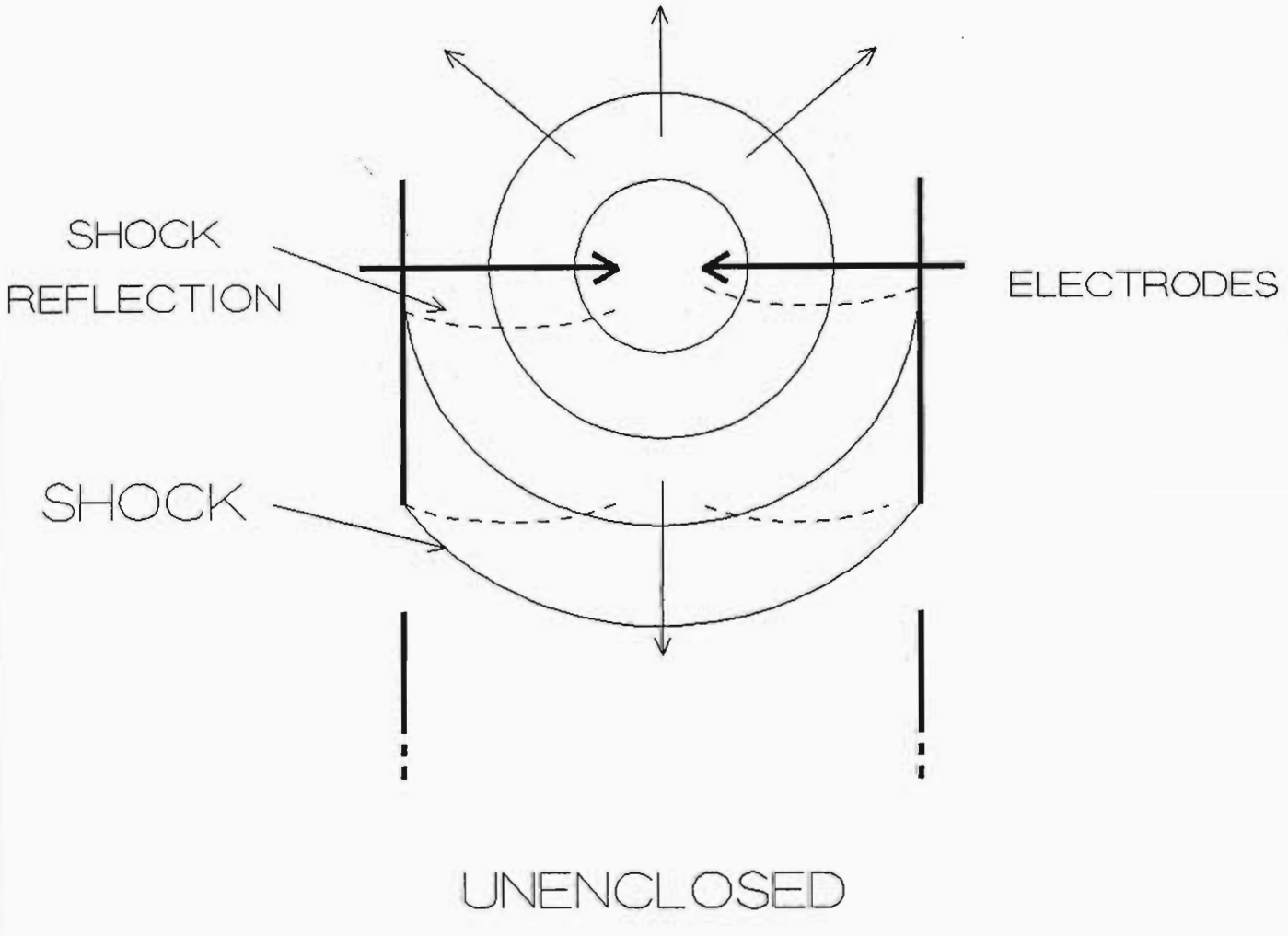

Figure 3.22: Shock behaviour in an unenclosed CSL

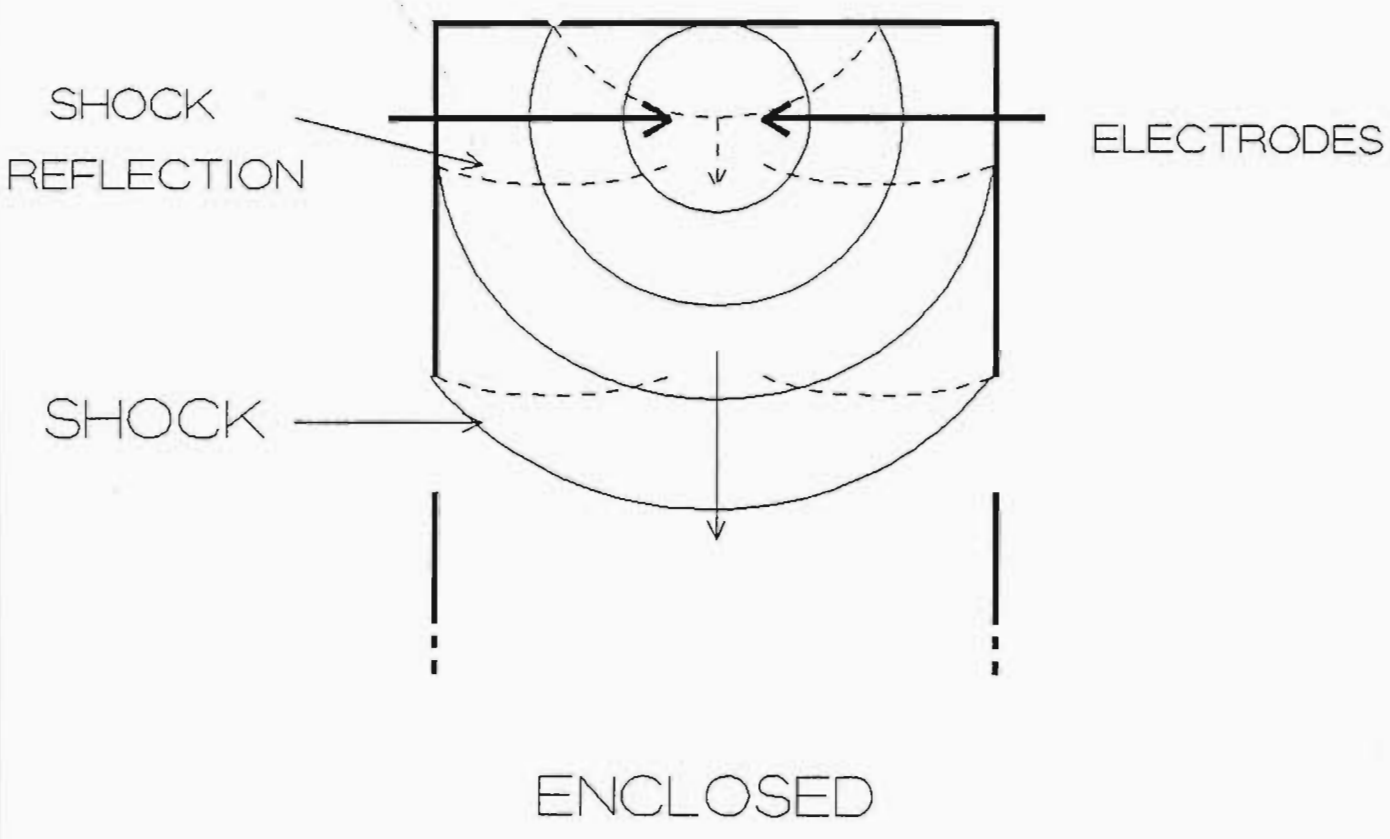

Figure 3.23: Shock behaviour in an enclosed CSL

would only be true provided the reflected wave speeds up, catches up with the inward moving wave and they combine in some way. However, experimental evidence (figure 3.24) shows that the reflected shock only reaches the centre long after lensing has taken place. The first collision occurs at 38.0μs (figure 3.24c) and the collision of the shocks reflected off the outer wall takes place at a time of 64.8μs after shock creation. See figure 3.24. This is reasonable considering that the reflected wave has to travel towards the wall (it gets weaker as it moves outwards) and on reflection has to travel through the disturbed region created by the tail of the inward moving wave.

Quite clearly the mechanism causing the strengthening of the shocks in the enclosed lens is not simple. It has been suggested that the UV radiation created during the electric arc could play a role. It is quite possible that in the enclosed case, the outward going UV radiation is reflected back into the lens whereas in the unenclosed case this UV is lost. It is conceivable that the additional UV radiation serves to further ionise the air in the enclosed CSL. This would raise the electrical conductivity of the gas and hence the conversion efficiency of the discharge resulting in a stronger shock wave being generated.

To determine very approximately what the UV contribution due to the boundary walls are, we can proceed as follows :

The Fresnel equations for the amplitude reflection coefficients are :

$$r_{\perp} = \frac{n_i cos\theta_i - n_t cos\theta_t}{n_i cos\theta_i + n_t cos\theta_t} \tag{3.1}$$

and

$$r_{\parallel} = \frac{n_t cos\theta_i - n_i cos\theta_t}{n_i cos\theta_t + n_t cos\theta_i} \tag{3.2}$$

where $r_{\perp}$ and $r_{\parallel}$ represent the reflection coefficients for the two polarisations of the incoming light source. Since we have an air-perspex interface,

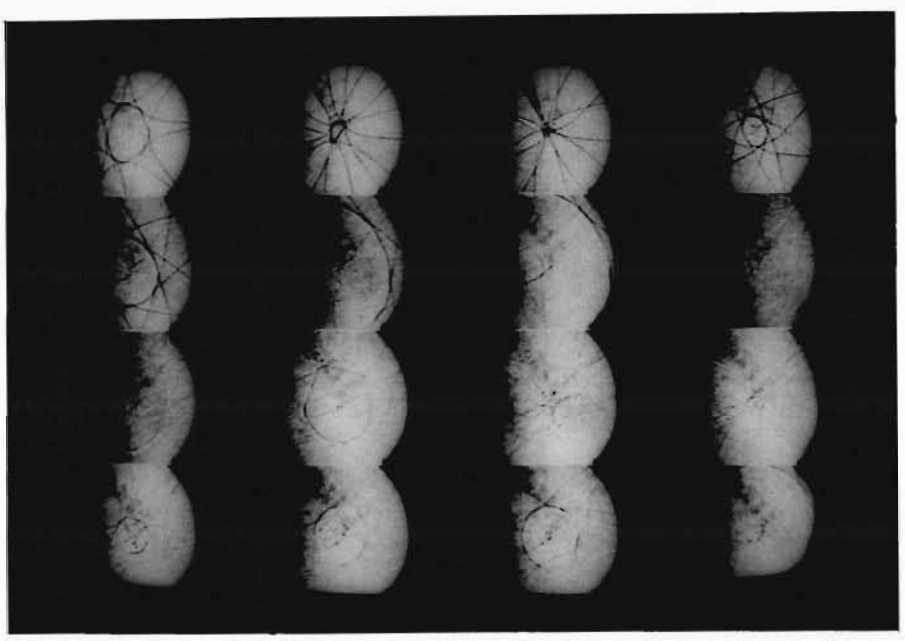

Figure 3.24: Sequence of shock profiles taken using CSL3. Times after shock generation (a) 33.6μs, (b) 36.8μs, (c) 38.0μs, (d) 40.8μs, (e) 43.6μs, (f) 48.0μs, (g) 49.2μs, (h) 52.4μs, (i) 57.6μs, (j) 58.8μs, (k) 64.6μs, (l) 66.4μs, (m) 67.2μs (n) 68.4μs, (o) 69.6μs and (p) 76.8μs. The frames are labelled from left to right.

and the wave is travelling from the air to the perspex, n_i represents the refractive index of air and n_t the refractive index of the perspex.

At normal incidence, i.e. $\theta = 0$,

$$r_\perp = -r_\parallel = \frac{n_t - n_i}{n_t + n_i} \tag{3.3}$$

We can assume that the absorption due to the perspex is high and hence the contribution to the reflected UV is due primarily to the front surface.

We can define "Reflectance" :

$$R = \frac{reflected\ \ flux}{incident\ \ flux} \tag{3.4}$$

but

$$R = \left(\frac{E_{reflected}}{E_{incident}}\right)^2 = r^2 \tag{3.5}$$

Therefore $R_\perp = r_\perp^2$ and $R_\parallel = r_\parallel^2$. The reflectance due to the perpendicular (and the parallel) component of the light is given by :

$$r_\perp^2 = \left(\frac{n_t - n_i}{n_t + n_i}\right)^2 \tag{3.6}$$

Since the UV light emitted by electric sparks can be estimated to be in the wavelength range 115nm to 200nm (see Babcock et al (1976)), to calculate the reflectance we would ideally need to know the refractive index of perspex in this range. Unfortunately light sources in this wavelength range are not easily accessible. We were nevertheless able to determine the refractive index at 248nm. Using this value for n_t of 1.53 and a value of 1 for n_i, we calculate a reflectance of 4.48%. Since the refractive index of perspex should increase when the wavelength is lowered, we can conclude that more than 4.48% of the outgoing UV radiation is reflected back into the CSL. This reflected UV

contributes towards further ionisation of the gas. As to whether this added contribution is sufficient to account for the improved performance that we observe experimentally, is strictly a guess at this stage. Admittedly, this process is not well understood. At best we have proposed a simplistic scenario. A quantitative assessment of how different types of enclosure strengthen the shocks, will require further investigation. But clearly, this is a promising feature of colliding shock lenses.

Varying the energy

Having established that the enclosed lens works well, we now adopt it for the energy dependence studies.

Three different capacitor sizes are used with CSL3. They are 5nF, 21nF and 100nF. These corresponded to energies of 0.8J, 3J and 16J respectively. The energy increases by up to a factor of 20.

Figure 3.25 shows the focal length versus optical aperture for CSL3 at the different energies. We achieve an optical aperture of 4mm at a focal length of 1.3m for 100nF. Plotting the f number versus focal length (figure 3.26) we see an improvement in f number for 100nF as compared to the 5nF and 21nF. It should be pointed out that the shock strength for the 100nF capacitor was of the order of Mach 2.4.

An attempt to use a 250nF capacitor to increase the input energy by a factor of 2.5, was not successful. Although a cigar shaped core did form, the quality of the focus was very poor indeed. We attribute this to the onset of turbulence, known to occur when strong shocks collide. The shock strength was measured to be of the order of Mach 3. This is beyond the limit for intermediate shocks.

Increasing the electrical diameter (enclosed CSL)

Increasing the electrical diameter alone will not result in a larger optical aperture for similar focal lengths. This increase must also be accompanied by an increase in the input energy. There are two reasons for this. The first is

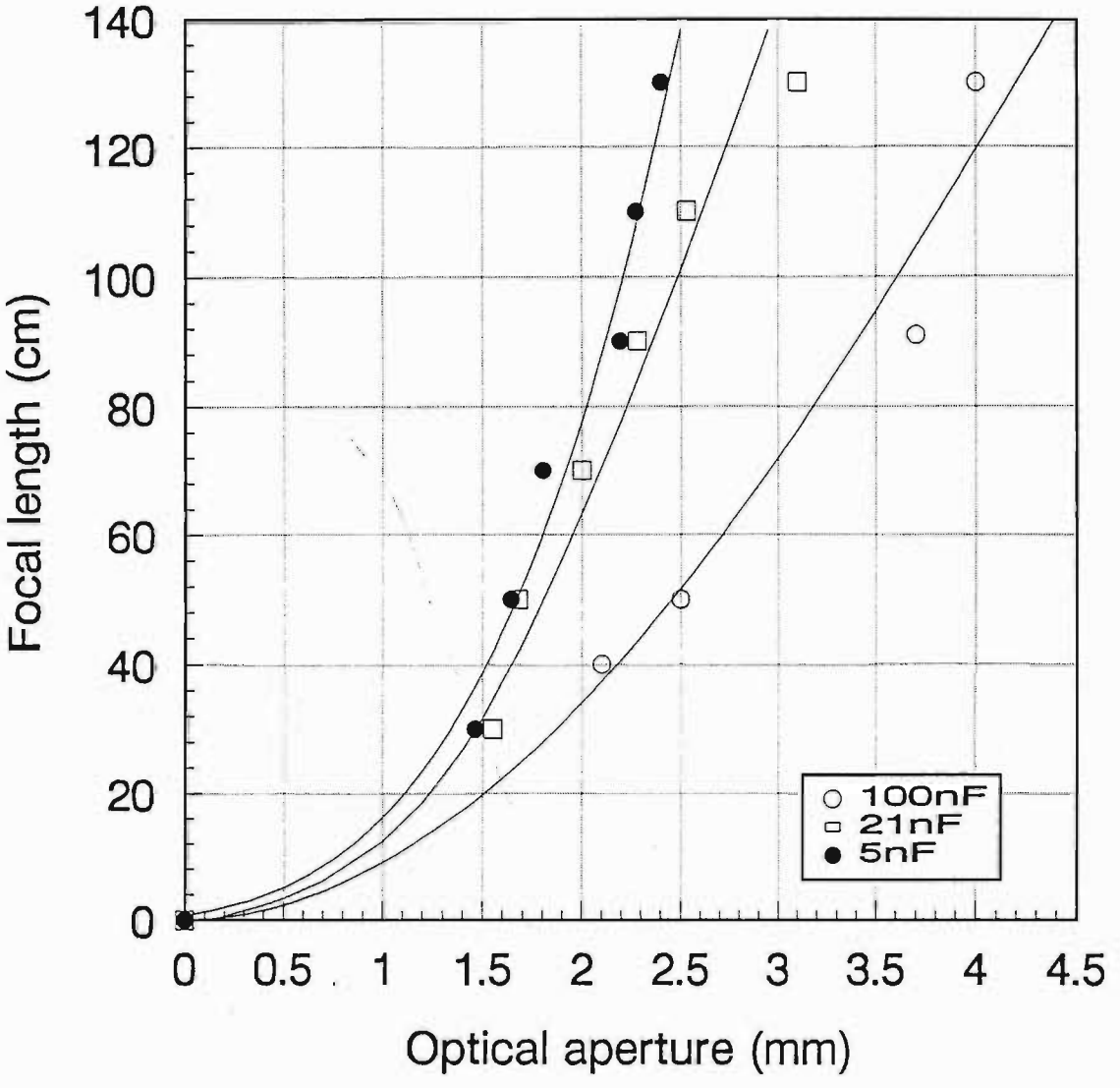

Figure 3.25: Focal length versus optical aperture for CSL3 using 5nF, 21nF and 100nF charging capacitors

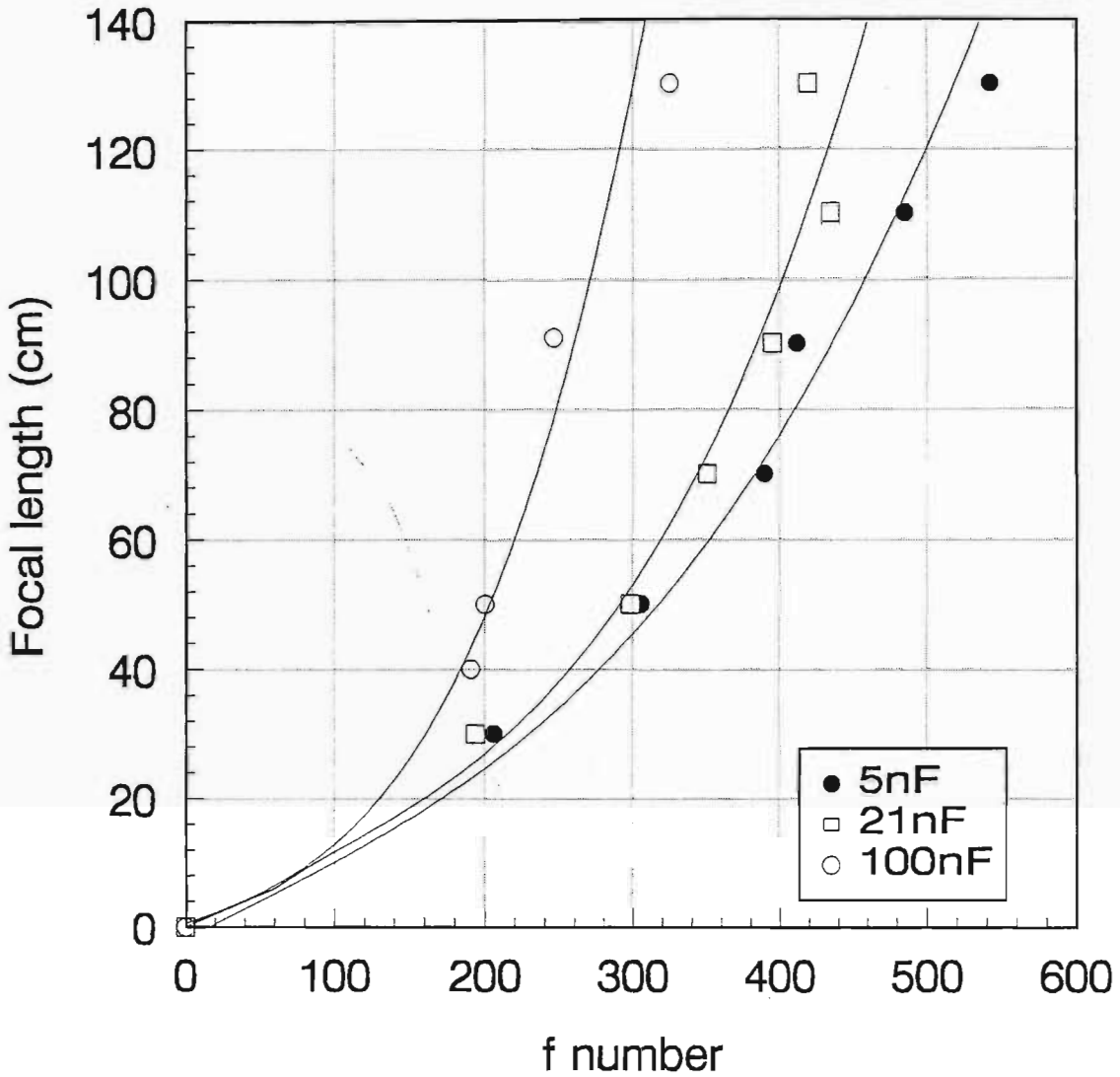

Figure 3.26: f number versus focal length for CSL3 using 5nF, 21nF and 100nF charging capacitors

that Mach addition requires large included angles (as discussed previously). The second is that addition only occurs for strong shocks.

A larger electrical diameter results in weaker shock waves colliding near the centre. Circular symmetry may then not be attained. We tried CSL4 with an 8 electrode pair configuration. As expected this does not form a good lens since circular symmetry of the cigar is not achieved. Figure 3.27 shows the polygonal shock structure created by the collisions in this configuration. Circular symmetry has not been obtained.

Changing the number of electrodes

To regain circular symmetry in CSL4, 8 more pairs of electrodes were inserted converting it into a 16 pair electrode CSL. The imploding shock waves achieve symmetry early. This can be seen from the sequence of 4 pictures showing the shocks after collision (figure 3.28). The circularly symmetric nature of the shock structure is evident. Therefore, adding more shocks was necessary for this large diameter CSL to symmetricise and to form a lens.

Figure 3.29 shows the focal length vs optical aperture for three different capacitor sizes viz. 21nF, 100nF and 250nF. Since we now have larger radii shock waves forming an axi-symmetric cigar, we can expect a larger optical aperture. But since the density gradients for the same input energy may be weaker, we would expect to see an increase in the focal length (see figure 3.30). Figures 3.31 and 3.32 show the experimental and theoretical spot sizes for CSL3 and CSL4 using a 100nF capacitor. The theoretical spot size (diameter) or diffraction limit is calculated in the following way :

$$\phi_{theoretical} = \frac{2.44 f_{csl} \lambda_{probebeam}}{d_{csl}} \tag{3.7}$$

As already mentioned, the experimental spot size is determined by measuring the diameter of the central lobe (Airy disk) in the focal plane. This is then compared to the theoretical spot size as calculated in the above equation (3.7).

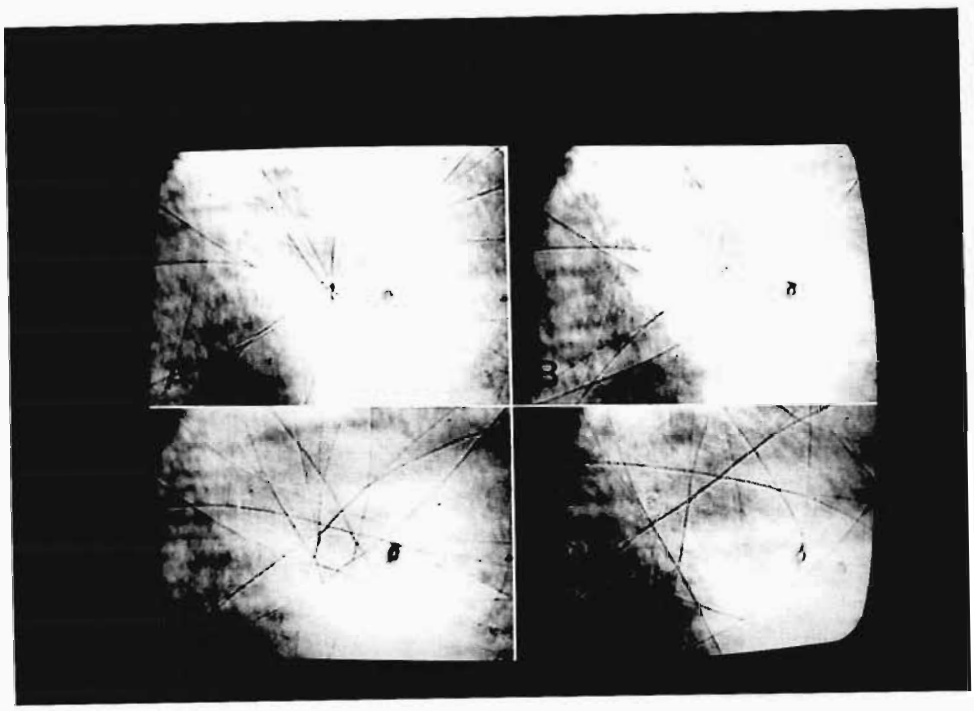

Figure 3.27: Sequence of colliding shock images ((a) implosion; (b) 6.2μs; (c) 7.4μs and (d) 14μs after implosion) taken using CSL4 having an 8 pair electrode pair configuration and a charging capacitor of 100nF. Magnification = 0.33

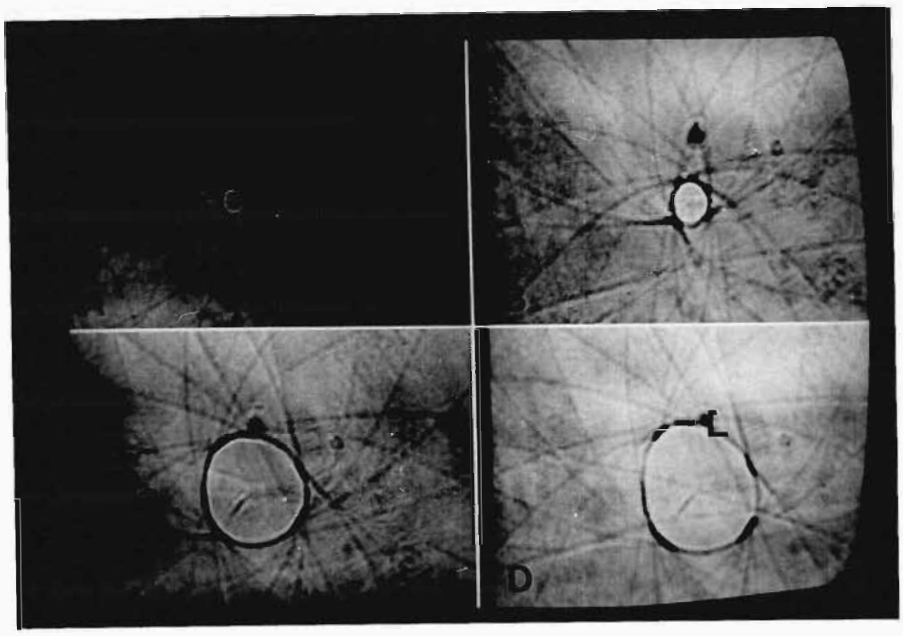

Figure 3.28: Sequence of colliding shock images ((a) 0.3μs ; (b) 1.5μs ; 3.9μs and (d) 4.3μs after implosion) taken using CSL4 with a 16 electrode pair configuration and a charging capacitor of 100nF. Magnification = 0.5.

As expected CSL3 outperforms CSL4 at the same energy.

It is interesting to note that CSL3 becomes turbulent at 250nF. If we could increase the input energy into this CSL, it would perform better than CSL4. However every CSL has an upper limit for input energy. CSL4 with 16 pairs of electrodes was very stable for the 250nF capacitor. From figure 3.29 we see that CSL4 at 250nF has an optical aperture of 8.2mm for a focal length of 1.3m. Figure 3.33 is a plot of spot size versus focal length for CSL4 at 250nF. It can be seen that the spot size is of the order of 5 times the diffraction limit. The focal spot at this distance is shown in figure 3.34. It has a FWHM of 200μm. By gas lens standards, this is "close" to diffraction limited.

Due to saturation of the central lobe in the focal spot patterns, we were unable to accurately calculate what fraction of the light is contained in the central lobe (Airy disk) in relation to the rest of the pattern. At best we can provide a "guesstimate" of between 20% and 40%. A careful calculation of this fraction would serve to further define the performance of the different CSLs. The author therefore proposes that this could serve as the basis for further study.

Pressure and gases

Since CSL3 was a fairly good lens (in terms of f number and reliability), it was decided to use this lens for the pressure and gas studies. It should be pointed out at this stage that since the performance of the CSL varies on a daily basis due to humidity, the setting of the electrodes, the spark gap separation and so on, the pressure measurements reported hereafter were conducted in consecutive runs of the system with little or no time delay between different data sets.

We placed CSL3 inside the chamber described earlier and using a charging capacitor of 100nF conducted measurements on the lens using atmospheric pressure (1 bar), 0.5 bar above atmosphere and finally 2 bar above atmosphere (3 bar absolute). Figure 3.35 shows the results obtained.

It is clear from the graph that as the ambient pressure increases, the

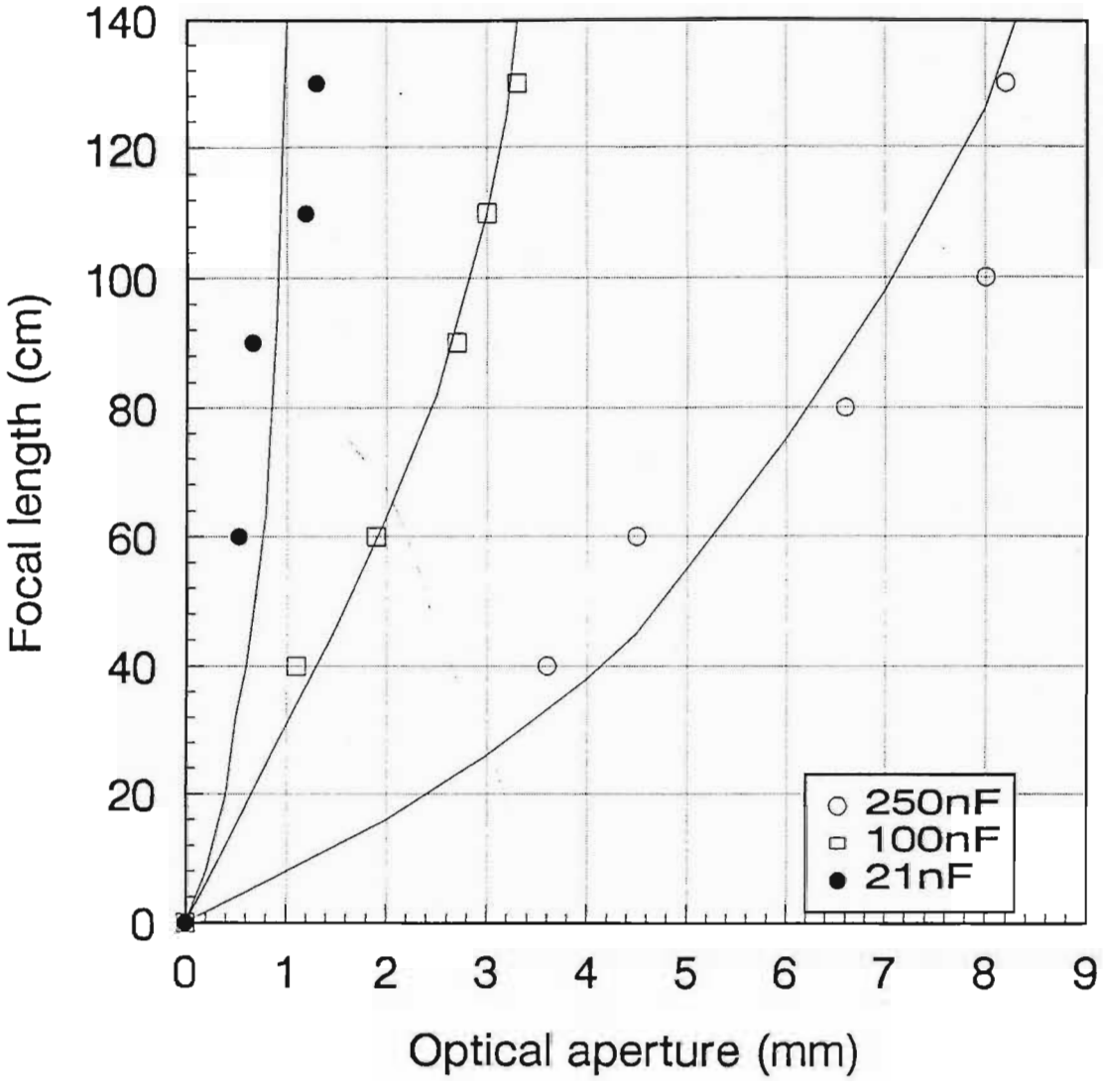

Figure 3.29: Focal length versus optical aperture for CSL4 (16 electrode pairs) using 21nF, 100nF and 250nF charging capacitors

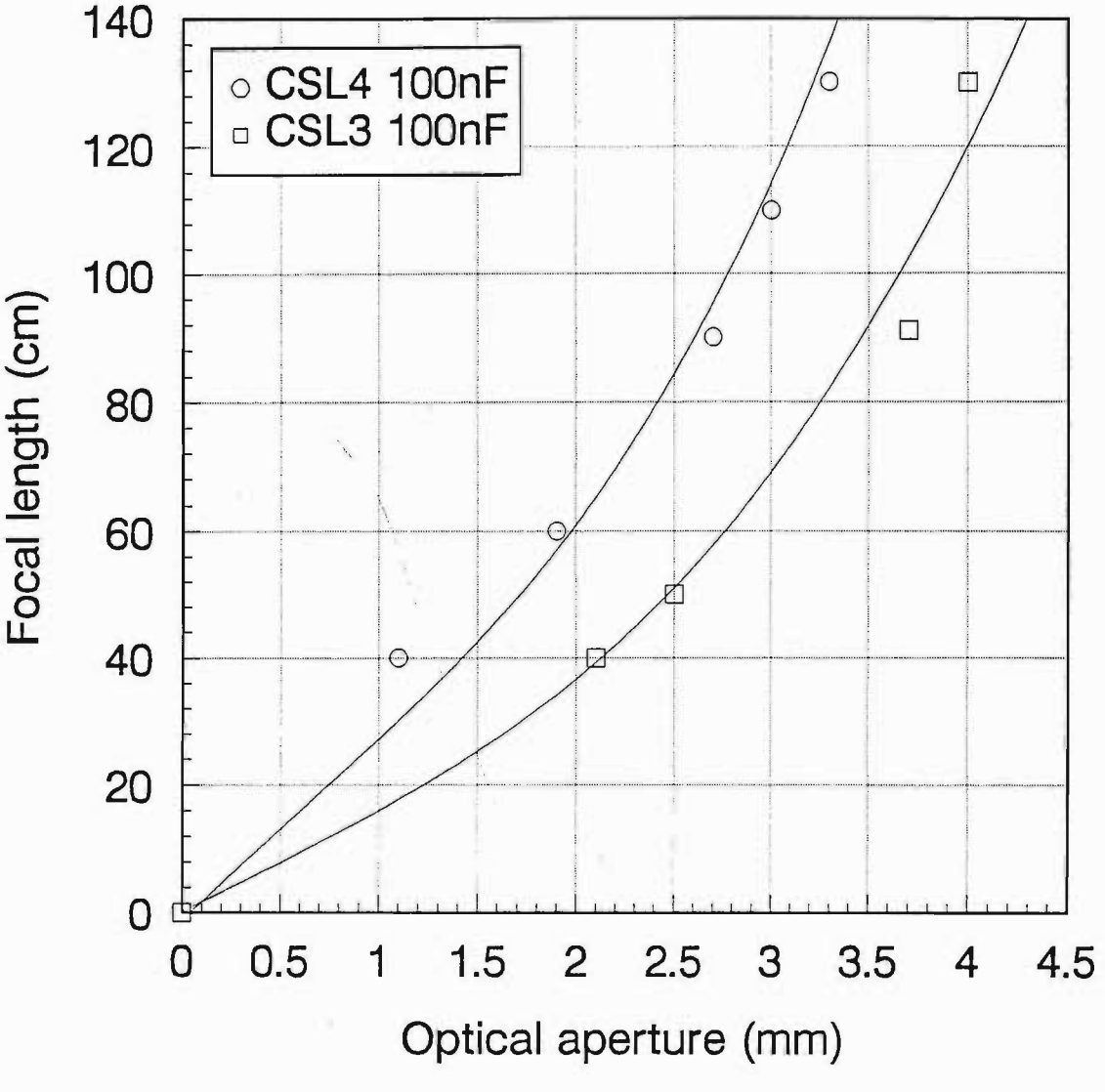

Figure 3.30: Focal length versus optical aperture for CSL3 and CSL4 using a 100nF capacitor

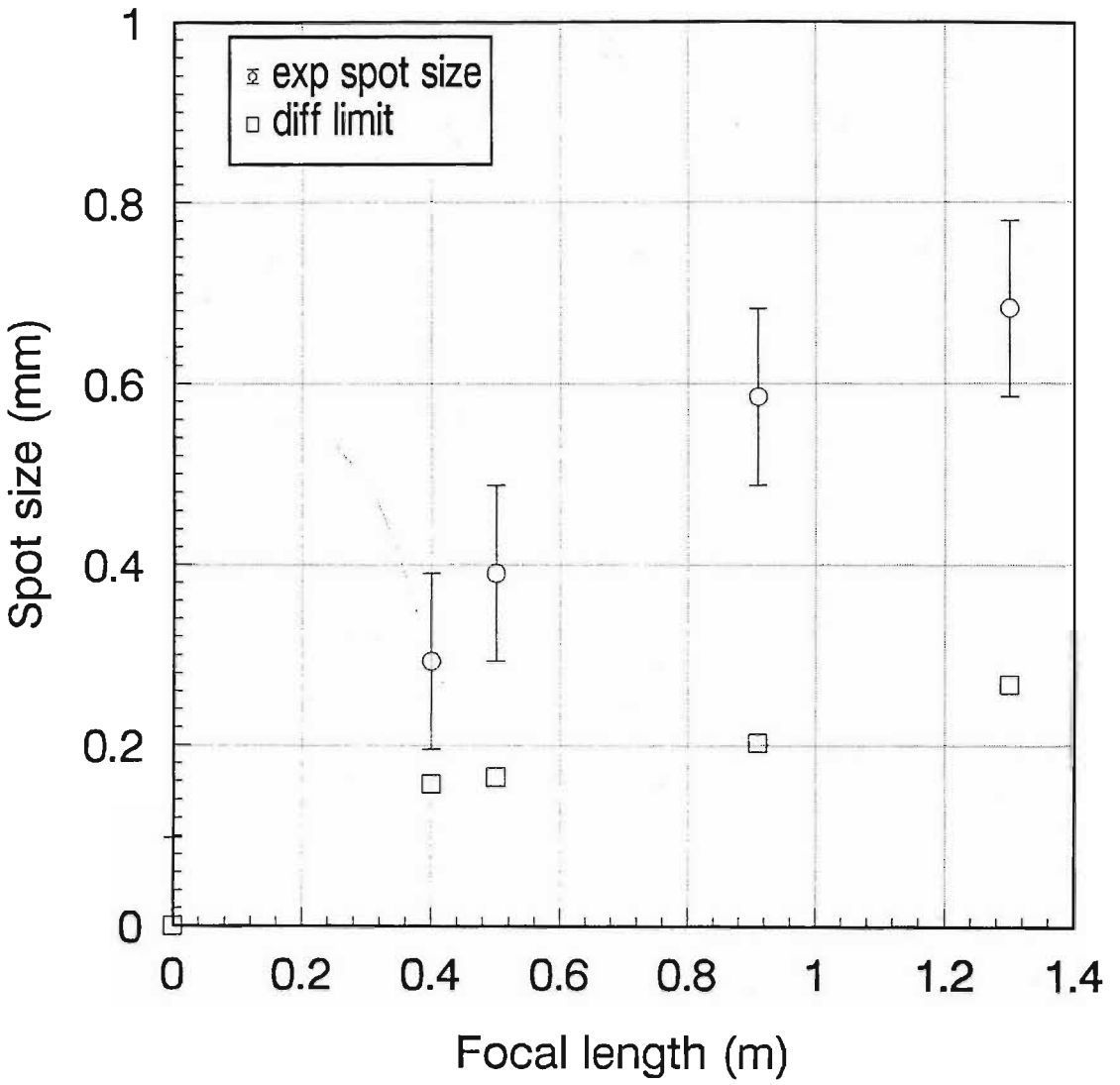

Figure 3.31: Graph of experimental and theoretical spot size versus focal length for CSL3 at 100nF

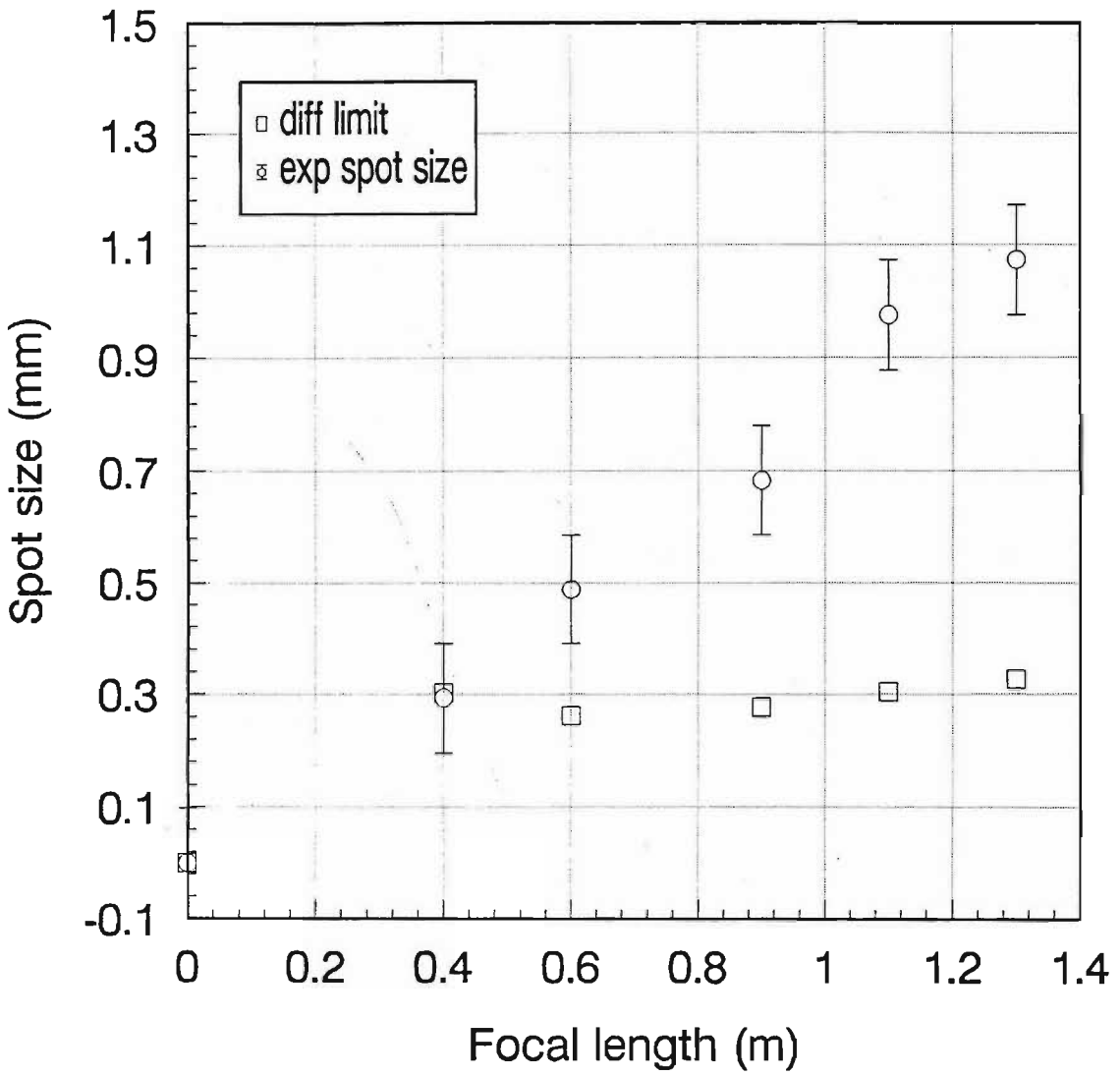

Figure 3.32: Graph of experimental and theoretical spot size versus focal length for CSL4 at 100nF

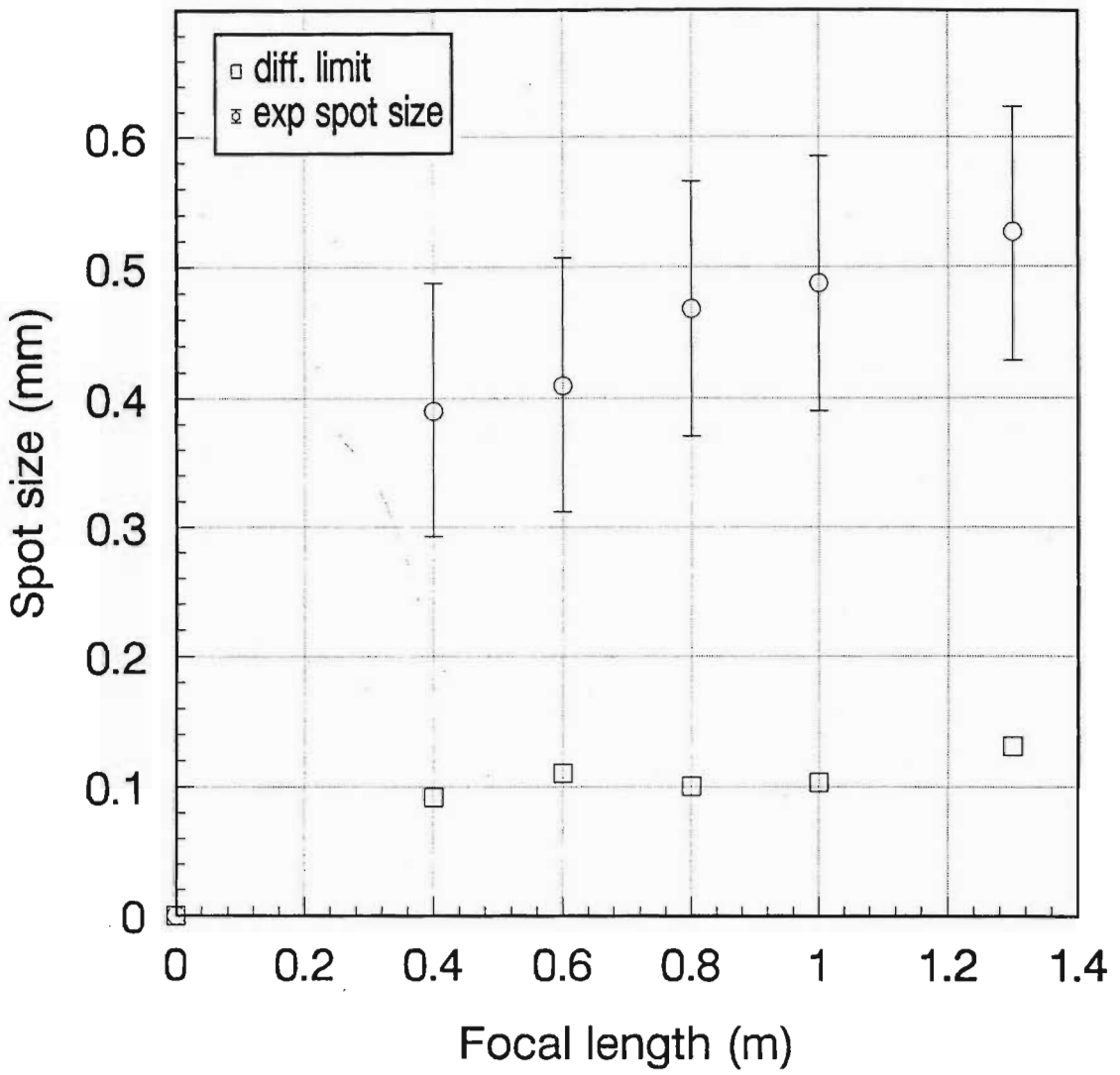

Figure 3.33: Spot size versus focal length for CSL4 at 250nF

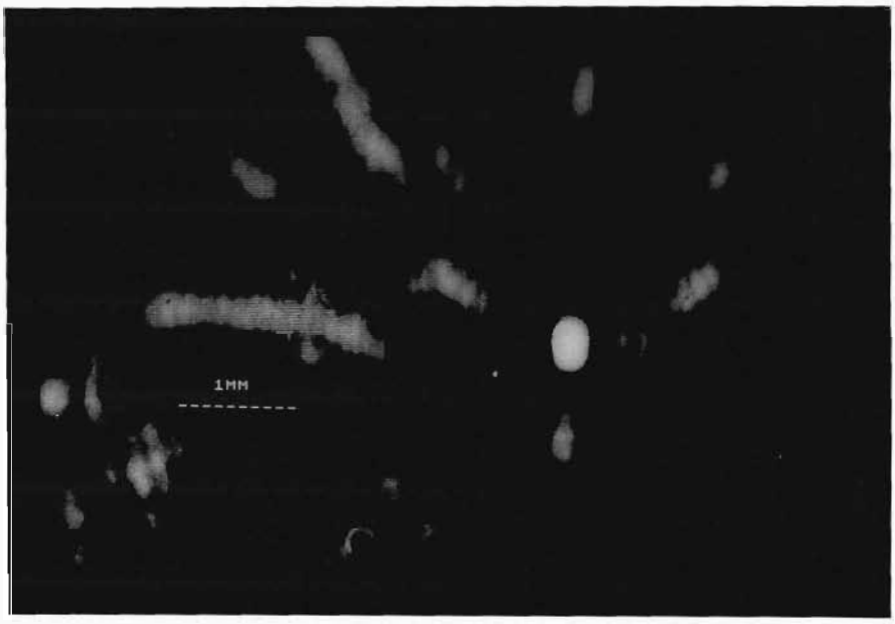

Figure 3.34: Focal spot at 1.3m away from CSL4 (250nF charging capacitor)

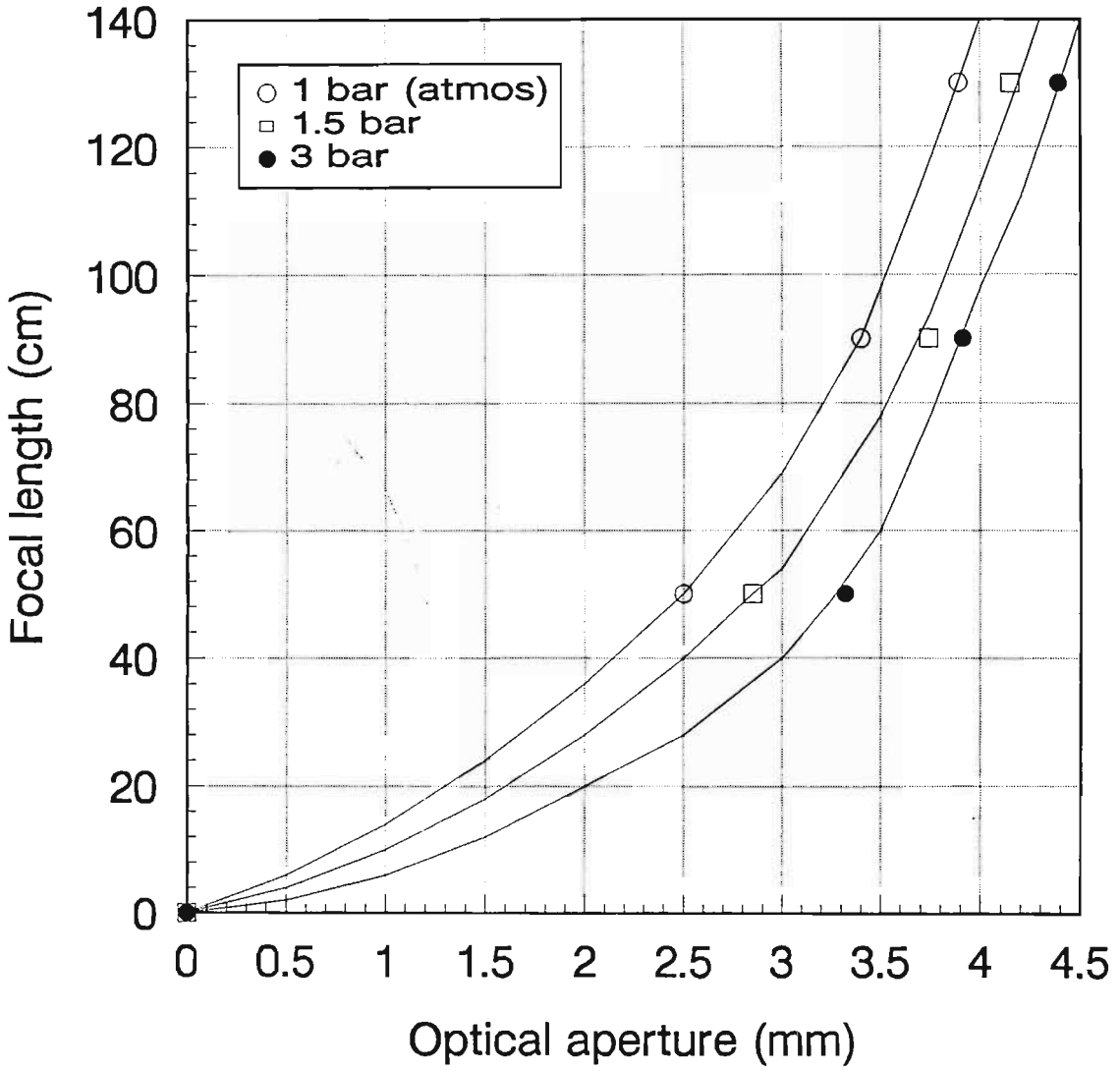

Figure 3.35: Focal length versus optical aperture for CSL3 using 100nF capacitor at pressures of 1 bar, 1.5 bar and 3 bar

focal length decreases for a corresponding optical aperture. More correctly we should say that for the same focal length, an increase in pressure results in a larger optical aperture. This can be explained by the fact that the shocks travel faster in a higher pressure (higher density) medium.

We see from figure 3.36, the f number increases by a factor of 1.2 between the 1 bar and 3 bar results.

This is indeed encouraging as it corresponds with our suspicions. Unfortunately, our pressure range was limited by the equipment at hand. The author has no doubt that the performance of the CSL could be improved even more markedly with much higher pressures.

We also conducted an investigation on the effect of different gases on the performance of the CSL. The gases used were air, CO_2 and Ar. Figure 3.37 is a plot of focal length versus optical aperture for CSL3 at 100nF obtained using the three gases mentioned. The pressure for each data set was maintained at 1 bar. As we would expect, as the density gets higher, the shock speed should increase. If we consider air to consist primarily of nitrogen then its molar mass is 28g. The molar mass for Ar is 40g and that for CO_2 is 44g. We would therefore expect CO_2 to yield the largest optical aperture for a corresponding focal length, which is indeed the case.

An attempt was also made to observe the behaviour of the CSL using a gas lighter than air. He, being the most readily available, was used. Unfortunately, under these conditions, the CSL was unable to hold charge at 17kV without arcing either to the chamber or to the high voltage electrodes. After several attempts, this investigation was abandoned. Nevertheless, we feel that the behaviour of the CSL is predictable enough to conclude that under a less dense gas, the performance would deteriorate.

The scaling experiments described above lead us to construct a final enclosed CSL with an electrical diameter of 16cm powered by a 500nF capacitor charged to 17kV. Our first experiments with this lens showed it to be capable of generating a 1.5cm aperture lens with a focal length of 1.5m. The focal spot at this distance is shown in figure 3.38.

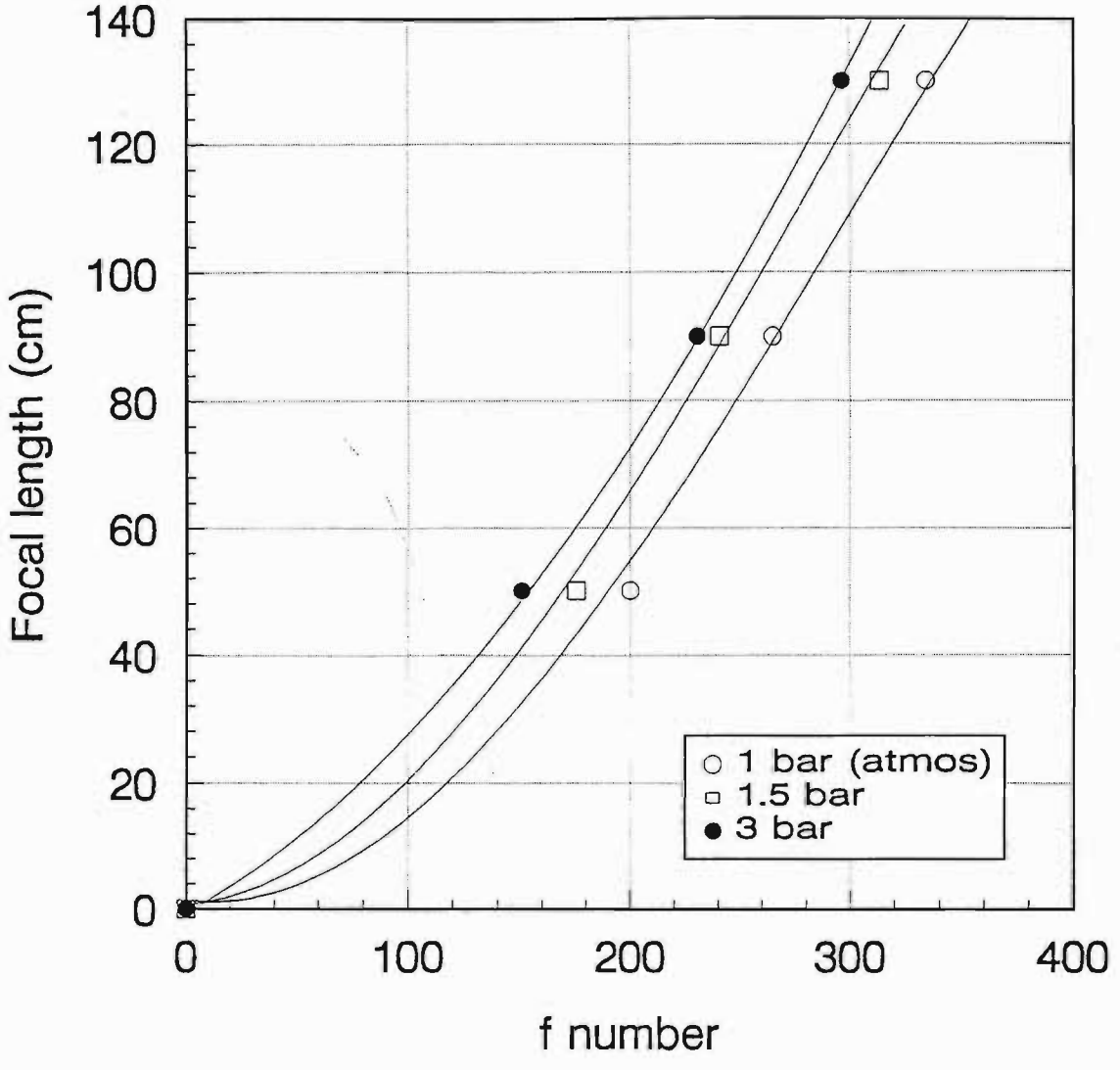

Figure 3.36: f number versus focal length for CSL3 at different pressures

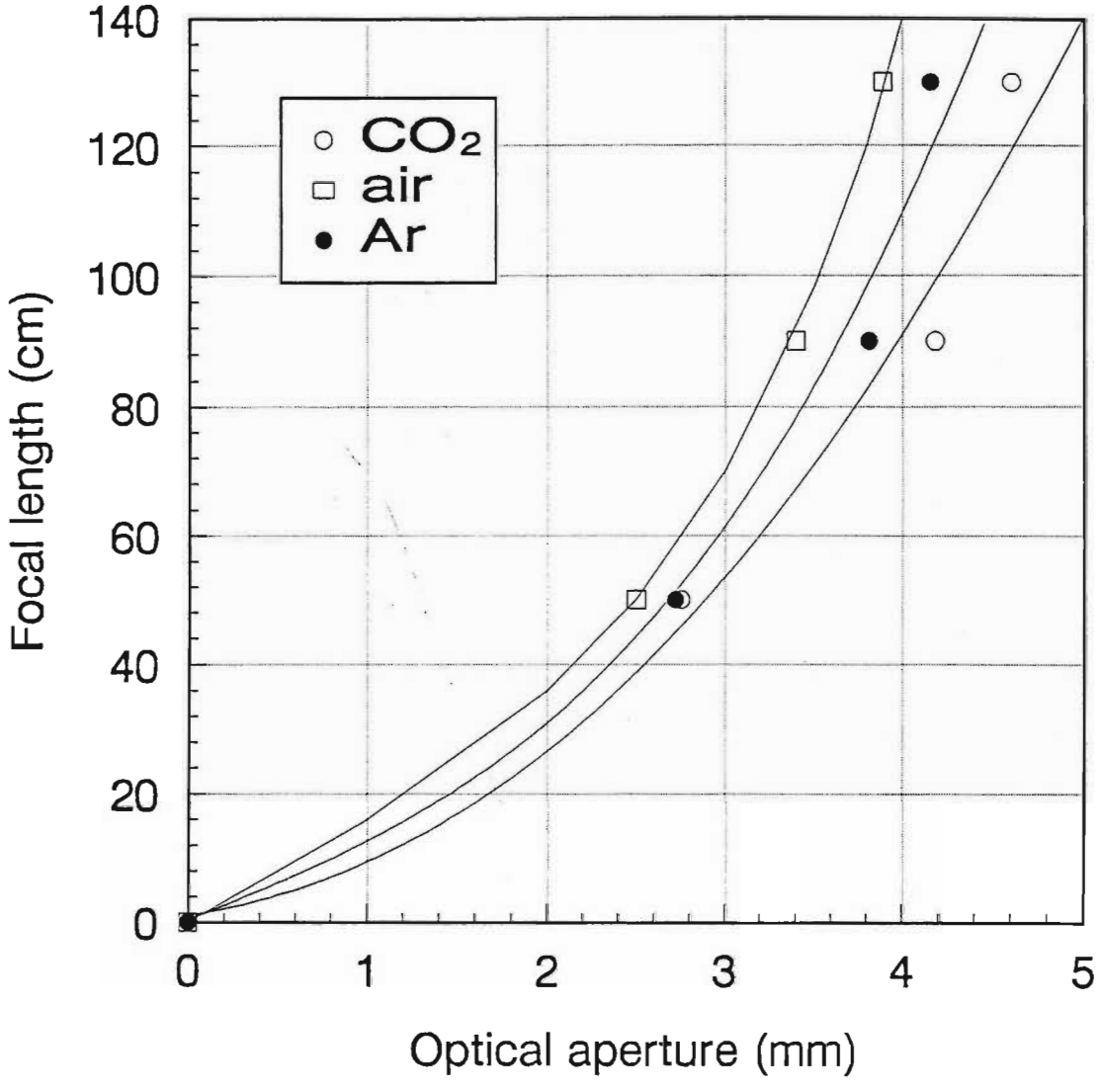

Figure 3.37: Focal length versus optical aperture for CSL3 using air, Ar and CO_2

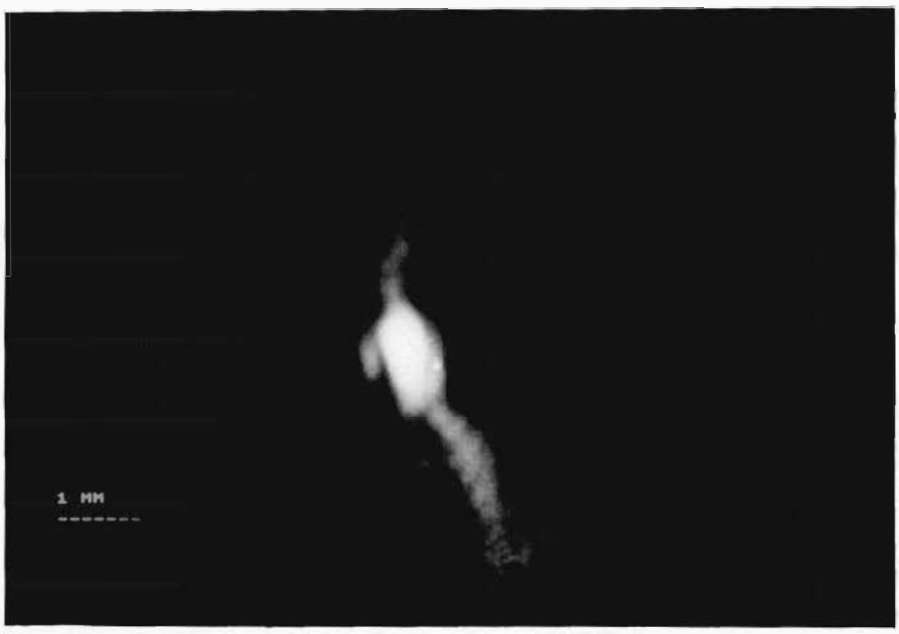

Figure 3.38: Focal spot obtained using CSL5 at a focal length of 1.5m

Chapter 4

Colliding Shock Lens Simulation

4.1 Theoretical review

In what was perhaps the first study of its kind, Guderley (1942) studied the case of a very strong shock and found that there exists a similarity solution representing a converging cylindrical or spherical shock wave. Guderley found that the solution existed only in the vicinity of the axis and was singular at the axis for ideal gases. For real gases, viscosity and heat conduction is present.

In 1950 Von Neumann and Richtmyer described a finite difference method for calculating compressible fluid flows containing shock waves, in which they introduced an artificial diffusion (viscosity) term. Most finite difference methods, when applied to problems with discontinuities, produce oscillations behind the shock. The artificial viscosity term served to reduce the oscillations while having a negligible effect on the smooth regions.

Lax (1954) modified the method introduced by Von Neumann and Richtmyer (1950) and introduced a diffusion term of the form

$$\Delta x^2/2\Delta t$$

where Δx is the width of the space mesh used and Δt the time interval. It was found that although not the correct viscosity or heat conduction term,

the flow will be similar except in the structure of the diffused shock.

In 1956, Payne used the finite difference method due to Lax (1954) to solve the equations of motion for a cylindrically symmetric flow of a compressible fluid. A converging cylindrical shock was found to increase in strength. This was in agreement with the formula of Chisnell (1957). Special consideration was given to the flow at the axis and a reflected shock was found to exist. The pressure at the axis was found to remain finite due to the diffusion introduced. Payne's numerical calculations were found to agree closely with Guderleys (1942) solution even though the initial conditions were slightly different.

Lee (1966) extended the analysis a little farther away from the axis and showed that the results approached Guderleys solution near the axis.

Bach and Lee (1969) gave an accurate and complete description for the initial stages of collapse of a spherical and cylindrical shock wave in a perfect gas. The shock wave was initiated by an instantaneous deposition of a finite quantity of energy at a finite radius. It was recognised that although this analysis accurately described the behaviour of the shocks close to the walls, numerical integration schemes (Payne 1956) are needed for a complete description of the implosion process. Nevertheless, Bach and Lee (1969) found an increase in pressure and density behind the shock near the centre of collapse in agreement with Guderley (1942).

Sod (1977) introduced a numerical procedure to solve the 1 dimensional equations of gas dynamics for a cylindrically and spherically symmetric flow. He used a combination of Glimm's (Random Choice) method (Glimm 1965) and operator splitting. This procedure was applied to the problem of converging cylindrical shocks. It was found that as the shock propagates towards the axis, its strength increases and the pressure behind the shock also increases. At the axis the strength rises to a large but finite value. Thereafter the shock is reflected and the pressure behind the shock decreases with time.

Up to this point, analysis of converging shock waves had been limited to two cases. One concerned with shock waves which propagate in the vicinity of the axis (Guderley (1942), Payne (1956), Lee (1966) and Sod (1977)) and the other with the propagation near the cylindrical wall (Bach and Lee

(1969)).

Matsuo (1979) showed that the application of the second order approximations of Bach and Lee (1969) might be limited to the region of deceleration (close to the cylindrical wall). Matsuo analysed the shock waves travelling in the intermediate region not covered by Guderley's (1942) solution and the Bach and Lee (1969) theory using the method of integral relations. It was found that the results were in good agreement with the second order approximations of Bach and Lee (1969) and were smoothly continued to Guderley's solution near the axis, however never quite reaching the selfsimilar implosion limit of Guderley (1942). Results showed that shock waves generated by instantaneous release of energy over cylindrical surfaces, first decelerate near the wall, remain stationary in the intermediate region and then accelerate in the vicinity of the axis. Matsuo found that the convergence of the method of integral relations tends to deteriorate in the region close to the axis, and although this treatment accurately described the behaviour of the shocks in the transition region, it was suggested that other numerical methods be considered to investigate more closely the transition from the non-selfsimilar region to the selfsimilar region.

Schwendeman and Witham (1987) used an approximate theory of shock dynamics to study the behaviour of converging shocks. It was shown by Witham (1957), that a converging cylindrical shock wave would be unstable to very small disturbances. Exact solutions were found by Schwendeman and Witham (1987) for cylindrical shocks with regular polygonal-shaped cross sections. It was shown that an original polygonal shape repeats at successive intervals with successive contractions in scale.

Matsuo (1988) further extended the analysis of Matsuo (1979) to the focussing stage and compared the results with the selfsimilar solution. Good agreement was found.

The abovementioned treatments serve to completely describe the behaviour of converging cylindrical and spherical shock waves from the moment of initiation to the implosion and reflection stage.

In the sections to follow we attempt to model the behaviour of the colliding shock lens by :

i) proposing a simple scaling theory and

ii) using the Fluid in Cell (FLIC) method to numerically simulate the behaviour of the CSL.

The results of both of these models will be compared with the experimental results.

4.2 Simple scaling theory

An approximate scaling theory for CSL's, can be derived with the help of the following assumptions :

(**i**) All the electrical energy stored in the charging capacitor is transferred to the shock waves by the arcs.

(**ii**) A certain fraction of this energy is contained in the gas forming the lens. This fraction is represented by the product of a "geometric energy factor" G and a "shock weakness factor" G'.

(**iii**) For the purpose of calculating refraction, the actual density profile, however complex, can be approximated by a cigar shaped, high density region with a constant refractive index gradient.

(**iv**) A simple order of magnitude focal length calculation is acceptable.

Clearly, all these assumptions can be examined and refined in great depth. But at this stage of development, we find the following simple calculation useful.

Only a fraction W = G .G' (1/2 C .V^2) of the total energy in the shocks is contained in the compressed gas of the lensing region. The fraction of the energy contained in the lens volume itself is simply given by the cross section of the lens divided by $4\pi R^2$ where R (the electrical radius of the lens) is 1/2 the electrical diameter. G is the areal cross section that the lens offers up

to the spherically expanding shock front. It is obtained by assimilating the cigar to two cones, each of height l and base radius r (see figure 4.1).

From the figure we see that the cross section offered to the shock waves by the lens can be given as :

$$A = 2rl \tag{4.1}$$

Therefore the areal cross section G is given by :

$$G = \frac{2rl}{4\pi R^2} \tag{4.2}$$

Hence

$$G = \frac{rl}{2\pi R^2} \tag{4.3}$$

Simple trigonometry shows that the half length of the cigar is

$$l = \sqrt{2.r.R}$$

where R is the radius of two intersecting shocks (see figure 4.1b).

We can therefore conclude that :

$$G^2 \approx \frac{1}{20}\left(\frac{r}{R}\right)^3 \tag{4.4}$$

The fitted parameter G', represents the fraction of shock wave energy contained in the supersonic front as opposed to that which has been dissipated in forming the long shock rear and the shock tail. No figures are available for

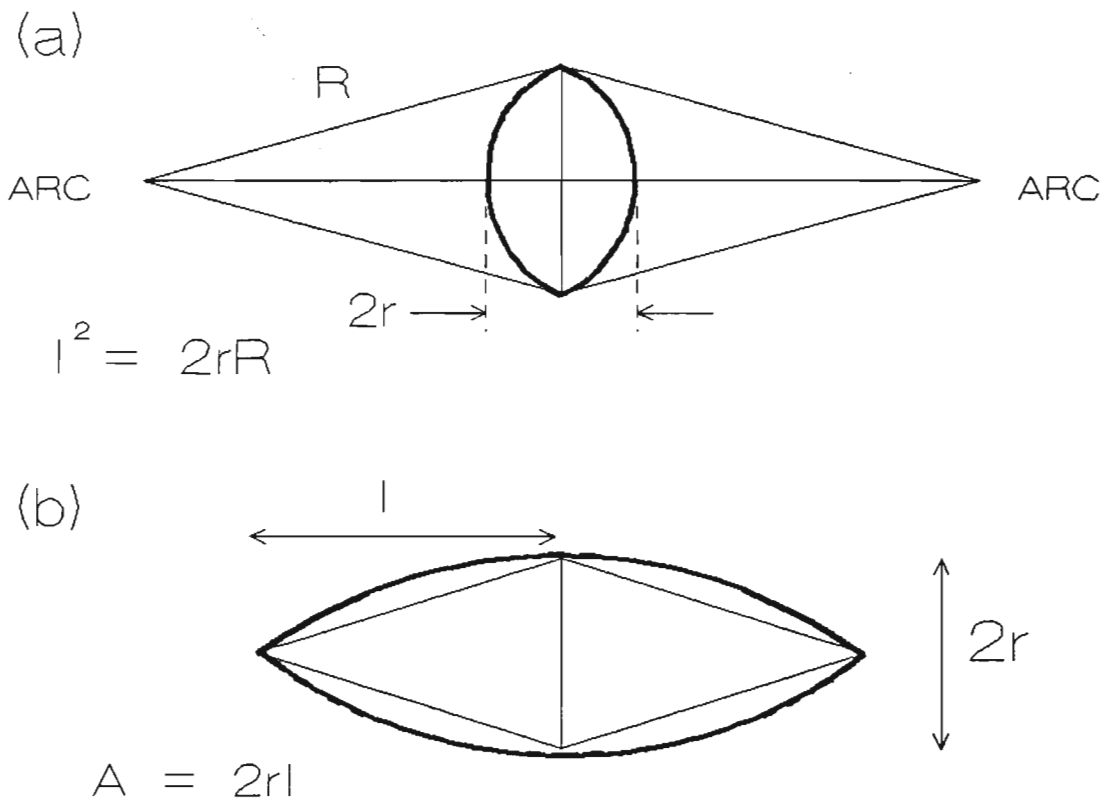

Figure 4.1: Schematic showing approximate area of lens

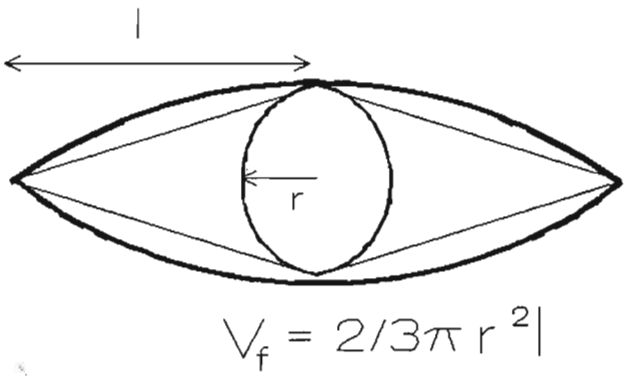

Figure 4.2: Schematic showing volume of lens

this factor, but simple visual examination of typical density and temperature curves (Sedov (1959)), show that it can vary from unity (all the energy is in the strong shock) to a few percent (very little energy is left in the shock itself which now resembles a sound wave). G' is also made to contain the small geometric errors, deliberately made in the rough calculation of G and that following for the focal length f.

In order to calculate the density of the gas in the lens, we now assume that the lens is formed adiabatically, so that

$$W = \frac{1}{\gamma - 1}(p_f V_f - p_o V_o) \tag{4.5}$$

where the symbols have their usual meaning. The known quantities in this expression are the volume of the lens V_f and the initial pressure: p_o. The volume of the lens is approximated to that of two cones (figure 4.2) :

$$V_f = \frac{2}{3}\pi r^2 l \tag{4.6}$$

Taking $\gamma = 1.4$ and writing

$$p_o V_o^\gamma = p_f V_f^\gamma \tag{4.7}$$

one obtains

$$V_o = \left(\frac{p_f}{p_o}\right)^{1/\gamma} V_f \tag{4.8}$$

We can represent equation 4.5 as :

$$0.4W = p_f V_f - p_o V_o \tag{4.9}$$

Substituting for V_o and dividing throughout by p_o we get

$$\frac{p_f}{p_o} - \left(\frac{p_f}{p_o}\right)^{1/\gamma} = \frac{0.4W}{p_o V_f} \tag{4.10}$$

The right hand side is known and $\frac{p_f}{p_o}$ may be obtained graphically.

Knowing the average density $\rho_f = \frac{V_o}{V_f}\rho_o$ in the lens, the refractive index gradient may be calculated very approximately as follows.

The refractive index of air is roughly $n = 1 + 3 \times 10^{-4}\rho$. The uniform refractive index gradient is therefore $(n_f - n_o)/r$ and a median ray traversing the lens $r/2$ mm away from the axis, is refracted (using the small angle

approximation) by an angle

$$\theta = l(n_f - n_o)/r \tag{4.11}$$

and comes to a focus a distance $f = (r/2)/\theta$ away. (n_o is the refractive index of undisturbed air). See figure 4.3.

A little algebra yields the convenient formula

$$f^2 = \frac{1.4r^3}{(\rho_f - \rho_o)^2 R} \tag{4.12}$$

For $\rho_o = 1kg/m^3$ we can write the above equation as :

$$f^2 = \frac{1.4r^3}{(\rho_f - 1)^2 R} \tag{4.13}$$

where f is in meters and r and R in millimeters.

We now attempt to model our large lens, CSL4. This has an electrical diameter of 8cm, which yields an 8mm GRIN lens with a focal length of the order of one meter. If G' is taken as unity, then the calculated focal length is too small.

This example and others, show that predicted focal lengths are a little short for strong shocks and far too short for weak. This was the reason for introducing the G' correction factor. If we take G' as $\frac{1}{2}$ for the strong 250nF shocks, $\frac{1}{30}$ for the weaker 100nF and $\frac{1}{100}$ for the very weak 21nF , we obtain good agreement. Figure 4.4 shows the theoretical results obtained using the simple scaling theory for CSL4 at 21nF, 100nF and 250nF.

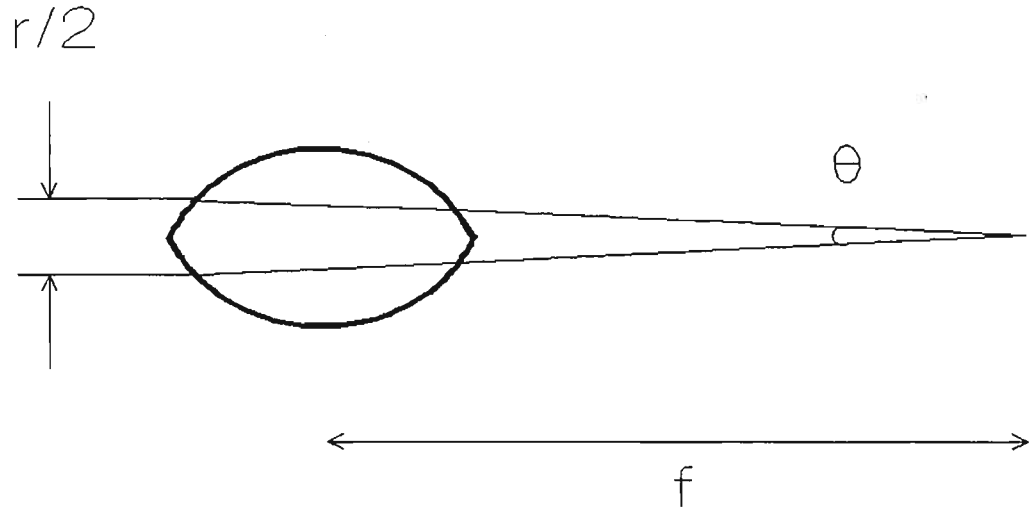

Figure 4.3: Schematic showing angles involved in focussing for CSL

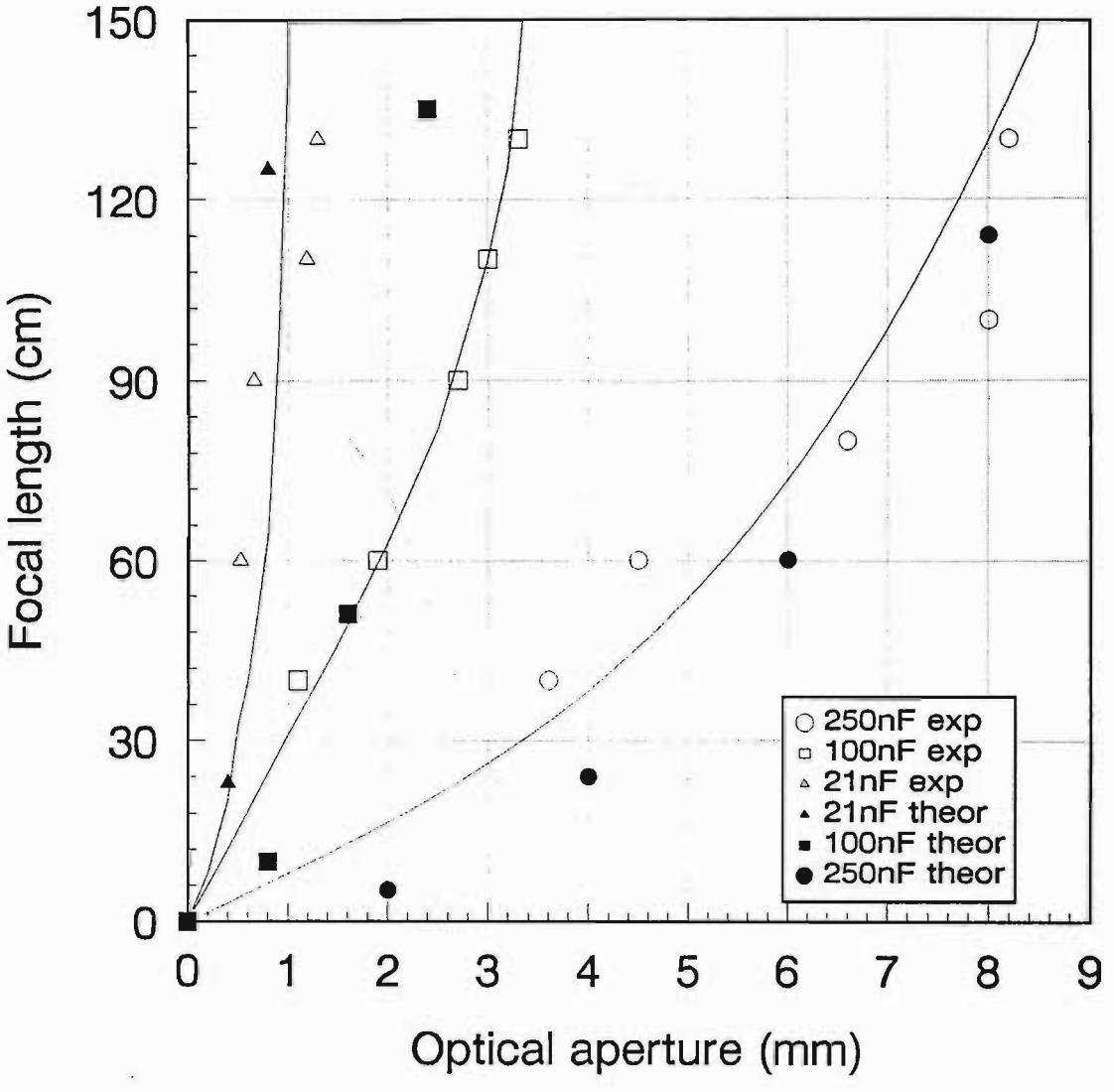

Figure 4.4: Experimental versus theoretical curves for CSL4 at 21nF, 100nF and 250nF

4.2.1 Conclusions

With the simple scaling theory developed above we find good agreement between the theoretical predication and the experimental results for CSL4 based on the correct choice of the correction factor.

4.3 The Fluid in cell differencing method

In this section we use the numerical method of Gentry et al. (1966) to simulate the behaviour of the colliding shock lens. This method is known as the Fluid in Cell (FLIC) method.

The FLIC method developed as an outgrowth of the work of Rich (1963). This method (FLIC) is similar to the Particle in Cell (PIC) method of Evans and Harlowe (1957). The PIC method utilizes Lagrangian fluid particles to transport mass, momentum and energy through an Eulerian mesh of cells. The use of the particles, while facilitating the calculation of multi-fluid problems, results in non-physical fluctuations of the fluid quantities.

The difference equations used in the FLIC method are very similar to those used in the PIC method. The transport calculation of the FLIC method does not require the use of particles. The elimination of particles allows solutions which are free from fluctuations which are characteristic of PIC.

The FLIC method is a finite difference method which solves the time dependent equations of motion for compressible fluid flow. The flowfield under consideration is subdivided into a mesh. Initial values of density (ρ), velocity (v) and specific internal energy (I) are assigned to each mesh cell at the beginning of the problem. The value of each cell quantity is advanced in time (δt) using a finite difference approximation for the equations of motion of the fluid.

Intermediate values are calculated for velocities and specific internal energy taking into account the effects of accelerations due to pressure gradients. The mass flow across cell boundaries during time (δt) is determined using the intermediate values of velocity. The flow of momentum and energy are

then computed assuming that the mass which has crossed the cell boundary carries momentum and energy corresponding to the intermediate values of velocity and specific energy of the donor cell. The final values for ρ, v and I are then calculated using the conservation of mass, momentum and energy.

A complete and detailed description of the FLIC method is given in Appendix A.

For the colliding shock lens simulation, the FLIC FORTRAN code of Meintjies (1975) was used. With this code we are able to study in two dimensions the convergence of a cylindrical shock wave (with known initial energy) and its subsequent divergence after colliding with a fixed boundary (wall). This is analogous to two shock waves of equal strength colliding. We study the refractive index profile as well as the change in optical path length both before and after collision. These quantities enable us to calculate the focal length for any particular lens diameter as a function of time.

The computational mesh used to simulate the converging shock waves is shown in figure 4.5.

The mesh as shown in figure 4.5 is a cylindrical co-ordinate system of m $\times$ n cells. For the purposes of the simulation to follow, m = 160 cells and n = 80 cells. We simulated the behaviour of CSL3 and CSL4 under different conditions of shock strength and ambient pressure. For CSL3, the cell size $\delta z = \delta x = 200\mu m$ and for CSL4, $500\mu m$. The time step δt was 25ns. The pressure was varied from 1 bar to 3 bar and the initial shock strength from Mach 1 to Mach 3. No artificial viscosity terms were used.

4.3.1 Results

The simulation was first conducted for CSL3 having an electrical diameter (distance between electrodes) of 40mm ($\delta z = \delta r = 0.02\mu m$). The time step chosen was 25ns and a maximum time of $50\mu s$ was used. The shock was given an initial radius 50 cells and a thickness of 2 cells. These correspond to a radius of 10mm and a thickness of 0.4mm. The reason for the choice of the initial radius was to reduce computing time. This was found to be a satisfactory initial condition provided that the initial shock strength at this

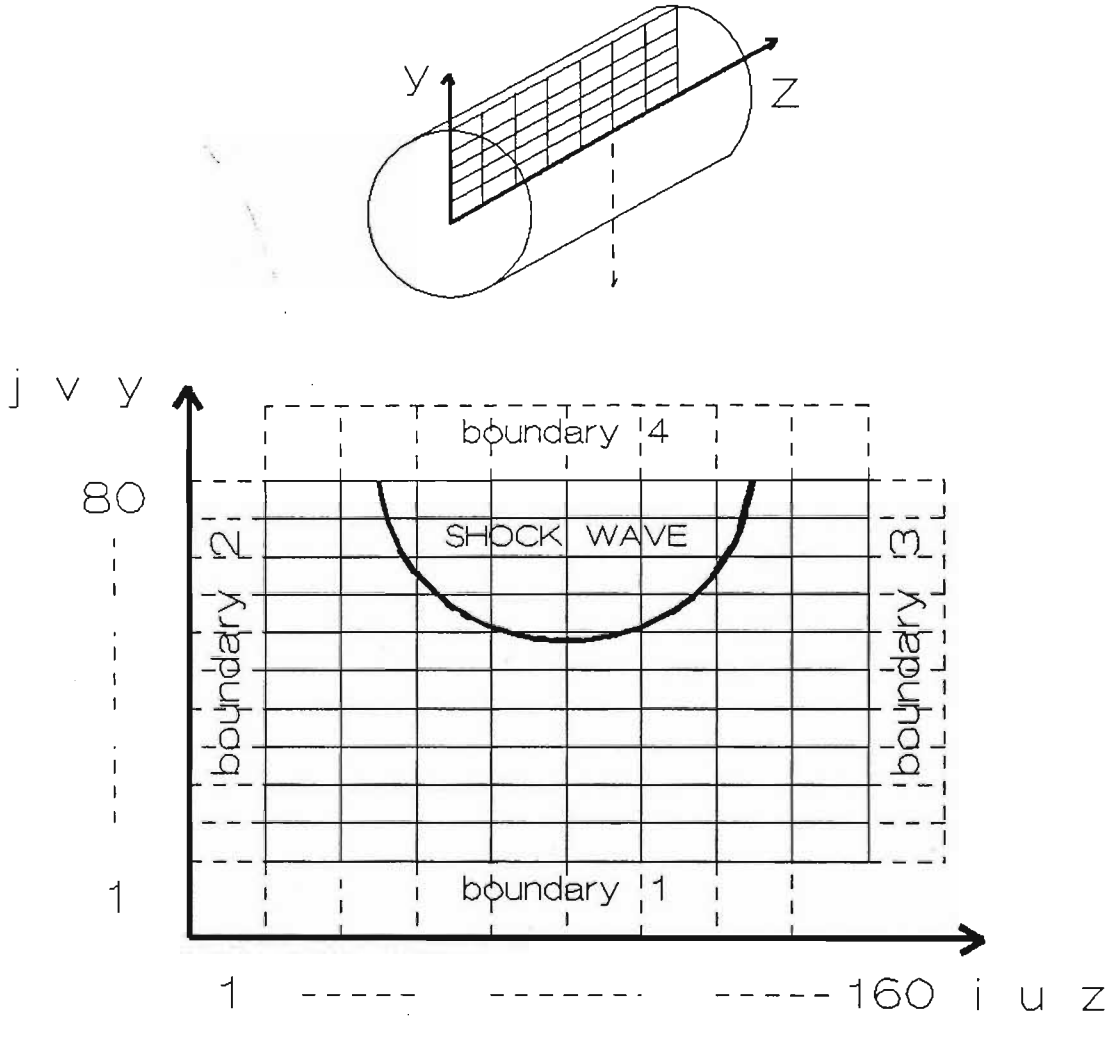

Figure 4.5: Computational mesh for CSL simulation

point is related to the experimental shock strength at the electrodes when comparisons between experimental results and the simulation are made.

To illustrate the analysis procedure we ran the simulation for CSL3 with a pressure of 1 atmosphere and an initial shock strength of Mach 1.5. Figure 4.6 shows a time sequence of 20 profiles. Each profile represents the refractive index versus radius and the profiles are temporally separated by 2.5μs. Although only 20 files are represented here, during subsequent simulations 200 data files out of a possible 2000 were saved to disk. This enabled us to achieve a temporal resolution of 0.25μs. It is evident from the figure that the refractive index increases as the shock reaches the boundary. We also see a steepening of the shock front before collision. After interacting with the boundary, the shock diverges to the right. The refractive index decreases as the shock relaxes. The profile at 12.5μs represents the condition just before collision and the one at 15μs, just after collision.

The oscillations below the axis are due to the fact that no artificial viscosity was introduced into the simulation. We found that although the inclusion of artificial viscosity terms reduced the shock instability below axis, it increased the instability close to and at the point of collision with the boundary. This was clearly unacceptable. The inclusion of these terms did not change the shock evolution characteristics before and after collision. It was therefore decided to work without artificial viscosity.

Using the refractive index values at each point for each time step, we computed the change in optical path length for each point. These profiles are shown in figure 4.7.

The times indicated in the previous plot (figure 4.6) are again indicated to give the reader an idea of the corresponding values. Once again, the wild fluctuations below the axis are visible but since these do not affect the calculations they can be safely ignored.

Using the data for figure 4.6 we calculated the optical aperture versus time after collision for this simulation. This is shown in figure 4.8. We assume that the refractive index peak represents the edge of the lens and use this diameter as the optical aperture for any particular time.

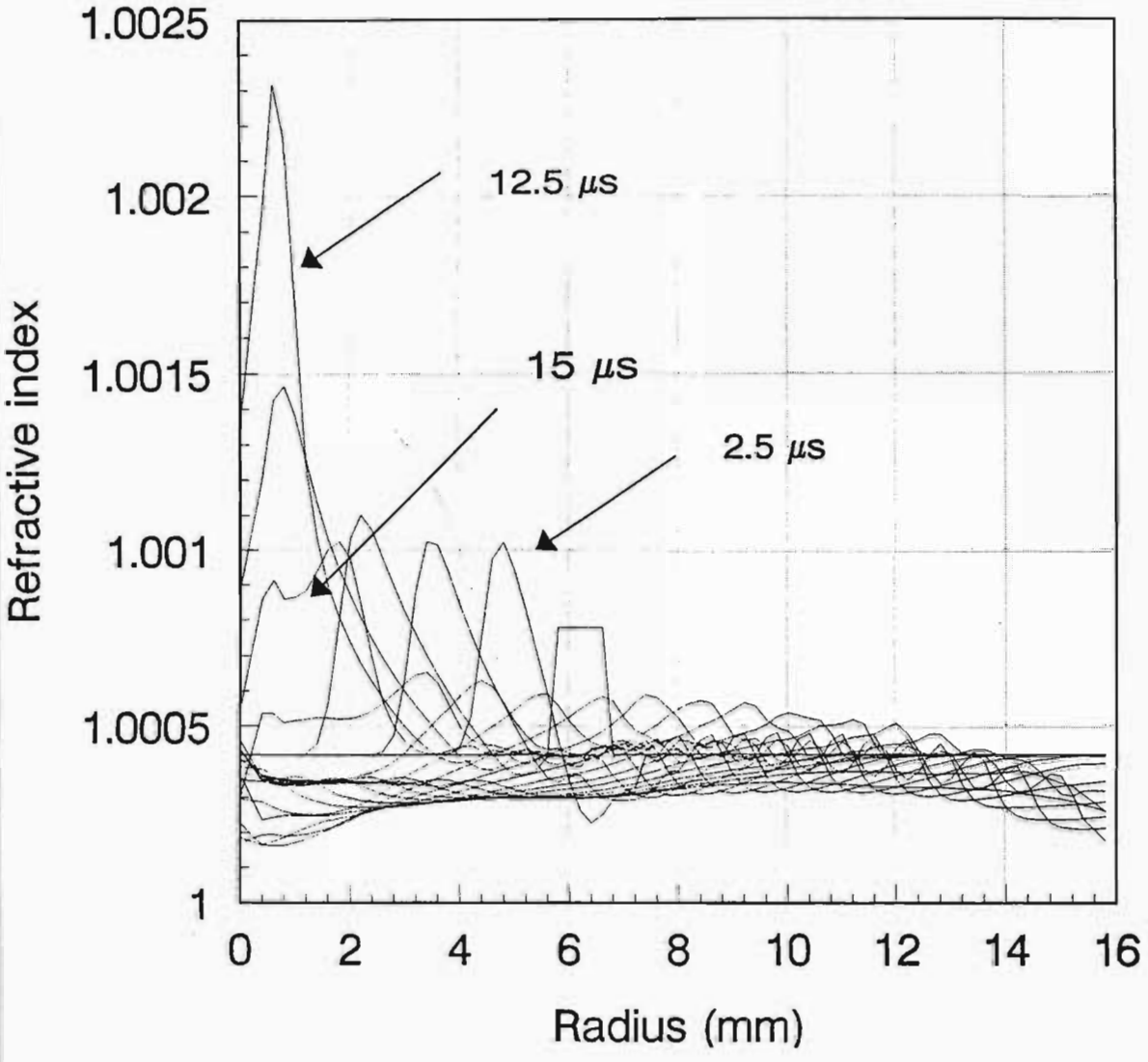

Figure 4.6: Refractive index versus radius for various times before and after collision.

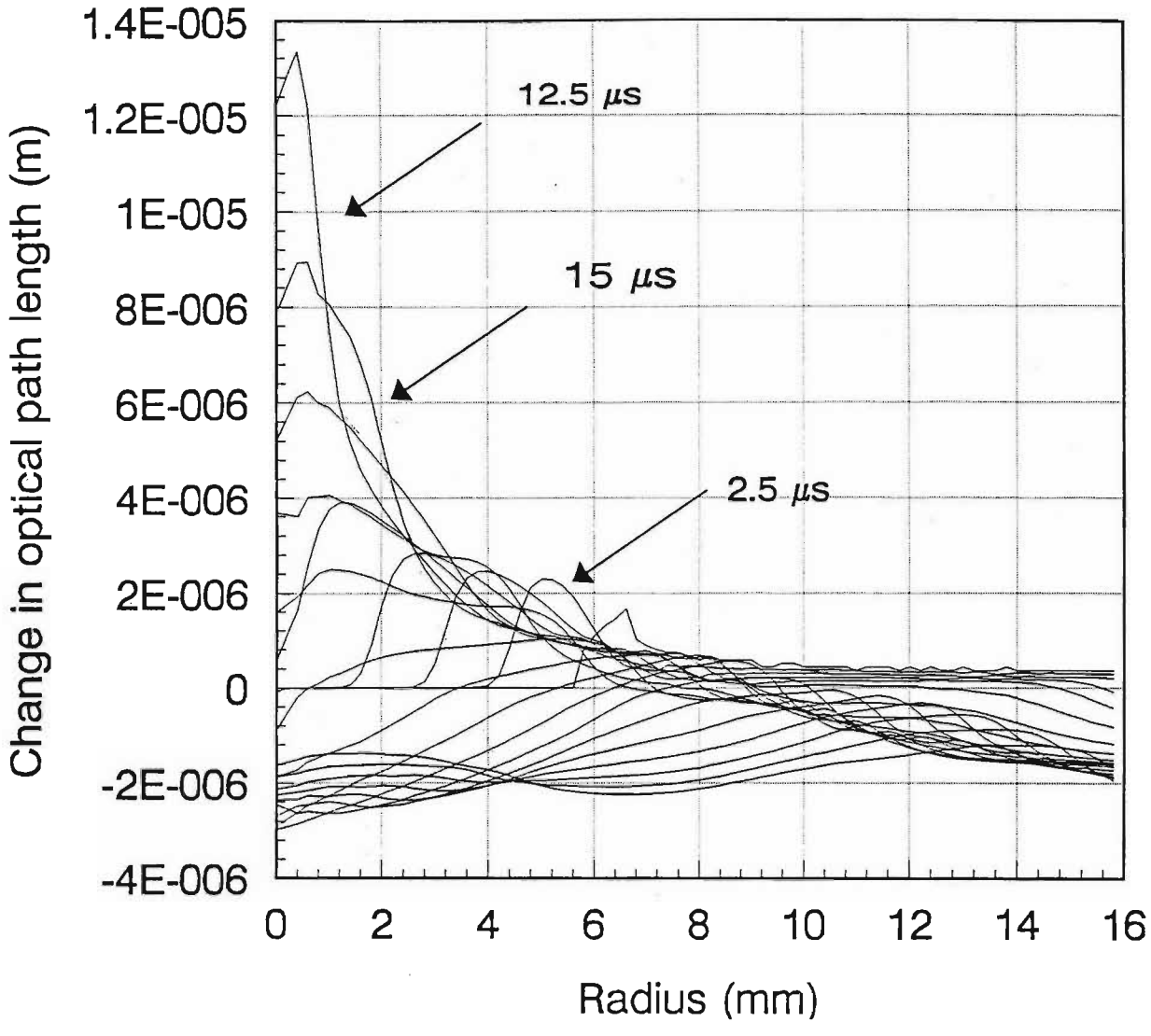

Figure 4.7: Change in optical path length versus radius for various times before and after collision.

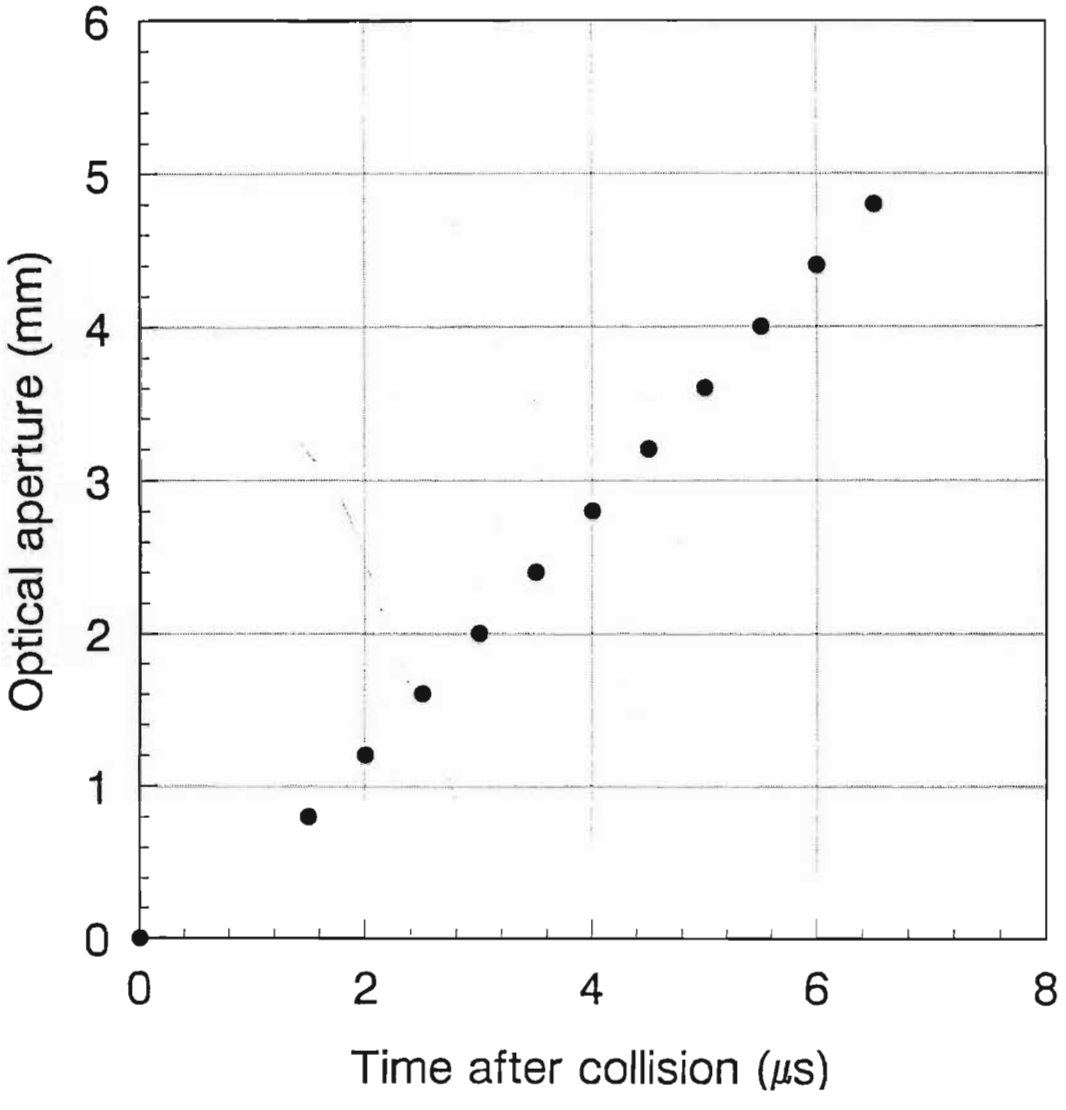

Figure 4.8: Optical aperture versus time after collision

Using the now known optical aperture and the change in optical path length for that aperture for a particular time (figure 4.7), we then calculated the focal length as a function of time after collision. See figure 4.9.

Combining these two graphs (fig. 4.8 and fig. 4.9) we then plot a graph of optical aperture versus focal length (figure 4.10) for this lens under the given initial conditions. It is this plot that we use to compare the simulation with the experimental results.

We first chose to simulate CSL3 for different input energies. Choosing an initial pressure of 1 bar, we varied the input energy of shocks from Mach 1 to Mach 2. The plot of optical apertures versus focal length is shown in figure 4.11.

As expected, as the input energy increases, the focal length gets shorter for the corresponding optical aperture. This is the same relationship that we observed experimentally. Comparing the simulated profiles with the experimentally obtained ones for CSL3 (figure 4.12), we see that there is good correlation between the 100nF profile and the Mach 1 simulation. The Mach 1.5 and 2 profiles have a much shorter focal length than any of the experimental ones. This is interesting since the experimentally measured shock speed for the 100nf charging cap size was 1.5 just after shock creation. This can be explained by virtue of the fact that since in the simulation, the shock has an initial radius of 6mm, a shock having an energy corresponding to a speed of Mach 1 at this point corresponds to a higher speed measured at the point of shock creation. It is quite reasonable to assume therefore that a speed of Mach 1.5 measured on the outside, is the same as a speed of Mach 1 as measured 10mm from the centre. Assuming this to be the case, we therefore find good agreement between the 100nF experimental plot and the Mach 1 simulated plot. Since the Mach 1.5 and 2 simulations correspond to much higher input energies than those used experimentally, these simulations show much smaller focal lengths than any of the three experimental ones. We can deduce from the simulation that if the input energy were higher than those used, much shorter focal lengths could have been obtained. Unfortunately, we have seen that there is a limit on the energy used in each lens because of turbulence.

We then kept the input energy (Mach number) constant i.e. Mach =

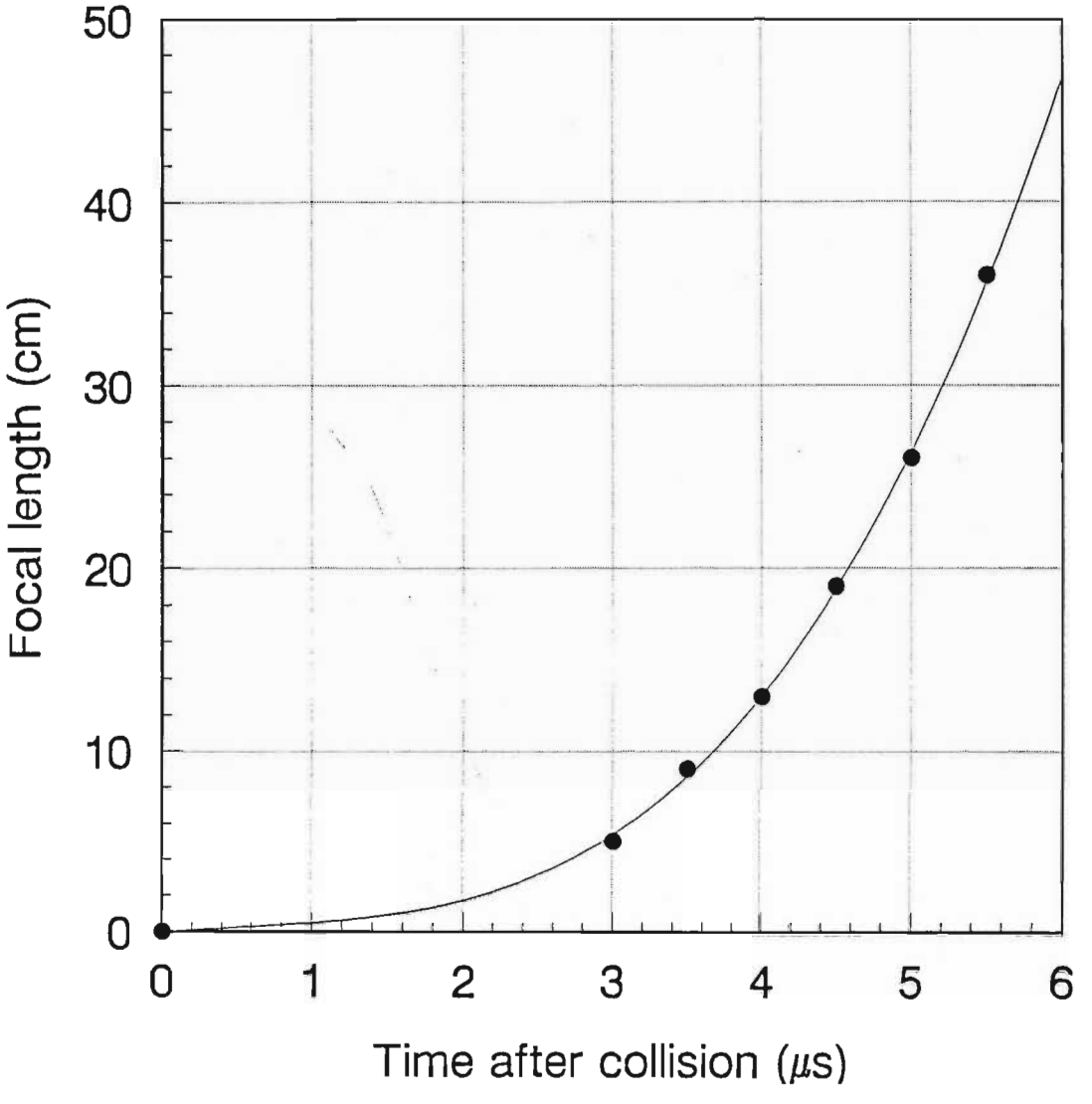

Figure 4.9: Focal length versus time after collision

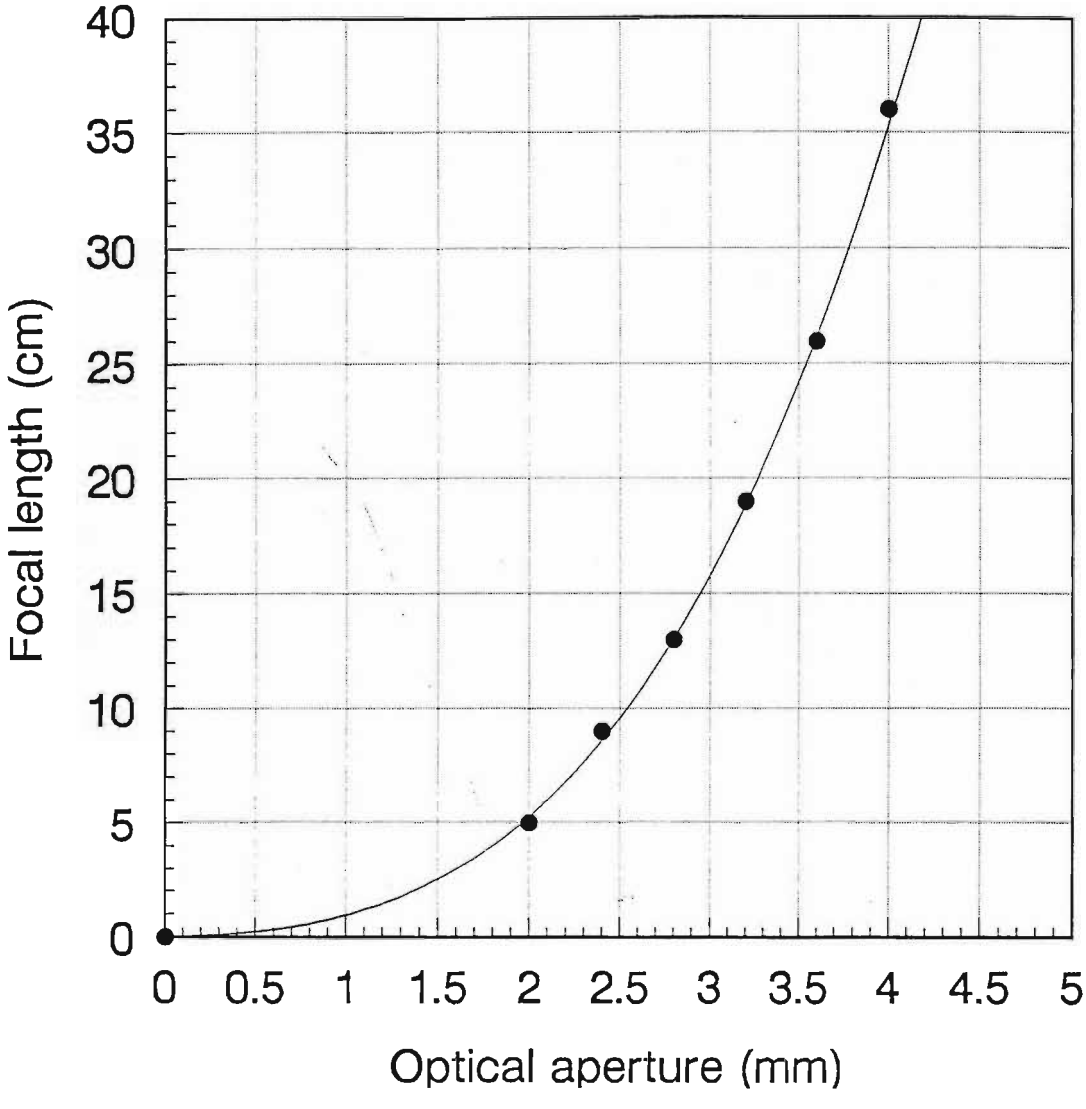

Figure 4.10: Optical aperture versus focal length

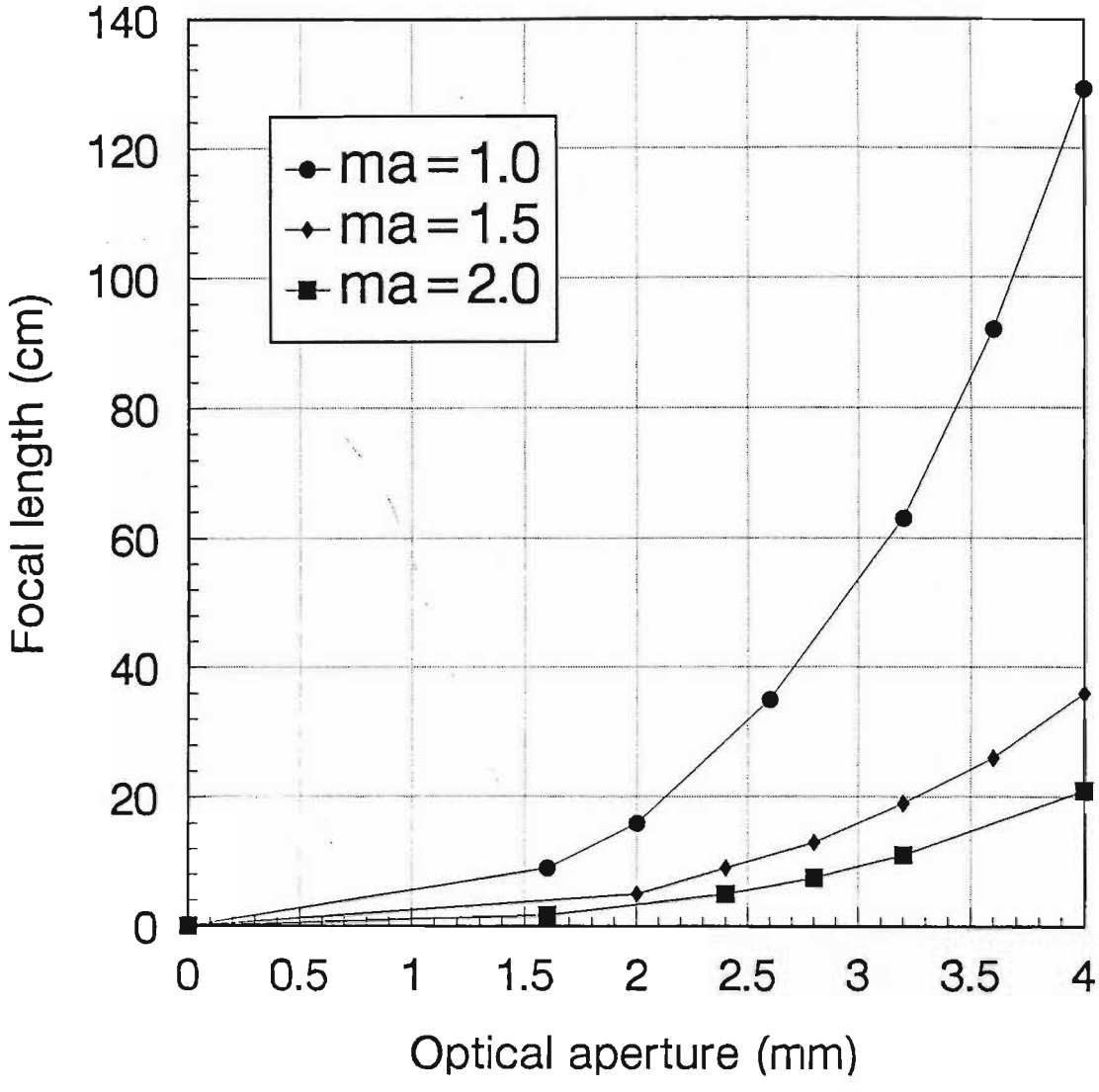

Figure 4.11: Simulated optical aperture versus focal length for CSL3 at Mach 1, 1.5 and 2

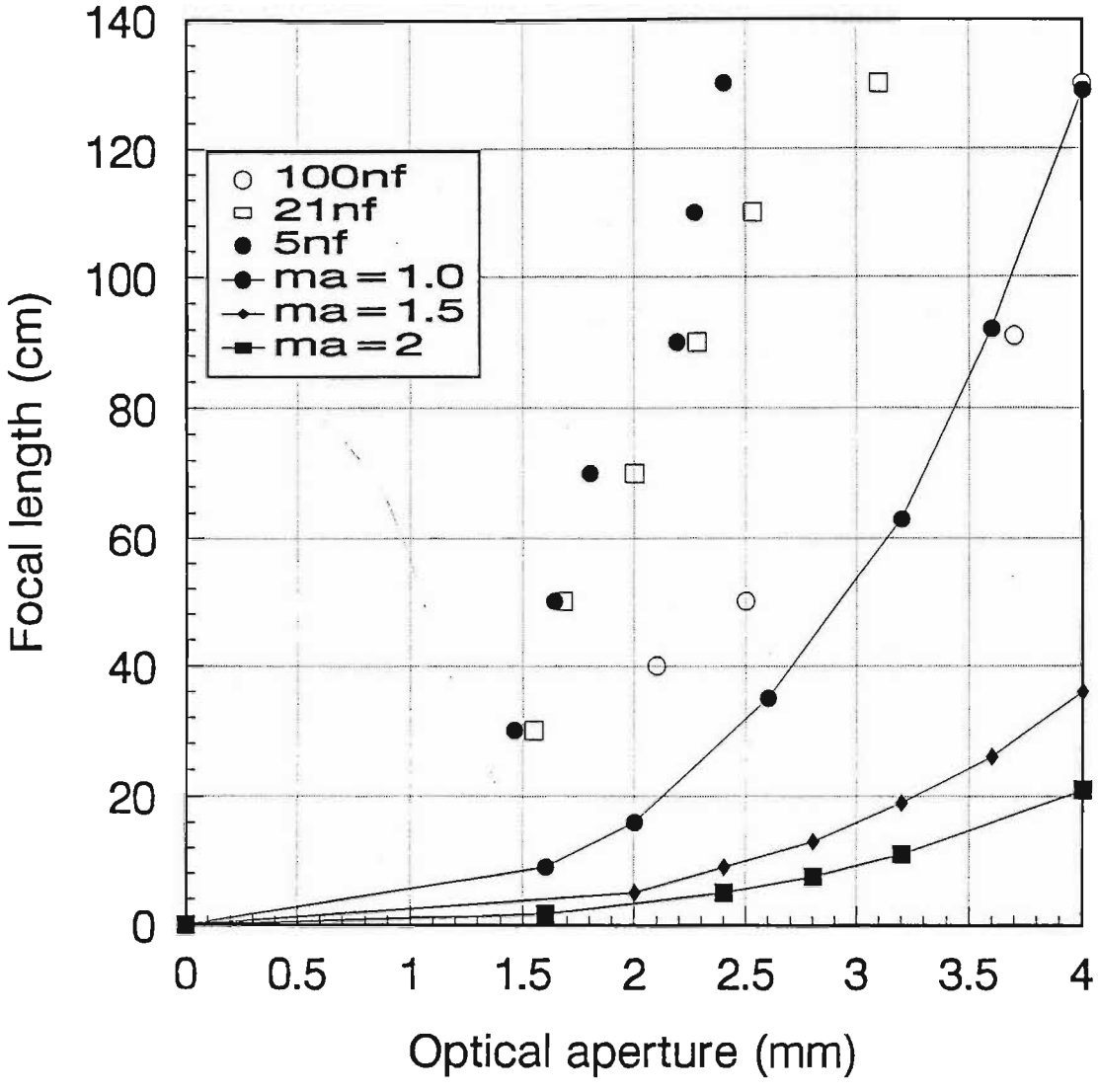

Figure 4.12: Comparison of experimental and simulated profiles for optical aperture and focal length for CSL3 at Mach 1, 1.5 and 2

1 and varied only the ambient pressure of CSL3 to see how the focussing qualities change. Figure 4.13 shows the simulated plots for optical aperture versus focal lengths for 1 bar (atmospheric pressure), 1.5 bar, 2 bar and 3 bar.

Unsurprisingly, as the ambient pressure is increased, the focal lengths for corresponding optical apertures decreases. A comparison with the experiment (100nF) is shown in figure 4.14.

It is encouraging to note that the slopes of the graphs are all roughly the same. We see fairly good correlation between the 1 and 1.5 bar results. The 3 bar simulation shows a larger optical aperture than the corresponding 3 bar experimental result. This 1mm difference in optical aperture is nevertheless acceptable and can be attributable to experimental uncertainty. Once again as expected, the simulated results are fairly consistent with the experimentally derived results.

We now model CSL4. In order to do this we need only change the cell size. Since CSL4 has an electrical diameter of 80mm, this is easily accomplished by setting $\delta z = \delta r = 0.05\mu m$. The initial shock radius and thickness were again set to 50 cells and 2 cells respectively. For CSL4, we varied only the input energy (Mach number) to see how this compares with the experiment. The ambient pressure was 1 bar.

Figure 4.15 shows the simulated optical aperture versus focal length for CSL4 at two different Mach numbers viz. Mach 1 and 2.5. These two values were chosen since the lens was operated experimentally at 100nF and 250nF.

The figure shows the usual trend of shorter focal length for a corresponding optical aperture as the input energy increases. We see that for a focal length of 70cm for example, the optical aperture doubles from 6mm to 12mm as the input energy is increased by 2.5 times. This represents a halving of the f number. Comparing the simulation with experiment (figure 4.16) we find that there is good correlation between the Mach 1 simulated shock and the profile obtained using the 250nF cap. This can be explained as follows. Since CSL4 has a diameter which is twice that of CSL3, we would expect that approximately twice the energy would be needed to attain the same shock structure after collision as in the case of CSL3. We would therefore expect that an input energy of 100nF in CSL3 is the same as 200nF in CSL4. Since

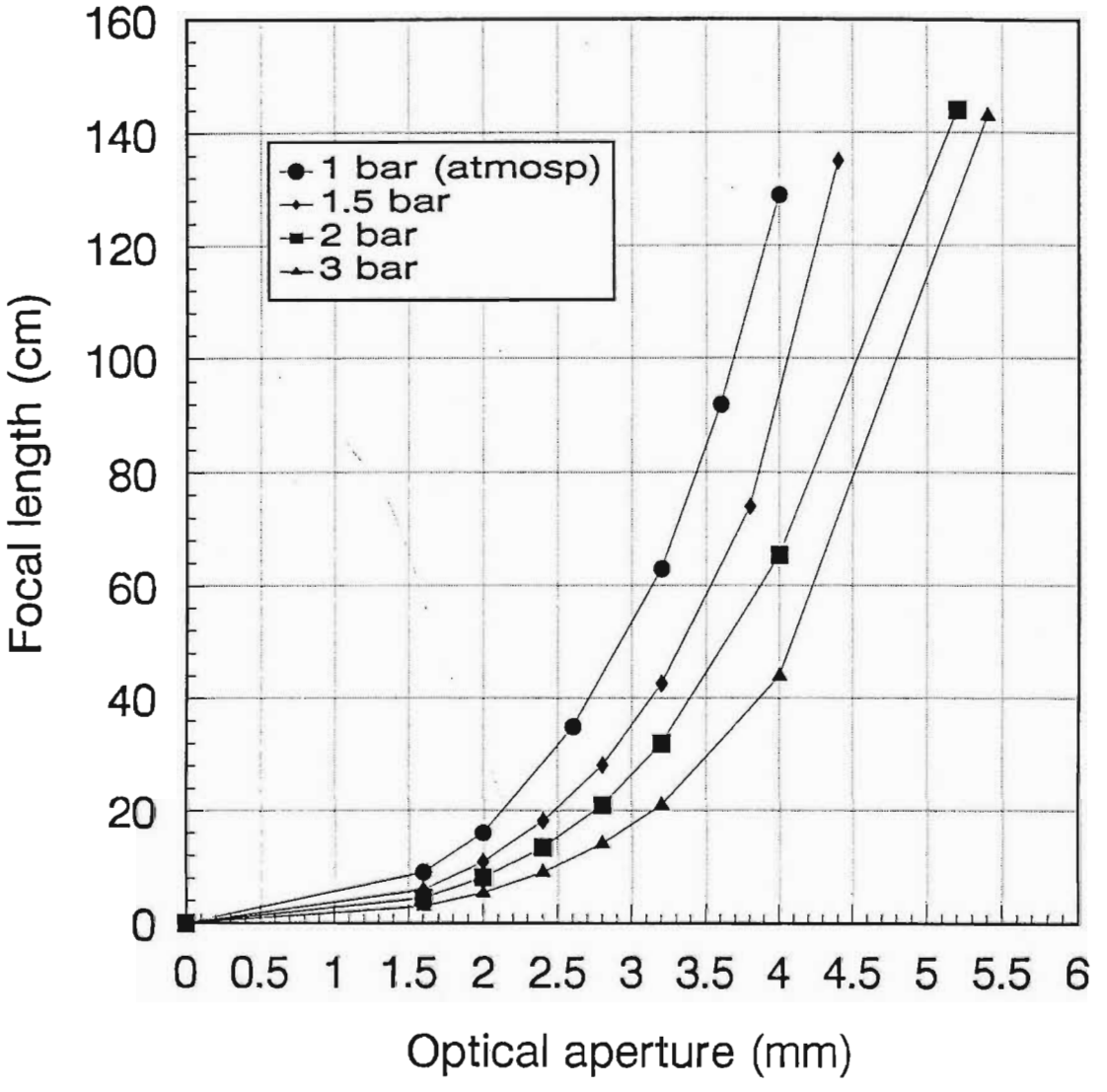

Figure 4.13: Simulated optical aperture versus focal length for CSL3 at 1, 1.5, 2 and 3 bar with a constant Mach number =1

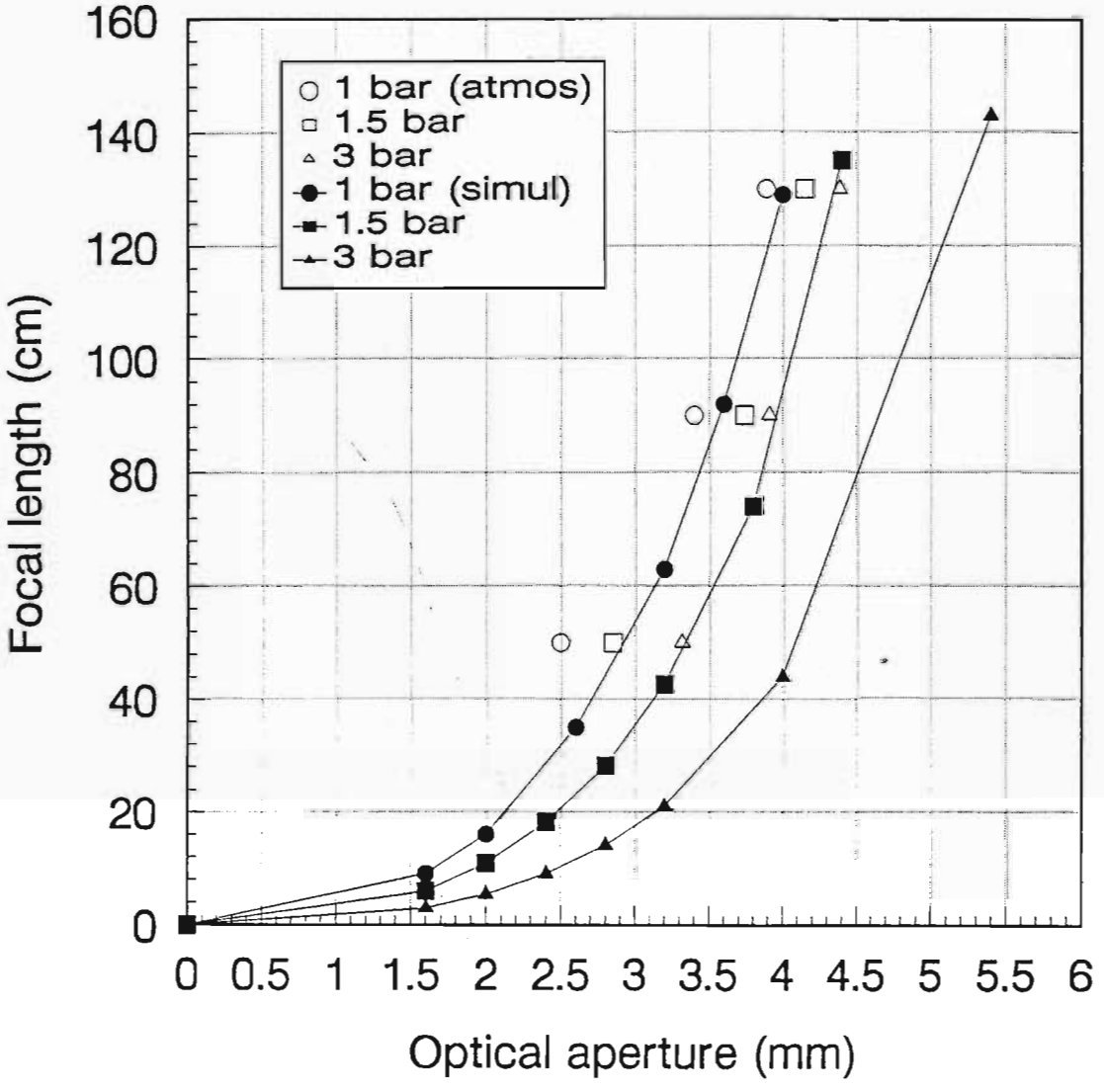

Figure 4.14: Comparison of experimental and simulated profiles for optical aperture and focal length for CSL3 at 1, 1.5, and 3 bar

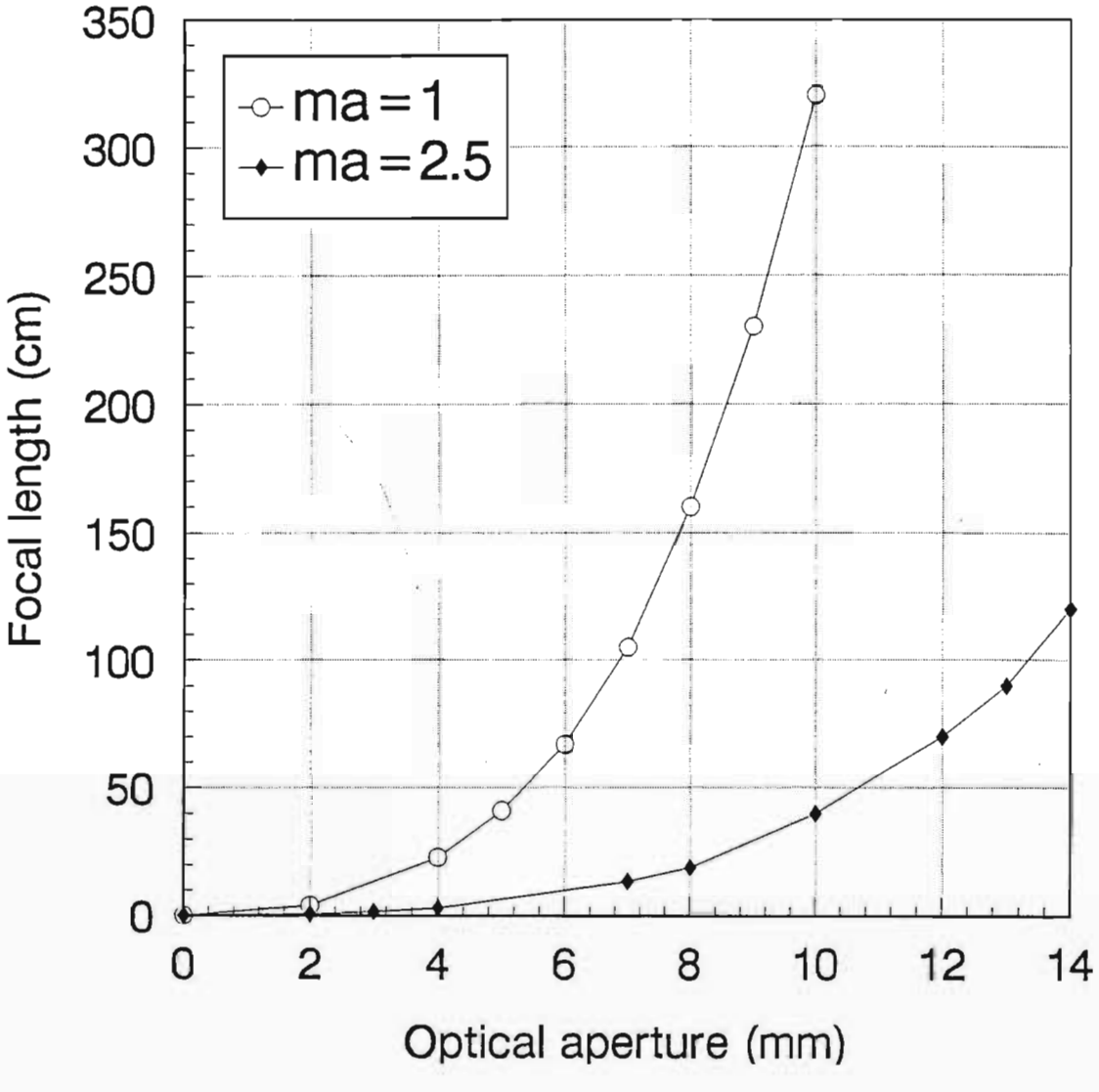

Figure 4.15: Simulated optical aperture versus focal length for CSL4 at Mach 1 and 2.5

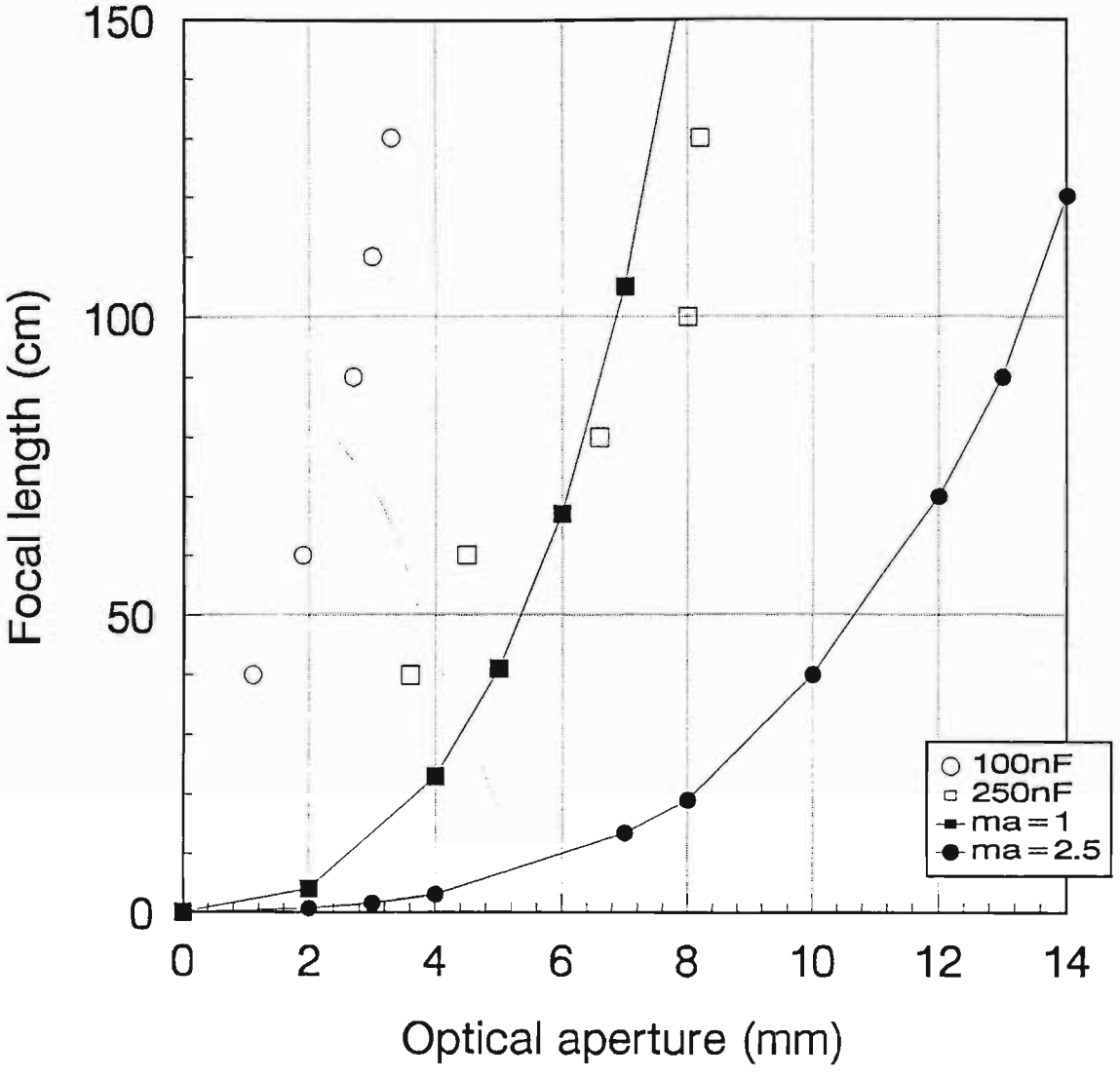

Figure 4.16: Comparison of experimental and simulated profiles for CSL4 at Mach 1 and 2.5

a simulated shock of Mach 1 corresponds with 100nF in CSL3, it is plausible the a simulated shock of Mach 1 would correspond with an input energy of 250nF in CSL4.

From the simulation we can deduce that were we to increase the charging capacitor size from 250nF to 625nF we could achieve an optical aperture of 14mm at a focal length of 1.2m.

4.3.2 Conclusions

The simulation for CSL3 and CSL4 show the same trends as the experiment i.e. as the input energy is increased, the focal length decreases and as the ambient pressure is increased, the focal length also decreases for the corresponding optical aperture. There is good correlation between the Mach 1 shock simulation and the 100nF CSL3 profile and the 250nF CSL4 profile. The simulation indicates that for CSL3, doubling the input energy from 100nF to 200nF would result in a lowering of the focal length from 130cm to 20cm for a 4mm optical aperture. Unfortunately, the simulation cannot predict the onset of turbulence in the CSL, which prevents an increase in input energy beyond a certain value for each lens. We can also conclude that for CSL3, increasing the pressure from 1 bar (atmospheric pressure) to 3 bar reduces the focal length from 130cm to 64cm.

Chapter 5

The Cylindrical Colliding Shock Lens

5.1 Cylindrical lenses

Lenses with spherical surfaces are commonly used in most optical applications. Such surfaces are easy to produce with high precision at a comparatively low cost. Thin spherical lenses or combinations thereof, satisfy many of our optical needs. They form real or virtual images some distance away from the lens surface and are capable of focussing (bi-convex) light sources down to a point. However, occasions do arise when lenses of other external form and behaviour are required.

The correction of *astigmatism* is one common example of such an occasion.

Astigmatism arises from an uneven curvature of the cornea of the eye. In other words, the cornea is asymmetric. If we pass two meridional planes through the eye (with both the planes containing the optic axis), we find that the curvature is maximal on one plane and minimal on the other. For the case where the two planes are perpendicular to each other, this is known as *regular astigmatism.*

Regular astigmatism manifests itself in different forms. For example, the eye can be myopic (shortsighted) or hyperopic (farsighted) in various degrees

depending on the relationship between the powers (or curvatures) of the two meridians. Due to this condition, when looking at a chess board, the viewer will find that whereas the columns might be focussed, the rows might appear bleared or vice versa. Clearly, spherical lenses (having constant curvature along both meridians) cannot be used for the correction of this problem. The lens to be used must have different powers in different meridians. This implies that the lens surfaces cannot each have a constant curvature. A cylindrical lens satisfies these requirements.

Conventionally, cylindrical lenses have one face which is cylindrical and the other face which is plane (plano-cylindrical) or spherical (sphero-cylindrical).

5.1.1 Refraction by a plano-cylindrical lens

In figure 5.1a let X_1 be a luminous point on the axis OX_1 of a thin plano-cylindrical lens.

The divergence of rays from X_1 and in the vertical plane containing the principal axis of the cylindrical surface is not affected by their passage through the lens. See figure 5.1b. In any other plane, the change in the divergence of the light will depend upon the power (or curvature) of the lens in that plane.

In the horizontal plane through X_1, the rays may be brought to a real focus at X_H or X_2 (figure 5.1c). The position of this focus is determined by the fundamental paraxial equation for a thin spherical lens :

$$\frac{1}{f} = \frac{1}{i} + \frac{1}{o} \tag{5.1}$$

where f is the focal length, i the image distance and o the object distance.

For any oblique plane the light from X_1 will be refracted so that it is focussed at a point in the vertical line through X_H. This is termed the **focal line** and is parallel to the axis of the cylinder. If the plane face of the lens is

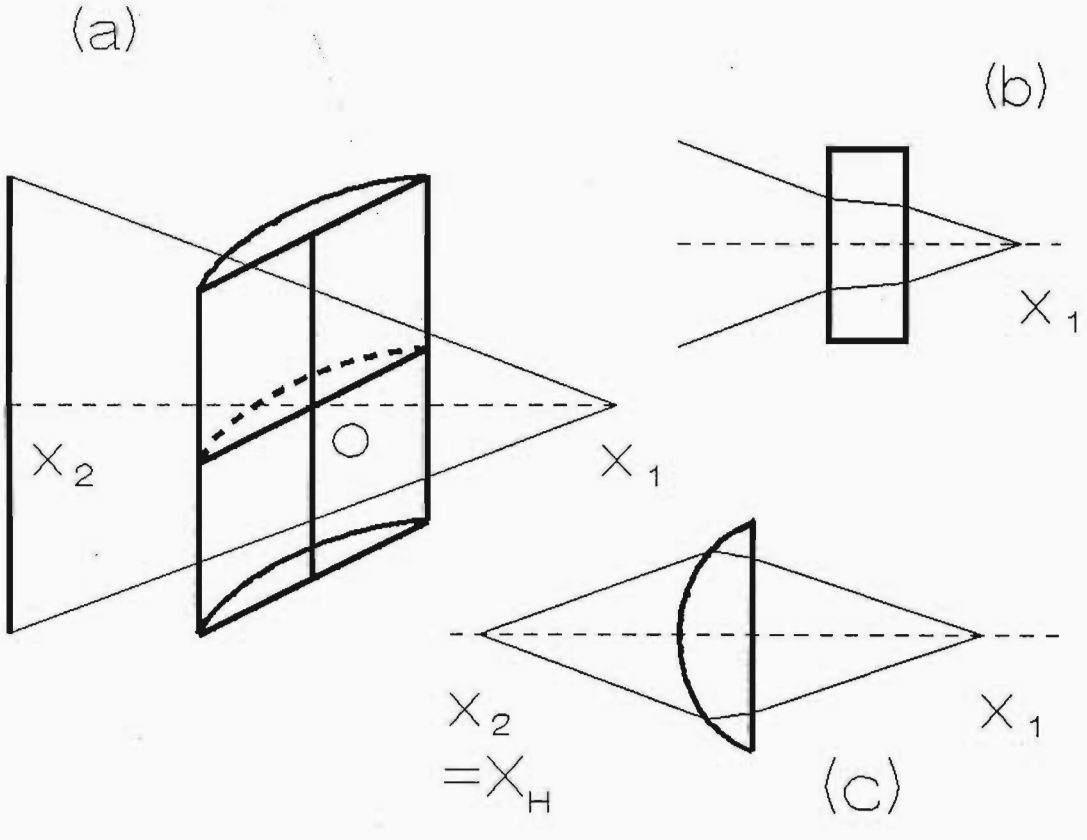

Figure 5.1: Refraction by a plano-cylindrical lens

rectangular and completely illuminated with light from X_1, the section of the emergent beam at any plane normal to OX_1 is also rectangular. However, its height increases and its width decreases as the plane moves away from the lens until it passes through X_2 when the width is zero.

The uses of cylindrical lenses are wide and varied. In what must be the first use of a cylindrical lens to correct astigmatism, Sir George Airy used a concave sphero-cylindrical lens in 1825 to correct his own myopic astigmatism. Opthalmologists have since adopted this method on a large scale. Cylindrical lenses are also used in other fields. They are, for example, used in the making of wide screen motion pictures where an extra large horizontal field of view is compressed onto the regular format.

Of greater interest is the use of cylindrical lenses for the line focussing of laser beams. This is widely used in the production of x-ray lasers. In the schemes which involve laser vapourisation of thin foils (Rosen et al. 1985) or laser ablation off solid targets for the production of x-rays (Chenais-Popovics (1987)), a uniform line focus is desirable. This is achieved by the use of cylindrical optics. Recently, Daido et al. (1993) used cylindrical optics to focus two arms of the Gekko XII laser onto a neon-like germanium foil for the production of x-rays. The focus was 6cm long and 100μm wide.

Although we have only discussed plano-cylindrical lenses, it is not uncommon to find cylindrical rods used for line focussing. These rods can be envisaged as a combination of two plano-cylindrical lenses placed back to back. See figure 5.2.

The focal length for this arrangement, in terms of the radii of curvature of the two surfaces, is given using the formula for thick lenses as :

$$\frac{1}{f} = (n_l - 1)\left(\frac{1}{R_1} - \frac{1}{R_2}\right) \tag{5.2}$$

where n_l is the refractive index of the lens material, R_1 and R_2 are the radii of curvature of the two surfaces.

We have seen in chapter 3 that the colliding shock lens behaves like a spherical lens due to the geometry of the shocks and the density profile of

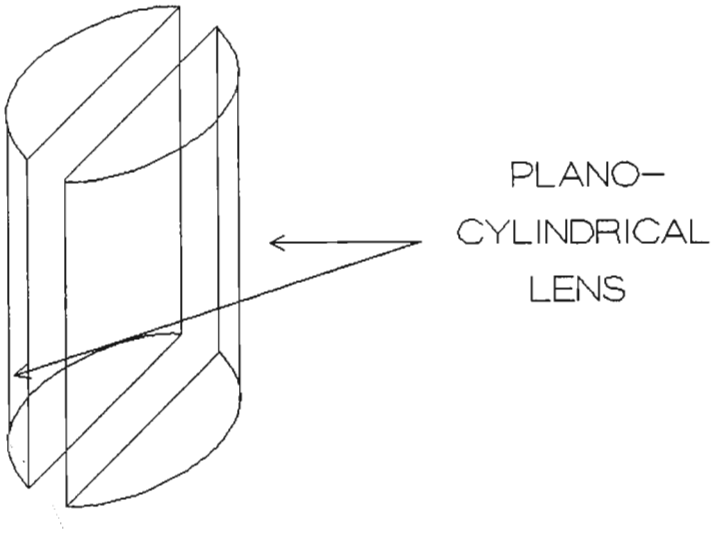

Figure 5.2: Cylindrical rod lens

the cigar shaped lensing region. It was proposed by Michaelis that a cylindrical shock structure would similarly behave like a cylindrical lens with a varifocal length line focus. We therefore constructed a device using converging shocks (based on the same principal as the CSL) to create a cylindrical graded index lens after collision. This device we called the Cylindrical Colliding Shock Lens (CCSL).

5.2 Description of the CCSL

The CSL as described previously consists of opposing pairs of electrodes arranged on the circumference of a circle. The CCSL's geometry is completely different. The CCSL consists of a plastic tube 10cm long and 6cm in diameter (see figures 5.3 and 5.4).

The tube is split and spacers are added to create a rectangular optical window (1cm by 8cm) through which a laser beam can be passed. The electrodes are constructed from steel screws having a shaft diameter of 3mm and a head diameter of 5mm. Four opposing lines of electrodes are arranged lengthwise along the tube. The orientation of the electrodes is such that the

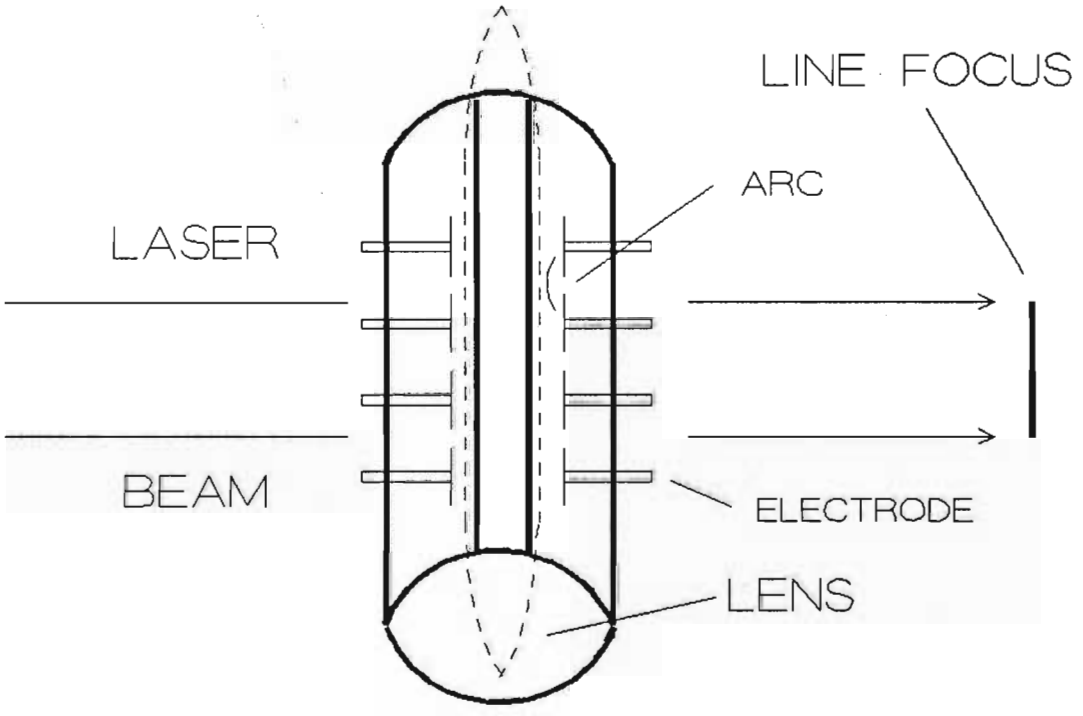

Figure 5.3: Schematic representation of the cylindrical colliding shock lens

Figure 5.4: Photograph of prototype CCSL

heads of each screw is located on the inside of the device to form the closest point of contact between adjacent electrodes and hence the point at which electrical discharge (shock creation) takes place. The geometry of the CCSL and the size of the electrodes chosen has resulted in a gap of 1mm between electrodes, with the separation between each line being of the order of 2cm.

The distance between the head of each screw and the tube wall was set at 1cm. The effect of this separation on the resulting shock structure was not clear at the time of experimentation and is a subject for future investigation. The present device has 10 electrodes per line, but for the initial experiments described in this thesis only four electrodes per line were used. The experimental set-up used in this experiment is the same as that used for the CSL (described earlier in section 3.2).

5.2.1 Mode of operation

The four lines of electrodes of the CCSL are connected in parallel with each other, thus ensuring that each line charges up to the same voltage. The lines are charged to 11kV through the charging capacitor C. For the preliminary investigations a 250nF capacitor was used. When fully charged. one end of each line is switched to ground through a pressurised spark gap (pressurised to 3 bar). The electric discharge between pairs of adjacent electrodes create shock waves (3 per line in this case) which converge towards the centre of the CCSL. At the moment of discharge, a Rogowsky coil located on the main discharge line picks up the signal. A short time after convergence of the shock waves (approximately 22μs) the shocks produce a cylindrical shaped high density region which acts as a graded index lens. The signal from the Rogowsky coil is delayed by this time and this delayed signal is used to trigger the laser beam to be focussed. For our experiments a nitrogen laser having a 1ns pulse (FWHM) is utilised. This beam then passes through the optical window and is focussed down to a line some distance away. This distance depends on the time delay chosen. A TV camera together with a 337nm interference filter is used to detect the laser beam.

Like the CSL, the CCSL is a vari-focal length lens.

The 1cm wide optical window makes it possible to focus a laser beam of

similar diameter. The size of this window can be increased to accept a larger laser beam.

5.3 Results

To study the behaviour of the CCSL, we first probed the shock structure in the plane of the CCSL. Figure 5.5 shows a sequence of shocks imaged in the shock plane at different times after shock creation.

We have seen (Buccellato et al. 1993) that the converging shocks in the CSL initially have a polygonal structure which smooths out into a very circular expanding structure after convergence due to Mach addition. In a similar way, the shocks in the CCSL before collision have a very distinct circular structure (figs 5.5a - 5.5c) which becomes fairly linear after convergence. Hence we have the formation of a cylindrical density profile which is capable of focussing down a laser beam to a line some distance away.

We then removed the imaging optics and using the faceplate of a CCD camera as the screen, we imaged the focussed beam at a distance of 1m away from the CCSL. Figure 5.6 shows a time sequence of images obtained using this configuration.

The first image (5.6a) was obtained before focussing. Figure 5.6b shows the focussed laser beam and figures 5.6c and 5.6d are images taken after focussing. The line focus is clearly visible in fig. 5.6b. The size of the line is of the order of 1cm by 500μm. The limitation on the length of the line lies with the size of the laser beam and the size of the detection optics. In our case, the face plate of the TV camera is 1cm by 1cm. It is possible with this device to focus down a much larger laser beam. Focus lines of the order of 10cm (physical length of the CCSL) should in principle be achievable.

Figure 5.7 is a magnification of figure 5.6b. The fringes on either side of the central focal line are due to diffraction by the tails of the shock waves having moved through each other. The symmetry of the illumination pattern is encouraging for future work.

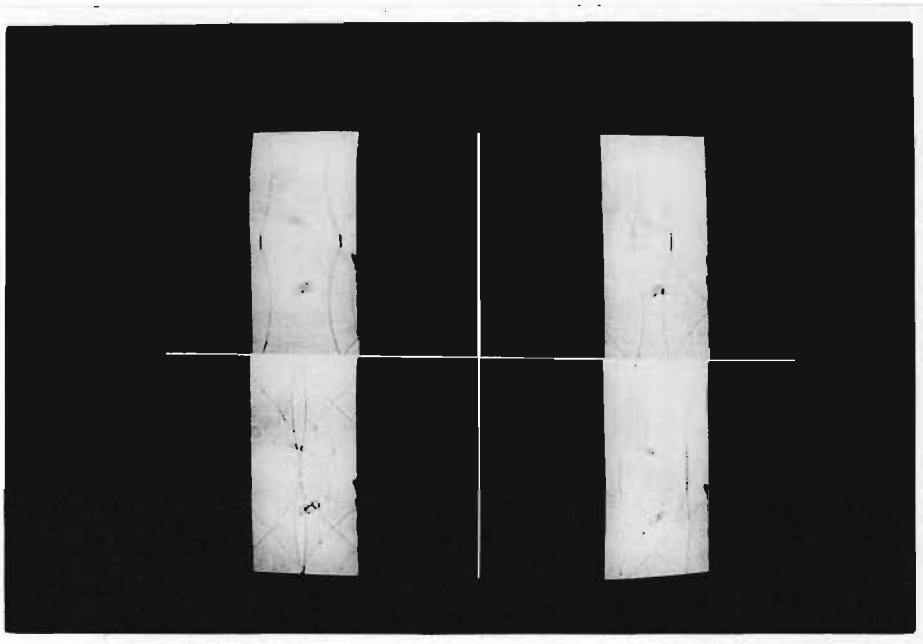

Figure 5.5: Shock sequence imaged in the plane of the CCSL. a) 20.8μs b) 21.2μs c) 21.6μs - convergence d) 22.0μs - lensing

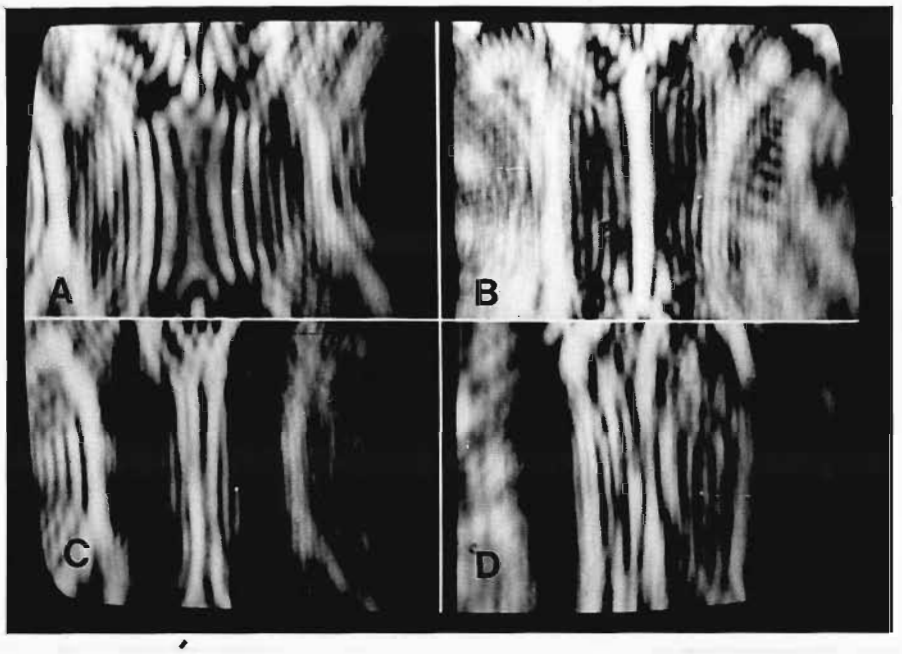

Figure 5.6: Shock sequence imaged at a distance of 1m from the CCSL . a) 20.0μs, b) 21.0μs, c) 22.0μs and d) 22.4μs after shock creation.

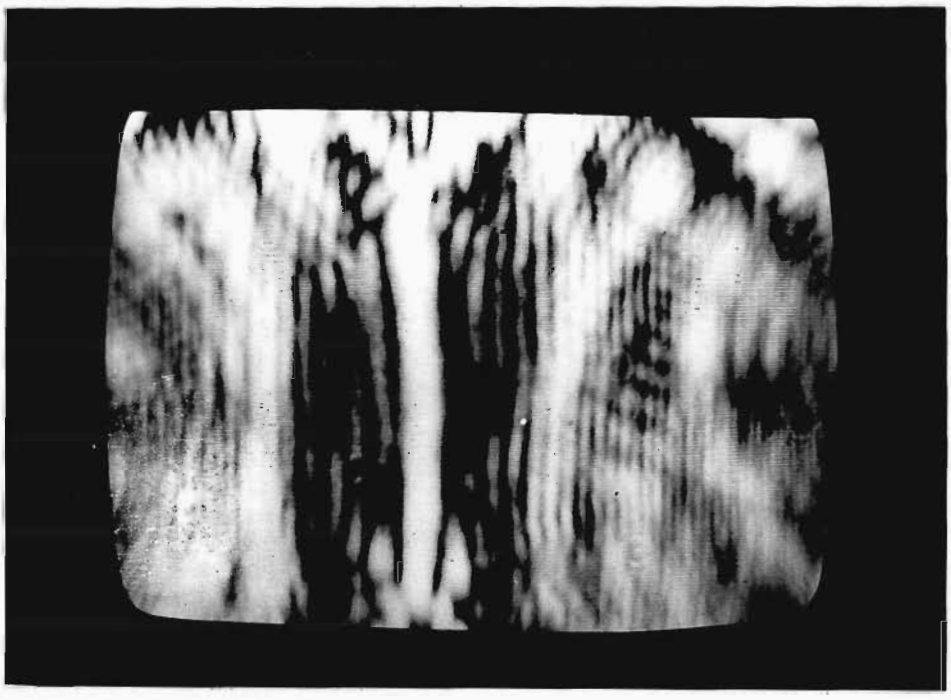

Figure 5.7: Line focus of CCSL at a distance of 1m

An attempt was also made to use the CCSL as a point focussing device by passing the laser beam down the central axis as in figure 5.8.

Numerous attempts were made to obtain a point focus at distances ranging from 0.5m to 1.5m away from the CCSL with no success. In an attempt to explain this, the shock structure of the CCSL was imaged in the shock plane. Figure 5.9 is a sequence of images taken in this configuration.

It is clear that the shock structure is not as symmetric along this axis as opposed to the orthogonal axis. In the previous configuration (see figure 5.5), the shock profile smooths out due to Mach addition. In this case, the individual shocks each contribute independently to the focussing. Hence any asymmetry results in no or poor focussing. This is indeed what has happened. To get point focussing, all shocks need to be created at exactly the same time and their evolution has to be identical. Much work needs to be done in this respect.

5.4 Conclusions

In this chapter, we have demonstrated a device (the cylindrical colliding shock lens - CCSL) capable of generating a line focus. With this device we have been able to focus a nitrogen laser beam to a line of 1cm by 500μm at a distance of 1m. This is a prototype device and has served as a "proof of principle". The reported results are therefore strictly preliminary and much work needs to be done to improve the performance.

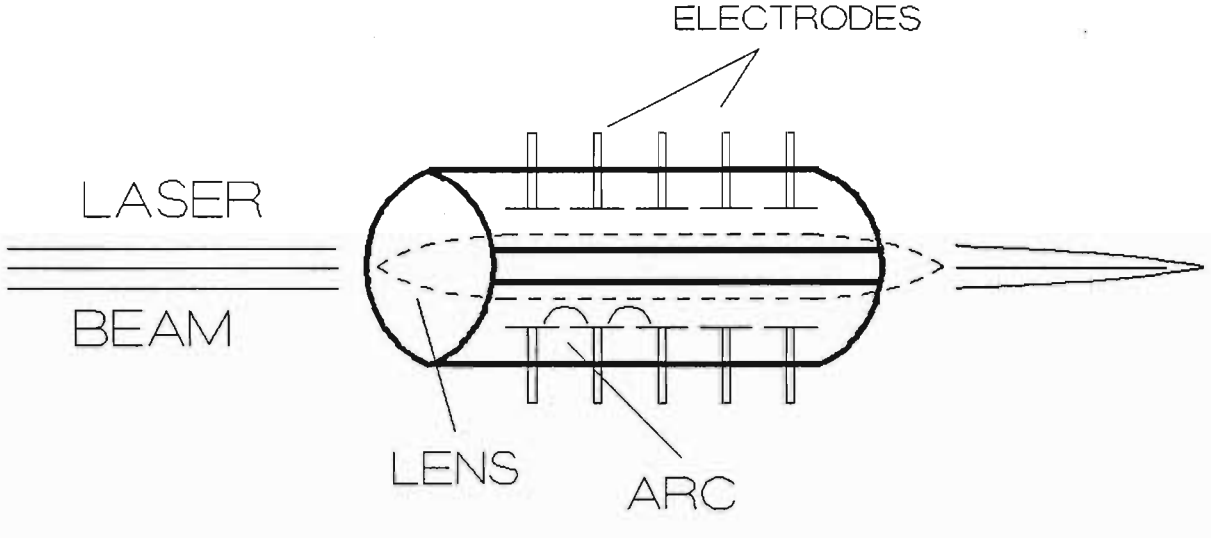

Figure 5.8: Schematic of experimental set-up for point focussing with the CCSL

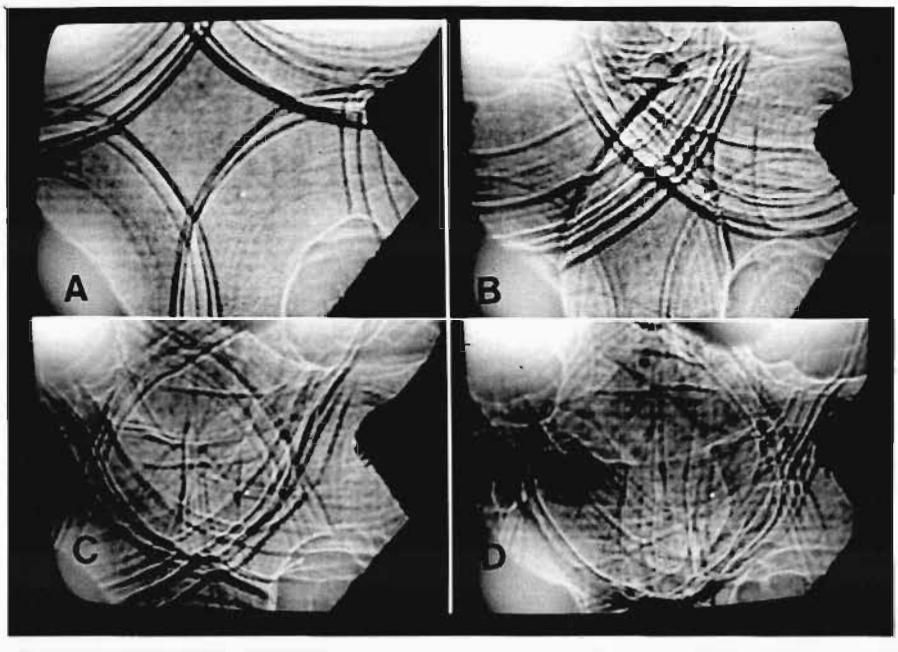

Figure 5.9: Shock sequence imaged in the collision plane along the "long" axis of the CCSL. a) 21μs , b) 22μs, c) 22.4μs and d) 22.9μs after shock creation.

Chapter 6

Colliding Shock Lens Conclusions, Applications and Future Work

6.1 Conclusions

In the attempt to determine whether the aperture of the CSL can be scaled up, we found that :

1. Enclosing the lens improves its performance.

2. Increasing the input energy also increases the aperture and decreases the focal length. However, there is an upper limit to the amount of energy one can put into the shocks. The small lens (CSL3) with 8 pairs of electrodes becomes unstable with the 250nF capacitor, whereas with more electrodes and a larger electrical aperture, CSL4 (16 electrode pairs) is very stable.

3. Simply scaling up the electrical diameter doesn't necessarily increase the lens aperture. There has to be an accompanying increase in energy and perhaps more importantly, enough shocks for circular symmetry to be attained before implosion. The smaller CSLs (CSL2 and CSL3) worked with 8 sets of electrodes whereas the large CSL (CSL4) needed more electrodes to achieve symmetry.

4. We have also seen that increasing the pressure improves the f number of the lens. Unfortunately only a small change in pressure could be effected due to equipment limitations.

5. The first CSLs were operated at atmospheric pressures. This contributed towards making them fairly simple devices. It has been demonstrated that not only an increase in pressure but also the use of more dense gases improves the performance. Although more difficult to operate, the improvement might very well mean that CSLs of the future will be operated in some sort of pressure chamber using a gas other than air.

6. During the course of this study we developed a simple scaling theory that shows fairly good agreement with the experimental results obtained with CSL4.

7. We have also applied the FLIC method of Gentry et al. (1966) to verify the experimental trends observed in the scaling experiments. It was found that the numerical simulation corresponds well with the behaviour of CSL3 and CSL4 under conditions of different input energies and pressures.

In conclusion, we have shown that the colliding shock lens can be scaled up to useful apertures and how to do so.

We have also developed a novel type of colliding shock lens called the cylindrical colliding shock lens (CCSL). This device has been shown to be capable of line focussing a nitrogen laser beam having a 1cm diameter to a line of 500μm at a distance of 1m away.

We now outline applications of the CSL and the CCSL and detail possible future work to be performed on these devices.

6.2 Applications

Some of the possible applications of the CSL and CCSL are

1. Drilling, cutting and welding.

2. Q-switching.

3. Line focussing.

6.2.1 Drilling, cutting and welding

The use of the CSL for drilling, cutting and welding has been proposed for some time (Buccellato et al. (1993), Michaelis et al. (1994)) as one of the industrial applications of the CSL. Michaelis et al. (1991c) showed that CO_2 lasers coupled with gas lenses were capable of drilling through thick metal sheets. However, these lenses were large continuous wave gas lenses having long focal lengths (of the order of 80cm). The colliding shock lens is a shorter focal length lens (from 30cm) and is much easier to operate. A more attractive feature is the possibility of a rep-ratable CSL used in conjunction with a high frequency laser for drilling and cutting. Unfortunately, up to this point, the lens diameters were too small. Although during the course of this study the CSL was not used for this purpose, the development of the 1cm diameter lens now makes this application an industrial viability.

The same argument goes for focussing of large industrial laser beams. It has been shown by Buccellato (1994) that the CSL can be used to focus a Ruby laser. However, the diameter of the beam that could be focussed was of the order of 2mm (the size of the optical aperture of the CSL). The large diameters that have now been achieved enable us to use the CSL in larger laser systems for focussing. It is envisaged that in the not too distant future, a gas lens (possibly the CSL) would be used as the final focussing element in a laser fusion scheme. Its ease of operation and high energy threshold (in the terrawatt/cm^2 regime) makes the CSL ideal for this purpose.

6.2.2 Q-switching

Together with Lisi et al. (1995), the author was involved in an experiment which used the CSL to Q-switch a Ruby laser. The experimental setup is

shown in figure 6.1.

In the figure above, L2 represents the CSL and L1 represents either a fixed focal length glass lens or a spinning pipe gas lens (Michaelis (1991c)).

In this experiment, the CSL in conjunction with L1 was used as an intra-cavity Q-switch. The mode of operation is simple. When the CSL is switched off, the fixed focal length lens (L1) renders the cavity unstable. When the CSL is switched on and the two focal regions of the two lenses overlap, the cavity becomes stable and cavity losses are consequently low. If this condition is achieved when population inversion in the lasing medium is at its peak, then lasing takes place in the form of a giant pulse.

The laser cavity was operated in one of three modes.

Mode a was when L1 was a 200cm focal length glass lens.

Mode b was when L1 was a 50cm focal length glass lens and

Mode c was when L1 was the spinning pipe gas lens operated at a focal length of 200cm.

We found that in *mode a*, a 2.0J laser pulse of duration 360ns was observed. In *mode b*, a 100mJ pulse of 175ns duration was observed and in *mode c*, a 3.0J pulse having a FWHM of 375ns was observed. This experiment proved that the CSL could be used as an intra-cavity Q-switch. The advantages are low cost and ease of operation. The only disadvantage was found to be the fact that by necessity the laser cavity had to be long.

6.2.3 Line focussing

The applications of a device capable of giving a good quality line focus are varied. Perhaps the most interesting application lies in the field of x-ray lasers. In what was the first laboratory x-ray laser, cylindrical optics were used by Rosen et al. (1985) to line focus the Nova laser beam (10MW in a 1ns pulse) onto a Selenium target for the production of soft x-rays. The target was completely vapourised creating a plasma, which on recombination,

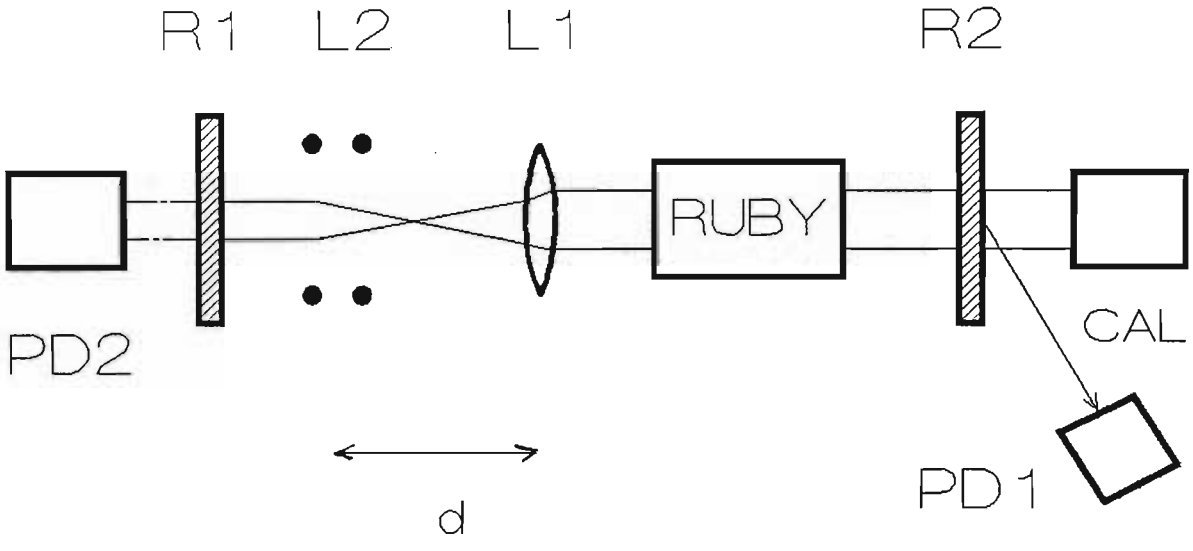

Figure 6.1: Schematic of colliding shock - Q-switch experiment - after Lisi et al. (1995)

resulted in the emission of 20nm wavelength soft x-rays. The size of the focus was of the order of 0.1mm wide and several centimeters long.

Later, Chenais-Popovics et al. (1987) used cylindrical optics to focus down the neodymium glass Vulcan laser system (10TW in a 70ps pulse) onto carbon fibres 7μm thick and 5mm long. With this scheme lasing was achieved at 18.2nm.

Cylindrical optics have been used extensively in the x-ray laser field for the vapourisation and ablation of targets. The laser ablation schemes all require good quality line focussing of high energy laser beams. The CCSL is a gas lens and like the CSL does not suffer from a low energy threshold like most conventional optics.

6.3 Future work

6.3.1 Multiple focussing

We have seen in figure 3.24 that in the enclosed CSL, the reflected shocks form a secondary and sometimes tertiary lens. These multiple lenses are somewhat weaker than the initial one and hence will have different focussing properties. A laser beam fired at regular intervals will therefore experience multiple focussing, with each successive focus being longer than the preceding one. The number of successive lenses can be controlled by the input energy. What is really interesting about this is that the CSL would still strictly be a single shot device but having a multiple focus. This variable multiple focus could be used in laser acceleration of targets.

This effect (multiple lenses) although observed on a regular basis, has not been used to focus down a laser beam. This certainly bears further investigation.

6.3.2 Rep-rating the CSL and CCSL

In the same vein as above, for use in industrial drilling and cutting, it would be ideal to operate a high rep-rate CSL (with constant focal length) in conjunction with a laser operating at high frequency. The CSL as mentioned above is presently a single shot device. Due to the nature of the charging circuit (the lens is charged through a large charging capacitor) the CSL in its present form cannot be operated at high energies in repetitive mode. The smallest device (CSL1) was operated up to a frequency of 10Hz. However the energy was low and the lens diameter of this device hardly useful. Plans are currently underway to construct a high frequency power supply to enable the CSL to operate at high frequency.

In rep-rate mode, one of two options are possible :

i) Either only the inward travelling shock wave could be utilised or

ii) Use could be made of the reflected wave. The reflected wave in this case refers to the primary shock wave which, upon creating the first lens on implosion, moves outwards and is reflected back into the centre by the outer boundary walls. Careful timing and firing of the CSL could see the reflected wave reinforced by a newly generated inward moving wave to maintain or even shorten the focal length on a shot to shot basis.

The two approaches present different restrictions on the upper limit of frequency. In the former case, the maximum rep-rate is determined by the time it takes for the lens to form. This is governed by the input energy and the physical dimensions of the CSL. In the latter case, the time it takes for the reflected shock to form a second lens is the limiting condition. This lens would consequently operate at a slightly lower frequency.

Clearly much work still needs to be done on the CSL in this respect.

It would also be desirable to run the CCSL in conjunction with a high rep-rate laser. At present the CCSL is also a single shot device.

6.3.3 Improving the quality of the CCSL focus

Since the CCSL introduced in this thesis is only the prototype device, much work needs to be done on improving the quality of the focus. Attention needs to be given to the shape of the electrodes, the electrode spacing, electric breakdown and shock uniformity. We have employed only four lines of electrodes but it might be necessary to increase the number of lines to create a more uniform cylindrical lens. Any or all of these factors could have an effect on the quality of the focal line. This is a subject that warrants extensive investigation.

6.3.4 All gas laser

Michaelis et al. (1991c) proposed the use of the CSL as part of an all gas laser. The details of the scheme are the subject of future investigation. Sufficed to say, the large optical aperture achieved with the final CSL now makes this (all gas laser) a distinct possibility.

Chapter 7

Lidar Measurements of Aerosols

Lidar is an acronym for Light Detection and Ranging. This follows the terminology of Ligda (1963). In what is perhaps a very simplistic description, lidar systems consists of two main components. The first being the transmitter and the second the receiver. The transmitter is a very bright light source (usually a laser beam) while the receiver is a telescopic arrangement with light detection optics at the focus. The light source is directed up into the atmosphere (or down if the lidar system is airborne). Depending on the wavelength of operation, it interacts with a particular atmospheric constituent. The scattered light is collected by the telescope and analysed using electronic data collection techniques. This might be in the form of a simple digitising oscilloscope or pulse counting circuitry. More will be said about this later. The time of arrival of the scattered signal gives a direct indication of the altitude from which the scattering takes place. The intensity of the return is related to the density of the scatterer. In this way profiles of density versus altitude can be built up.

7.1 Historical development of lidar

The earliest documented use of light to study atmospheric effects dates back to the 1860's. In one of the first experiments of its kind, Tyndall (1869) investigated the polarisation of light scattered from smoke. The light source

used was an electric lamp. Synge (1930) proposed that a vertically directed searchlight beam could be utilised to measure density and temperature profiles of the upper atmosphere. Shortly afterwards (1937), Hulburt used a searchlight beam to study atmospheric turbidity and molecular scattering. This was accomplished by photographing the searchlight beam over an observation station 18.4km away. With this set-up Hulburt was able to obtain information up to an altitude of 28km.

Modulation of the searchlight beams were then carried out in an attempt to obtain better spatial resolution. In 1939 Johnson et al. used a modulated searchlight beam and a photoelectric detector to make quantitative measurements of the scattered intensity up to 30km. Eltermann (1951) used a rotating shutter to modulate a searchlight beam. The receiver was a parabolic reflector with a photomultiplier tube (PMT) at the focus. The transmitter and receiver were spatially separated in an arrangement referred to as a bistatic lidar. Using this experimental set-up, he was able to study temperature and density profiles up to an altitude of 60km. The altitude was determined by triangulation hence a single profile took an entire evening. This was a serious limitation of the system since atmospheric changes take place on a much smaller time scale.

In 1956 Friedland recognised that there were several problems associated with the integration times used by Eltermann. Firstly, because of the short time scales of most atmospheric processes (as mentioned above) there was little scientific value in obtaining profiles over such long periods. More importantly, a change in weather conditions could force the cessation of observations before a profile was completed. It was therefore necessary that the duration of sampling be decreased. As opposed to using a mechanical chopper, Friedland opted for the use of a pulsed searchlight. His experimental scheme was also bistatic in nature. The transmitter and receiver were spatially separated by 170m. With this system, Friedland was able to study density profiles up to an altitude of 40km. The integration times were of the order of 500μs. This compared to Eltermanns time of 1 night was a dramatic improvement. The implications were that micro-variations of atmospheric constituents could now be studied. This in itself meant that more meaningful atmospheric physics could be done.

The invention of the laser by Maiman (1960) provided a high intensity,

monochromatic collimated beam of light to replace the searchlight that had been used up to that point. The invention of Q-switching by McClung and Hellwarth (1962) made the generation of short pulses of laser energy possible.

The laser was first used by Fiocco and Smullen (1963) in a lidar system. They used a Q-switched pulsed ruby laser operating at 694.3nm with a pulse-length of 50ns to study atmospheric aerosols. With this system it was proved that aerosols up to 25km could be detected.

The early lidar systems recorded the return signal as an analogue one. The intensity of the return was measured by the photomultiplier and was displayed as an integrated voltage versus time plot on an oscilloscope. Thus the resolution of the profile was limited by the temporal resolution of the oscilloscope. For qualitative measurements, this system was adequate. However, for more detailed analysis of densities, a more temporally sensitive system was needed. Pulse counting of the returned laser signal has now become commonplace.

Figure 7.1 shows a typical return from a lidar system using an oscilloscope for data storage and display.

Lidar systems have subsequently become much more sophisticated and their applications more varied. Today (using different wavelengths and pulse-lengths) lidar systems are capable of studying various atmospheric constituents and indeed atmospheric properties. Some of the constituents include aerosols, Na, Ca, Li, O_3, together with wind speeds, temperature and humidity. We will concentrate on the measurement of atmospheric aerosols.

Lidar systems are now not only ground based but airborne (Spinhurne (1982)) and will very soon be space-borne as well. Mobile lidars (Houston (1987)) are also in use.

Lidar is a remote sensing device. There exist other techniques for the study of atmospheric aerosols. These techniques by nature are all in-situ. These include balloon and rocket-borne detectors. Initially, in-situ measurements were carried out by instruments mounted on giant kites. Currently, instruments are borne on free balloons and their measurements are telemetered back to the ground. These systems are referred to as radiosondes.

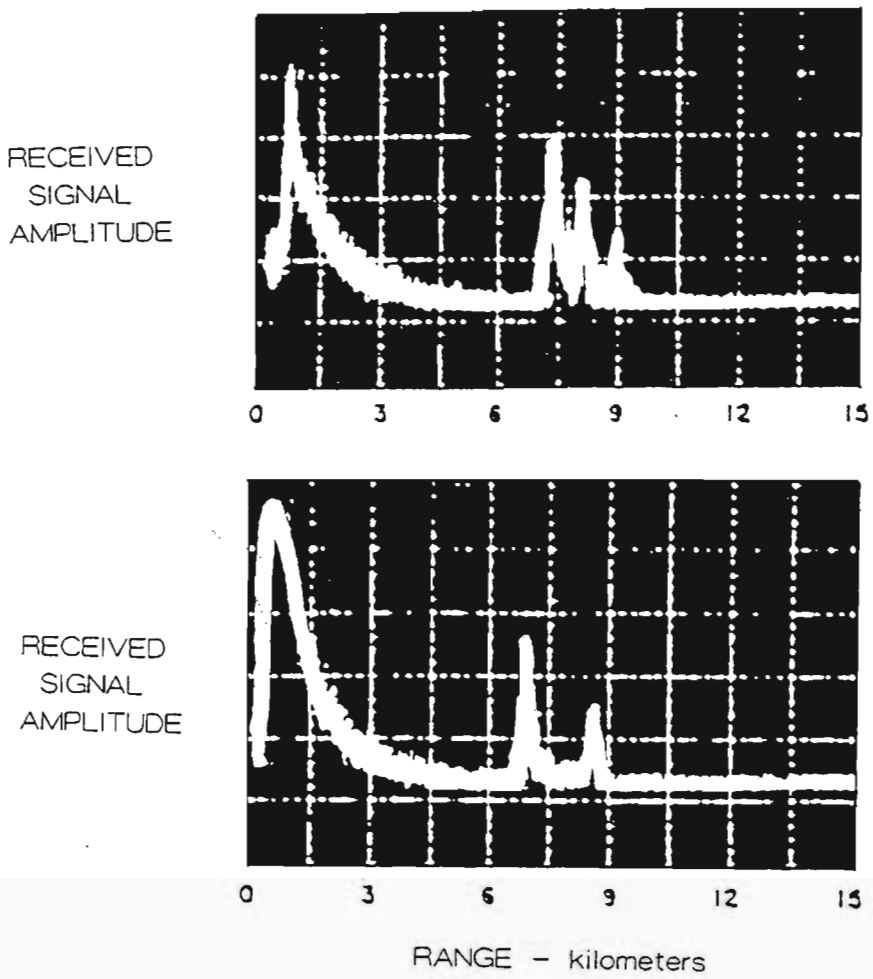

Figure 7.1: A typical lidar return from clouds - Measures 1984

Radiosondes are capable of measuring pressure, temperature and density as a function of altitude. Particle counters fixed to balloons (called dust-sondes) are capable of measuring aerosol size and concentration.

Modern radiosondes and dust-sondes have resolutions typically of 100m. The balloons are capable of reaching altitudes of 30km. High altitude balloons capable of reaching altitudes of up to 100km are available. However, they are fairly expensive and their use is therefore limited. Radiosondes have a high degree of reliability and are convenient to use. However there are two limitations :

1. Winds sometimes carry the balloons way off course (sometimes up to 30km away - Northam 1974). The profiles are therefore not strictly vertical.

2. It could take up to 2 hours to obtain an entire profile, whereas ideally one would want the integration time to be as short as possible so that no appreciable changes in the atmospheric conditions take place.

Lidar profiles on the other hand are very localised and vertical. The integration time for the system is restricted only by the pulselength and repetition rate of the laser. In most cases, these times are much shorter than that for radiosonde data. Another important consideration is that most lidars are capable of sampling up to altitudes of 100km (although depending on the constituent of interest this altitude may vary).

7.2 Lidar theory

7.2.1 Scattering form of the lidar equation

The following derivation for the scattering form of the lidar equation follows from Measures (1984).

For a pulsed monostatic lidar, the signal power received by the detector in the wavelength interval ($\lambda, \lambda + \Delta\lambda$) from the range ΔR is given by :

$$\Delta P(\lambda, R) = \int J(\lambda, R, r)\Delta\lambda\Delta R p(\lambda, R, r) dA(R, r) \tag{7.1}$$

$J(\lambda, R, r)$: laser induced spectral radiance at wavelength λ, position r in the target plane located at range R

dA(R, r) : element of target area at position r and range R

$p(\lambda, R, r)$: probability that radiation of wavelength λ will strike the detector

$$p(\lambda, R, r) = \frac{A_o}{R^2} \times T(\lambda, R) \times \xi(\lambda) \times \xi(R, r) \tag{7.2}$$

$\frac{A_o}{R^2}$: acceptance solid angle of the receiver optics

A_o : area of receiver mirror

$T(\lambda, R)$: atmospheric transmission factor at wavelength λ over range R

$\xi(\lambda)$: receivers transmission factor

$\xi(R, r)$: probability of radiation from position r at range R reaching the detector

$$J(\lambda, R, r) = \beta(\lambda_L, \lambda, R, r) I(R, r) \tag{7.3}$$

where *I(R,r)* is the laser irradiance at position r and range R.

$$\beta(\lambda_L, \lambda, R, r) = \sum_i N_i(R, r) \left\{ \frac{d\sigma(\lambda_L)}{d\Omega} \right\}_i^s L_i(\lambda) \tag{7.4}$$

is the volume backscattering coefficient.

$N_i(R,r)$: represents the number density of the scatterer

$\left\{\frac{d\sigma(\lambda_L)}{d\Omega}\right\}_i^s$: represents the differential scattering cross-section under laser irradiation λ_L

$L_i(\lambda)$: fraction of scattered radiation that falls into the wavelength interval $(\lambda, \lambda + \Delta\lambda)$

The total signal power received by the detector at the instant t(= 2R/c), corresponding to the time taken for the leading edge of the laser pulse to propagate to range R and return to the detector, is given by :

$$P(\lambda,t) = \int_0^{R=ct/2} dR \int_{\Delta\lambda_o} d\lambda \int J(\lambda,R,r)p(\lambda,R,r)dA(R,r) \qquad (7.5)$$

We integrate over the range to account for the fact that radiation reaching the detector originates along the entire path from R = 0 to R = ct/2.

$\Delta\lambda_o$ represents the bandwidth of the receiver.

Using equations 7.4 and 7.5 and assuming the region under interest is homogeneous we then get :

$$P(\lambda,t) = A_0\xi(\lambda)\int_0^{R=ct/2} \beta(\lambda_L,\lambda,R,r)T(\lambda,R)\frac{dR}{R^2}\int \xi(R,r)I(R,r)dA(R,r) \qquad (7.6)$$

Assume $\xi(R,r) = 1$ where the receivers field of view overlaps with the transmitters field of view.

If we also assume that the laser pulse is rectangular with a pulse length of τ_L and it is uniform over an area $A_L(R)$ at range R, the expression for the received power now becomes :

$$P(\lambda,t) = A_0\xi(\lambda)\int_{R=c(t-\tau_L)/2}^{R=ct/2}\beta(\lambda_L,\lambda,R)T(\lambda,R)\frac{dR}{R^2}\xi(R)I(R)A_L(R) \quad (7.7)$$

The total scattered power received at a time t=2R/c can be expressed as

$$P(\lambda,t) = A_0\xi(\lambda)\beta(\lambda_L,\lambda,R)T(\lambda,R)\xi(R)I(R)A_L(R)\frac{c\tau_L/2}{R^2} \quad (7.8)$$

where

$$I(R) = \frac{E_L T(\lambda_L,R)}{\tau_L A_L(R)} \quad (7.9)$$

E_L represents the output energy of the laser pulse and
$T(\lambda_L,R)$ represents the atmospheric transmission factor at wavelength λ and range R

$$T(\lambda_L,R) = e^{-\int_0^R \kappa(\lambda_L,R)dR} \quad (7.10)$$

$$T(\lambda,R) = e^{-\int_0^R \kappa(\lambda,R)dR} \quad (7.11)$$

The above two equations represent the transmission factors at the laser wavelength and the detector wavelengths respectively.

$\kappa(\lambda_L,R)$: atmospheric attenuation coefficient at laser wavelength
$\kappa(\lambda,R)$: atmospheric attenuation coefficient at the detector wavelength

Hence the total atmospheric transmission factor is :

$$T(R) = T(\lambda_L, R)T(\lambda, R) = e^{-\int_0^R \kappa(\lambda_L,R)+\kappa(\lambda,R)dR} \tag{7.12}$$

The radiant energy received by the detector is related to the power by the following relationship :

$$E(\lambda, R) = \int_{2R/c}^{2R/(C+\tau_d)} P(\lambda, t)dt \tag{7.13}$$

In the event that we are interested in elastic scattering (Mie and Rayleigh), the wavelength of observation (λ) is equal to the laser wavelength (λ_L). In this case the transmission factor becomes

$$T(R) = e^{-2\int_0^R \kappa(\lambda_L,R)dR} \tag{7.14}$$

and the energy received is now

$$E(\lambda_L, R) = E_L\xi(\lambda)\xi(R)\frac{A_0}{R^2}\beta(\lambda_L, R)\frac{c\tau_L/2}{R^2}e^{-2\int_0^R \kappa(\lambda_L,R)dR} \tag{7.15}$$

This is commonly known as the scattering form of the lidar equation.

Since the received energy $E(\lambda_L, R)$ and the transmitted energy E_L are both directly related to the number of photons received and transmitted ($n_{\lambda R}$ and n_0 respectively); we can rewrite the scattering form of the lidar equation as follows :

$$n_{\lambda R} = n_0 \xi(\lambda)\xi(R)\frac{A_0}{R^2}\beta(\lambda_L, R)\frac{c\tau_L/2}{R^2}e^{-2\int_0^R \kappa(\lambda_L, R)dR} \tag{7.16}$$

or

$$n_{\lambda R} = n_0 K' \frac{A_0}{R^2}\beta(\lambda_L, R)\Delta R T(R) \tag{7.17}$$

where ΔR is the range resolution of the lidar system and $K' = \xi(\lambda)\xi(R)$ represents the optical efficiency of the system.

For air molecules and aerosols equation 7.17 then becomes :

$$n_{\lambda R} = n_0 K' \frac{A_0}{R^2}\Delta R T(R)[\beta_m + \beta_r] \tag{7.18}$$

where

β_m : represents the volume backscattering coefficient for air molecules
β_r : represents the volume backscattering coefficient for aerosols

But

$$\beta_i = \frac{\sigma_i N_i}{4\pi} \tag{7.19}$$

where N_i is the concentration of species i and σ_i is the backscattering cross section.

Hence

$$n_{\lambda R} = n_0 K' \frac{A_0}{R^2} \Delta R T(R) \frac{[N_r(R)\sigma_r + N_m(R)\sigma_m]}{4\pi} \tag{7.20}$$

σ_r and σ_m represent the Rayleigh and Mie backscattering cross section and N_r and N_m the air molecule and aerosol densities respectively.

If the height range is such that only air molecules are present (i.e. Rayleigh scattering dominates) then the number of backscattered photons is related to the molecular density as follows :

$$n_{\lambda R} = \frac{K N_r(R)}{R^2} \tag{7.21}$$

where

$$K = \frac{n_0 K' A_0 \Delta R T(R) \sigma_r}{4\pi} \tag{7.22}$$

T(R) can be assumed to be constant provided the lidar profile is taken over a short enough period such that no appreciable atmospheric changes take place.

We can evaluate K by assuming that at some altitude the scattered contribution is only from air molecules (aerosol free region) and using Standard Atmospheres or balloon data to evaluate $N_r(R)$. Northam et al. (1974) suggest that it is preferable to use balloon data to calculate atmospheric densities since these are more accurate.

Once a value for K is determined the density for any altitude can be calculated using equation (7.22) above.

7.2.2 Scattering ratio

In much of the lidar work involving elastic backscattering from aerosols it is necessary to separate the Mie component from the total return signal. We therefore introduce a scattering ratio - Measures (1984).

$$K_s(\lambda_L, R) = 1 + \frac{\beta_m(\lambda_L, R)}{\beta_r(\lambda_L, R)} \tag{7.23}$$

The symbols have the same meaning as before.

From the scattering form of the lidar equation it follows that :

$$K_s(\lambda_L, R) \approx \frac{E(\lambda_L, R)}{E^R(\lambda_L, R)} \tag{7.24}$$

$E^R(\lambda_L, R)$ represents the lidar return that would be observed in the absence of any Mie scattering and $E(\lambda_L, R)$ is the measured lidar return.

We can therefore write the scattering ratio as :

$$K_s(\lambda_L, R) \approx \frac{N_{exp}}{N_{Ray}} \tag{7.25}$$

where

N_{exp} is the calculated density using the number of backscattered photons and N_{Ray} represents the standard atmospheric density calculated from temperature and pressure using balloon data (Northam et al. 1974). For a

more detailed treatment of the scattering form of the lidar equation and the derivation of the scattering ratio, the reader is referred to Measures (1984).

Scattering ratios are used quite widely in analysing lidar returns. However they have one serious drawback. The ratio is based on the assumption that at some particular altitude there are no aerosols present. This enables one to calculate the value of K using the return counts at that altitude and standard atmospheres. Sometimes the determination of this "pinned altitude" is non-trivial. This occurs when the atmosphere is aerosol rich.

In cases like this, although the relative ratios between any two altitudes would be the same as for the case when there are no aerosols, the absolute scattering ratios will be incorrect.

We therefore need another technique whereby the strength (density) of the aerosol layer can be determined. This method is referred to as the Klett inversion method. This is also a popular tool for analysing lidar signals. As opposed to the scattering ratio calculation which yields a relative value, the Klett inversion method yields an extinction coefficient which is absolute.

It follows that high density aerosol layers result in high extinction coefficients. In many respects this technique is more widely used than the scattering ratio technique since it requires no assumptions on the part of the person analysing the raw data. Hereafter follows a simplified derivation of Kletts inversion method after Klett (1981). The reader is referred to Klett (1981) for a more complete treatment.

7.2.3 Kletts inversion method

For a monostatic pulsed lidar system, the scattering form of the lidar equation can be written as :

$$P(r) = P_o \frac{c\tau}{2} A_o \frac{\beta(r)}{r^2} exp\left[-2\int_0^r \sigma(r')dr'\right] \tag{7.26}$$

where

P(r) : instantaneous power received at time t
P_o : power received at t_o
c : velocity of light
τ : pulse duration
A_o : effective system receiver area
r : range
$\beta(r)$: volume backscattering coefficient
$\sigma(r)$: the attenuation coefficient.

The logarithmic range adjusted power can be defined as :

$$S(r) = ln[r^2 P(r)] \tag{7.27}$$

We can now rewrite equation 7.26 in the system independent form :

$$S - S_o = ln\frac{\beta}{\beta_o} - 2\int_{r_o}^{r} \sigma dr' \tag{7.28}$$

where $S = S(r)$ and $S_o = S(r_o)$ and $\beta_o = \beta(r_o)$.

The differential equation corresponding to equation 7.28 is

$$\frac{dS}{dr} = \frac{1}{\beta}\frac{d\beta}{dr} - 2\sigma \tag{7.29}$$

The solution to this equation requires either knowing or assuming a relationship between β and σ whenever $d\beta/dr \neq 0$. If however, the atmosphere is homogeneous so that $d\beta/dr = 0$, the attenuation coefficient can be expressed

directly in terms of the signal slope :

$$\sigma_{hom} = -\frac{1}{2}\frac{dS}{dr} \tag{7.30}$$

This is the basis for what is commonly known as the slope method of inversion. However, it has often been assumed that since the atmosphere is more likely to be homogeneous over small rather than large intervals, by applying the slope method to a succession of small intervals a reasonable first approximation to $\sigma = \sigma(r)$ in a notably inhomogeneous atmosphere may also be achieved.

From equation 7.29 this amounts to the conjecture that $\beta^{-1}(d\beta/dr) << 2\sigma$. Unfortunately, this condition is not satisfied under conditions of cloud, fog, smoke or even dust.

It is known that under a wide range of conditions for which particulate backscattering dominates that due to atmospheric gases (i.e. cloudy, hazy or dusty conditions), β and σ can be related according to a power law of the form :

$$\beta = const.\sigma^k \tag{7.31}$$

k depends on the lidar wavelength and various properties of the aerosols. Reported values of k are generally on the interval $0.67 \leq k \leq 1.0$ (Curcio (1958), Fenn (1966), Twomey (1965)).

If such a relationship is assumed then equation 7.29 becomes

$$\frac{dS}{dr} = \frac{k}{\sigma}\frac{d\sigma}{dr} - 2\sigma \tag{7.32}$$

The general solution to this equation is :

$$\sigma^{-1} = exp\left(-\int^{r} \frac{1}{k}\frac{dS}{dr'}dr'\right) \times \left[C - 2\int^{r} \frac{exp}{k}\left(-\int^{r'} \frac{1}{k}\frac{dS}{dr''}dr''\right)dr'\right], \quad (7.33)$$

where C is the integration constant. If k is regarded as a constant, then we may rewrite equation 7.33 as

$$\sigma = \frac{exp[(S - S_o)/k]}{(\sigma_o^{-1} - \frac{2}{k}\int_{r_o}^{r} exp[(S - S_o)/k]dr')} \quad (7.34)$$

where $\sigma_o = \sigma(r_o)$.

In spite of the evident theoretical superiority of equation 7.34 over the slope method (which corresponds to setting $k = 0$), it is the latter method that was used more frequently. This is because equation 7.34 has a tendency to produce marginal results at best.

From a purely mathematical point of view Klett summarised the problem with this equation as follows :

Since on average the signal decays with range beyond r_o due to attenuation, σ is determined as the ratio of two numbers, with each becoming progressively smaller with increasing r. Also, the denominator which must approach zero at the same rate as the numerator, is expressed as the difference between two relatively large numbers. This produces a strong tendency for instability.

Klett introduced a more appropriate solution form than equation 7.34 by evaluating the integration constant C in equation 7.33 in terms of a reference range r_m so that the solution is generated for $r \leq r_m$ rather than for $r \geq r_o$. For a constant k, the result is :

$$\sigma(r) = \frac{exp[(S - S_m)/k]}{(\sigma_m^{-1} + \frac{2}{k}\int_r^{r_m} exp[(S - S_m)/k]dr')} \tag{7.35}$$

where $S_m = S(r_m)$ and $\sigma_m = \sigma(r_m)$. Klett (1981) showed that this is a more stable solution than equation 7.34 and that great accuracy in the choice of k is not needed. Typically k is set to 1.

Equation 7.35 is now widely used for the evaluation of lidar extinction coefficients.

7.3 Monostatic and bistatic lidar systems

We have already established that lidar systems consist of two main components viz. the transmitter and receiver. Based on the manner in which these can be arranged relative to each other, lidar systems fall into one of two broad categories :

1. Bistatic lidar and

2. Monostatic lidar

7.3.1 Bistatic lidar

In a bistatic lidar system, the receiver and transmitter are spatially separated. The distance can vary from 50cm (Hamilton 1966) to 170m (Friedland 1956). The fields of view of the transmitter and receiver are orientated in such a way that they overlap completely at some required height. This height is the height at which data gathering will take place. Figure 7.2 is a schematic of a bistatic lidar arrangement. The region of total overlap is indicated by h_3. The region from the ground up to height h_1 is where no overlap takes place and that height from h_1 to h_2 is where only partial overlap of the two fields of view takes place. Bistatic lidar's are notoriously difficult to align since the two fields of view have to be in the same vertical plane as well as in

the required region of interest. For this reason and the fact that the bistatic lidar's are by nature very large devices, they are not very popular.

The second type of arrangement is referred to as a monostatic lidar.

7.3.2 Monostatic lidar

In a monostatic lidar system the receiver and transmitter are located along the same axis or very close together. Two types of monostatic lidar systems are possible.

Biaxial lidar

In this arrangement, the transmitter and receiver although very close together are situated slightly off axis. This arrangement can be seen in figure 7.3(a). This set-up like the conventional bistatic arrangement, requires that the two fields of view overlap at some required height. However, the alignment is much simpler in this case.

Uniaxial lidar

In a uniaxial lidar system, the receiver and transmitter are located along the same axis. The field of view of the transmitter is therefore located within that of the receiver. Monostatic lidars have three fundamental advantages over bistatic lidars.

1. Since the two fields of view are located in the same place, alignment of this system is much easier than that of a bistatic lidar.

2. Overlap essentially starts from the ground, therefore, one can sample from a much lower altitude.

3. By nature, monostatic lidars are small and they lend themselves to portability. This is perhaps the primary reason for monostatic lidar's being

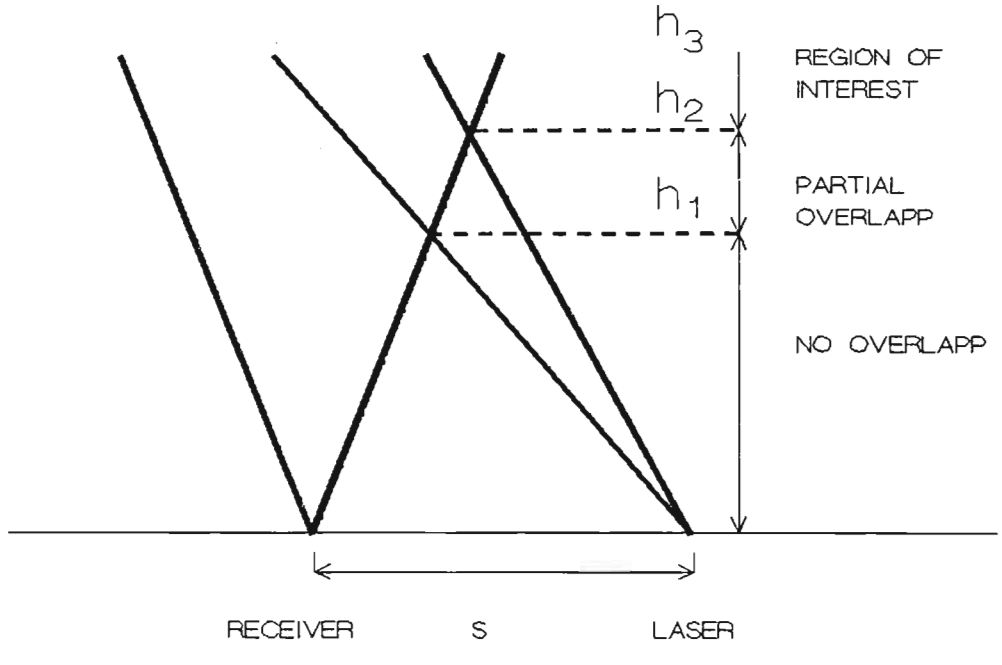

Figure 7.2: Fields of view of a bistatic lidar

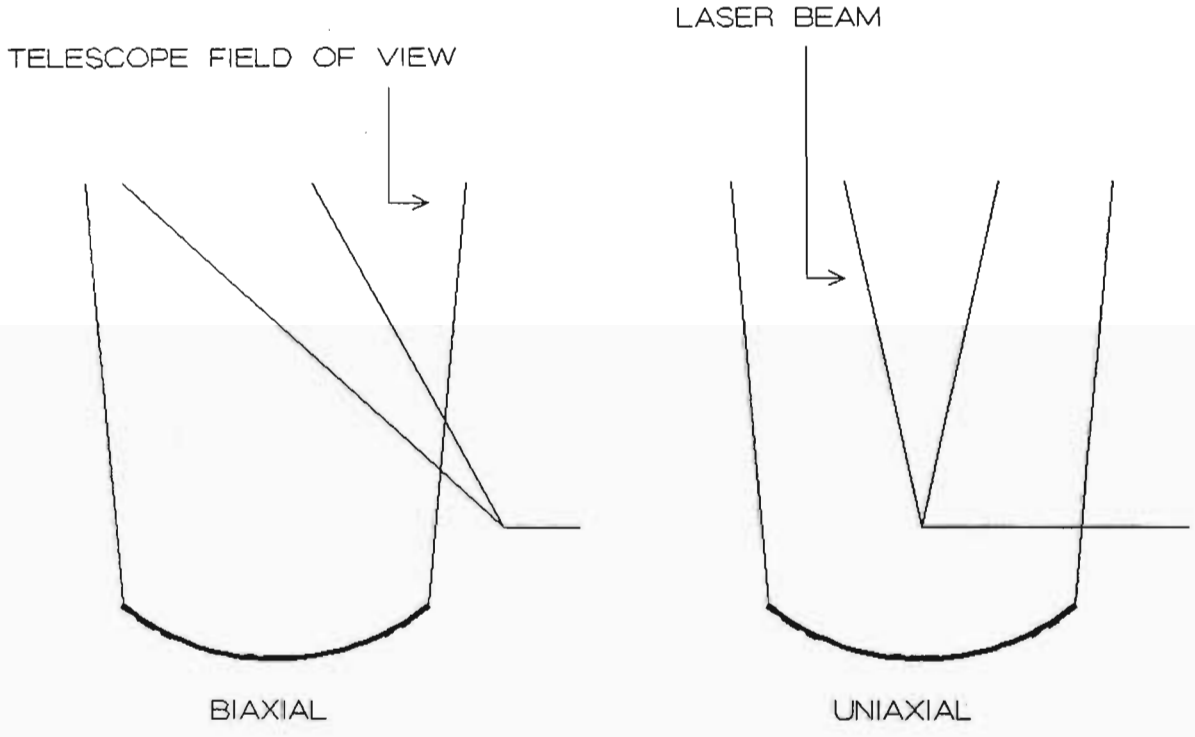

Figure 7.3: Fields of view of a biaxial (a) and a uniaxial (b) lidar system

favoured over their bistatic counterparts.

There is one problem associated with monostatic lidar systems. Since overlap starts from the ground upwards, the returned signal from the lower altitudes is very strong. The photomultipliers which are used for collection of light saturate when exposed to high intensity light. This problem can be overcome in one of two ways :

1. Off-gating the photomultiplier :

This is a scheme whereby the photomultiplier is electronically shut off during that period when the return is too strong and then very quickly switched on again for the return from higher altitudes. Cooke (1972) found that it was possible to off-gate an Amperex 56 TVP photomultiplier and still obtain a return from 30m away. Although this process can result in very short down-times of the detection system, it is not that simple to implement.

2. Mechanical shutter :

In this scheme, a very fast chopper blade is attached in front of the aperture of the collecting optics. The spinning of the blade is synchronised with the firing of the laser beam in such a way that the aperture is blocked for the period when returns are strong and then opens up when the returns can be detected by the photomultiplier without saturating. The minimum altitude in this case is determined primarily by the speed of the blade. Kent et al. (1966) studied densities up to 80km. They used a mechanical shutter to block off the laser returns from the first 20km. Since this is a mechanical process, the lowest altitude one can start sampling from is usually slightly higher than when off-gating is employed.

7.4 Major components of the Durban lidar system

The lidar system used was constructed during the period 1991 - 1992 (M.Sc Thesis - M. Kuppen (1992)). We will present a brief description of the exper-

imental set-up and system specifications. However, for a detailed description the reader is referred to Kuppen (1992).

7.4.1 The transmitter

The transmitter in the Durban lidar system consists of a flashlamp-pumped dye laser manufactured by Phase-R. The dye used is Rhodamine 6G in a concentration of 0.5 $\times 10^{-4}$ moles/litre of methanol. This produces an output beam of 589nm with a maximum energy of 0.7J when operated in a flat-flat cavity. The laser pulselength was found to be 0.6μs (FWHM) at 589nm.

Figure 7.4 shows a plot of discharge flashlamp voltage versus output energy.

Although the laser is designed to run at 1Hz, during operation of the lidar system, the laser is usually run at a repetition rate of 0.5Hz with an energy of 0.5J per shot, in order to conserve the flashlamp.

7.4.2 The receiver

The receiver consists of a 1.5m backsilvered parabolic searchlight mirror with a focal length of 654mm. Collimating optics are located at the focus of the mirror. These consist of a microscope objective with a field of view of 79° followed by a variable aperture (1mm - 10mm). This aperture is used to attenuate the returned signal if necessary. In normal practice, this aperture is set to 5mm. A 589nm interference filter with a bandwidth of 10nm and a transmission of 50% is positioned in front of the collimating optics. This filter serves to discriminate against background light.

The small field of view of the microscope objective restricts the collection area on the mirror to only 1.05m. However, we have found that this area gives a sufficiently strong return not to warrant any concern. The photomultiplier tube (EMI 9558B) is mounted immediately after the collimating optics.

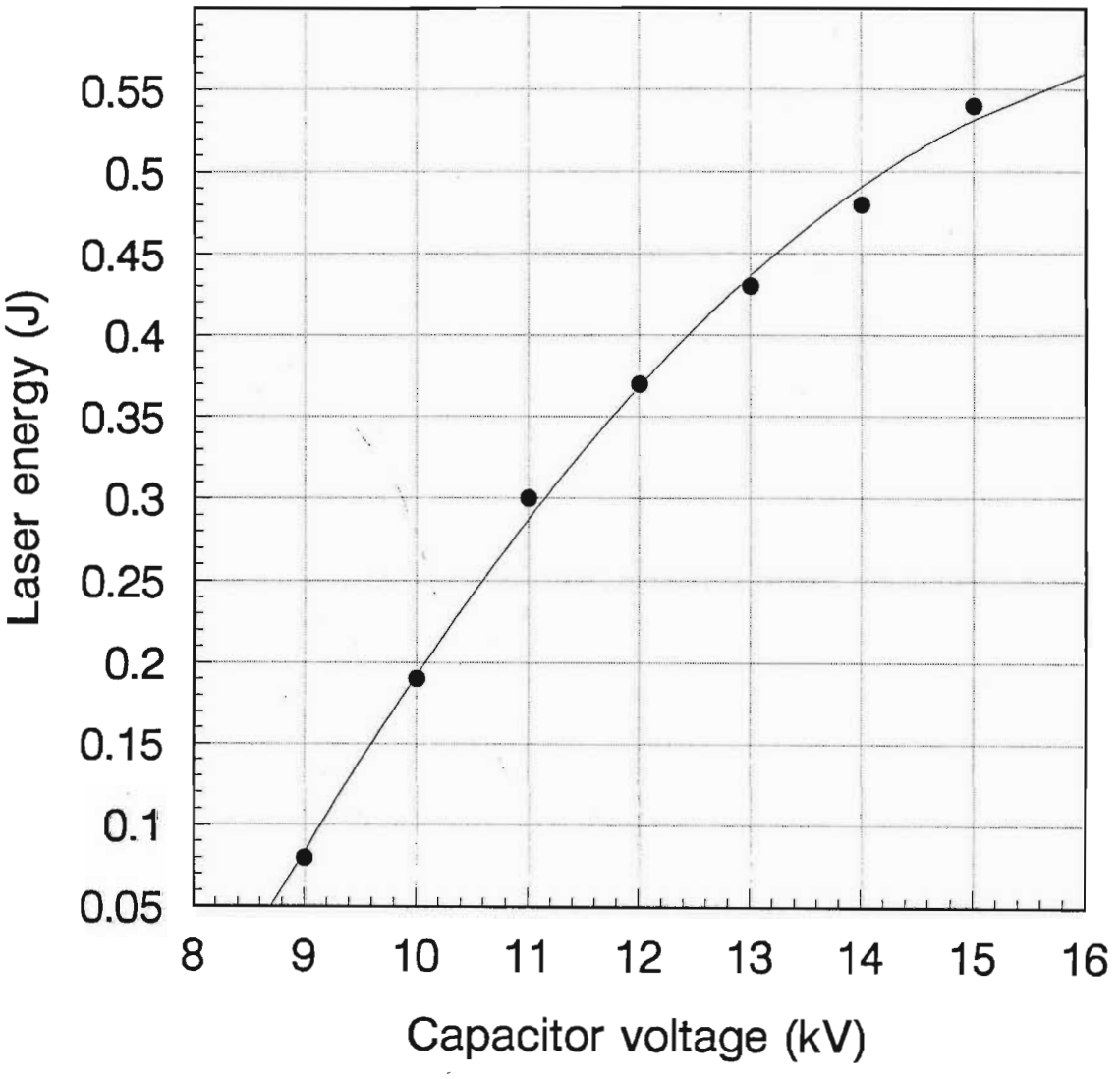

Figure 7.4: Dye laser energy versus discharge voltage - Kuppen (1992)

7.4.3 The pulse counting system (PCS)

The pulse counting system has been described in detail by Kuppen (1992). It consists of two electronic counters which integrate the signal from the photomultiplier in 1μs bins. This gives the system a vertical resolution of 150m. More will be said about this later.

7.5 Experimental set-up

A schematic of the lidar system is shown in figure 7.5. As can be seen, the Durban lidar has a monostatic, uniaxial configuration.

The laser beam is fired onto a 90^o prism located on a steerable table which is located on top of the collection optics. This makes alignment of the system fairly simple since (as already mentioned) the field of view of the laser lies within that of the receiver. The steerable prism table is necessary for fine adjustment of the system.

To avoid saturation of the photomultiplier due to strong laser returns from low altitudes, a mechanical shutter is employed. This shutter rotates at a frequency of 24000 rpm and blocks out the scatter from the first few hundred meters. This altitude can be set by means of a variable delay. A complete description of the design and operation of the shutter is given in Kuppen (1992).

7.5.1 Mode of operation

Two computers are used in the system. One computer controls the motor drive for prism alignment and the second computer controls the data acquisition and storage.

The laser is fired (either manually in single shot mode or automatically in repetitive mode). Each laser shot is detected by a photodiode which is placed at the back of the laser cavity. The photodiode then sends a voltage pulse to the pulse counting system. This starts the counters in the PCS running

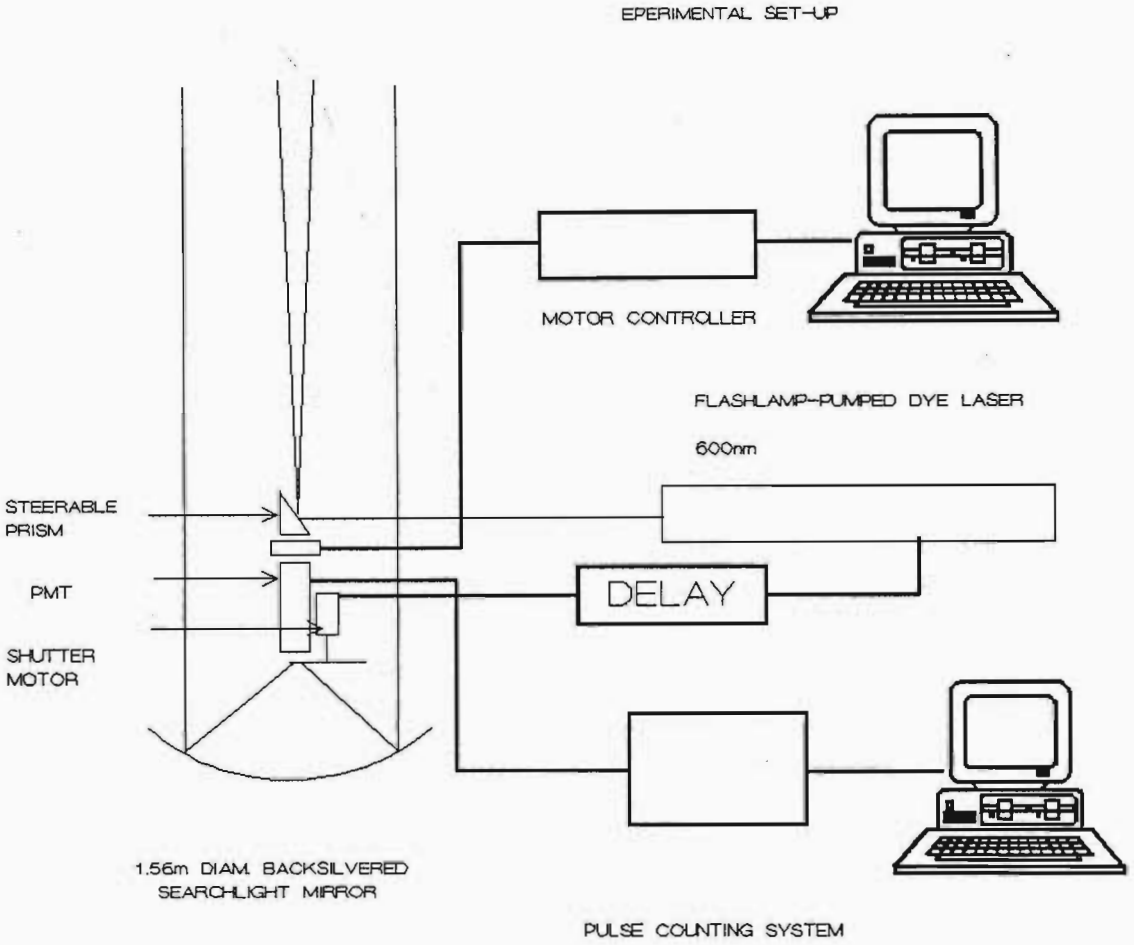

Figure 7.5: Schematic of experimental set-up of the Durban lidar system

and it is at this stage that data collection begins.

When the optical chopper is used, the laser is triggered off the position of the blade via some delay circuitry. The delay determines the altitude from which data acquisition begins. This takes place automatically every two seconds. The counters in the PCS are started by the signal from the photodiode as above.

The laser beam strikes the directing prism from where it is reflected upwards into the sky. As it interacts with the atmospheric molecules and aerosols it is backscattered. Since the telescope points vertically upwards, only the scattered laser radiation coming straight back down is collected by the mirror and focused onto the aperture.

The light then passes through the aperture, is collimated and finally a "parallel bundle" of light strikes the photocathode on the PMT. As already mentioned, the collimating optics have a 79^o field of view so only 1.05m of the mirror surface can be utilised. Ideally we would want a larger collimating system with a greater field of view which would enable us to utilise the entire mirror surface.

The light incident on the photocathode consists of a large number of photons. A fraction of these photons cause electrons to be emitted from the photocathode of the photomultiplier. Each electron gives rise to a number of pulses out of the photomultiplier. These are passed through an amplifier which discriminates against the noise and amplifies the signal 100 times.

These amplified pulses are then fed into the PCS via a long 50 Ω cable where they are counted. The pulse amplifier is situated close to the PMT and the PCS is located in the next chamber (see figure 7.6) near the computer and the laser power supply. The PCS is shielded from the laser HT supply by means of a Faraday cage.

The PCS which starts counting the moment the laser is fired integrates counts for every microsecond. Since the speed of light is constant at 3 $\times 10^8 m.s^{-1}$, $1\mu s$ corresponds to 300m. However, since the laser light directed upwards travels a distance of 2d before being detected, after $1\mu s$ the collected return has originated from a height of 150m. The PCS therefore

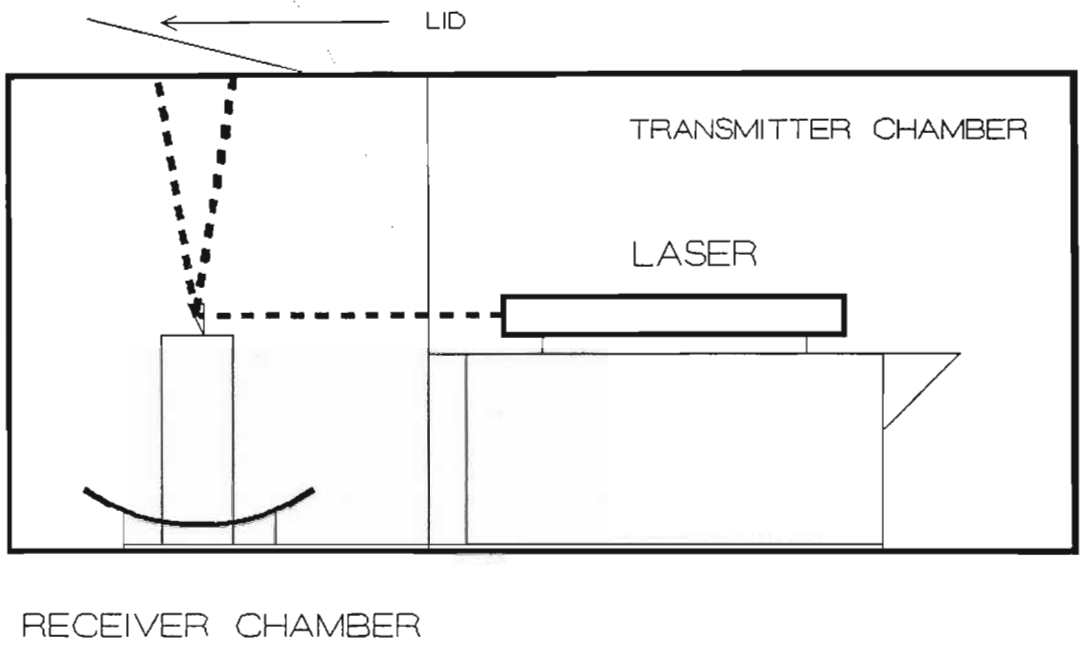

Figure 7.6: Internal layout of the lidar system

stores counts for every microsecond for 667 microseconds. A profile is therefore built up for each laser shot having a resolution of 150m. A number of laser shots are taken and the counts are added to produce a single profile.

It should be pointed out that due to the bandwidth of the interference filter (10nm), the lidar system at present is strictly a nighttime instrument. To convert to daytime studies, a very narrowband filter would need to be purchased. This is however too costly at this stage. Therefore all profiles presented hereafter are profiles obtained at night.

7.5.2 Comparison with other aerosol lidars

The following table represents a comparison between the Durban lidar transmitter and two other aerosol lidar transmitters :

1. Kent et al. (1966)

2. Hirono et al. (1984).

Both of the abovementioned lidars were used for nighttime study of aerosols.

Characteristics	*Durban*	*Kent (1966)*	*Hirono (1984)*
laser	dye	ruby	Yag
pulselength	0.6μs	5μs	2μs
energy/pulse	0.7J (max)	3J	0.5J
rep. rate	1Hz	0.2Hz	10Hz
wavelength	589nm	694nm	1064nm
range	10-25km	10-80km	12-28km

We can conclude from the above table that :

1. The pulselength of the Durban lidar is very good.

2. The repetition rate is comparable to the other lidars, and

3. For the altitudes we are interested in, the energy of the laser is adequate.

7.6 Location of the lidar system

The lidar system is housed in a transport container (see figure 7.6) which is situated on top of the Physics Building at the University of Natal. This building is five stories high. This location was chosen so that stray light from offices in the building and street lamps would not swamp the returned signal.

If measurements need to be done in the field, the system can be lowered from its present location and transported to the site on a flat-bed truck. Geographically, the lidar is the only one we know of doing aerosol measurements in this part of the continent.

7.7 Early results

The first results obtained with the Durban lidar was that of cloud profiles. Figure 7.7 shows one of the profiles obtained during 1992 by Kuppen (1992).

From this plot two cloud layers can be distinguished. One layer at an altitude of 6km and another at 11km. The thicknesses of the two layers could also be established. They were 300m and 1000m respectively. Although cloud studies were (and are) easy to carry out (due to the high density of the water molecules), they served only to prove that the system was working. At the time, interest lay in high altitude aerosols.

The first detection of high altitude aerosols occurred in October 1992. The profiles were taken under clear sky conditions hence eliminating the possibility of returns from clouds. This is necessary for high altitude measurements since due to the weak return, the laser beam has to remain fairly unattenuated until it interacts with the layer of interest.

Figure 7.8 shows the plot obtained on 13 October 1992. This is the raw

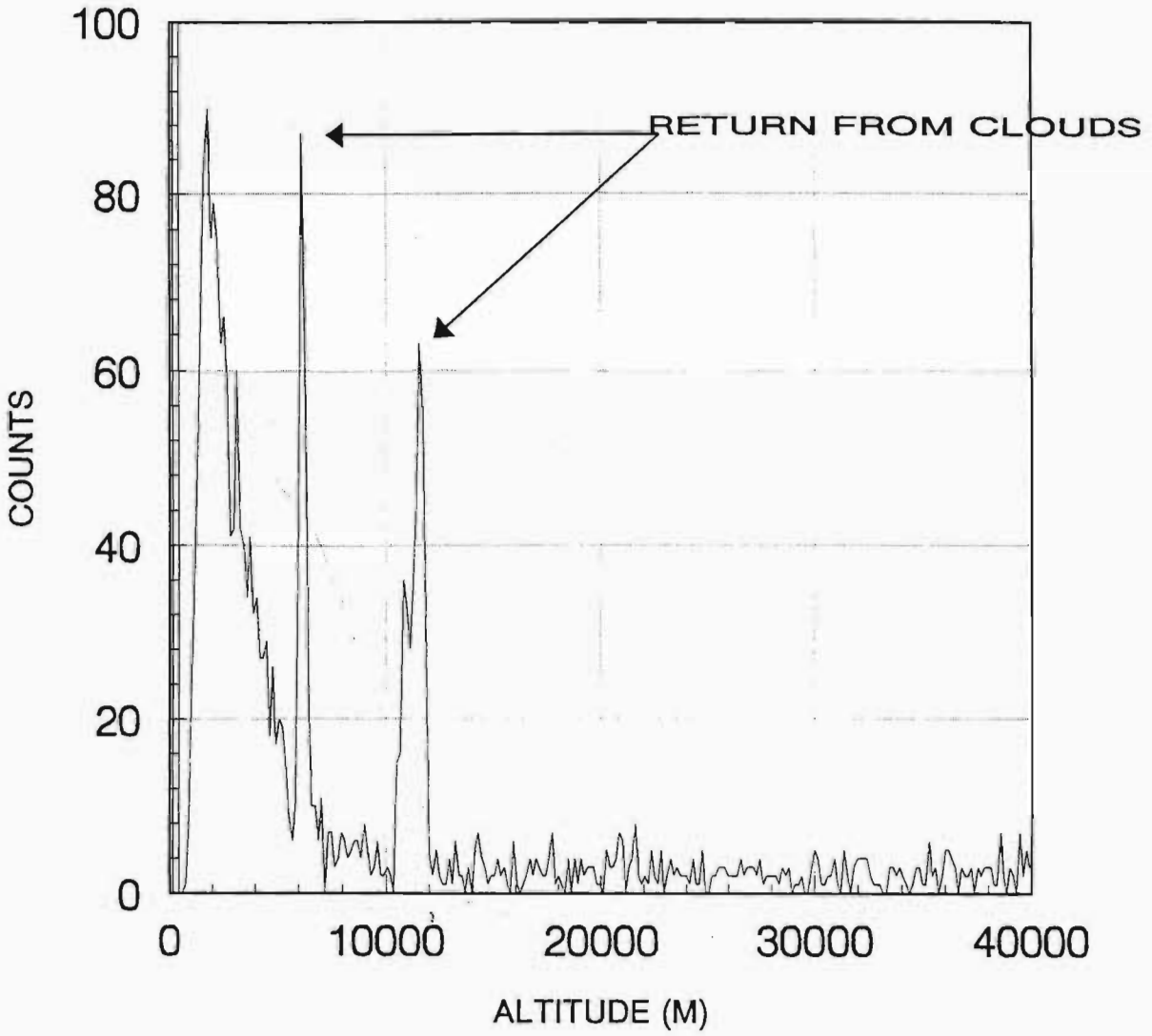

Figure 7.7: Lidar return from clouds taken by Kuppen (1992)

data from the lidar system. The atmospheric fall-off in the signal due to molecules has a $1/R^2$ relationship where R is altitude. Superimposed on this in the raw data is the contribution due to aerosols.

Two interesting features are evident from the graph. The first one is the saturation region in the 0-4km altitude range. The mechanical shutter was not in operation at the time resulting in the saturation of the photomultiplier due to the high intensity of the return from the lower altitudes. Since the region of interest was much higher up, this was not a problem. It can be seen that recovery of the instrument took place at about 5km.

The second and more interesting feature is the increase in the return at 18km. This indicates a high density aerosol layer at this altitude. From as early as 1964, Fiocco and Grams (1964) detected the presence of an aerosol layer at 19km. See figure 7.9.

More recently, Hirono et al. (1984) detected the remnants of the aerosols ejected into the atmosphere by Mt. St Helens 1 year after the eruption. It is clear from the figure (figure 7.10) that there exists a layer in the 15km-30km region. The evolution of the peak is interesting and will be discussed later.

The layer observed at Durban was believed to be volcanic in nature. It was proposed that the aerosol layer observed was due to the eruption of Mt. Pinatubo in June 1991. This seems reasonable.

The layer was studied for two months and some of the results obtained are presented here. The data is presented in two forms :

1. Raw data - this is just a plot of counts versus altitude.

2. Scattering ratio - to determine how dense the aerosol layer is, some comparison with the purely molecular return is necessary. A scattering ratio was therefore plotted as a function of altitude. The scattering ratio as defined earlier is given by the ratio of the calculated atmospheric density (which consists of aerosols and molecules) to the standard atmospheric density (which consists of molecules only). This can also be represented as a ratio of the detected counts for the backscattered photons divided by the expected counts for a purely molecular atmosphere.

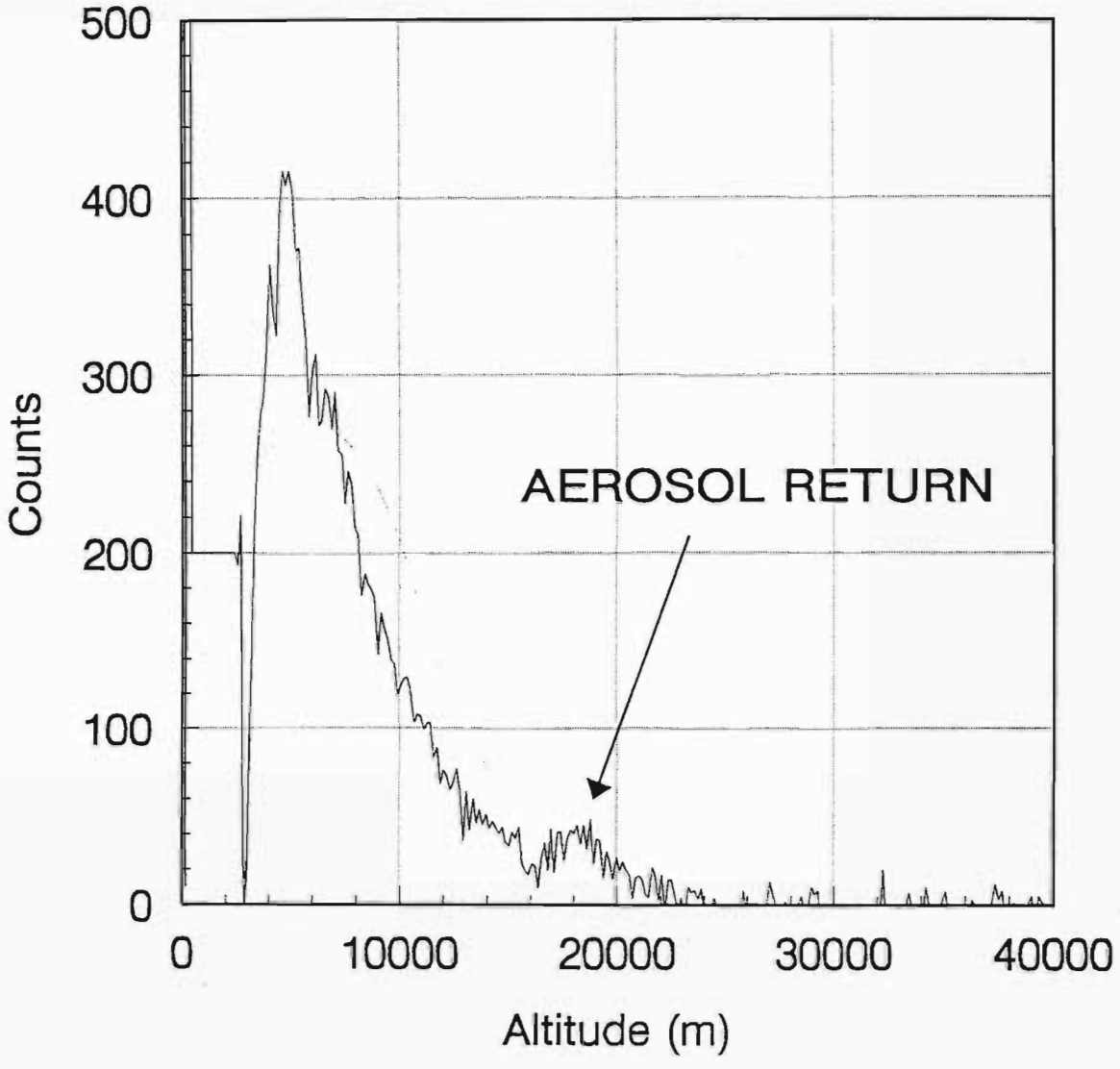

Figure 7.8: Lidar profile obtained under clear sky conditions on 13 October 1992 - 10pm - Kuppen (1992)

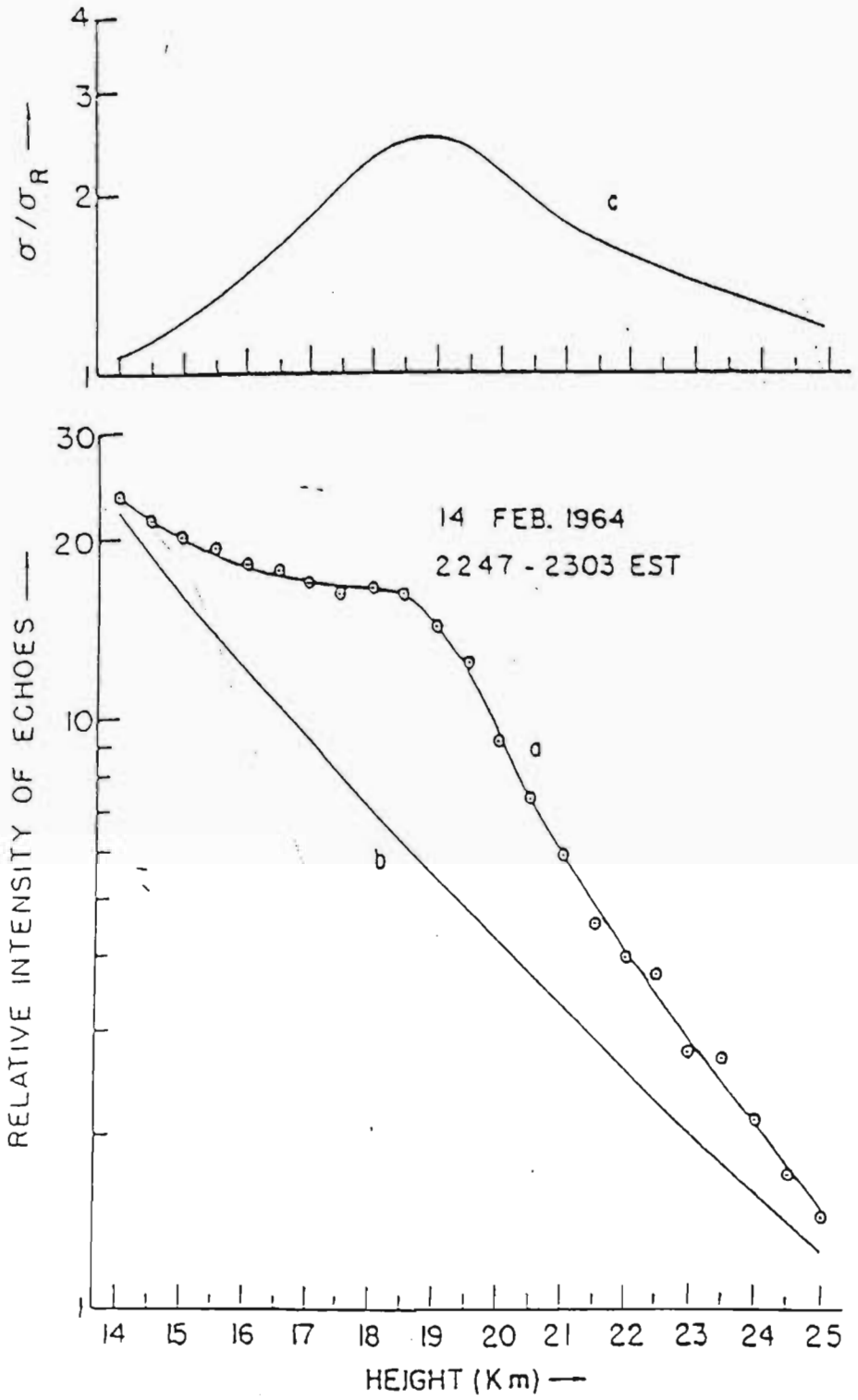

Figure 7.9: Experimental results from Fiocco and Grams (1964) - Curve "a" is the observed relative intensity of scattered light; curve "b" is the theoretical intensity of echo return from a purely molecular atmosphere and curve "c" is the ratio of the curves a and b.

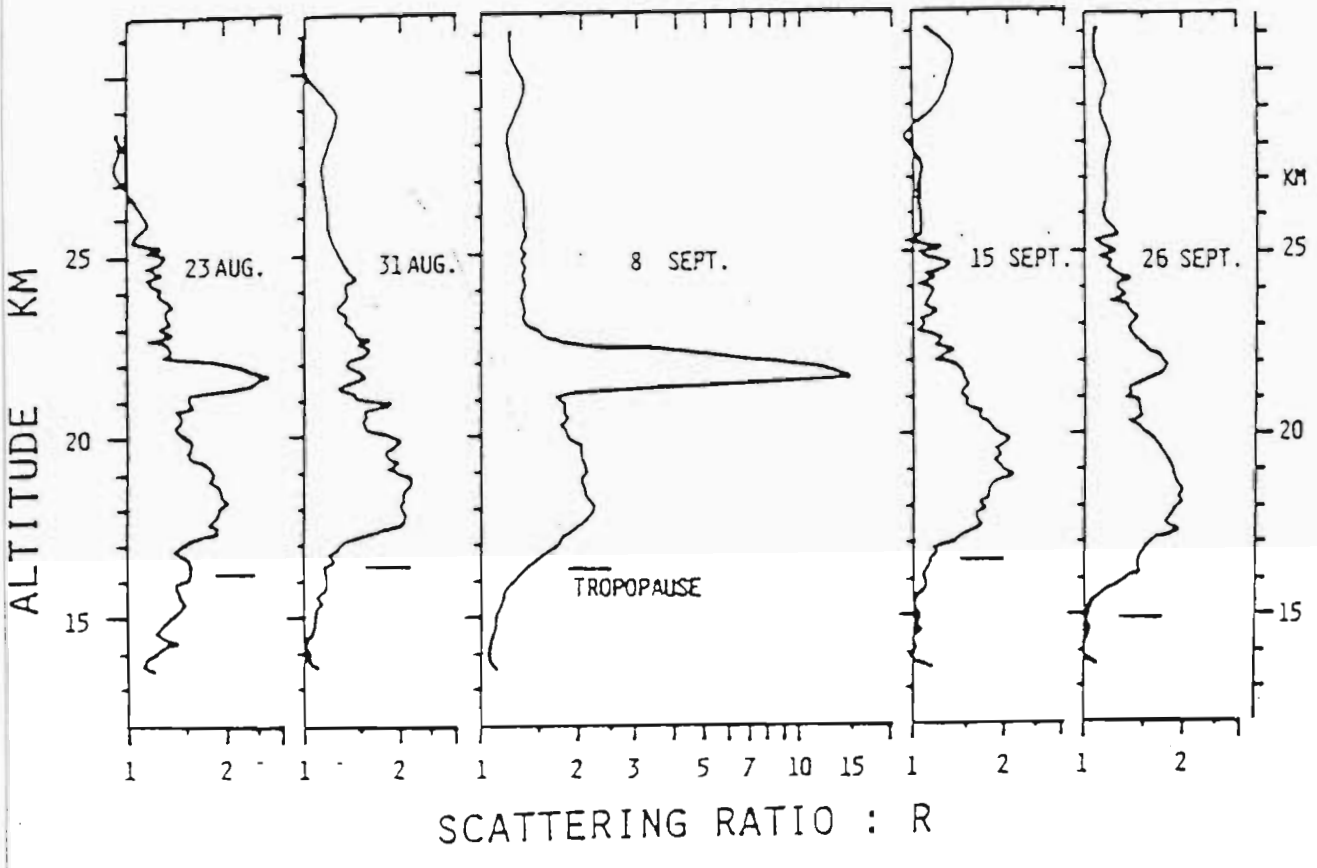

Figure 7.10: Aerosols detected 1 year after the eruption of Mt. St. Helens by Hirono et al. (1984)

A scattering ratio of 1 indicates a purely molecular atmosphere (no aerosols) and a very large ratio indicates a very dense aerosol layer (relative to a pure atmosphere). A listing of the programme Scatrate.pas is given in Appendix B. This programme is based on the theory of section 7.2 and requires 3 inputs :

i) the raw data file to be processed

ii) the standard atmospheric density profile for the location in question - these were taken from the CIRA standard atmospheres

iii) the altitude at which to "pin" the data down i.e. the altitude at which it is assumed there are no aerosols.

The programme then uses the counts received at this altitude and the actual molecular density to calculate a conversion factor K for the data set. This conversion factor is then used to calculate the scattering ratios for all altitudes.

The profile obtained on 13 October 1992 was analysed to yield a scattering ratio profile. This is presented in figure 7.11.

The enhanced scattering ratio is visible in the 16km - 22km region. It was concluded that an aerosol layer is present at these altitudes. The fluctuations in the signal at higher altitudes is due to system noise.

Figure 7.12 shows scattering ratios for three profiles taken approximately 1 month later (6 November 1992 by Kuppen). From the smoothed scattering ratios it is clear that the layer was still present and that changes in its nature take place over very small time scales.

Kuppen (1992) demonstrated that with the lidar system aerosol layers could be detected at high altitudes, and that these layers (believed to be volcanic in nature) exist for long periods of time.

As mentioned already, the results obtained in 1992 were preliminary and although the system was run on a regular basis between the period 1992 to

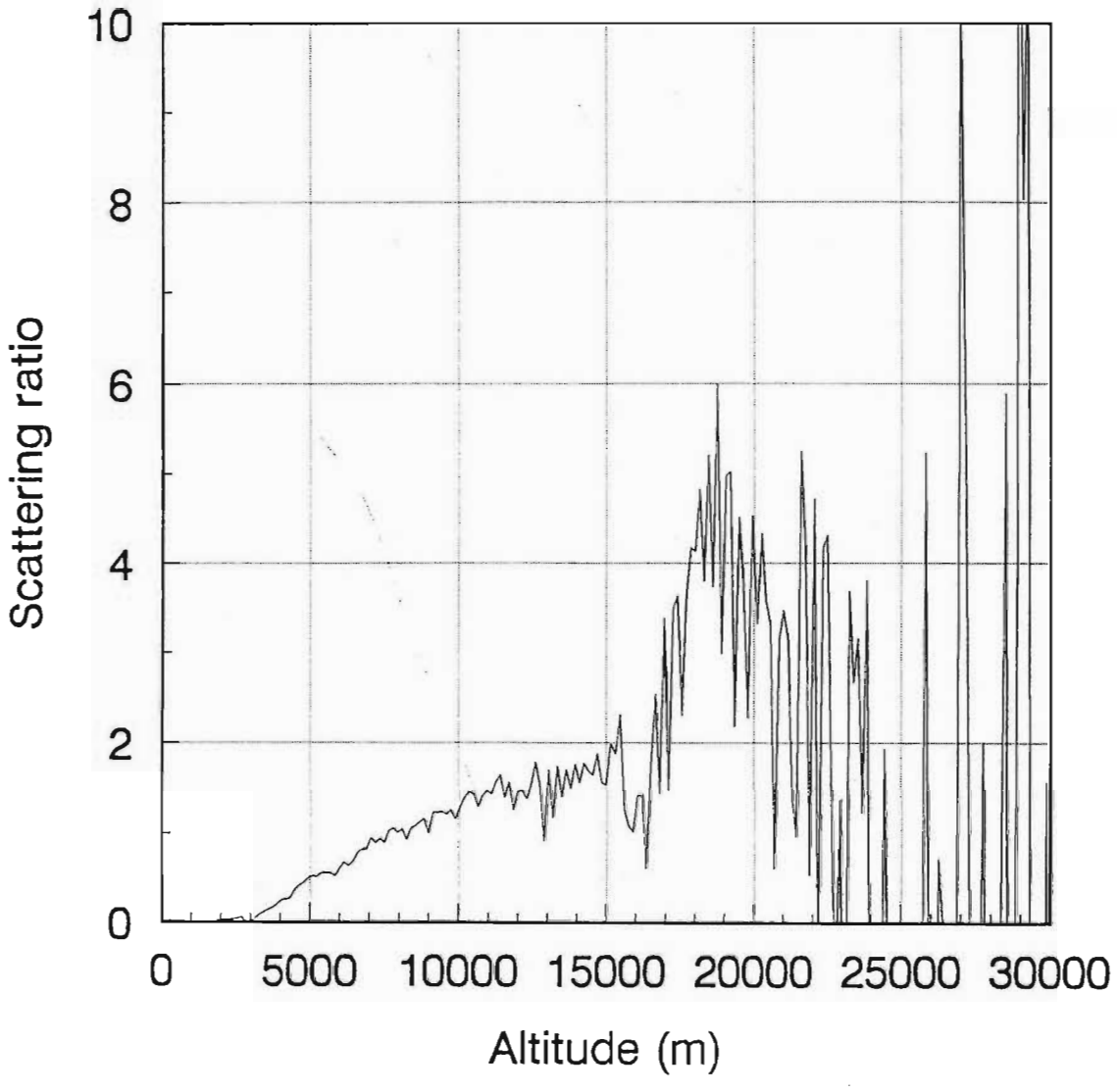

Figure 7.11: Scattering ratio for 13 October 1992 - Kuppen (1992)

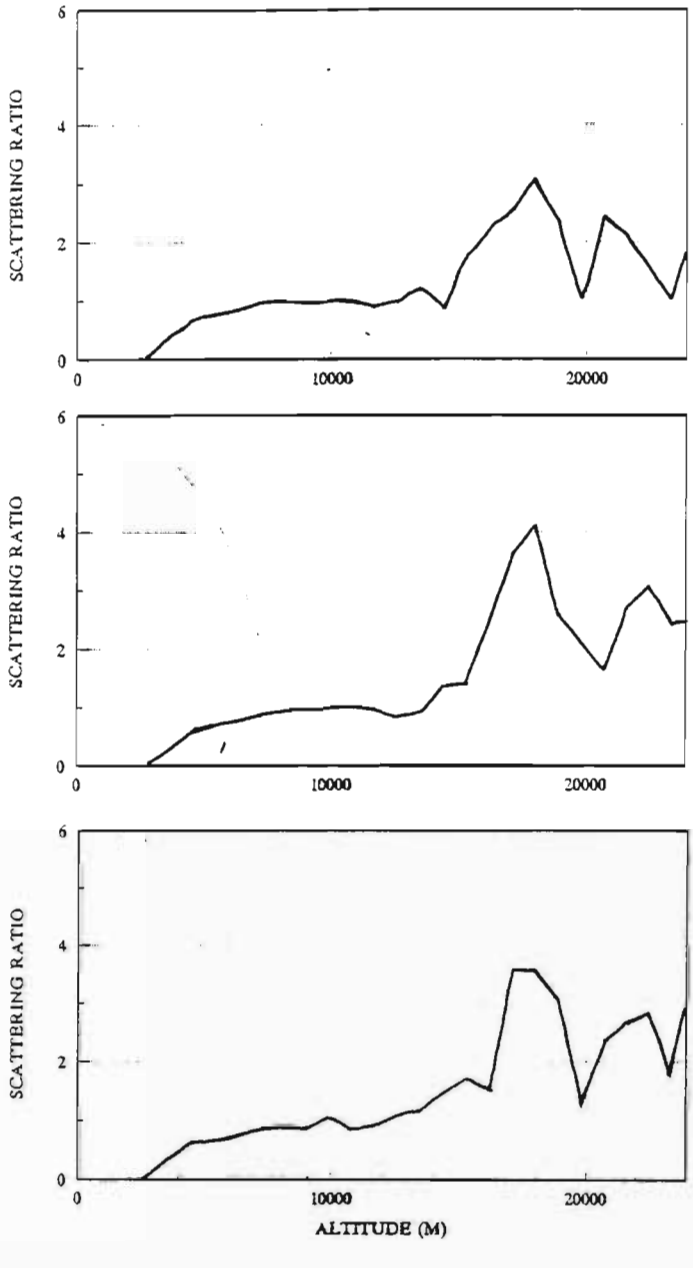

Figure (a)

Figure (b)

Figure (c)

Figure 7.12: Scattering ratios versus altitude after smoothing obtained on 6 November 1992 by Kuppen. (a) taken 7:45pm, (b) taken at 8:00pm and (c) at 8:15pm

May 1994, no serious effort was made to undertake a long term campaign, either to study high altitude or low altitude aerosols.

It was decided that a more complete picture of the evolution of atmospheric aerosols over Durban should be composed. The period June 1994 to October 1994 was chosen. This was prompted by the fact that during this period sugar-cane burning on the Natal coast results in very high concentrations of low level dust particles. These increased concentrations are known to affect local ozone concentrations. The lidar data was to form an integral part of a joint campaign with the Space Physics Research Institute (studying O_3 concentrations) and the Environmental Sciences group (investigating the associated weather patterns) in an attempt to completely characterise the effect of the sugar-cane burning on local climate.

It should be pointed out at this stage that although the period chosen was interesting as far as low altitude (0km to 10km) aerosols were concerned, the lidar system being capable of simultaneous high altitude (10km to 90km) sampling, yielded profiles spanning the entire altitude range for some of the nights during which the system was operated. This offered the opportunity of analysing aerosols in one or both of the regions in question.

The data collection campaign was regimented in the following way :

1. The system was operated on all clear nights during the period in question. It is important that clouds are not present during data acquisition. The high water vapour content of the clouds result in beam attenuation which results in much weaker returns from higher altitudes. This is undesirable.

2. Lidar returns from 100 laser shots were integrated to form each profile. This corresponds to an integration time of 3 minutes and 20 seconds at a laser repetition rate of 0.5Hz. It was determined that 100 shots were sufficient to average out random fluctuations in the signal. Also this time was short enough to assume that no appreciable atmospheric changes took place between the first and last laser shot. If this were not the case then the results would be physically meaningless.

3. As a standard, profiles of 100 laser shots were taken at regular intervals of 15 minutes. This would give some indication of the short term behaviour

of the aerosol layers. The number of profiles per night was determined by prevailing weather conditions and the availability of personnel.

4. The laser energy was maintained at a level so that profiles from as low down as possible were obtained and at the same time, high altitude aerosols could be detected. It was found that with an output energy of 0.5J a satisfactory compromise could be reached. On exceptionally clear nights, the sampling region extended from a few kilometers to approximately 90km. A complete data set extending over the entire altitude range was therefore obtained.

During the course of the campaign, interesting features were noticed at high altitudes. We will now proceed with a description of these features.

7.8 High altitude aerosols

7.8.1 Results and discussion

The very first lidar profile was taken on the night of 13 June 1994 at 6:00pm. The skies above the site were visibly very clear with no low or high altitude clouds present. Low level haze which is usually present over Durban at this time of the year was also absent.

Figure 7.13 is a plot of the raw data as recorded by the pulse counting system. The values on the y axis (as before) are counts out of the photomultiplier and the x axis represents the altitude.

Three interesting features are visible in this plot of raw data.

The first is the saturation and recovery of the photomultiplier in the first few kilometers. As mentioned earlier, the high signal return from the low level molecules causes the photomultiplier to saturate. Unfortunately the mechanical shutter was not in operation at the time. This would have prevented photomultiplier saturation and lowered the lower altitude limit of the system to a few hundred meters. As the saturation/recovery altitude was not that high ($\approx$ 2km), this did not pose a problem.

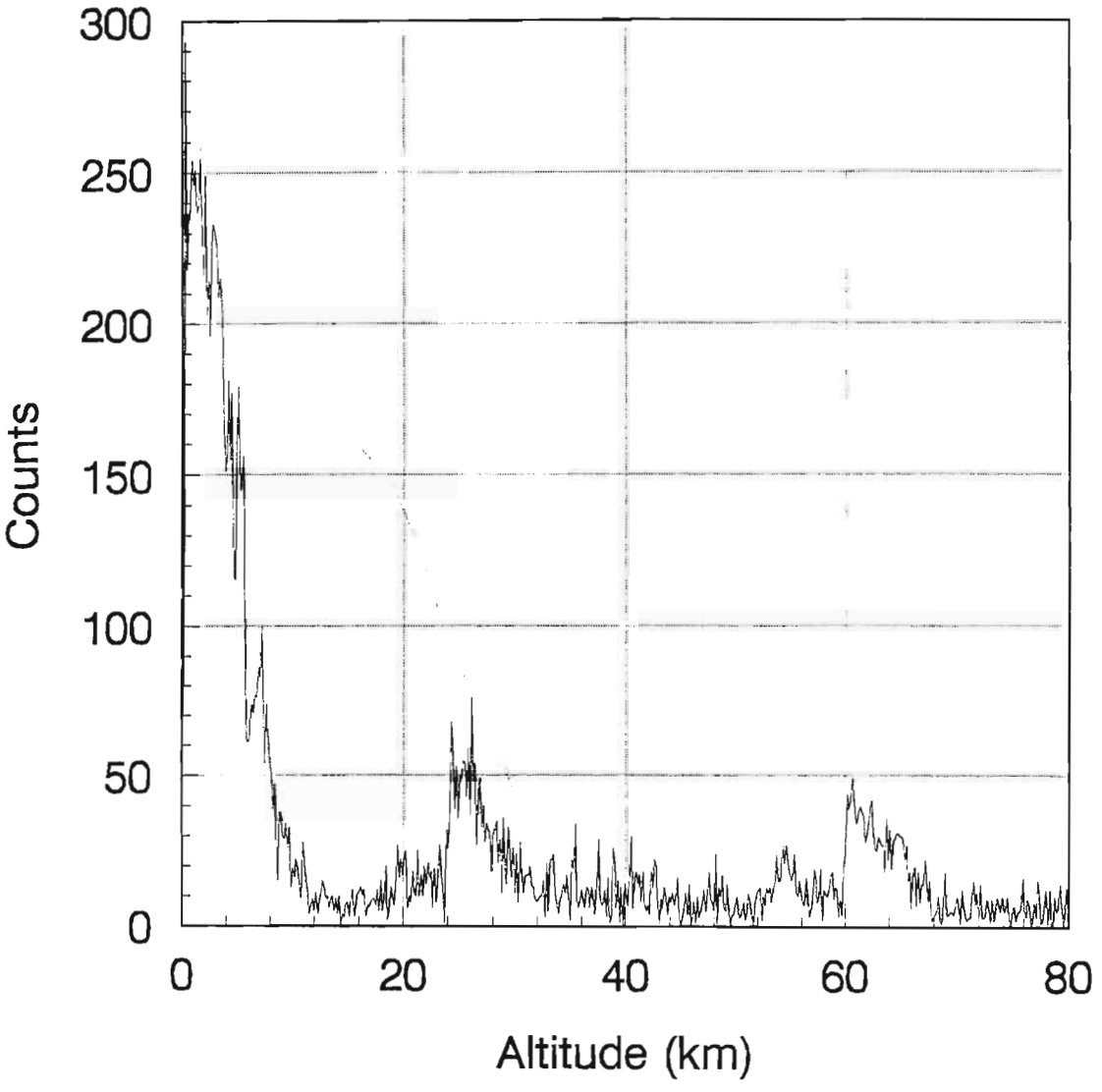

Figure 7.13: Lidar profile of 13 June 1994 - 6:00pm

The second feature of note is the aerosol layer at 25km. This increased concentration of aerosols is due to volcanic debris. It was the same feature that was detected at 18km in October 1992. It would seem as if upward tropospheric circulation has transported this aerosol layer to higher altitudes. This volcanic aerosol layer has been detected worldwide and is very well documented.

The third interesting feature is the aerosol layer observed at 60km. We will elaborate on this feature later.

Figure 7.14 is a sequence of scattering ratios vs altitude for 3 different days taken on the Island of Reunion. The data has been obtained courtesy of Hassan Bencherif.

The Reunion lidar system consists of a Nd:Yag laser as the transmitter and a system of photomultipliers as the detector. The system uses the frequency doubled output of the Yag laser (532nm) as the probe wavelength. The photomultipliers are filtered to detect the elastically scattered 532nm wavelength. Although the lidar wavelength of the Durban system (589nm) and that of the Reunion system (532nm) are marginally different, both systems are equally capable of detecting these high altitude aerosols. We have seen that volcanic debris has been detected with systems having wavelengths of 694.3nm (Fiocco and Smullen 1963). Even Hirono (1984) studied volcanic debris using the fundamental line of the Nd:Yag laser at 1064nm.

Due to the size of these high altitude aerosols (of the order of microns), lidar systems having outputs anywhere from the visible to the infra-red wavelength regions can be used to analyse them.

It is clearly evident that an aerosol layer with a scattering ratio of up to 1.2 is present in the 20 - 30km region. The aerosol layers show an altitude broadening over the period of 3 days. The height of this layer as detected in Reunion corresponds well with that of the 25km layer detected over Durban. The thickness of about 10km is also in accordance with that seen in the raw data plot of the 13 June 1994 (7.13).

To make a direct comparison with the Reunion data, we plotted the scat-

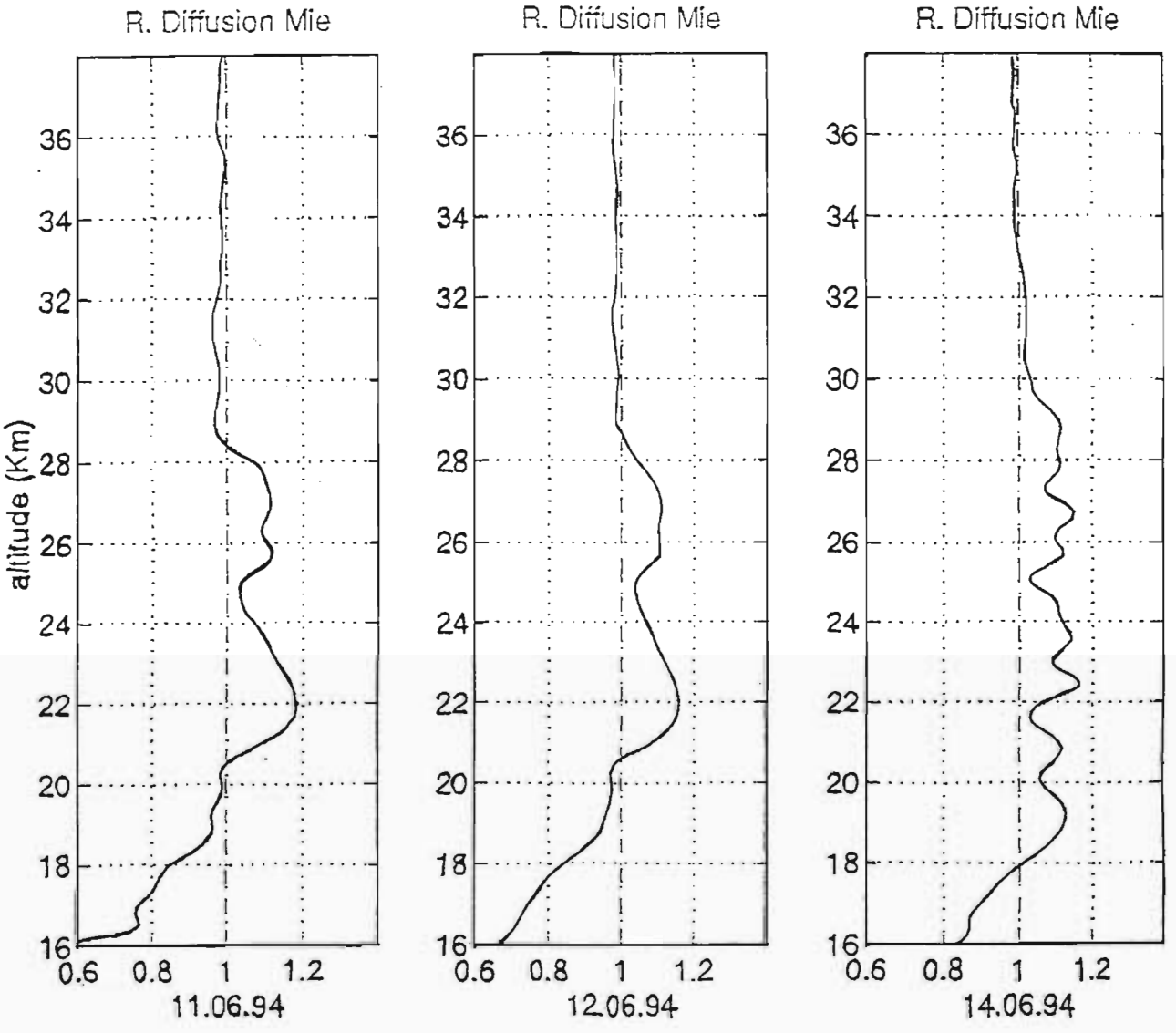

Figure 7.14: Scattering ratios versus altitude obtained on the Island of Reunion - courtesy Hassan Bencherif.

tering ratios for the data of 13 June 1994 using the programme Scatrate. This is shown in figure 7.15.

We see a maximum scattering ratio of 2.9 at 26km. This is of the order of 2.5 times that of the corresponding altitude in the Reunion plots. We note also that the layer is $\approx$ 10km thick. The fluctuations that we see in the plot from 32.5km to 40km are due to the background noise.

Unfortunately the scattering ratio analysis is based on the assumption that at some particular altitude there are no aerosols. When analysing high altitude signals with high aerosol concentrations over most of the altitude range (as was the case for our data during this period), the determination of this aerosol free altitude (or pinned altitude as it is commonly known) becomes very difficult. An incorrect choice of the pinned altitude in an aerosol rich atmosphere yields unreasonably high scattering ratios. This is compounded by the fact that at very high altitudes the noise in the lidar return results in wild fluctuations in the scattering ratio plot.

For the calculation of the scattering ratios in figure 7.15 we chose an altitude of 24km as a best guesstimate for the pinned altitude. This could account for the difference in magnitudes to the Reunion profiles. The scattering ratio profile nevertheless gives a good indication of the thickness of the layer.

We should point out that for lower altitude analysis, the strong laser return signal together with a better understanding of the atmospheric processes enables us to pick out a reasonable pinned altitude. Hence the calculation for low altitude scattering ratios is simpler than for higher altitudes. We elected to use a more reliable analysis technique (the Klett inversion method - as discussed earlier) to analyse the high altitude features. We therefore calculated the extinction coefficients for the different altitudes. This is an absolute value as opposed to the relative values of the scattering ratios and hence a better quantity with which to compare our detected aerosols with for example satellite data.

The plot of extinction coefficient versus altitude in the 15km to 30km range for the June 13 lidar profile is shown in figure 7.16. The programme Lidar0.pas was used to calculate these coefficients. The programme is based

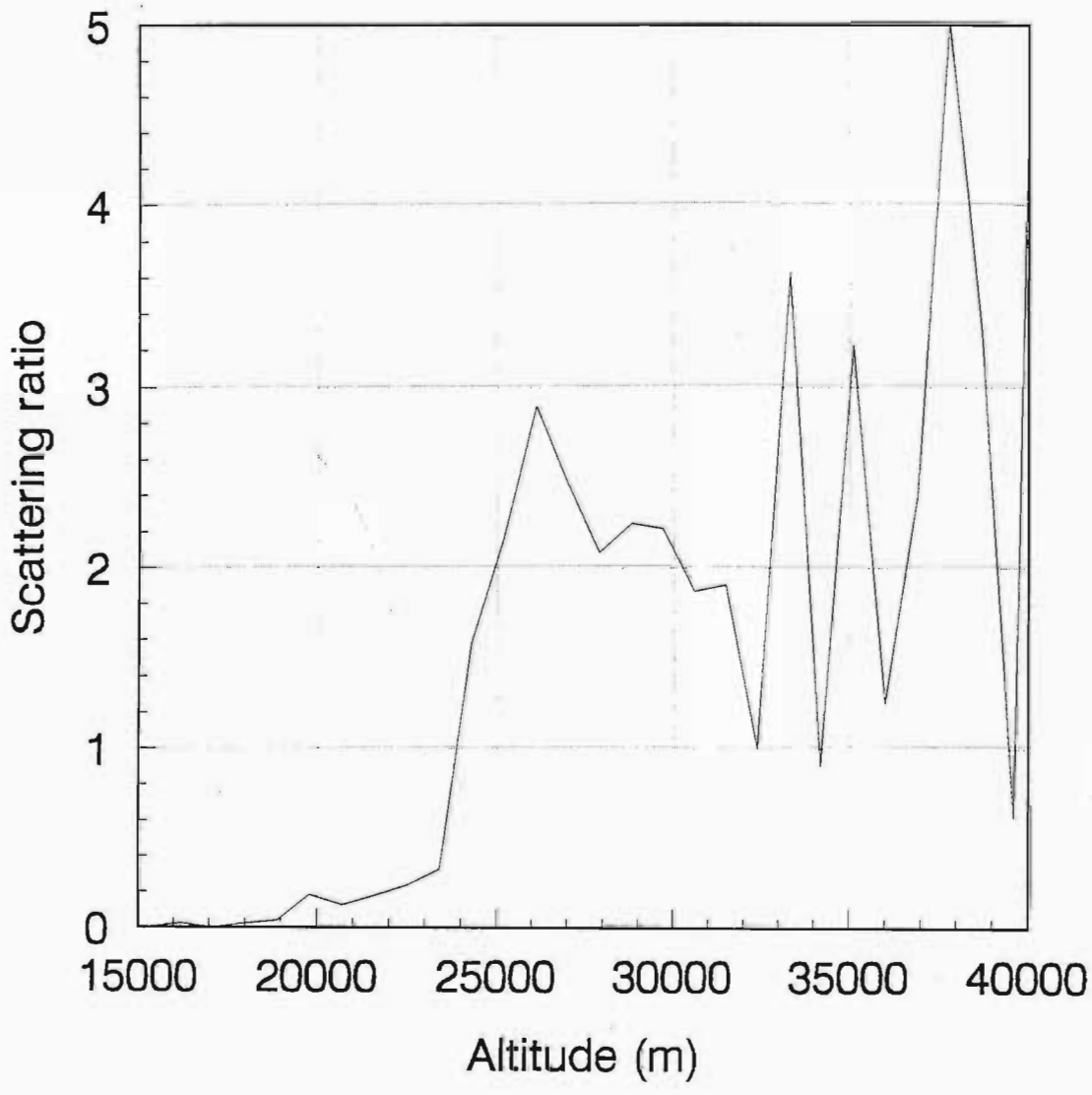

Figure 7.15: Scattering ratios versus altitude for 13 June 1994

on the Klett inversion method and a listing of the source code can be found in Appendix C.

This programme requires 4 inputs :

i) the raw data file to be processed

ii) the value of the constant k which in this case was taken to be 1

iii) the lower altitude limit for the integration (r_o)

iv) the upper altitude limit for the integration (r_m).

The limits r_o and r_m are chosen according to the region of interest.

The volcanic aerosol layer at 25km shows a peak extinction coefficient of 0.02 km^{-1}.

Returning to figure 7.13 we have already discussed two features of interest viz.

1. The saturation of the photomultiplier and

2. The aerosol layer at 25km.

These are features that were detected previously (Kuppen 1992), with the exception of the fact that over the space of 2 years the volcanic debris over Durban has migrated upwards in altitude from 18km to 25km. As alluded to previously, there is obviously some tropospheric upwelling taking place.

Perhaps a more interesting feature that manifests itself in figure 7.13 is the dramatic increase in the lidar return at 60km. Up to this point, this "60km layer" (as we shall henceforth refer to it) had never been detected with the Durban lidar system. There are three possible reasons for this :

1. Careful attention was paid to dye concentration and laser energy. The output energy of the laser was optimised (0.5J per pulse) and maintained at its optimal value for most of the June-October 1994 campaign. This was

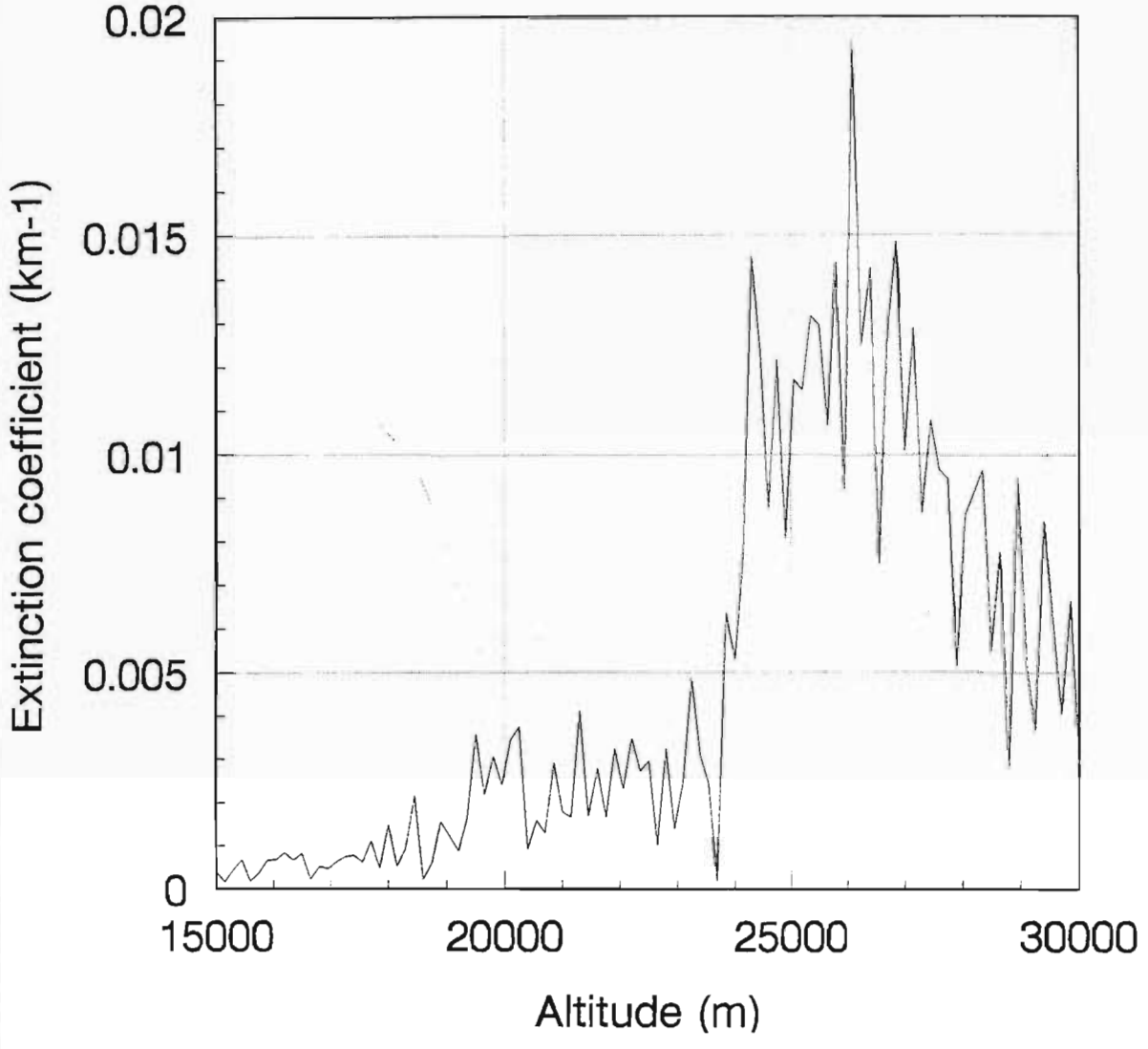

Figure 7.16: Extinction coefficient versus altitude in the 15km to 30km region - 13 June 1994

possibly not the case previously.

2. Weather conditions might have been ideal at the start of the campaign i.e. low water vapour concentrations resulting in detectable signals from much higher altitudes.

3. This 60km layer was only present at the time of detection i.e. June 1994.

It would seem as if a combination of the above three reasons to a greater or lesser degree could have contributed to the detection of the layer. More will be said about this later.

The detection and composition of this "60km layer" was intriguing. Personal correspondence with the Reunion lidar group (Hassan Bencherif) and the lidar group in Lauder, New Zealand (Leopoldo Stefanutti) showed that neither of the two groups had detected any aerosols at these altitudes.

Due to the extremely high altitudes involved, two assumptions can safely be made :

1. These aerosols have not been formed on the surface or due to surface processes. To the best of the authors knowledge, there are no circulation systems which could be responsible for the kind of transport necessary to carry aerosols from the ground up to an altitude of 60km.

2. It is also safe to conclude that these aerosols are not volcanic in nature. This follows from the fact that the last energetic eruption was that of Mt. Pinatubo and debris from this eruption has been found between 15km and 30km. The volcanic aerosols are trapped by the tropopause and apart from minor fluctuations in altitude would not manifest themselves above 35km.

The constituent detected at 60km has its origins in the upper atmosphere. From the early 1970's the scientific interest in upper atmospheric studies lay in the detection of Na. Structural changes in the mesospheric Na layer have been detected by Kirchoff and Clemesha (1973), Megie and Blamont (1977), Thomas et al. (1976), all using lidars of 589nm wavelength. Quite coincidentally the transmitters were all flashlamp-pumped dye lasers.

This Na layer detected in the 70km to 100km altitude range has been used as an indicator to gravity waves (Shelton et al. (1980)) as well as to measure the middle atmospheric temperature structure (She et al. (1990)). The abovementioned systems all operate on the principle of resonant scattering. This process can be described very simplistically as follows :

When radiation of a frequency approaching an isolated absorption line of an atom (or molecule) is incident on this atom, the atom gains energy. It may collide with another particle (atom or molecule) and an increase in the average velocity of the particles is brought about in such collisions. The length of time that an energized atom can exist as such before a collision is about 10^{-7}s. Unless a collision occurs before this time, the atom will get rid of its energy as radiation. At low pressures where the time between collisions is relatively long, the atoms will become secondary sources of radiation. The re-emitted photons usually have the same frequency as the photons of the incident radiation. This process is termed resonant scattering.

Although resonant scattering has a large cross section, collision quenching with the more abundant atmospheric species usually results in a small return signal. Resonant scattering is best used to study trace elements in the upper atmosphere.

Based on the fact that the lidar wavelength (589nm) corresponds to the Na resonant line; Na layers have been detected by other experimenters in the altitude range close to that in which we see our layer (using the same wavelength); there is no possibility that these constituents can be ground-based, we can safely conclude that the constituent we detect between 60km and 70km over Durban is indeed mesospheric Na.

This being the case, this would be the first documented detection of this constituent using a lidar system in Southern Africa. Or for that matter, the first documented detection of any constituent at this altitude.

We plotted the extinction coefficients for this altitude range (50km to 70km) using the raw data from figure 7.13. This is shown in figure 7.17. The peak of the "60km layer" has a coefficient of $\approx 0.1 km^{-1}$.

As a method of verification of the data, we compared our extinction coefficient with that obtained by the SAGE II experiment. SAGE is an acronym for Stratospheric Aerosol and Gas Experiment. The SAGE instrument was launched by shuttle on the Earth Radiation Budget Satellite. SAGE II is a sun photometer that measures the extinction of solar radiation caused by the earth's atmosphere in seven spectral channels ranging from 0.385μm to 1.02μm. These measurements which occur twice each orbit during satellite sunrise and sunset are inverted to yield vertical distributions of stratospheric aerosols, ozone, water vapour and nitrogen dioxide.

The SAGE II instrument consists of a Cassegrain telescope with a two axis gimbal mounting, a grating spectrometer and a 12 bit data system. The instrument tracks the solar centroid in the azimuth plane and vertically scans the instrument's instantaneous field of view across the sun for tangent altitudes ranging from the earths horizon to 150km. Hence the instrument generates vertical profiles up to 150km.

We extracted 3 profiles from the 1994 data set. The closest wavelength to our lidar wavelength of 589nm was 525nm. The three SAGE profiles extracted were taken on :

(i) 3 June 1994 at co-ordinates 32.75S and 33.58E,

(ii) 26 June 1994 at co-ordinates 30.4S and 26.14E and

(iii) 6 October 1994 at co-ordinates 34.76S and 26.84E.

These profiles are shown in figures 7.18, 7.19 and 7.20.

In all three of these plots, we notice what we have up to now referred to as the "60km layer". Note also that the extinction coefficients range from $0.00025km^{-1}$ to $0.0015km^{-1}$ whereas our calculated coefficients on 13 June 1994 was $0.1km^{-1}$ at 60km. The three SAGE plots taken at various times around Durban verify two things :

1. The 60km layer certainly manifests itself in this part of the Southern hemisphere at altitudes between 60km and 80km.

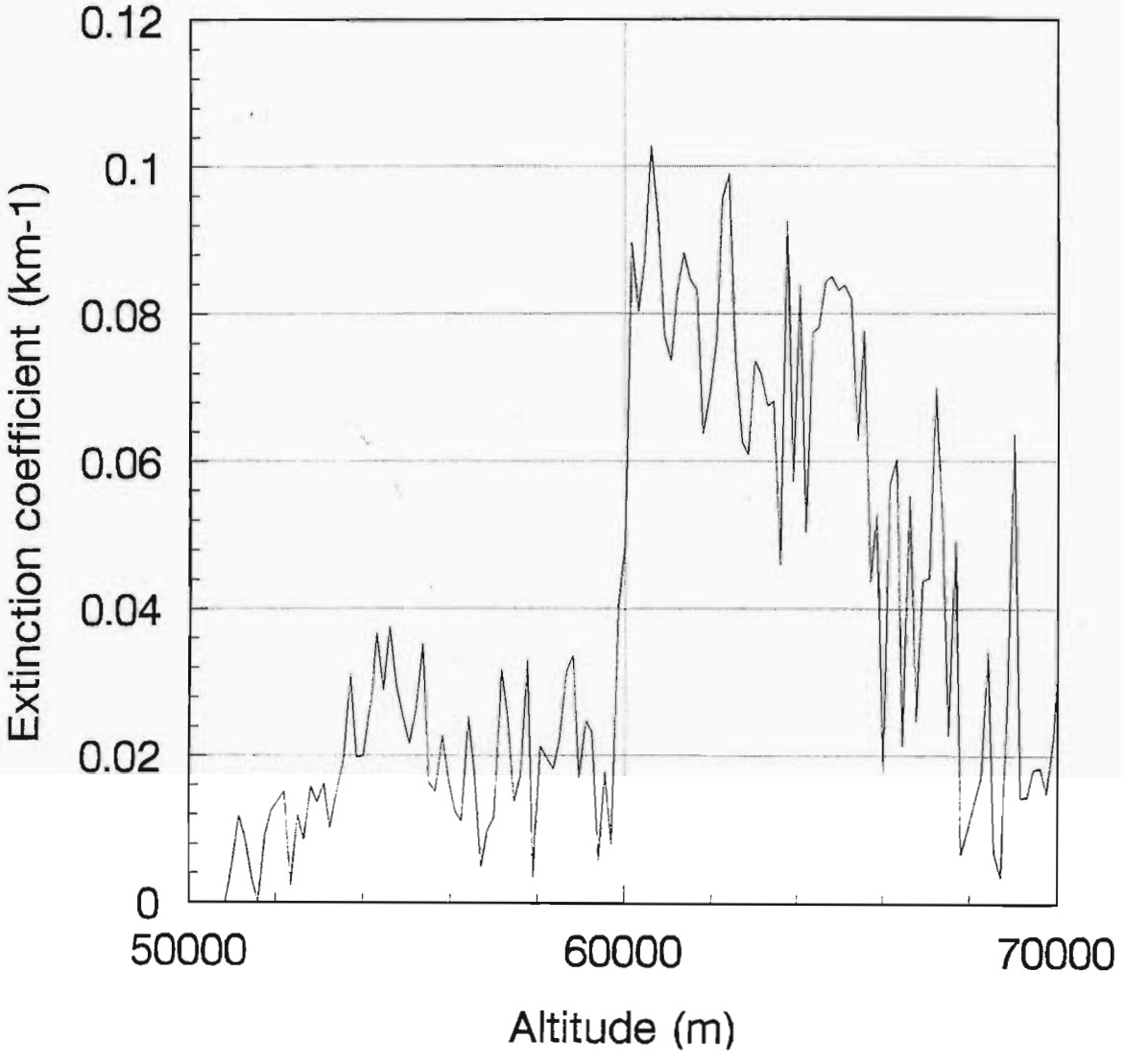

Figure 7.17: Extinction coefficient versus altitude for 13 June 1994 calculated from the lidar profile (50km to 70km)

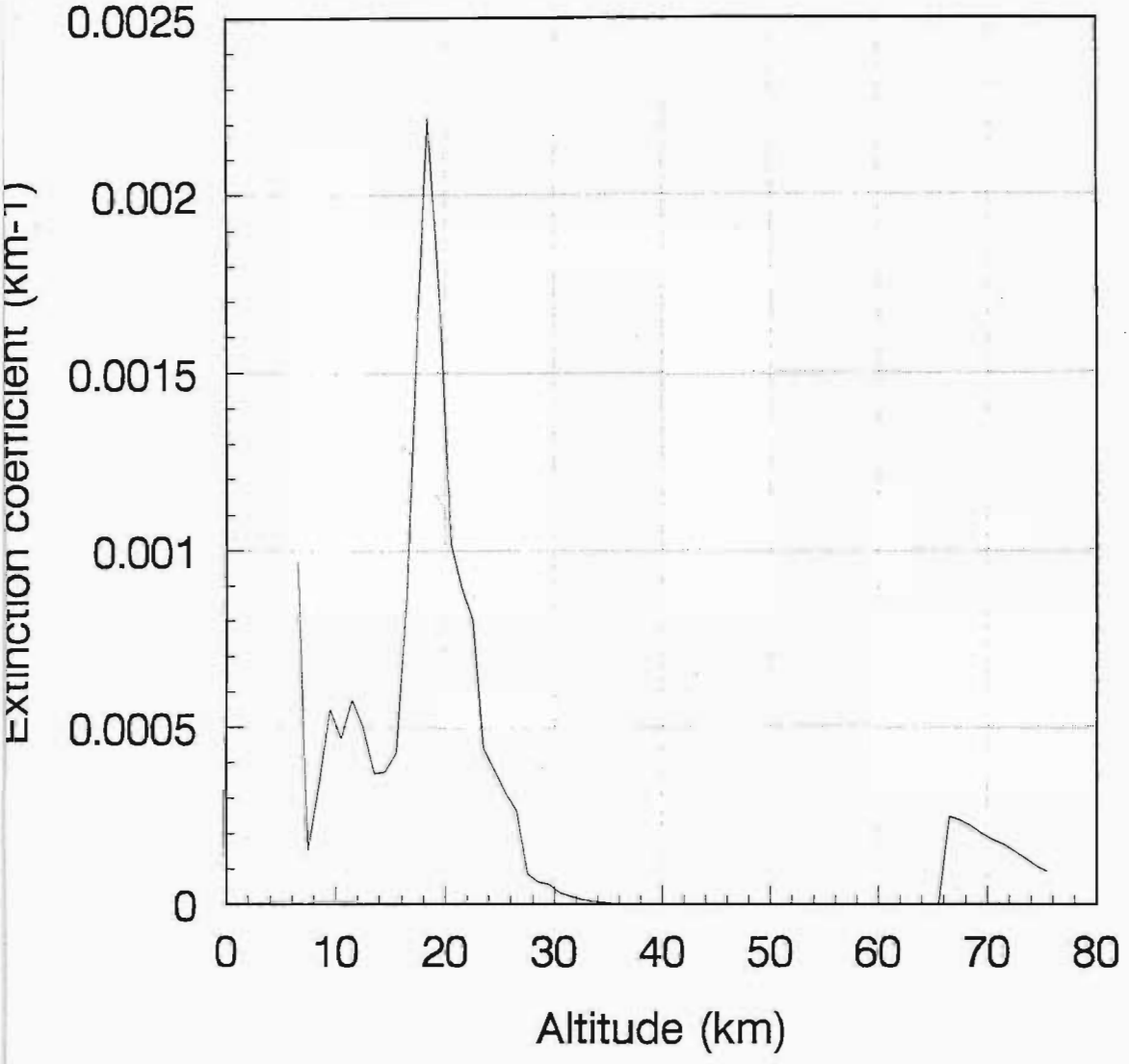

Figure 7.18: SAGE profile taken on 3 June 1994 at 32.75S and 33.58E (525nm)

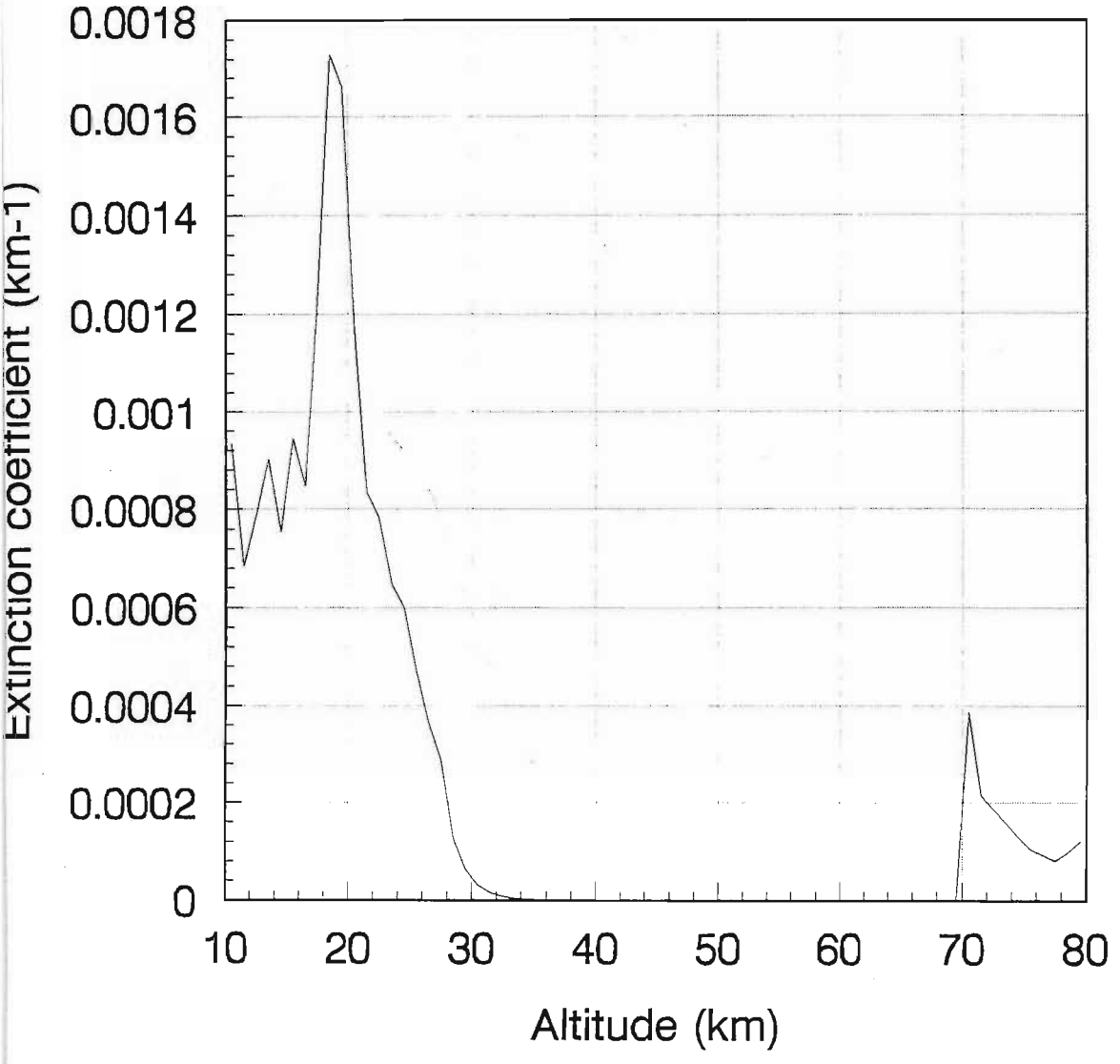

Figure 7.19: SAGE profile taken on 26 June 1994 at 30.4s and 26.14E (525nm)

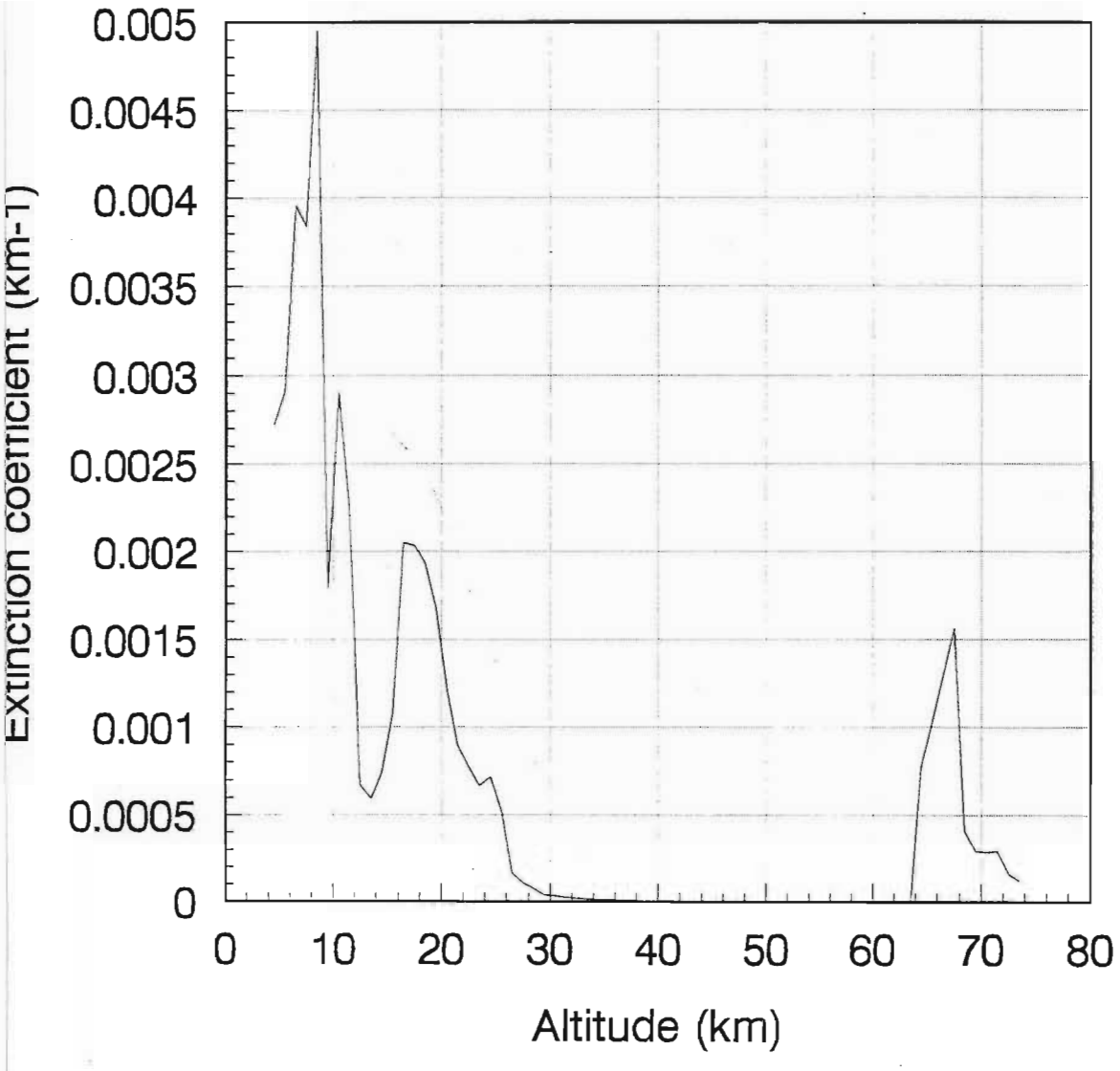

Figure 7.20: SAGE profile taken on 6 October 1994 at 34.76S and 26.84E (525nm)

2. It is present during the entire data gathering campaign. This contradicts our previous postulate that we only detect the layer when it is present.

Figure 7.21 is a composite showing the raw data versus altitude for 8 days during June 1994. All these profiles were taken at the same time viz. 6:00pm. The background signal was subtracted from each profile and the curves smoothed to give an idea of the evolution of the 25km peak and the 60km peak over large time scales. The processed profiles are shown in figure 7.22.

Looking firstly at the 25km peak. It starts off as a narrow (5km wide) feature on June 13, broadens out on June 14 and narrows again on June 15 before merging into the background. With special attention to the high altitude 60km layer, we notice that this layer seems very short lived. Its evolution seems much simpler than that of the lower (volcanic) layer. We notice that the concentration peaks on June 14 and then disappears.

To investigate the very short term behaviour of the two layers, we plot profiles from the 13, 14 (7.23) and 15 June 1994 (7.24). We see that both layers evolve over the space of 15 minutes. However, the lower layer demonstrates temporal broadening while the 60km layer does not. It is either present as a very narrow peak or it disappears completely. This points to the possibility that due to tropospheric circulation, the volcanic debris disperses (altitude-wise) over the observation site whereas the higher altitude layer could very well be passing over the site.

Unfortunately, neither of these two layers was observed again for the period of the campaign.

7.8.2 Conclusions

We can conclude at this stage that both layers demonstrate short term behaviour. It would seem from the satellite data that the 60km layer is always present. The reason we didn't see it again was probably due to unfavourable weather conditions. Perhaps the most important conclusion as far as the "60km layer" is concerned is that for the first time in Southern Africa a lidar system has detected a layer at these altitudes (verified by satellite data).

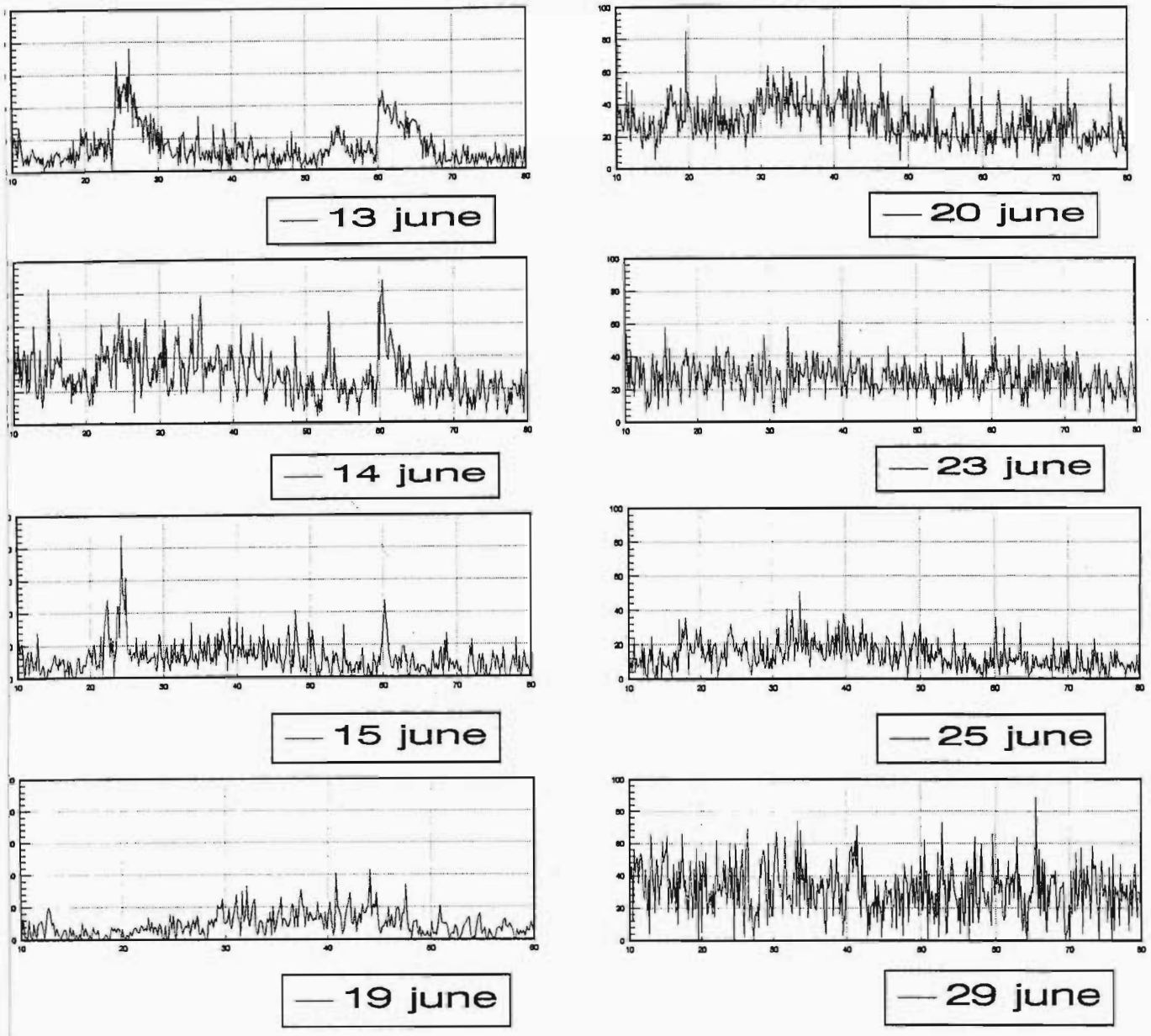

Figure 7.21: Raw data versus altitude for 8 days in June 1994 taken at 6:00pm

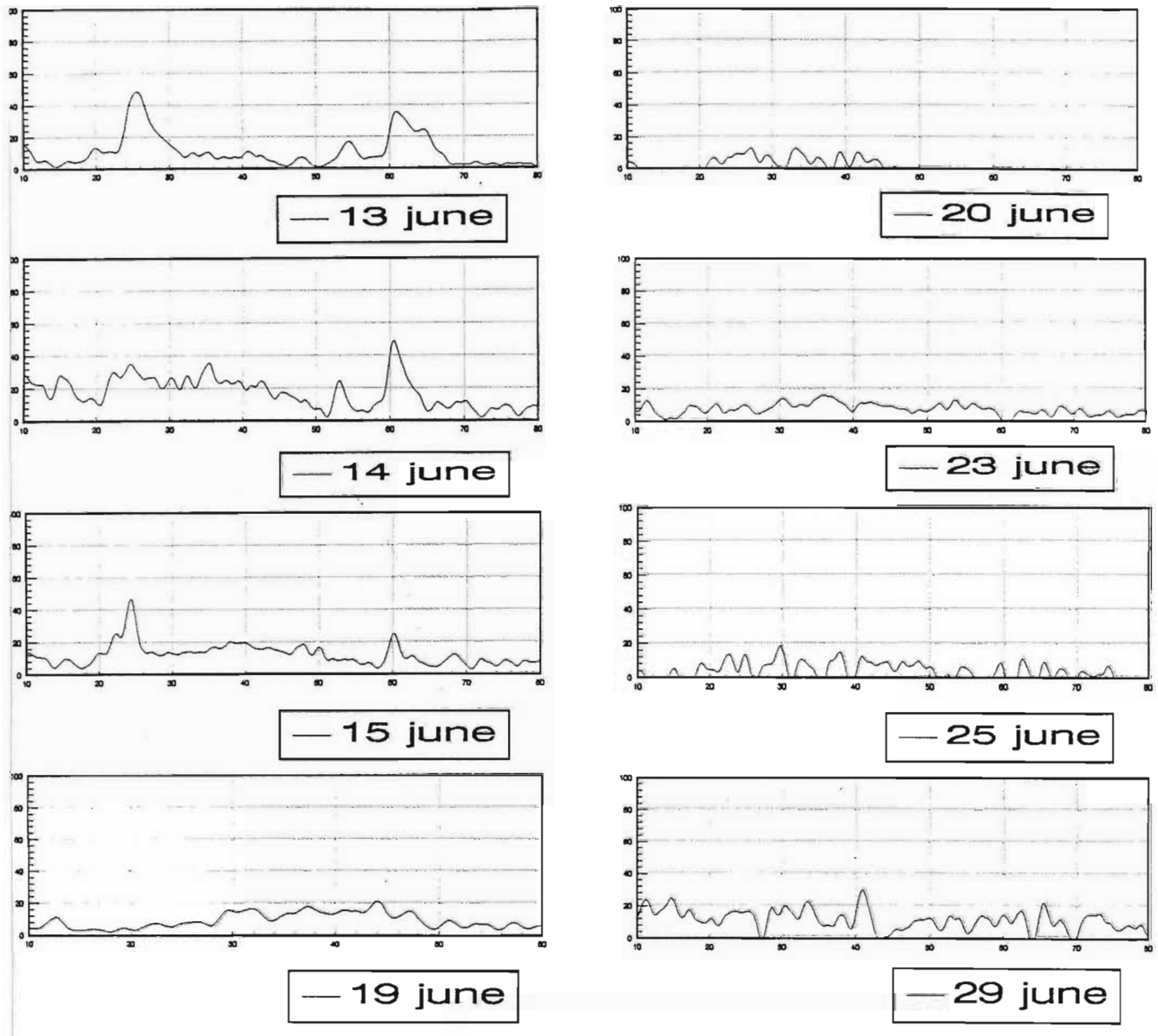

Figure 7.22: Processed lidar profiles for the same days in June 1994 taken at 6:00pm

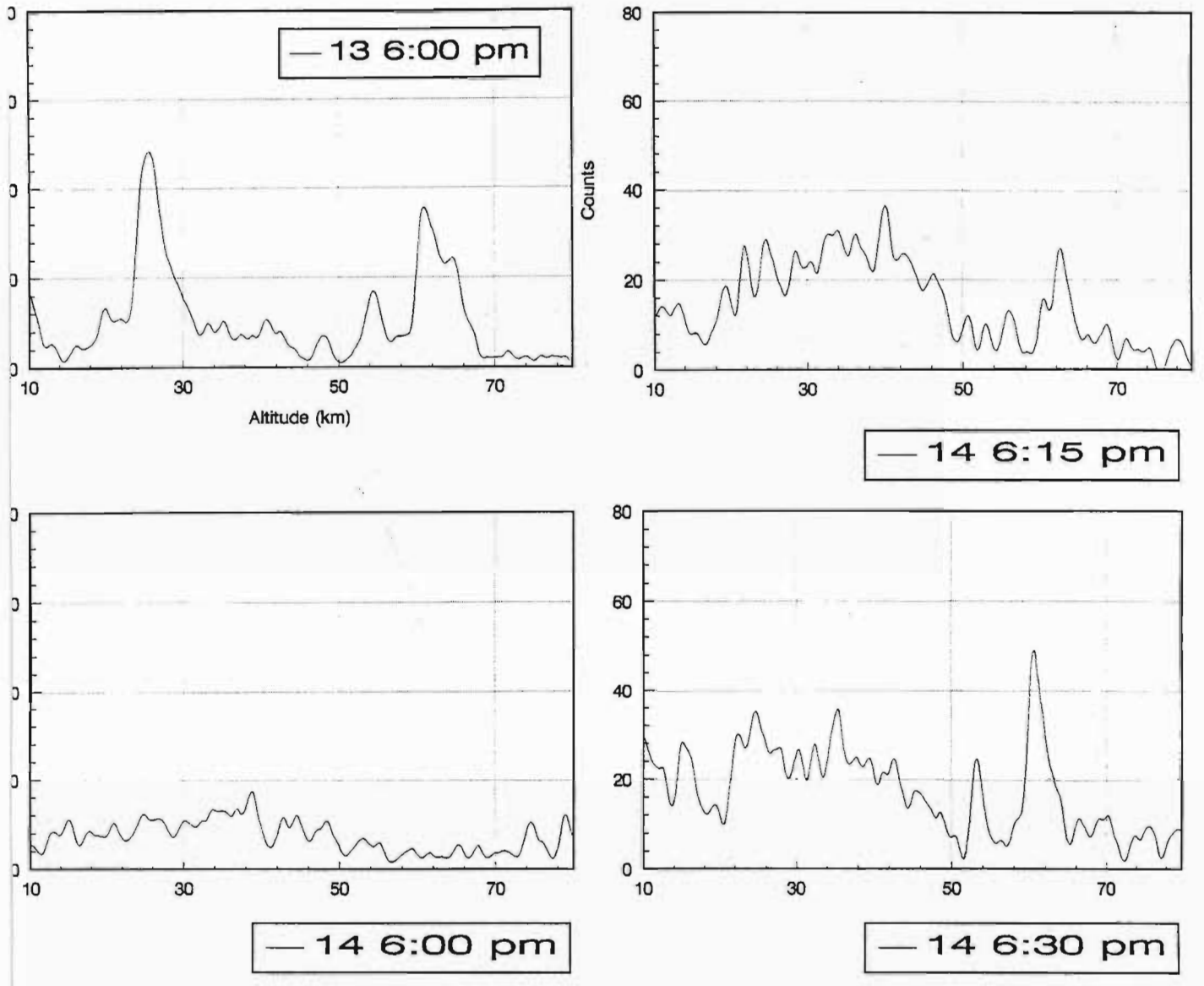

Figure 7.23: Smoothed lidar profiles taken on the 13 and 14 June 1994.

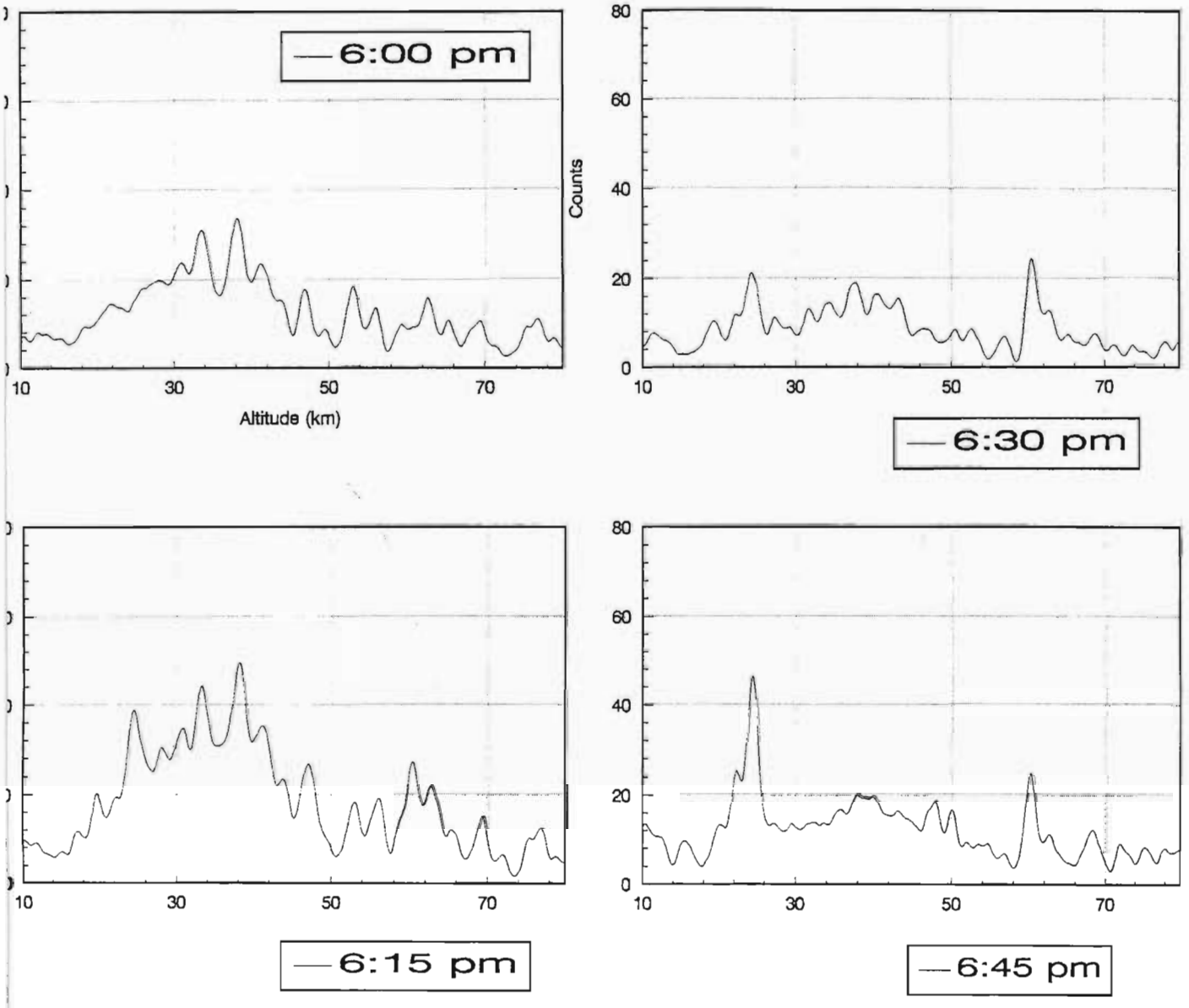

Figure 7.24: Smoothed lidar profiles taken on the 15 June 1994.

This layer is believed to be Na. Clearly more work needs to be done to investigate the long term trends.

7.9 Low altitude aerosols

7.9.1 Results and discussion

As already mentioned, the study of low altitude aerosols (0 to 10km) over the period June to October 1994 was the major source of interest as this was the period during which sugar cane burning took place on the Natal coast. The objective of this exercise was to detect these aerosols and to map their temporal behaviour. In this section we will also try and establish some correlation between the observed aerosol loading of the lower atmosphere and the local ozone values.

Although profiles were obtained in June, July, September and October, we will concentrate on June and September since we have data for a large number of days in these two months as compared to the others. June is mid-winter in Durban and September is the start of spring. This is fortunate because the data is then spread over two different seasons as well. The data obtained during July and October will be used later on when we attempt to compose a long term picture of the aerosol behaviour. This data will not be discussed in any detail.

Raw data

One of the earliest sets of data in June showing interesting behaviour in the lower altitudes was taken on the night of the 15th. Figure 7.25 shows a time sequence of four profiles taken from 6:00pm to 6:45pm at regular intervals of 15 minutes. The x axis represents the altitude in kilometers and the y axis the counts. These are raw profiles as recorded by the data capturing system.

Three aerosol layers are clearly evident. The first layer is at approximately 800m (as seen in the final plot). The second and third layers (more prominent than the first) are to be found at 3km and 5km respectively. At 6:15pm a layer is also discernible at 8km. From figure 7.25 we can make two

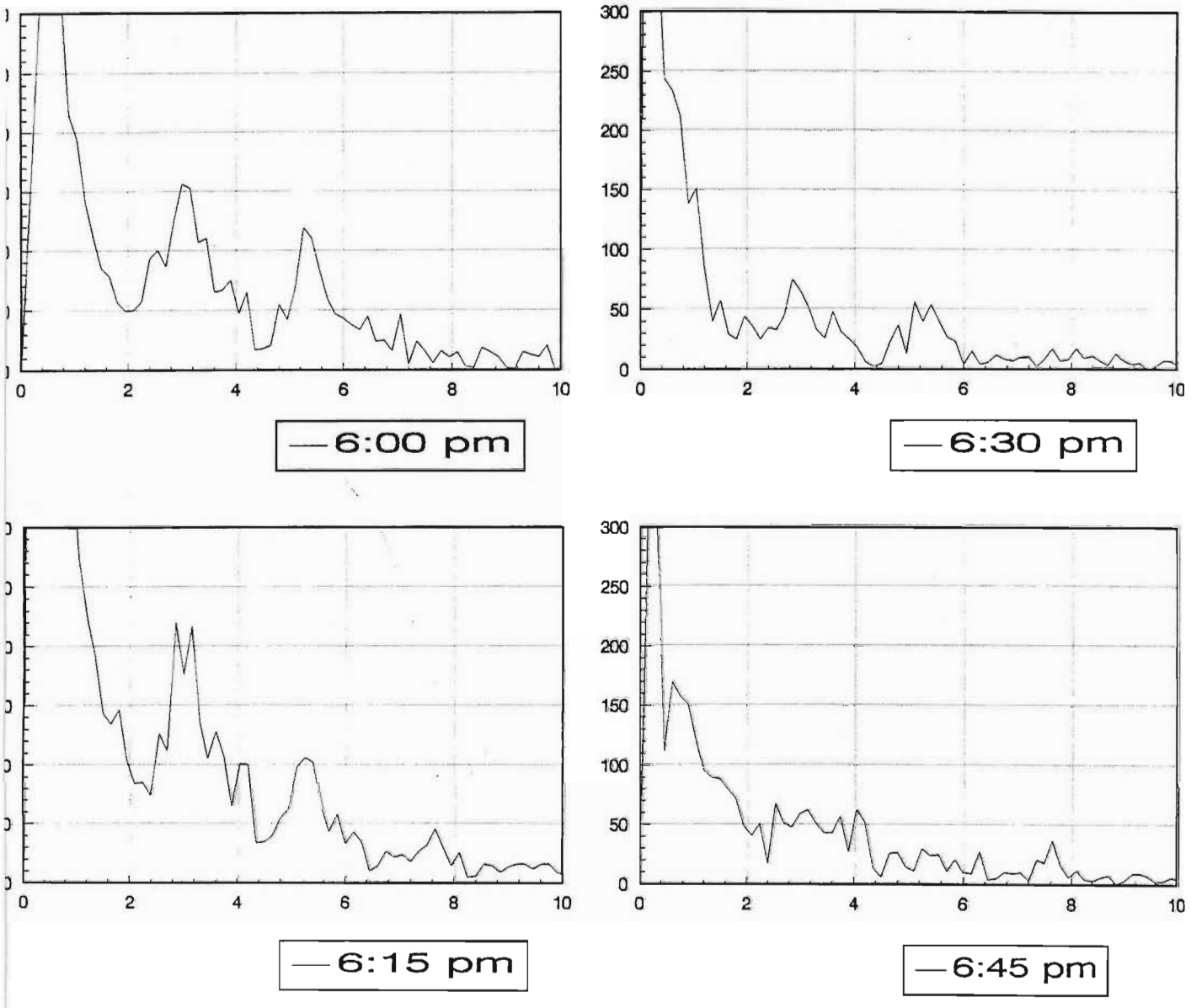

Figure 7.25: Lidar profiles taken at 6:00pm, 6:15pm, 6:30pm and 6:45pm on 15 June 1994

conclusions about the layers detected.

1. The 3km and 5km layer are fixed in altitude on this day.

2. They seem to behave independently of each other. This will be reinforced by the sequence of lidar profiles to follow (7.26).

Figure 7.26 is another sequence of 4 profiles taken 4 days later on 19 June 1994.

The times are once again 6:00pm, 6:15pm, 6:30pm and 6:45pm. The three layers detected on 15 June are again very much in evidence. We can see that the subsidence of one of the layers (e.g. the 5km layer at 6:15pm) is not necessarily accompanied by the subsidence of the 3km (or the 800m) layer.

Of course this subsidence that we refer to here is simply a relative decrease of the returned counts. This nevertheless corresponds to a decrease in absolute aerosol density.

Just looking at the raw data for the two days presented, we can conclude that there are three distinct aerosol layers and they are decoupled from each other. But is this true for the rest of the data set? Since it would be physically impossible to plot every single lidar profile taken, a composite of 8 days in June was produced. The profiles represented were all taken at 6:00pm on the respective days. The raw data was smoothed and plotted to give an idea of the evolution of the aerosol layers.

From the data represented (figure 7.27), the three aerosol layers are seen to persist for most of June. The scale on the y axis was chosen so as to enhance the 3km and 5km layer. These latter two layers disappear towards the end of the month. The estimated thickness of both these layers is 1km.

We now plot a composite of 8 profiles taken in September (figure 7.28), to see if the same behaviour persists. These profiles were also extracted from those taken at 6:00pm and were all smoothed before plotting.

The shape of these profiles is quite different to those taken in June. Although the lower layer ($\approx$ 1km) is still present, the absence of the 3km and

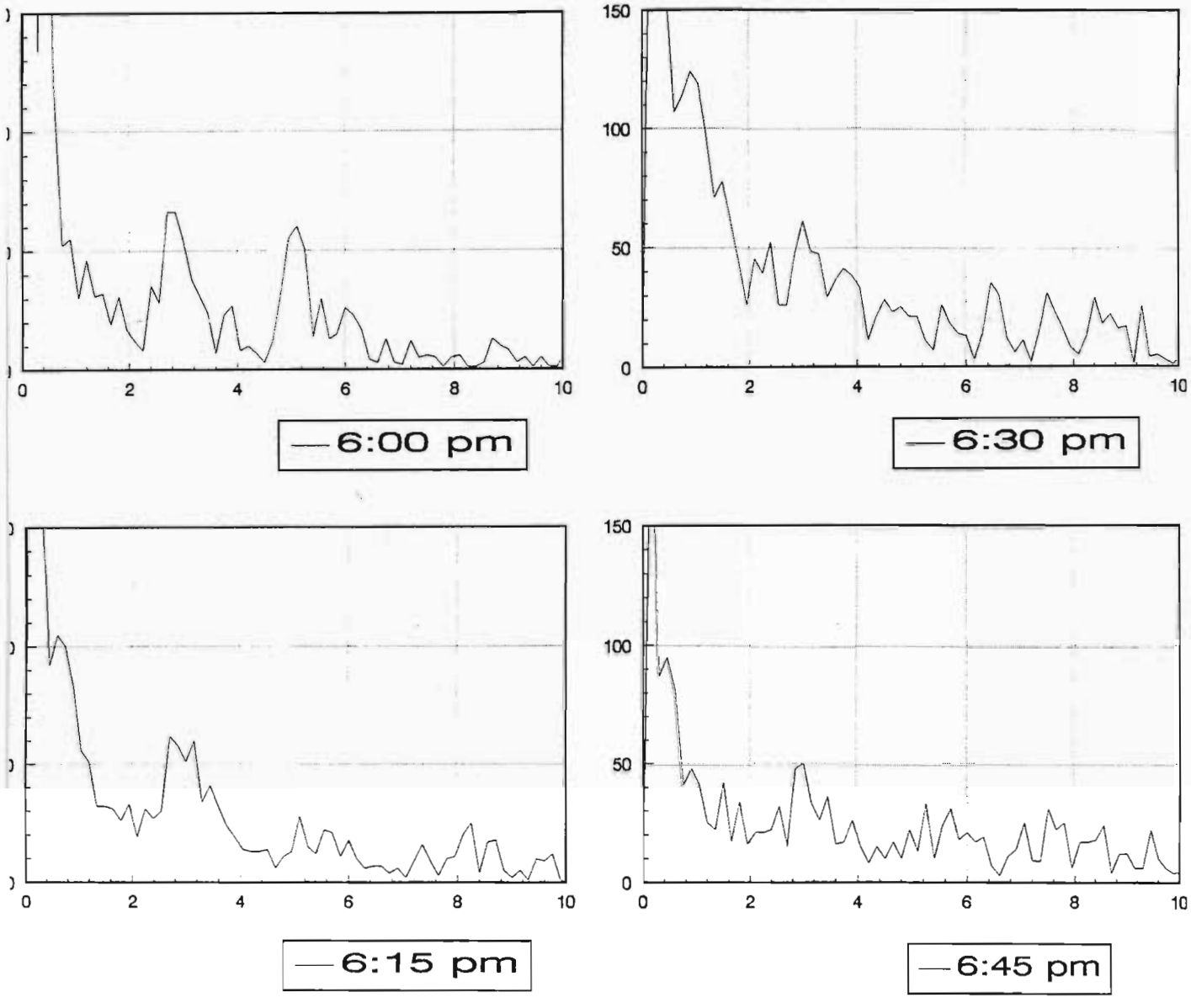

Figure 7.26: Lidar profiles taken at 6:00pm, 6:15pm, 6:30pm and 6:45pm on 19 June 1994

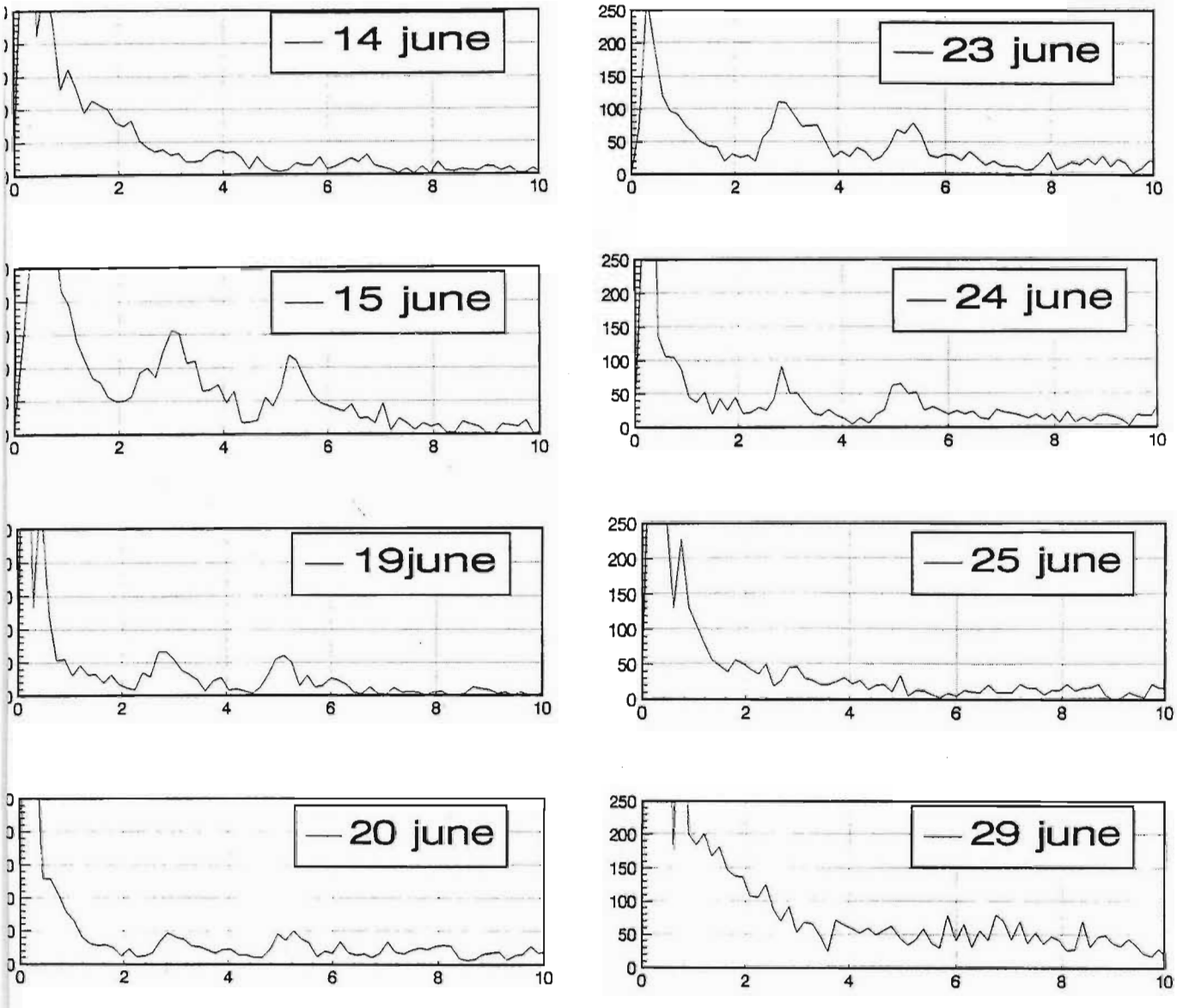

Figure 7.27: Composite of lidar profiles taken at 6:00pm during June 1994.

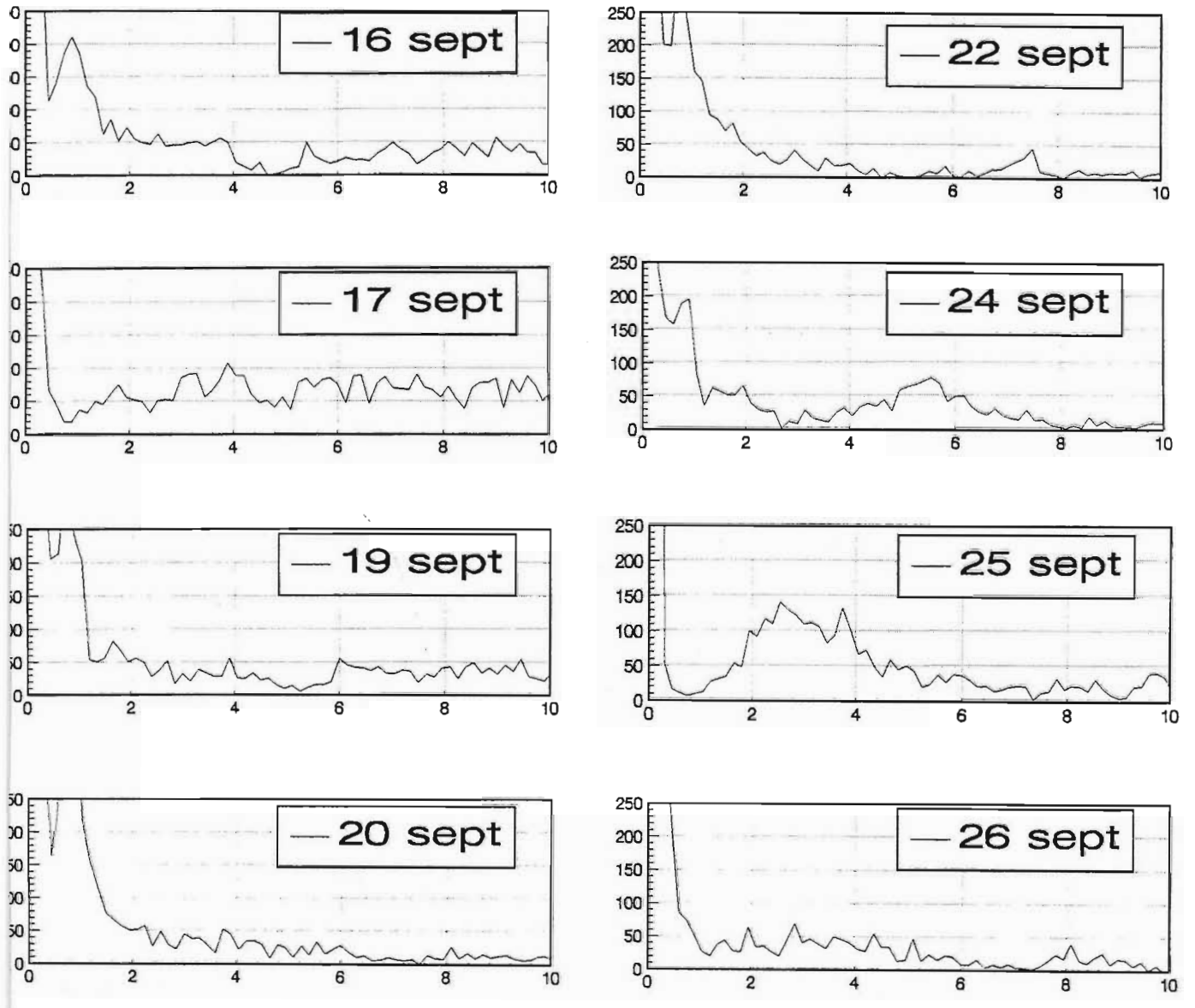

Figure 7.28: Composite of lidar profiles taken at 6:00pm during September 1994.

5km layers is striking. Although there does seem to be some development at the 5km (24 September) and 3km (25 September) altitude ranges, the behaviour is more erratic as compared to June and the respective layers seem much broader. The September 25 3km layer for example, is approximately 2km thick.

(Note that from the raw data, we can only deduce that layers are present, their altitude and thickness. We will need to plot scattering ratios and/or extinction coefficients to determine the relative densities of the layers in question.)

At this stage it was suspected that two factors could have contributed to the difference in aerosol profiles (as far as altitude is concerned).

(i) In winter it is not uncommon for multiple temperature inversion layers to exist in Durban (personal correspondence - Prof. Roseanne Diab). This would account for stratification of aerosols and the manifestation of multiple well defined stable layers. This condition is not prevalent in Spring.

(ii) The sugar cane burning campaign began in early June. The loading of the atmosphere would therefore be different early and later on into the campaign.

These factors do not explain the origin of the aerosols. However point (i) alludes to the cause of the multiple layer structure in June.

Before scattering ratios and extinction coefficients are calculated we need to understand the formation of the multiple layers in June. To do this we use the temperature profiles obtained by radiosonde launches at midnight at Louis Botha airport some 20km south of Durban. The radiosondes are balloon-borne instruments which are capable of measuring temperature, humidity, wind speed and direction as a function of altitude. These values are telemetered back to a receiver on the ground. The maximum altitudes are limited only by the range of the balloons which is typically 20km. In exceptional cases balloons are known to reach altitudes of the order of 30km before they burst.

It should be pointed out that although the lidar profiles were taken $\approx$

6 hours before the radiosonde data, the nighttime temperature profiles are known to be very stable hence comparisons between the two are fairly meaningful.

Radiosonde data

In order to get some feel for the structure in the temperature profiles, we plotted the profiles for the days of interest from the radiosonde data and then marked off regions exhibiting a change in the gradient of the temperature curve. It is assumed that a different gradient is indicative of different atmospheric conditions.

To clarify the procedure we plotted the temperature profile for 16 June 1994 and indicated by means of panels the regions having different temperature gradients. This is shown in figure 7.29.

In the analysis to follow we will ignore the aerosol layer at $\approx$ 1km since it is known that these aerosols are due to local pollution and this layer is strongly decoupled from the higher layers.

From figure 7.29 we see that there are four well defined regions between 2km and 10km. These are :

i) between 3.2km and 4.4km

ii) between 4.4km and 5.8km

iii) between 5.8km and 7.5km and finally

iv) from 7.5km upwards.

We now undertake exactly the same analysis for 6 days in June viz. 14, 15, 19 and 20, 23 and 29. This would enable us to detect trends in the behaviour of the temperature profile (if any). Figure 7.30 and 7.31 show the six plots together with the regions having different temperature gradients. It is interesting to note that on every day shown with the exception of June 20, there are well demarcated regions. These regions correspond surprisingly

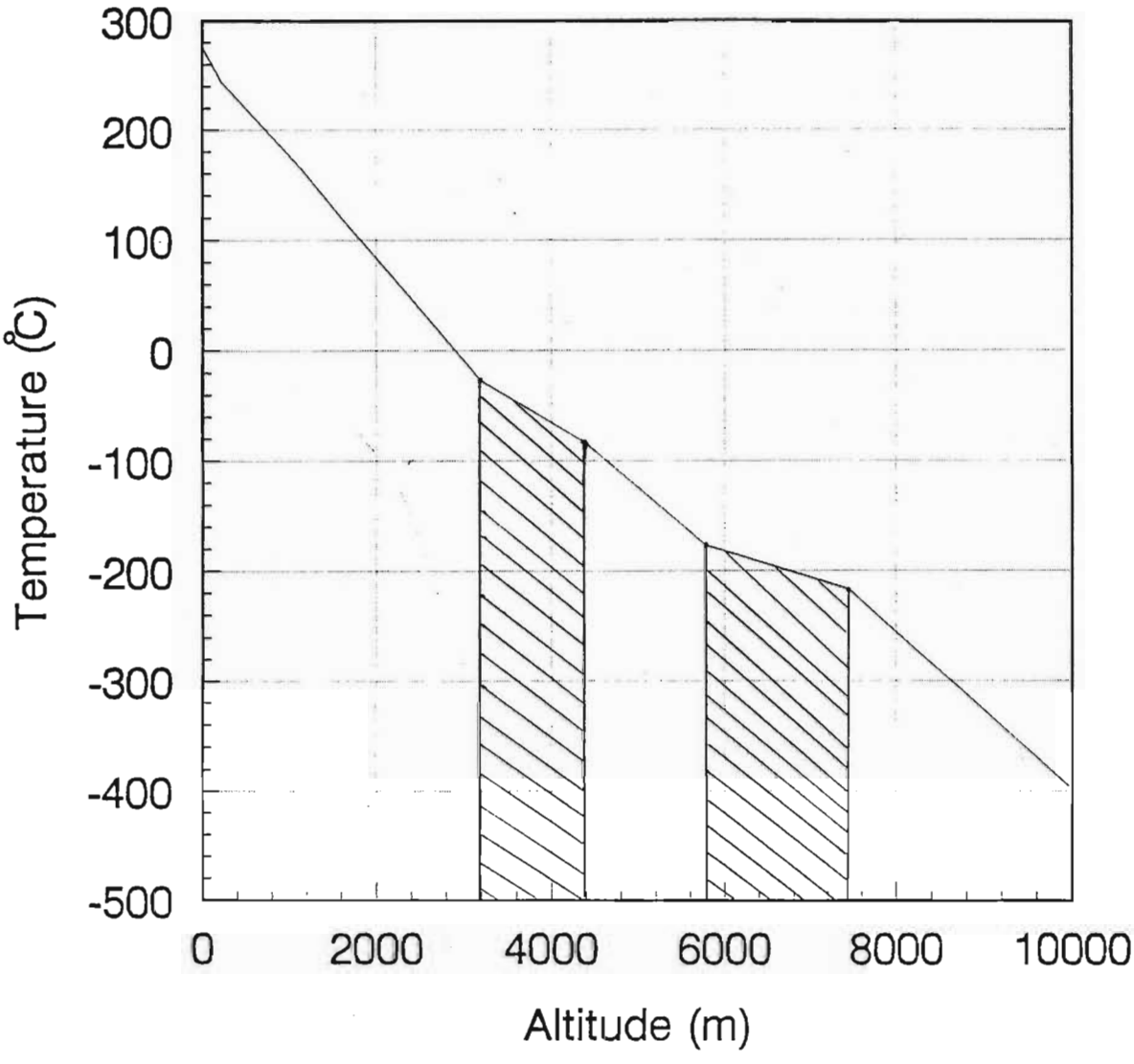

Figure 7.29: Temperature profile for 14 June 1994 with regions of different gradients superimposed

well with the four regions indicated on the profile for June 14. The first two regions that we see (that between 3.2km and 4.4km and that between 4.4km and 5.8km) correspond with the two aerosol layers found at these altitudes.

The stability of form (and altitude) of these regions of constant temperature gradients account very well for the stability in altitude and relative independence of the aerosol layers detected during June. The picture for September looks quite different.

Figures 7.32 and 7.33 show the radiosonde profiles for 6 days in September, again with regions of constant temperature gradients indicated.

We see that apart from the profiles for September 19 and 20 which show similar regions to those in June, there is no stability in the form of the temperature profiles. This accounts for the lack of constant structure in the September lidar data. Evidently, mixing between the layers is taking place during this period and this destroys the altitude structure in the aerosol profiles that might otherwise manifest itself under stable conditions.

The encouraging aspect of the observed temperature regions is that they correspond well with the observed lidar profiles. For example, looking at the temperature profile for September 24, we would expect aerosols to be found in one of three well defined regions : between 2.4km and 5.0km; between 5.0km and 7.6km or between 7.6km and 9.6km. The aerosol peak seen in the lidar profile (figure 7.28) between 4km and 8km is found exactly where the shaded temperature region is in figure 7.33.

Also, on the 25 September, we would expect from the temperature profile to see an aerosol layer between 2.4km and 5.8km or between 5.8km and 8km. The very dense aerosol layer that we observe (see figure 7.28) is found between 1.6km and 6km.

We can conclude from the temperature profiles that altitudes at which changes in the gradient of the temperature profiles take place form the boundaries for regions of constant temperature gradients. It is in these regions that aerosol layers are found. In June the temperature structure over Durban is very stable for the entire month i.e. the temperature regions are found at approximately the same altitudes over the entire period. This explains the

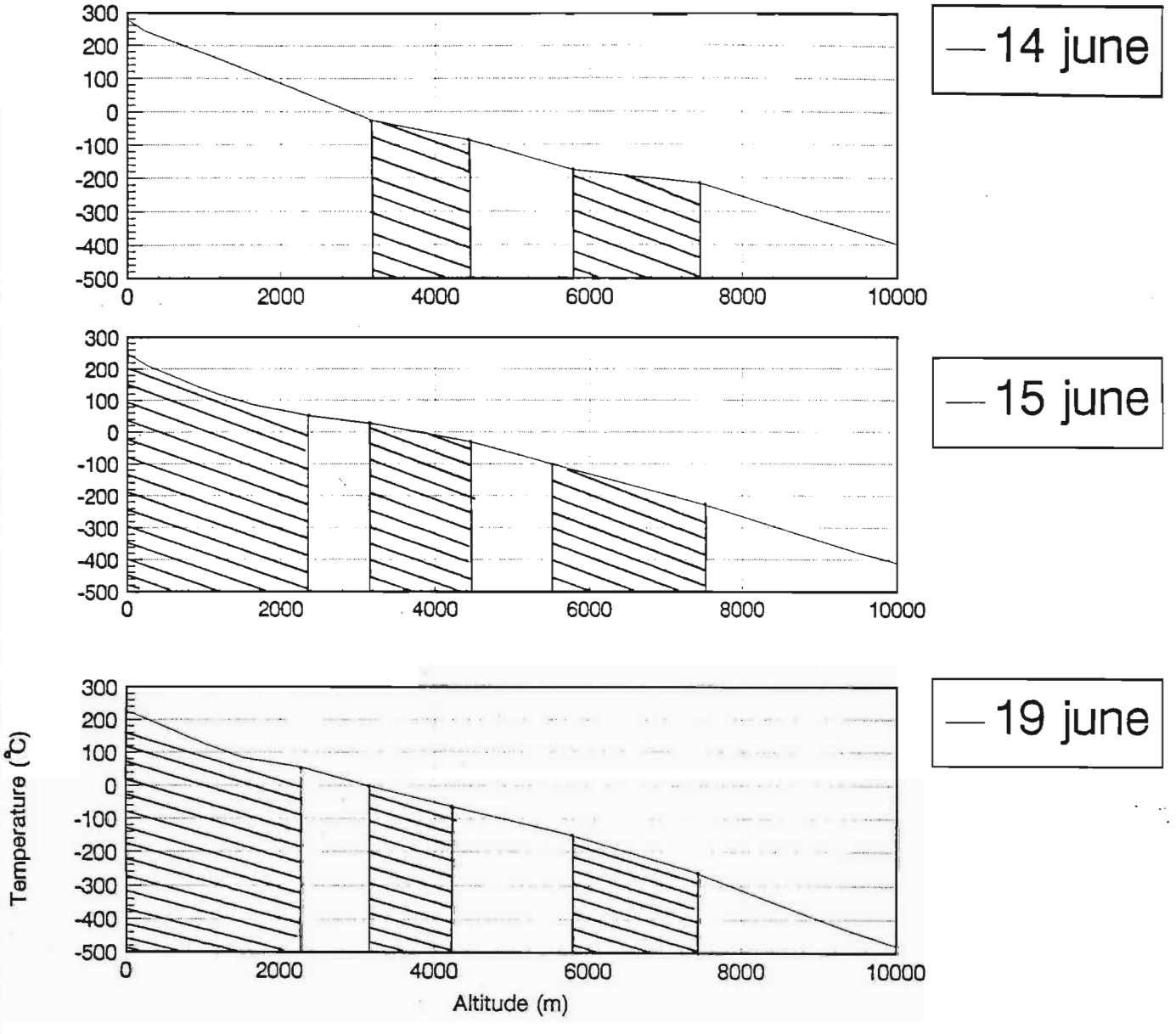

Figure 7.30: Temperature profiles for 14, 15 and 19 June 1994 as taken from radiosonde data - temperature regions superimposed

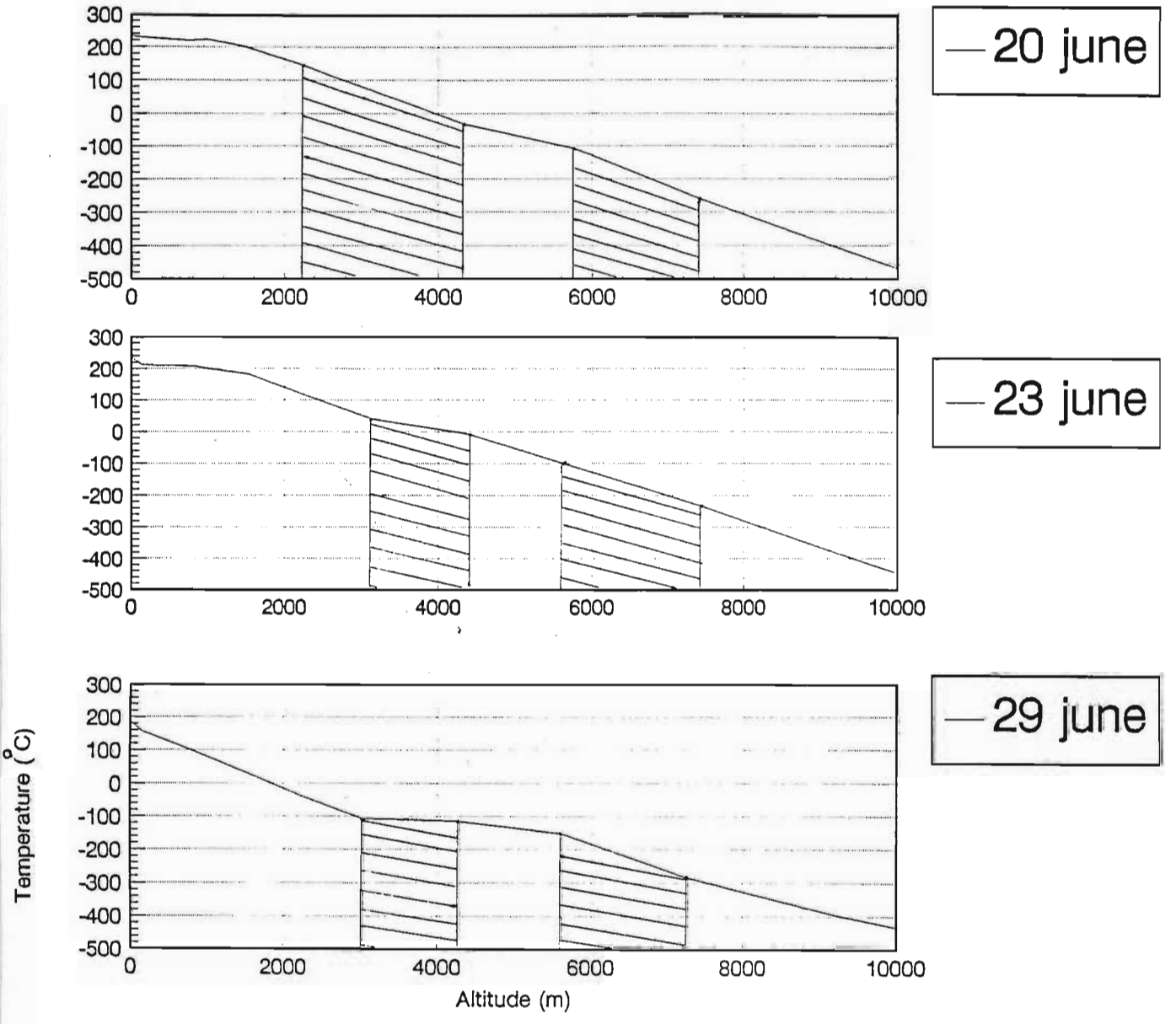

Figure 7.31: Temperature profiles for 20, 23 and 29 June 1994 as taken from radiosonde data - temperature regions superimposed

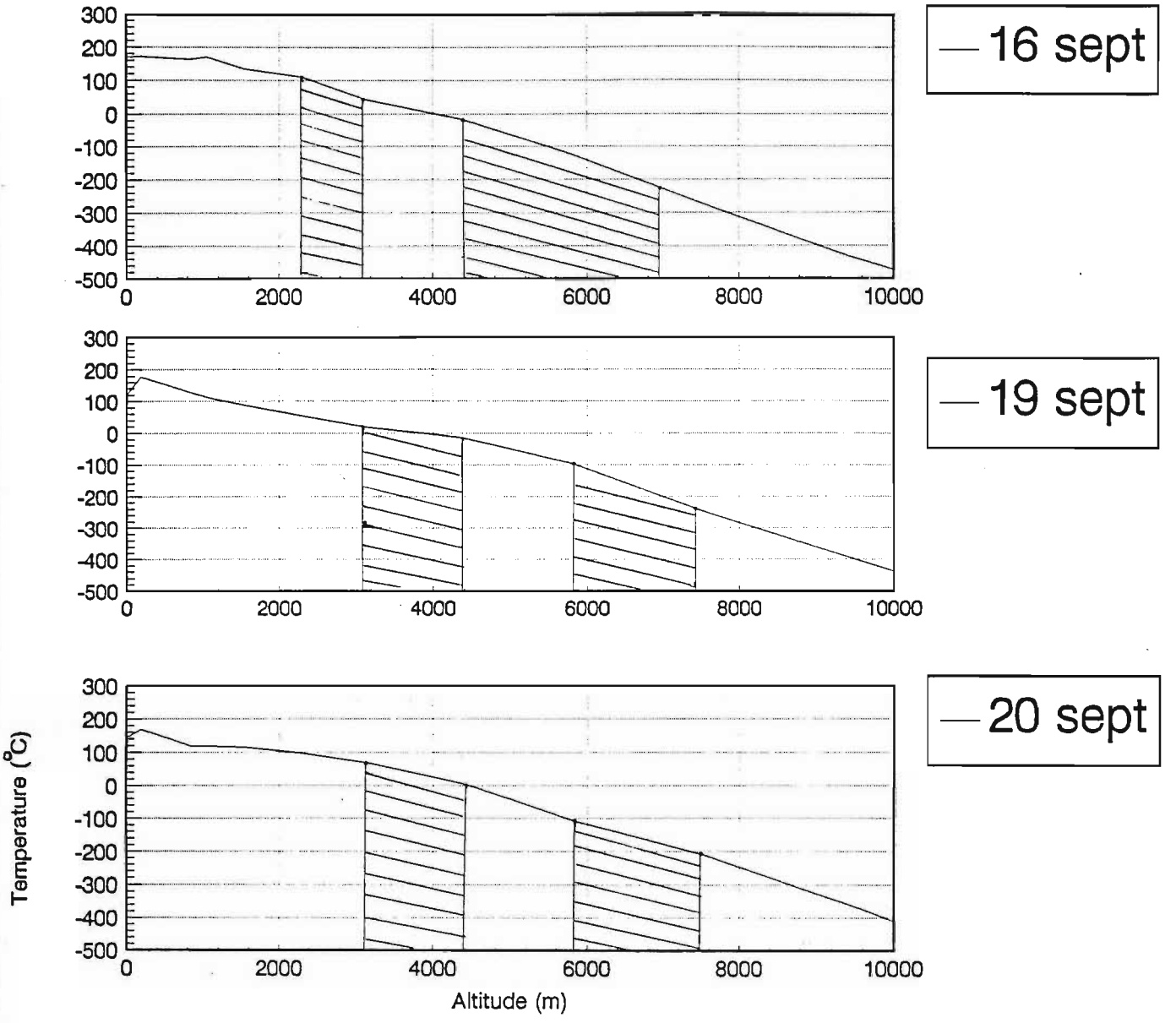

Figure 7.32: Temperature profiles for 16, 19 and 20 September 1994 as taken from radiosonde data - temperature regions superimposed

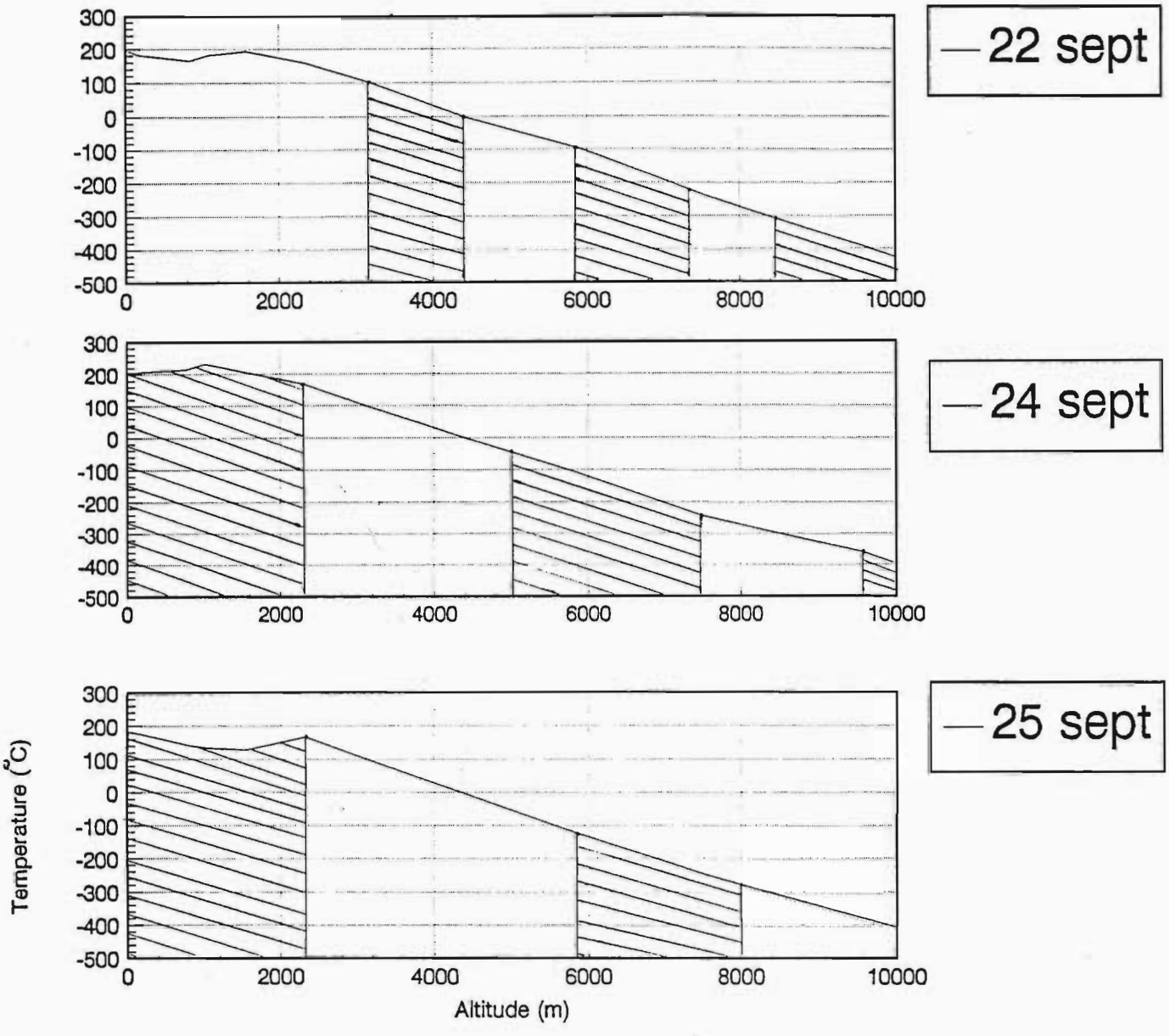

Figure 7.33: Temperature profiles for 22, 24 and 25 September 1994 as taken from radiosonde data - temperature regions superimposed

fact that we see well defined aerosol layers at constant altitudes viz. $\approx$ 3km and $\approx$ 5km.

Based on the lack of stability in altitude for the September temperature profiles, we can safely conclude that mixing is taking place. This would prevent the formation of aerosol layers at constant altitudes. This is indeed what we see. Since the burning campaign had reached its end in September, we should expect that the aerosol loading of the atmosphere would be higher than in June (the start of the campaign). This can be explained by virtue of the fact that the stable layers in June (and possibly in July and August) serve to trap the aerosols produced. Towards the end of September, although mixing is starting to take place, the aerosols produced during the campaign which have been trapped, result in a higher loading. Hence we should expect higher scattering ratios and extinction coefficients than those observed in June. Based on where (altitude-wise) these values are higher, we can tell whether the transport of aerosols is predominantly upwards, downwards or if the mixing is uniform.

Scattering ratios

We then calculated the scattering ratios for June and September i.e. for the same days for which the raw data was presented in figures 7.27 and 7.28. The data was pinned down at 1.8km for all the plots. This altitude was chosen as a safe guesstimate. In any event, we shall concentrate solely on the relative magnitudes of the signals between June and September and the positions of the peaks. The criticality of the choice of the pinned altitude therefore becomes a non-issue. For a more quantitative analysis of the aerosols, we will calculate the extinction coefficients in the section to follow.

The calculated scattering ratios for June and September are shown in figures 7.34 and 7.35 respectively. The x axis represents the altitude in meters and the y axis the scattering ratios in arbitrary units.

Referring back to figure 7.27 (the raw data for June) we see that the scattering ratio profiles show the "3km" and "5km" layers quite clearly on the days on which they are well defined in the raw data viz. 15, 19, 20, 23 and to a lesser extent 24 June. It should be noted that in the event the

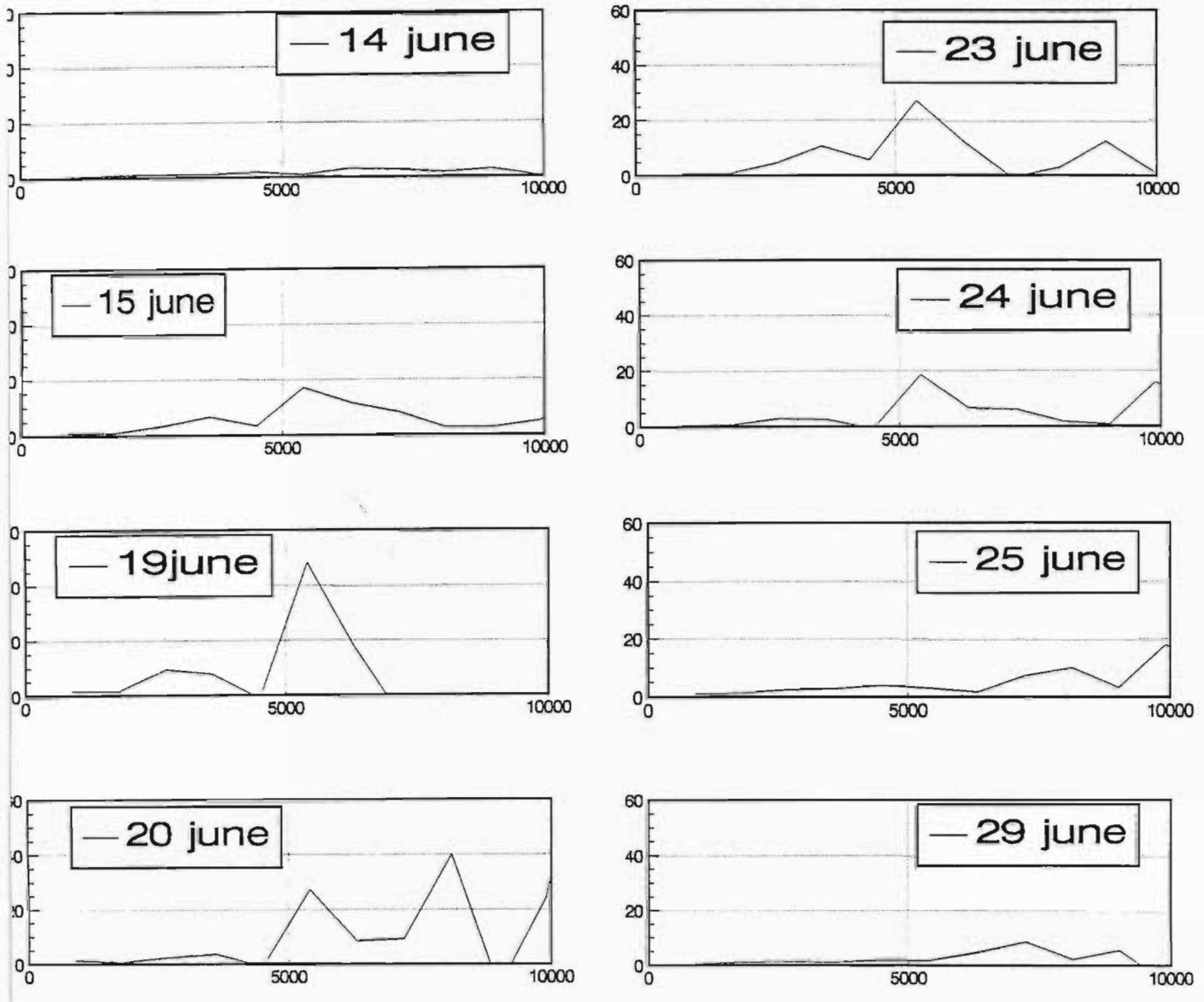

Figure 7.34: Sequence of scattering ratios (arb. units) versus altitude (m) for June 1994

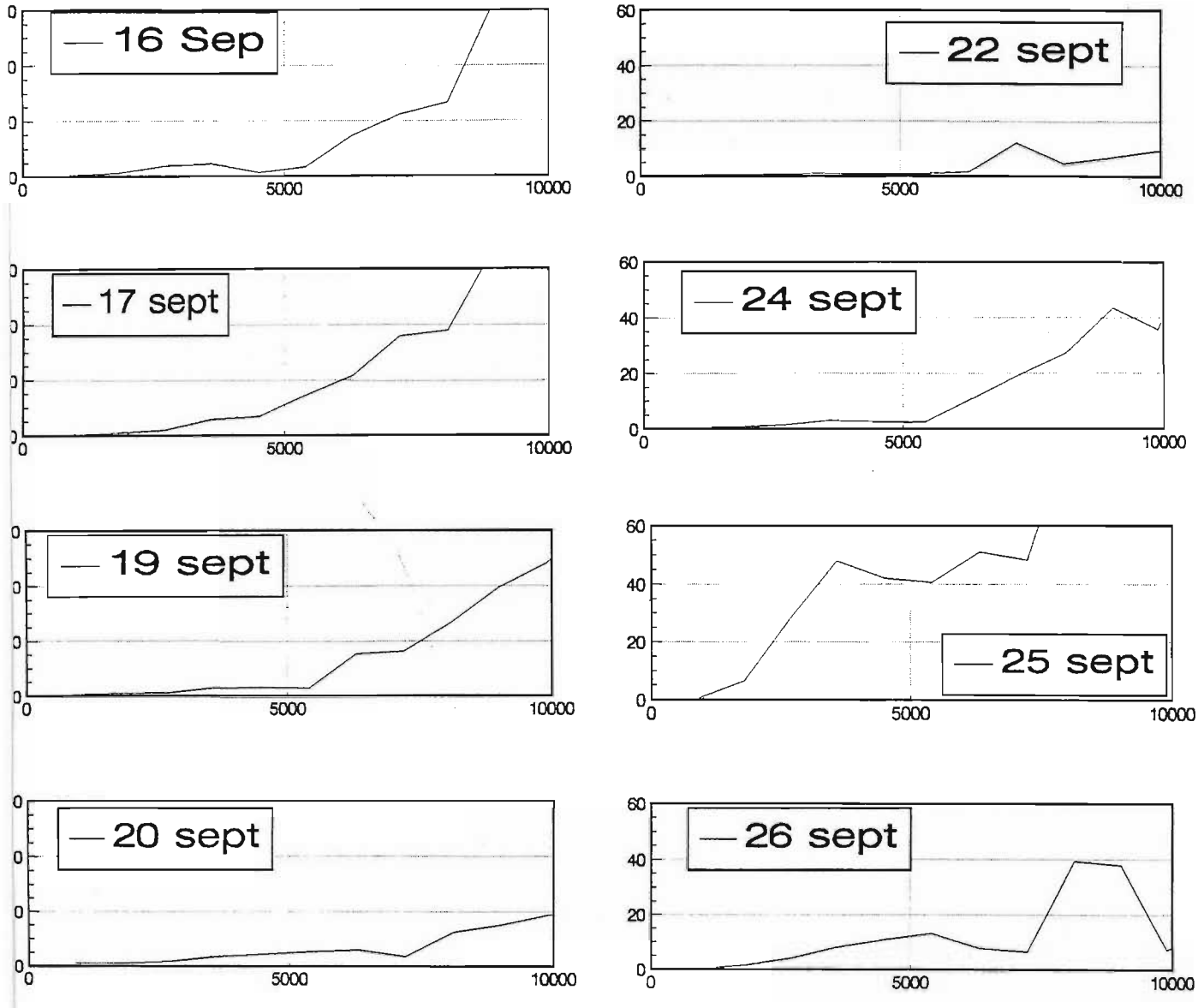

Figure 7.35: Sequence of scattering ratios (arb. units) versus altitude (m) for September 1994

return from two altitudes in the raw data is the same (or comparable) e.g. the raw data profile for June 19, since one would expect a smaller signal from a higher altitude due to beam attenuation, comparable returns in all cases would indicate a higher density at the higher altitude. This would explain the higher scattering ratio. This is also the case for the plot of June 25.

The scattering ratios for September are even more interesting. The structure low down is not evident (as we would expect). There are however very high values of scattering ratios higher up in altitude (between 8km and 10km for instance). For the September 25 profile this extends from $\approx$ 1km. The conclusion we can draw from this is that the aerosols have been transported upwards in most cases in September. The atmospheric mixing has destroyed any structure in the profiles.

As a method that can be used to get a general picture of densities, the scattering ratio is a good one. However, the Klett inversion method which yields extinction coefficients, is a much more sensitive technique. It is capable of bringing out the fine structure in the lidar profiles as well as yielding an absolute value which is directly related to the absolute density of the aerosols. We now calculate the extinction coefficients for the sequence of profiles in June and September.

Extinction coefficients

The calculated extinction coefficient profiles for June and September are shown in figure 7.36 and 7.37 respectively. The x axis on the plots again represents altitude in meters and the y axis represents the extinction coefficients in km^{-1}.

Looking firstly at the profiles for June (figure 7.36) we see that the two layers ("3km" and "5km") are still visible as in the plots for the 14, 15, 19, 23 and 24 June. What is interesting is that in all cases the extinction coefficient for the "5km" layer is higher than that of the "3km" layer by a factor of ≈ 4 times. What is also interesting is that this technique resolves structure higher up in altitude as well. On the 14, 15, 19, 23, 24 and 29 June we detect high density aerosol layers between 8km and 10km. This corresponds well with the temperature structure in June (figures 7.30 and 7.31). It is encouraging

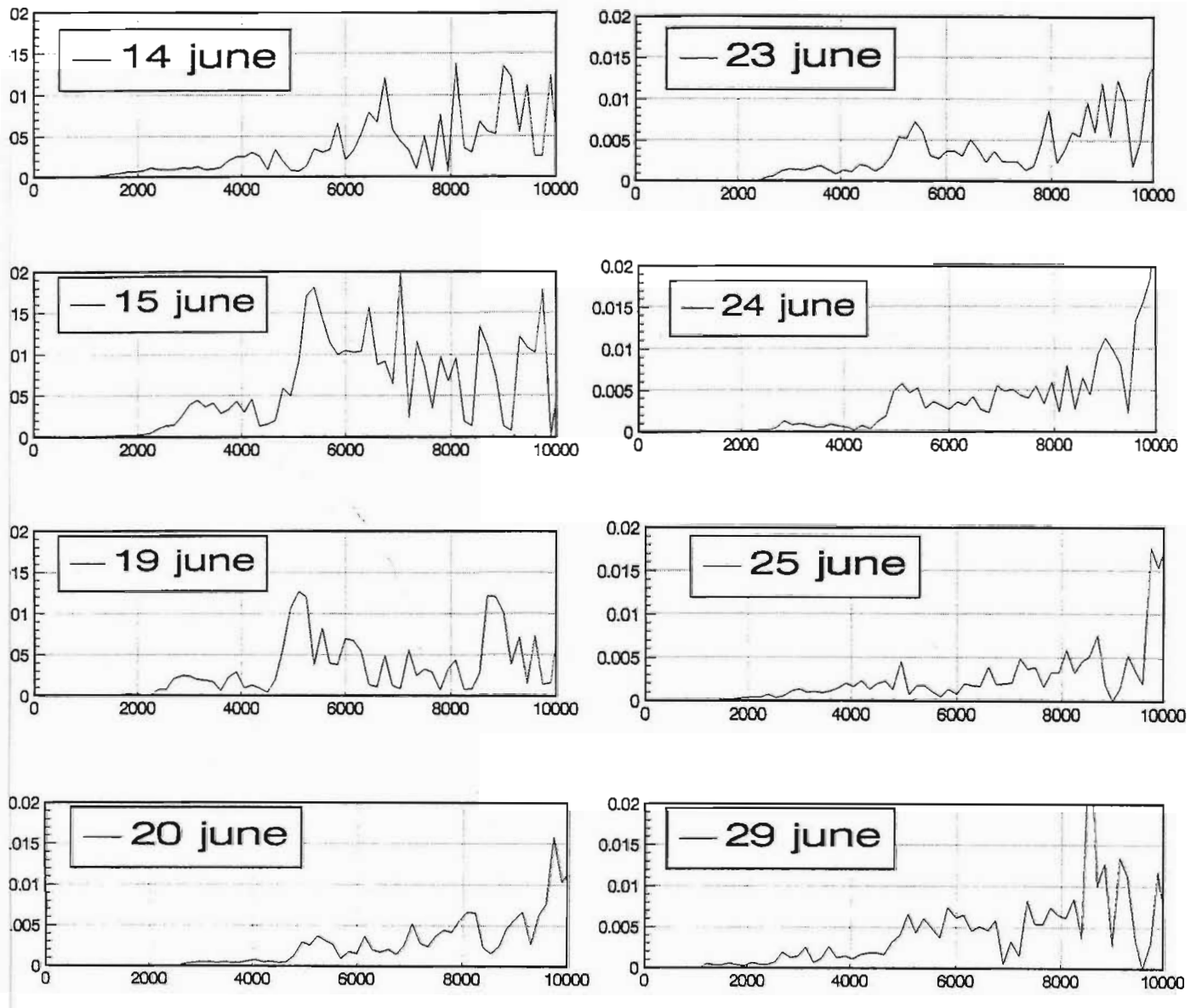

Figure 7.36: Sequence of extinction coefficients (km^{-1}) versus altitude (m) for June 1994

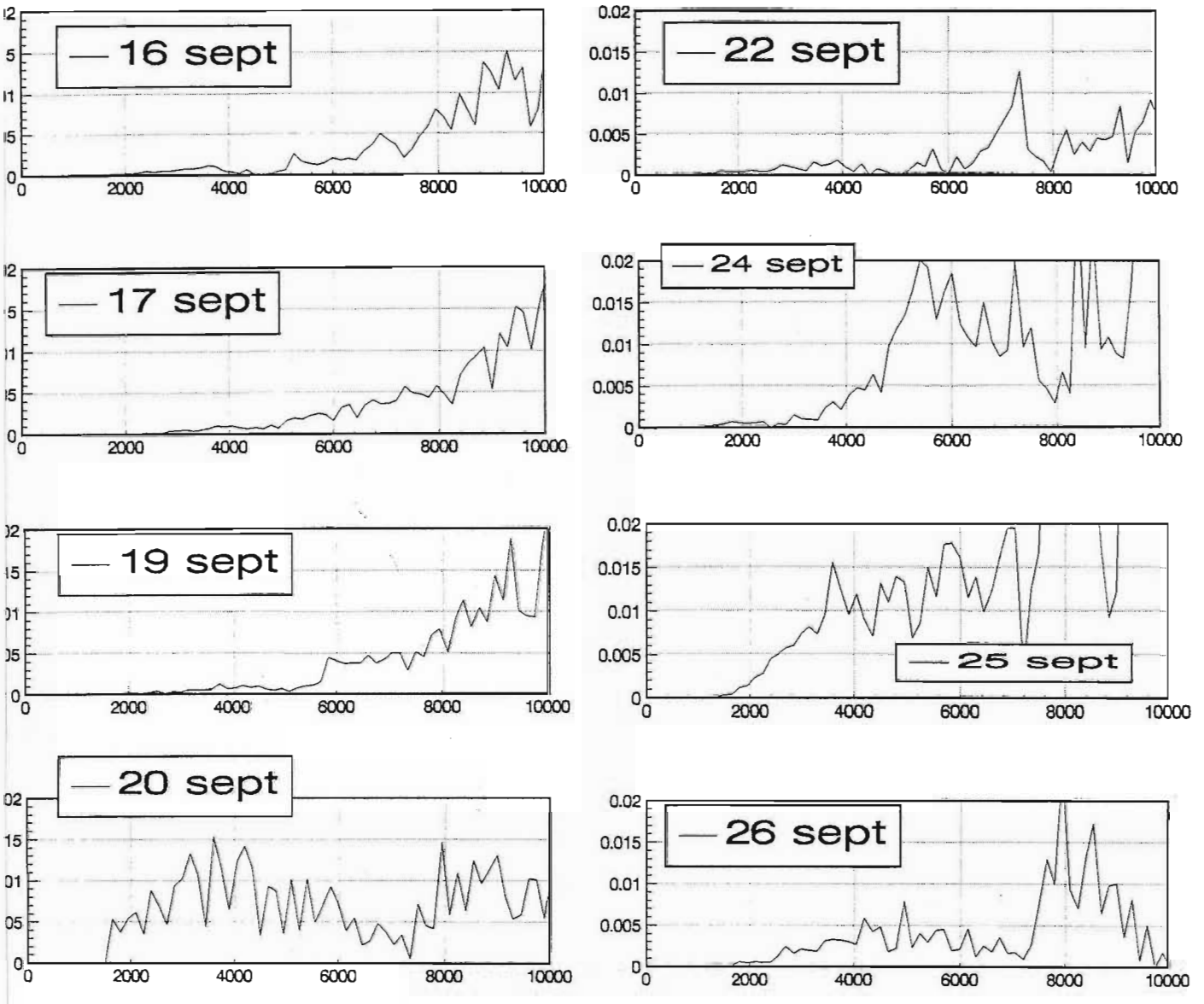

Figure 7.37: Sequence of extinction coefficients (km^{-1}) versus altitude (m) for September 1994

to note that the sensitivity of this technique is such that features not easily discernible in the raw data can still be resolved.

Examining the extinction coefficient profiles for September (figure 7.37) we see very high aerosol loading on the 24 and 25 September. This is (as we expect) based on the nature of the raw lidar data for these days. Perhaps slightly surprising is the loading on the 20 September and that on the 26 September at high altitude.

From the extinction coefficient profiles it would seem as if the aerosol loading reached a maximum on 25 September. To determine the long term trend in the aerosol behaviour, we define the Low Altitude Aerosol Coefficient (LAAC).

Low altitude aerosol coefficient

This coefficient was defined as the sum of all the scattering ratios from 1km to 10km. In effect this is simply an integrated index for aerosol loading of the atmosphere. We are therefore in a position to identify days on which the aerosol loading of the atmosphere was high and those on which it was low. The value of the LAAC is given in arbitrary units.

Although the primary reason for the defining of this coefficient was to determine the long term loading trends due to ground emissions, the LAAC can also be used as a comparison between the aerosol data from the lidar system with total column ozone values measured with the SAOZ instrument at Durban.

The SAOZ (Système d'Analyse par Observations Zenitales) is a fully automated measuring system. It uses a fixed-grating spectrometer together with a 512-element diode array to monitor concentrations of atmospheric trace gases (e.g. O_3) by observing the light scattered into its field. The system was developed in 1987 by Pommereau and Goutail for monitoring a wide range of wavelengths simultaneously. The range of wavelengths that can be measured runs from 290nm to 600nm. The SAOZ is a vertically looking instrument and measures solar light scattered by Rayleigh scattering. This detected light contains information on the atmospheric absorption bands and

on subtraction of a pure solar spectrum from the detected signal, concentrations of the major and minor constituents can be deduced. These signals are then used to calculate total column values for O_3, NO_2, O_4, H_2O, OClO and BrO.

It is well established (see Hofmann and Solomon (1989)) that aerosols in the atmosphere act as scavengers for single oxygen atoms and therefore prevent ozone from forming.

The ozone plots presented were obtained courtesy of Dr. E. Mravlag of the Space Physics Research Institute, University of Natal, Durban.

Figures 7.38 and 7.39 show the LAAC for days 160 to 200 and days 250 to 280 respectively as well as the corresponding ozone values for the respective days. The total column ozone values are presented in Dobson Units (D.U.).

Looking at the trend in the LAAC values we see a general increase towards September with a peak in the coefficient towards the end of September (day 268). The fall off towards early October is as we expect.

Comparing the LAAC and O_3 values between day 160 and 200 we detect a striking anti-correlation between the two data sets. Where the LAAC decreases, the O_3 values increase and vice versa. This would seem to imply that an increase in aerosols is accompanied by a decrease in ozone.

In figure 7.39 it would seem as if the same trend persists. The increase in the LAAC on day 268 is accompanied by a decrease (albeit small) in the ozone concentration. Also, the increase in the LAAC on day 267 corresponds to a low ozone value. Unfortunately, the relationship between the two values is not as obvious as for the period 160 to 180.

Unfortunately, the observance of an anti-correlation on some days and/or the lack thereof on others raises more questions than it answers at this stage. Cognisance should be taken of the fact that the LAAC represents an integrated aerosol count up to 10km (tropospheric) and the SAOZ produces a total column ozone value which incorporates the tropospheric as well as the stratospheric contribution. It is well known (see A D' Altorio et al. (1992) and A. Adriani et al. (1987)) that there exists an anti-correlation between

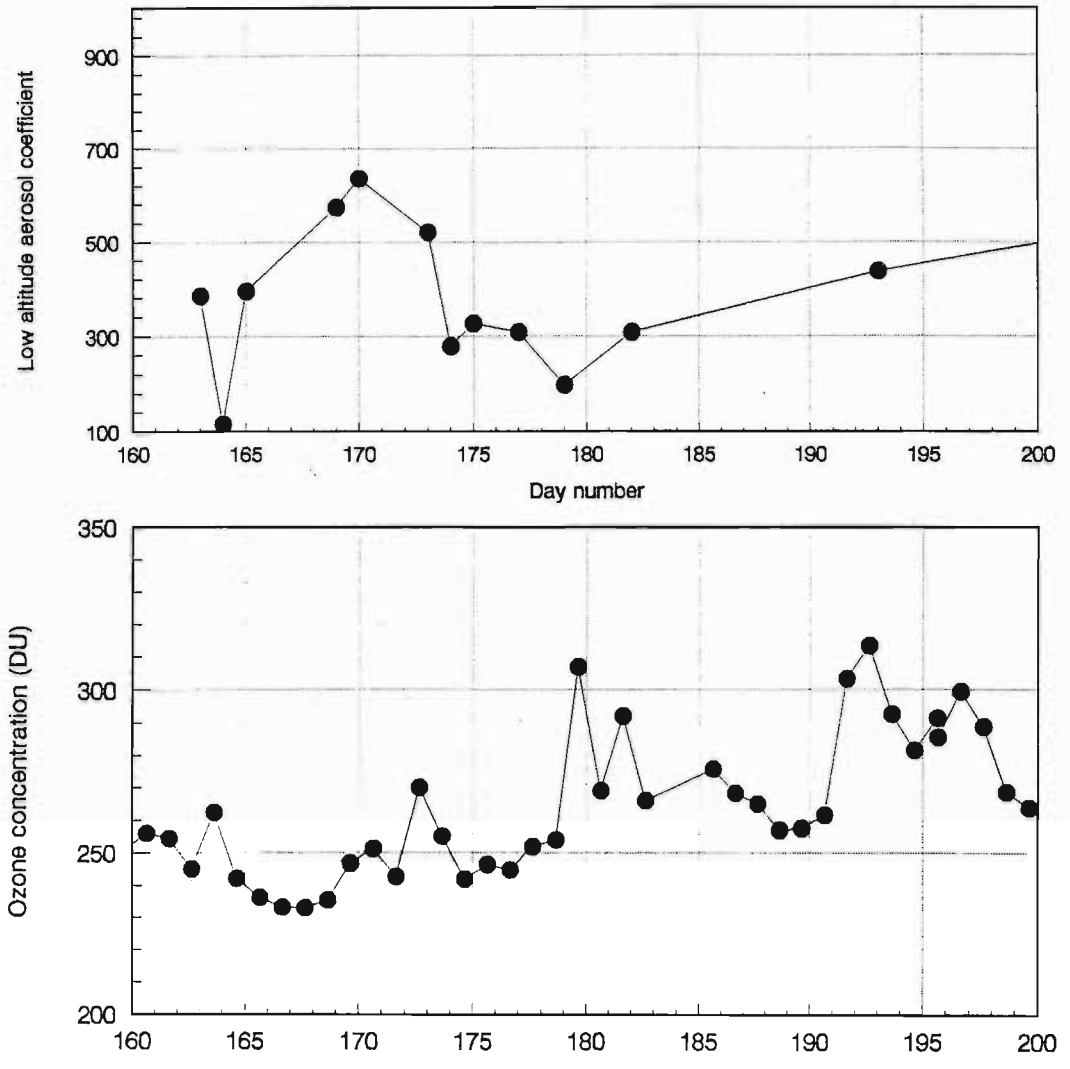

Figure 7.38: LAAC and O_3 concentrations for days 160 to 200

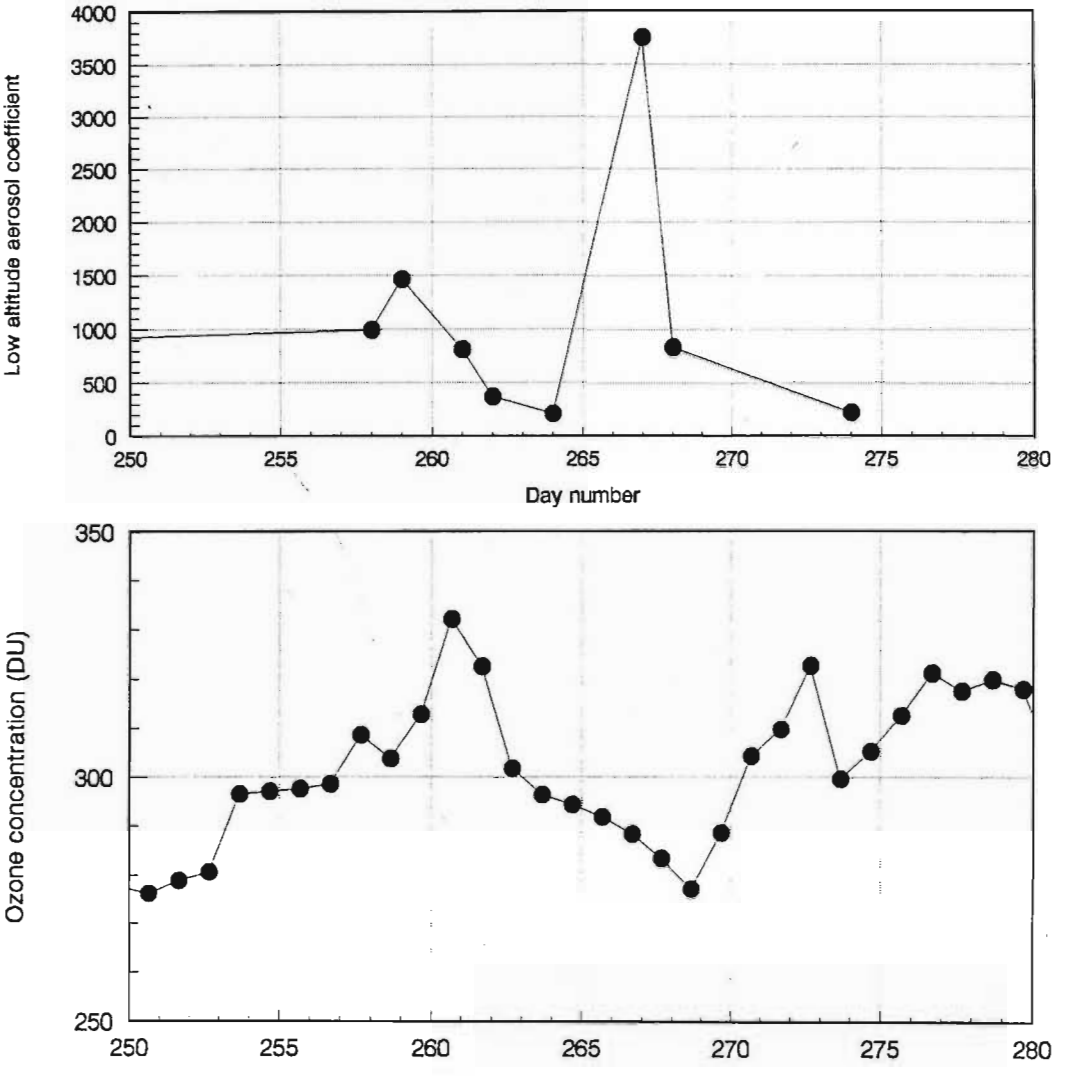

Figure 7.39: LAAC and O_3 concentrations for days 250 to 280

the integrated aerosol count and the total ozone count from the ground up to $\approx$ 30km. We can assume that since the sugar cane burning has resulted in very high levels of aerosols, these low altitude aerosols dominate those from higher up. Hence the LAAC can be used as an indicator for the total aerosol loading up to 30km.

This being the case, we can then easily explain the anti-correlation (or lack thereof) between the two values, provided that the change in ozone that we observe is also dominated by the change in the tropospheric component. However, this is not strictly correct since on average, the tropospheric ozone count is of the order of 15% of the maximum and the maximum deviation that we see in the total column ozone values is of the order of 25%. This would seem to suggest that the change is primarily taking place in the stratosphere. We can therefore conclude that although there is an anti-correlation on some days between the LAAC and the total column ozone values, we cannot categorically say that this is due to the increase or decrease in aerosols. An interesting comparison would be between the LAAC and an ozone profile spanning the same altitude range (0km to 10km). Since this data (and indeed the instrument to gather this data) is not available to us at this time, this could serve as a subject for future study.

7.9.2 Conclusions

From the low altitude lidar data we have seen well defined aerosol layers in June 1994. These aerosol layers are decoupled from each other and are found in stable atmospheric regions defined by regions of constant temperature gradients. The aerosols exhibit both short term (15 minutes) as well as long term behaviour.

In September these stable layers are not constant in altitude indicating atmospheric mixing. We have seen from the scattering ratio profiles and the extinction coefficients that the aerosol loading of the atmosphere increases towards the end of September.

Since the sugar cane burning campaign started in June on the Natal coast, we can conclude that the "3km" and "5km" aerosol layers are not local and are indeed the products of long range transport. Also, the campaign having

ended in September, we see enhanced aerosols during this period. These then start to disperse in early October.

Finally we see good anti-correlation between the LAAC and total column ozone values over Durban in June (days 160 to 180). However this anti-correlation is not as clear for the rest of the data set. We cannot draw any definite conclusions as to the reasons for this trend or the influence of the low altitude aerosols on the total column ozone values. This certainly bears further investigation.

Chapter 8

Conclusions and Summary

This thesis investigated :

(i) the effect of the refraction of light due to a cylindrically colliding shock structure in the CSL and attempted to understand/determine how the refractive (lensing) properties changed as the various factors were changed,

(ii) the scattering and reflection of light due to atmospheric aerosols using a ground-based lidar system, in an attempt to characterise the behaviour of low and high altitude aerosols over Durban.

During the course of the research into these two effects, valuable experience was gained with different types of laser systems. With hindsight, we can say that the outcome of the experimentation has been three-fold :

(a) Acquisition of laser experience,

(b) Scaling up the colliding shock lens and

(c) Detecting and studying the behaviour of low and high altitude aerosols.

8.1 Acquisition of laser experience

Several types of laser systems have been worked on during the period of involvement with the abovementioned projects. These included solid state lasers (ruby and diode), gas lasers (nitrogen, CO_2 and He-Ne) and liquid lasers (dye laser).

Following is a table describing the characteristics of the lasers used and their respective applications.

Laser	*Pulselength*	*Energy/pulse*	*Wavelength*	*Application*
Ruby	0.05μs	1J	694.3nm	Q-switching
Nitrogen	0.01μs	0.1J	337nm	focussing
Dye	0.5μs	0.5J	589nm	lidar
He-Ne	CW	0.1W ave	632.8nm	alignment
CO_2^*	CW	1W ave	10600nm	focussing
*Diode**	CW	1W ave	859nm	portable lidar

* : lasers worked on but not used in either the CSL or lidar experiments described.

The ruby, nitrogen and He-Ne lasers were all used in the CSL experiments. The spark-gap triggered nitrogen laser formed an integral part of the focussing and imaging of the various CSLs. It was with this laser that the performance of the CSLs was measured. The ruby laser was later used in the Q-switching experiments.

The nitrogen laser was built in-house and extensive experience was gained with the power supply and triggering circuits. This laser was consequently also used for demonstration purposes for undergraduate students. The He-Ne laser mentioned was strictly an alignment tool.

The CW CO_2 laser was recommissioned and it was envisaged that focussing experiments would be conducted at infra-red wavelengths to determine how well the CSL performed. Unfortunately, although some work was done on the power supply and the discharge tube, a lack of funds resulted in the work remaining unfinished. This laser (like the nitrogen laser) was used for teaching purposes.

The flashlamp-pumped dye laser formed an integral part of the transmitter in the lidar system. This too, being a spark-gap discharged system, required constant attention and maintenance. During the involvement with this laser system (a period spanning five years), intimate knowledge of the system was gained. Work was performed on all components including the circulatory system, the power supply, the discharge circuit and the laser head and optics.

It was hoped that a portable lidar system would be developed to study the very low altitude aerosols (10m to 1000m above the ground). This system was designed to use a modulated CW infra-red diode laser as the transmitter. Although the system was not completed, much developmental work went into building and testing the modulated power supply for this laser.

The experimental investigations have afforded the candidate the opportunity to gain hands-on experience with six different laser systems. This experience included the expertise in running, maintaining and reconditioning these systems. Some of this expertise was conveyed to undergraduate science students through teaching practicals and demonstrations.

8.2 Scaling up the colliding shock lens

The initial colliding shock lenses reported by Buccellatto (1993) were millimetric devices. These were hardly useful in industrial laser systems. We conducted experiments to understand how the various factors (electrical diameter, input energy, enclosure, etc) affected the performance (focal length and optical aperture) of the colliding shock lenses. It was found that simply by increasing certain factors (e.g. input energy, ambient pressure and gas density), the *f number* of the CSL can be improved. Enclosing the CSL also showed a marked improvement in the focussing properties. Unlike the aforementioned factors, this effect is not well understood and deserves further investigation. Based on results obtained, we have constructed a CSL having an optical aperture of 1.5cm and a focal length of 1.5m. This is a device which could be used to focus large (industrial scale) laser systems. We have also shown that apart from focussing, the CSL can be used as a cheap, easy to operate, intra-cavity Q-switch.

The work into scaling up the CSL has resulted in the development of a cylindrical colliding shock lens. This lens has successfully line focussed a laser beam having a 1cm diameter. The quality of the focus is however poor and much attention has to be given to this.

Focussing devices with very high energy thresholds and large enough (of the order of 10mm) apertures show serious potential for use in high power laser systems. We have developed two such devices : the one capable of generating point focii and the other line focii. We believe that in the foreseeable future some solid state lenses will be replaced in favour of gas optics of the kind described.

8.3 Lidar studies of high and low altitude aerosols over Durban

The ground-based lidar system designed and operated at Durban uses the elastic scattering technique to determine aerosol profiles over the site. With this system we have been able to study both high and low altitude aerosols (dust particles) in an altitude range from 1km to 80km.

The study has concentrated on the detection and tracking of low altitude aerosols due to sugar cane burning on the Natal coast. It was found that the stability of the atmosphere in June results in very well defined aerosol layers, whereas in September, the lack of stability causes mixing. We introduced a low altitude aerosol coefficient (LAAC) to quantify the atmospheric loading, and it was found that the loading of the low atmosphere (1km to 10km) increases towards the end of the burning season. Attempts were also made to compare the LAAC with the total column ozone values over Durban. Some anti-correlation was noticed but a further study using ozone profiles as a comparison should be carried out.

Of particular interest has been the detection of a very high altitude aerosol layer (at 60km) which is believed to be mesospheric sodium. The presence of this layer was confirmed using SAGE satellite data. This detection rep-

resents the first of its kind by a ground-based lidar system on the Southern African continent.

References

Adriani A, Fiocco G, Gobbi G. P and Congeduti F.
J. Geophys. Res. **92**, 8365 (1987).

Babcock R. et al.
IEEE J. QE. **12**, 29 (1976).

Bach G. G and Lee J. H.
J. Fluid Mech. **37**, 513 (1969).

Bacon M, Campbell R. N, Cunningham P. F and Michaelis M. M.
J. Appl. Phys. **66**, 1075 (1989).

Buccellato R, Lisi N and Michaelis M. M.
Optics Communications **101**, 350 (1993).

Buccellato R.
Refractive Effects in Phase Objects and Associated Phenomena. University of Natal Doctoral thesis. (1994).

Chenais-Popovics C et al.
Phys. Rev. Lett. **59**, 19 (1987).

Chisnell R. F.
J. Fluid Mech. **2**, 105 (1957).

Cook C. S, Bethke G. W and Conner W. D.
Appl. Optics **11**, 1742 (1972).

Curcio J. A and Knestrick G. L.
J. Opt. Soc. Am. **48**, 686 (1958).

D' Altorio A, Masci F, Visconti G, et al.
Geophys. Res. Lett. **19**, 393 (1992).

Daido H et al.
Laser and Ptcle Beams **11**, 109 (1993).

Eltermann L.
J. Geophys. Res. **56**, 509 (1951).

Evans M. E and Harlow F. H.
Los Alamos Scientific Laboratory Report **LA - 2139** (1957).

Fenn R. W.
Appl. Optics **5**, 293 (1966).

Fiocco G and Smullin L. D.
Nature **199**, 1275 (1963).

Fiocco G and Grams G.
J. Atmos. Sci. **21**, 323 (1964).

Flagg R. F and Glass I. I.
Research Notes - Instit. of Aerospace Studies, University of Toronto, 2282 1968.

Friedland S. S, Katzenstein J and Zatzick M. M.
J. Geophys. Res. **61**, 415 (1956).

Gentry R. A, Martin R. E and Daly B. J.
J. Compt. Phys. **1**, 87 (1966).

Gibson A. J and Sandford M. C. W.
J. Atmos. Terr. Phys. **33**, 1675 (1971).

Glass I. I and Heuckroth L. E.

The Physics of Fluids **2**, No. 5, 542 (1959).

Glimm J.
Comm. Pure Appl. Math **18**, 697 (1965).

Granier C, Jegou J. P and Megie G.
Geophysical Research Letters **12**, 655 (1988).

Guderley G.
Luftfahrt-forsch **19**, No. 9, 302 (1942).

Hamamoto M, Muraoka K and Akazaki M.
Jpn. J. Appl. Phys. **20**, 443 (1981).

Hamilton P. M.
Air and Water Pollut. Int. **10**, 427 (1966).

Hecht E and Zajac A.
Optics 2nd ed. (Addison-Wesley, Philipines, 1974).

Hertzberg A and Kantrowitz A.
J. Appl. Phys. **21**, 874 (1950).

Hirish M. N and Oskam H. J.
Gaseous Electronics Vol. 1 1st ed. (Academic Press, London, 1978).

Hirono M, Fujiwara M, Shibata T and Kugumiya N.
J. Atmos. Terr. Phys. **46**, 1147 (1984).

Hofmann D. J and Solomon S.
J. Geophys. Res. **94**, 5029 (1989).

Houghton J. T.
The Physics of Atmospheres 2nd ed. (Cambridge University Press, 1977).

Houston D. J and Evans B. T. N.
Photonics Spectra 93 (1987).

Hulburt E. O.
J. Opt. Soc. Amer. **27**, 337 (1937).

Johnson E. A, Meyer R. C, Hopkins R. E and Mock W. H.
J. Opt. Soc. Amer. **29**, 512 (1939).

Kent G. S, Clemesha B. R and Wright R. W.
J. Atmos. Terr. Phys. **29**, 169 (1966).

Kirchoff V and Clemesha B. R.
Atmos. Terr. Phys. **35**, 1493 (1973).

Klett J. D.
Appl. Optics **20**, 211 (1981).

Knystautas R, Lee B. H. K and Lee J. H. S.
Shock Tube Symposium, The Physics of Fluids Supplement I 165 (1969).

Kuppen M.
The Establishment of a Ground-Based Lidar System at Durban University of Natal Masters thesis. (1992).

Landau L. E and Lifshitz E. M.
Fluid Mechanics 3rd ed. (Pergamon Press, 1959).

Lax P. D.
Comm. Pure Appl. Math **7**, 159 (1954).

Lee J. H and Lee B. H. K.
Phys. Fluids **8**, No. 12 2148 (1965).

Lee B. H. K.
Ph.D Thesis McGill University (1966).

Ligda M. G. H.
Proc. Conf. Technol. 1st, Calif. 63 (1963).

Lisi N, Michaelis M. M, Buccellato R, Kuppen M and Prause A.

Appl. Optics **34**, No. 6 942 (1995).

Maiman T. H.
Nature **187**, 493 (1960).

Matsuo H.
Phys. Fluids **22**, 1618 (1979).

Matsuo H and Nakamura Y.
J. Appl. Phys. **51**, 3126 (1980).

Matsuo H and Nakamura Y.
J. Appl. Phys. **52**, 4503 (1981).

Matsuo H, Ebihara K and Ohya Y.
J. Appl. Phys. **58**, 2487 (1985).

Matsuo H, Ohya Y, Fujiwara K and Kudoh H.
J. Comput. Phys. **75**, 384 (1988).

McClung F. J and Hellwarth R. W.
J. Appl. Phys. **33**, 828 (1962).

Measures R. M.
Laser Remote Sensing 2nd ed. (John Wiley and Sons, N.Y., 1984).

Megie G and Blamont J. E.
Planet. Space Sci. **25**, 1039 (1977).

Megie G, Bos F, Blamont J. E and Chanin M. L.
Planet. Space Sci. **26**, 27 (1978).

Meintjies K.
University of the Witwatersrand Masters thesis. (1975).

Michaelis M. M, Waltham J. A and Cunningham P. F.
Opt. Laser Technol. **23**, 283 (1991a).

Michaelis M. M, Cunningham P. F, Notcutt M and Waltham J. A.
Laser and Ptcle Beams **9**, 641 (1991b).

Michaelis M. M et al.
Nature **353**, 547 (1991c).

Michaelis M. M, Lisi N, Kuppen R, Buccellato R and Prause A.
Laser and Ptcle Beams **12**, 1 (1994).

Muraoka K, Hamamato M and Akazaki M.
Jpn. J. Appl. Phys. **19**, 293 (1980).

Neumann J. von and Richtmyer R. D.
J. Appl. Phys. **21**, 232 (1950).

Northam G. B, Rosen J. M, Melfi S. H, Pepin T. J et al.
Appl. Optics **13**, 2416 (1974).

Payne R. B.
J. Fluid Mech. **2**, 185 (1957).

Perry R. W and Kantrowitz A.
J. Appl. Phys. **22**, 878 (1951).

Rich M.
Los Alamos Scientific Laboratory Report **LAMS - 2826** (1963).

Roig R. A and Glass I. I.
Phys. Fluids **20**, No. 10 1651 (1977).

Rosen M. D et al.
Phys. Rev. Lett. **54**, 2 (1985).

Rossi B.
Optics 3rd ed. (Addison Wesley, 1965).

Schwendeman D. W and Witham G. B.
Proc. R. Soc. Lond. A **413**, 297 (1987).

Sedov L. I.
Methods of Similarity and Dimensional Analysis in Mechanics 3rd ed. (Academic, NY, 1959).

She C. Y, Latifi H, Yu J. R, et al.
Geophysical Res. Letters **17**, 929 (1990).

Shelton J. D, Gardner C. S and Sechrist C. F.
Geophysical Res. Letters **7**, 1069 (1980).

Smith L. G.
NDRC No. A-350, OSRD No. 6271 (1949).

Sod G. A.
J. Fluid Mech. **83**, 785 (1977).

Spinhirne J. D, Hansen M. Z and Caulhill L. O.
Appl. Optics **21**, 1564 (1982).

Synge E. H.
Phil. Mag. **9**, 1014 (1930).

Thomas L, Gibson A. J and Battacharyya S. K.
Nature **263**, 115 (1976).

Twomey S and Howell H. B.
Appl. Optics **4**, 501 (1965).

Tyndall J.
Phil. Mag. **37**, 384 (1869).

Weinstock R.
Calculus of Variations (Dover 1974).

Witham G. B.
J. Fluid Mech. **2**, 145 (1957).

Appendix A

Fluid in Cell Differencing Method

In this appendix we outline the Fluid in Cell (FLIC) method of Gentry et al. (1966) used to solve the time dependent equations of motion for compressible fluid flow.

The FLIC method subdivides the flowfield under investigation into a mesh of m $\times$ n cells as in figure $A.1$.

If a Cartesian co-ordinate system is used then each cell is a right parallelepiped with dimensions δr, δz and of unit depth. If a cylindrical co-ordinate system is used each cell is a rectangular torus with inner radius jδr and outer radius (j+1)δr and width δz.

S_j^z is defined as the area of contact between cells (i,j) and (i+1,j), open to flow in the z direction. Similarly, $S_{j+\frac{1}{2}}^r$ is defined as the area of contact between cells (i,j) and (i,j+1), open to flow in the r direction. V_j is the volume of cell (i,j).

For Cartesian co-ordinates :

$$V_j = \delta r \delta z \tag{A.1}$$

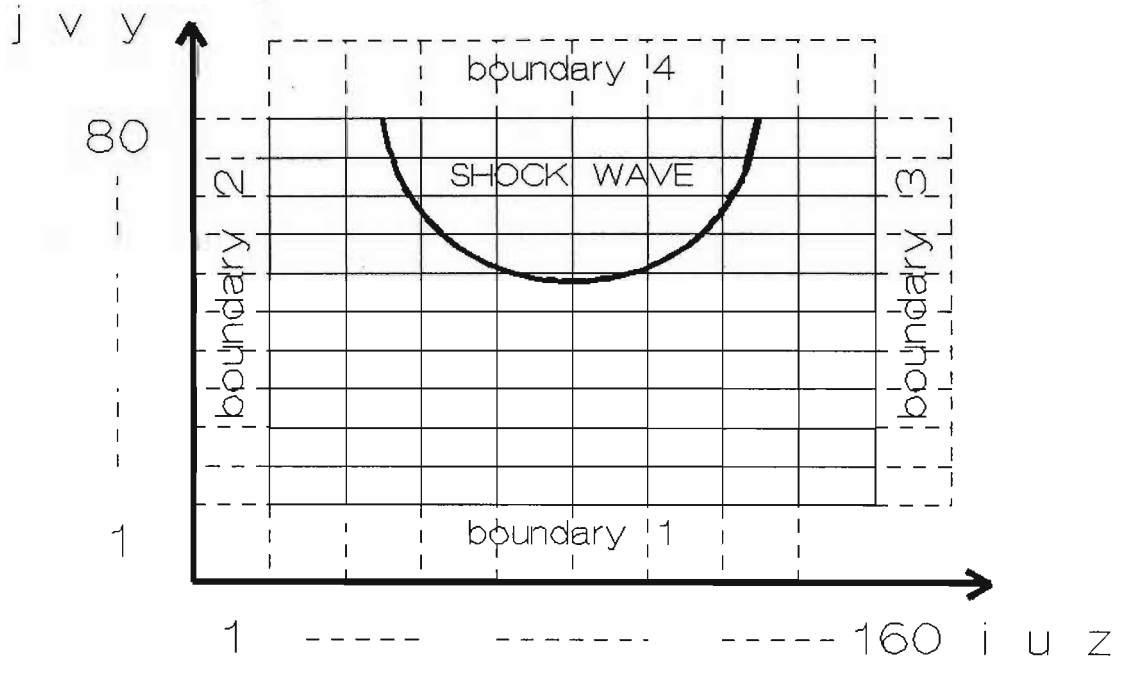

Figure A.1: Computational mesh used in the FLIC method

$$S_j^z = \delta r \tag{A.2}$$

$$S_{j+\frac{1}{2}}^r = \delta z \tag{A.3}$$

For cylindrical co-ordinates :

$$V_j = 2\pi(j + \frac{1}{2})\delta r^2 \delta z \tag{A.4}$$

$$S_j^z = 2\pi(j + \frac{1}{2})\delta r^2 \tag{A.5}$$

$$S_{j+\frac{1}{2}}^r = 2\pi(j+1)\delta r \delta z \tag{A.6}$$

At the start of the calculation cycle at time t = nδt where δt is the time increment and n is a time increment counter with initial value 0, each cell (i,j) is given an initial value of density ($\rho_{i,j}^n$), z-velocity component ($u_{i,j}^n$), r-velocity component ($v_{i,j}^n$) and pressure ($p_{i,j}^n$). The specific internal energy ($I_{i,j}^n$) for each cell (i,j) is calculated using the equation of state :

$$I_{i,j}^n = \frac{p_{i,j}^n}{(\gamma - 1)\rho_{i,j}^n} \tag{A.7}$$

Where γ is the ratio of the specific heats of the gas used.

The flow variables of each cell is advanced in time using the finite difference approximation for the equations of motion of the fluid. At time t = (n + 1)δt intermediate values for velocity ($\tilde{v}_{i,j}^n, \tilde{u}_{i,j}^n$) and specific internal energy ($\tilde{I}_{i,j}^n$) are calculated taking into account acceleration effects due to the pressure gradients :

$$\tilde{u}_{i,j}^n = u_{i,j}^n - \frac{\delta t}{\rho_{i,j}^n \delta z}((p+q)_{i+\frac{1}{2},j}^n - (p+q)_{i-\frac{1}{2},j}^n) \tag{A.8}$$

$$\begin{aligned}
\tilde{v}^n_{i,j} &= v^n_{i,j} - \frac{\delta t}{\rho^n_{i,j}}\Big(\frac{1}{2V_j}\big(S^r_{j+\frac{1}{2}}(p^n_{i,j+1} - p^n_{i,j}) \\
&- S^r_{j-\frac{1}{2}}(p^n_{i,j-1} - p^n_{i,j})\big) \\
&+ \frac{1}{\delta r}(q^n_{i,j+\frac{1}{2}} - q^n_{i,j-\frac{1}{2}})\Big) \qquad \text{(A.9)}
\end{aligned}$$

$$\begin{aligned}
\tilde{I}^n_{i,j} &= I^n_{i,j} - \frac{\delta t}{\rho^n_{i,j}V_j}\big(p^n_{i,j}(S^r_{j+\frac{1}{2}}\overline{v}^n_{i,j+\frac{1}{2}} - S^r_{j-\frac{1}{2}}\overline{v}^n_{i,j-\frac{1}{2}}) \\
&+ \frac{1}{2}q^n_{i,j+\frac{1}{2}}(S^r_{j+1}\overline{v}^n_{i,j+1} + S^r_j\overline{v}^n_{i,j}) \\
&- \frac{1}{2}q^n_{i,j-\frac{1}{2}}(S^r_j\overline{v}^n_{i,j} + S^r_{j-1}\overline{v}^n_{i,j-1}) \\
&- \overline{v}^n_{i,j}S^r_j(q^n_{i,j+\frac{1}{2}} - q^n_{i,j-\frac{1}{2}}) \\
&- \overline{u}^n_{i,j}S^z_j(q^n_{i+\frac{1}{2},j} - q^n_{i-\frac{1}{2},j}) \\
&+ S^z_j(\overline{u}^n_{i+\frac{1}{2},j}(p^n_{i,j} + q^n_{i+\frac{1}{2},j}) \\
&- \overline{u}^n_{i-\frac{1}{2},j}(p^n_{i,j} + q^n_{i-\frac{1}{2},j}))\big) \qquad \text{(A.10)}
\end{aligned}$$

where

$$p^n_{i+\frac{1}{2},j} = \frac{1}{2}(p^n_{i,j} + p^n_{i+1,j}) \qquad \text{(A.11)}$$

$$\overline{u}^n_{i,j} = \frac{1}{2}(u^n_{i,j} + \tilde{u}^n_{i,j}) \qquad \text{(A.12)}$$

$\overline{v}^n_{i,j}$ is similarly defined.

The quantity $q^n_{i+\frac{1}{2},j}$ is an explicit artificial viscosity term added to the pressure term to enhance the stability of the difference equations in regions where the fluid velocity is small compared to the local sound speed $c^n_{i,j}$.

If $K(u^2+v^2)^n_{i+\frac{1}{2},j} < (c^2)^n_{i+\frac{1}{2},j}$ and $u^n_{i,j} > u^n_{i+1,j}$ then :

$$q^n_{i+\frac{1}{2},j} = Bc^n_{i+\frac{1}{2},j}\rho^n_{i+\frac{1}{2},j}(u^n_{i,j} - u^n_{i+1,j}) \tag{A.13}$$

otherwise

$$q^n_{i+\frac{1}{2},j} = 0 \tag{A.14}$$

If $K(u^2+v^2)^n_{i,j+\frac{1}{2}} < (c^2)^n_{i,j+\frac{1}{2}}$ and $v^n_{i,j} > v^n_{i,j+1}$ then :

$$q^n_{i,j+\frac{1}{2}} = Bc^n_{i,j+\frac{1}{2}}\rho^n_{i,j+\frac{1}{2}}(v^n_{i,j} - v^n_{i,j+1}) \tag{A.15}$$

otherwise

$$q^n_{i,j+\frac{1}{2}} = 0 \tag{A.16}$$

The quantities K and B are user specified. K determines the maximum value of the Mach number at a cell interface for which the artificial viscosity will be applied. B denotes the magnitude of the viscous pressure term.

From the intermediate values of velocities calculated, the mass flow across the cell boundaries can be determined. This mass flow is proportional to the density of the donor cell. If $\Delta M^n_{i+\frac{1}{2},j}$ is the mass flow across the area S^z_j between cell (i,j) and (i+1,j) during time δt and similarly $\Delta M^n_{i,j+\frac{1}{2}}$ is the mass flow across the area $S^r_{j+\frac{1}{2}}$ between cell (i,j) and (i,j+1) during time δt then :

$$\Delta M^n_{i+\frac{1}{2},j} = S^z_j\rho^n_{i,j}\tilde{u}^n_{i+\frac{1}{2},j}\delta t \quad if \quad \tilde{u}^n_{i+\frac{1}{2},j} > 0 \tag{A.17}$$

$$= S^z_j\rho^n_{i+1,j}\tilde{u}^n_{i+\frac{1}{2},j}\delta t \quad if \quad \tilde{u}^n_{i+\frac{1}{2},j} < 0 \tag{A.18}$$

$$\Delta M^n_{i,j+\frac{1}{2},j} = S^r_{j+\frac{1}{2}} \rho^n_{i,j} \tilde{v}^n_{i,j+\frac{1}{2}} \delta t \quad if \quad \tilde{v}^n_{i,j+\frac{1}{2}} > 0 \tag{A.19}$$

$$= S^r_{j+\frac{1}{2}} \rho^n_{i,j+1} \tilde{v}^n_{i,j+\frac{1}{2}} \delta t \quad if \quad \tilde{v}^n_{i,j+\frac{1}{2}} < 0 \tag{A.20}$$

Using the law of conservation of mass, the density in each cell at time $t = (n+1)\delta t$ can be determined :

$$\rho^{n+1}_{i,j} = \rho^n_{i,j} + \frac{1}{V_j}(\Delta M^n_{i,j-\frac{1}{2}} + M^n_{i-\frac{1}{2},j} - M^n_{i,j+\frac{1}{2}} - M^n_{i+\frac{1}{2},j}) \tag{A.21}$$

Conservation of momentum is then used to determine new values of momentum and energy components of each cell, corresponding to t = (n+1)δ t , assuming that the mass which crosses the cell boundaries carries the intermediate components of velocity and specific internal energy of the donor cell, using the relationship of the form :

$$\begin{aligned} F^{n+1}_{i,j} &= \frac{1}{\rho^{n+1}_{i,j} V_j}(T_{i,j}(1)\tilde{F}^n_{i-1,j}\Delta M^n_{i-\frac{1}{2},j} + T_{i,j}(2)\tilde{F}^n_{i,j-1}\Delta M^n_{i,j-\frac{1}{2}} \\ &- T_{i,j}(3)\tilde{F}^n_{i+1,j}\Delta M^n_{i+\frac{1}{2},j} - T_{i,j}(4)\tilde{F}^n_{i,j+1}\Delta M^n_{i,j+\frac{1}{2},j} \\ &+ \tilde{F}^n_{i,j}(\rho^n_{i,j}V_j + (1 - T_{i,j}(1))\Delta M^n_{i-\frac{1}{2},j} + (1 - T_{i,j}(2))\Delta M^n_{i,j-\frac{1}{2},j} \\ &- (1 - T_{i,j}(3))\Delta M^n_{i+\frac{1}{2},j} - (1 - T_{i,j}(4))\Delta M^n_{i,j+\frac{1}{2},j})) \end{aligned} \tag{A.22}$$

where

$$F_{i,j} = \begin{pmatrix} u^n_{i,j} \\ v^n_{i,j} \\ E^n_{i,j} \end{pmatrix} \tag{A.23}$$

and

$T_{i,j}(k) = 1$ if fluid flows into cell (i,j) across side k and
$T_{i,j}(k) = 0$ if fluid flows out of cell (i,j) across side k.

Note : k = 1 corresponds to the left boundary of a cell, k = 2 corresponds to the bottom boundary of a cell, k = 3 corresponds to the right boundary of a cell and k = 4 corresponds to the top boundary of a cell.

The specific internal energy of each cell is found using the relation :

$$I_{i,j}^{n+1} = E_{i,j}^{n+1} - \frac{1}{2}(u^2 + v^2)_{i,j}^{n+1} \tag{A.24}$$

where E is the energy per unit mass.

Equation $A.24$ is used to compute the new pressures in each cell. This calculated cycle is repeated until the user defined time is reached.

The above difference equations are applicable to interior cells which are not adjacent to one of the boundaries of the computing mesh. The boundary of the computing mesh is made up of fictitious cells and the type of boundary determines the value of the flow variables in these cells.

For an open boundary, the flow variables in the fictitious boundary cells are made equal to the values in the adjacent interior cells. This allows flow of mass and energy across the boundary. For a closed boundary, no mass and energy can flow across the boundary. This requires that the velocity component of the fictitious boundary cell, normal to the boundary, be made equal in magnitude but opposite in direction to that of the interior adjacent cell. All other flow variables are treated in the same way as the open boundary. If the boundary has a corner then the fictitious corner boundary cell is assigned two sets of flow variables depending from which cell the calculation is made.

Meintjies (1975) found that the abovementioned boundary conditions introduced reflections from the output boundaries into the computational mesh. For output boundaries it was suggested that the flow variables in each fictitious cell be set to a linear interpolated value from two adjacent cells as opposed to the value of the adjacent cell. For example, the density of a fictitious boundary cell $\rho_{i+1,j}^n$ is given by :

$$\rho_{i+1}^n = 2\rho_{i,j}^n + \rho_{i-1,j}^n \tag{A.25}$$

These are the boundary flow variables used in the CSL simulation.

Appendix B

Programme listing of Scatrate.pas

```
{-------------------------------------***-------------------}
{ Program      : ScatRate.pas                                }
{ Language     : Turbo Pascal (c) v6.0                       }
{ Function     : Calculates scattering ratios from file of   }
{ standard density                                           }
{ and lidar data.                                            }
{ Comments     : Saves scattering ratio (raw and smoothed)   }
{ to file                                                    }
{ Usage        : SCATRATE DataFile DensityFile ScatterFile   }
{ SmoothFile                                                 }
{-------------------------------------***-------------------}

program Mg2;

uses
  Dos, Crt;

const
   MaxSize = 668;            {maximum data entries}
   offset  = 200;            {number of last bins to average}

type
```

```
  Range = array[1..MaxSize] of Real;

var
  theAltitude, theDensity : Range;
  expAltitude, expCounts  : Range;
  Rayleigh, ScatterRate   : Range;
  Size                    : Word;
  ScatterFileName         : String;
  ScatterFile             : Text;
  SmoothFileName          : String;
  SmoothFile              : Text;
  rK, rAvg, rAlt          : Real;
  rIndex                  : Word;

{-----------------------------------***-------------------}

procedure Initialise;

{initialise all array structures to zero}

begin
  FillChar(theAltitude, SizeOf(theAltitude), 0);
  FillChar(theDensity, SizeOf(theDensity), 0);
  FillChar(expAltitude, SizeOf(expAltitude), 0);
  FillChar(expCounts, SizeOf(expCounts), 0);
  FillChar(ScatterRate, SizeOf(ScatterRate), 0);
  FillChar(Rayleigh, SizeOf(Rayleigh), 0);
end; {Initialise}

{-----------------------------------***-------------------}

procedure ReadFiles;

{ read input files and verify that output files will not }
{ be overwritten }

var
  DataFile        : Text;
```

```
  DensityFile     : Text;
  DataFileName    : String;
  DensityFileName : String;
  i, j            : Word;      {loop increments}
  Responce        : Char;      {user responce}

    {-----------------------***-------------------------}

procedure ReadHeader(var InFile : Text);

{strip dimensions header from input file}

var
  rows, cols : Word;

begin
  Readln(InFile, rows, cols);
end; {ReadFiles}

   {-----------------------***-------------------------}

function FileError(var TextFile : Text; TextFileName :
 String; OverWriteFile : Boolean) : Boolean;

{ attempts to open a file for rewriting/appending - }
{ reports on its success }

begin
  {$I-}               {turn I/O checking off temporarily}
  Assign(TextFile, TextFileName);
  if OverWriteFile
    then Reset(TextFile)        {overwrite file}
    else Append(TextFile);      {append to file}
  {$I+}                         {turn I/O checking back on}
  FileError := (IOResult <> 0); {return success/failure}
end; {FileError}

 {-----------------------***-------------------------}
```

```
procedure ErrorMsg(TextFileName : String; Msg : Word);

{handles error messages}

begin
  case Msg of
    1 : begin
Writeln('File Error: Unable to open file: ' + DataFileName);
          Halt(1) {exit from program}
        end;
    2 : begin

Writeln('File Warning: File: ' + TextFileName + '
 already exists');

Write('User Action : Overwrite existing file
           (Y/N) : ');
        end;

   else begin
          Writeln('Undefined Error encountered');
          Halt(1) {exit from program}
        end;
  end; {case}
end; {ErrorMsg}

{------------------------***--------------------------}

begin
  if ParamCount <> 4
    then begin
{ incorrect number of parameters on command line - print }
{ usage }

Writeln('Usage: SCATRATE DataFile DensityFile ScatterFile
 SmoothFile');
       Halt(1); {and exit from program}
```

```
      end {then}
  else begin
         {get filenames from command line}
         DataFileName    := ParamStr(1);
         DensityFileName := ParamStr(2);
         ScatterFileName := ParamStr(3);
         SmoothFileName  := ParamStr(4);
       end; {else}

if FileError(DataFile, DataFileName, True)
    {True = overwrite file}
  then ErrorMsg(DataFileName, 1);

if FileError(DensityFile, DensityFileName, True)
   {True = overwrite file}
  then ErrorMsg(DensityFileName, 1);

if not FileError(ScatterFile, ScatterFileName, False)
  {False = append file}
  then begin
         ErrorMsg(ScatterFileName, 2);
         Responce := ReadKey; {get user's responce}
         Writeln;
           if (Responce = 'N') or (Responce = 'n')
             then begin
                    Close(DataFile);  {close open files}
                    Close(DensityFile);
                    Close(ScatterFile);
                    Halt(1)  {before exiting from program}
                  end; {then}
       end; {then}

if not FileError(SmoothFile, SmoothFileName, False)
  {False = append file}
  then begin
         ErrorMsg(SmoothFileName, 2);
         Responce := ReadKey;
         Writeln;
```

```
            if (Responce = 'N') or (Responce = 'n')
              then begin
                     Close(DataFile);     {close open files}
                     Close(DensityFile);
                     Close(ScatterFile);
                     Close(SmoothFile);
                     Halt(1)  {before exiting from program}
                   end; {then}
          end; {then}

  {read DataFile values into expAltitude and expCounts}
  i := 0;
  if not Eof(DataFile) then ReadHeader(DataFile);
  while not Eof(DataFile) do
    begin
      Inc(i);
      Readln(DataFile, expAltitude[i], expCounts[i]);
    end; {while}

  {read DensityFile values into theAltitude and theDensity}
  j := 0;
  if not Eof(DensityFile) then ReadHeader(DensityFile);
  while not Eof(DensityFile) do
    begin
      Inc(j);
      Readln(DensityFile, theAltitude[j], theDensity[j]);
    end; {while}

  Size := i;           {the number of data values read in}
  Close(DataFile);     {close open files before we leave}
  Close(DensityFile);
end; {ReadFiles}

{---------------------***-------------------------}

procedure SubtractNoise;

{ average the last offset bins and subtract from }
```

```
{ the rest of the Count values }

const
  offset = 200;

var
  i   : Word;
  sum : Real;
  avg : Real;

begin
  if Size < offset
    then begin
Writeln('Calc Error: Too few values to average last ',
    offset);
           Halt(1);
         end; {then}

  {find the average}
  sum := 0;
  for i := Size-offset to Size do
    sum := sum + expCounts[i];
  avg := sum/offset;
  rAvg := avg;

  {subtract from all the Count values}
  for i := 1 to Size do
    expCounts[i] := expCounts[i] - avg;
end; {SubtractNoise}


{--------------***-----------------------------}

procedure Calculate;

var
  Alt    : LongInt;
  Alt2   : Real;
```

```
  Index   : Word;
  K       : Real;
  i, j    : Word;

{-----------------------***-------------------------}

procedure GetUserValues(var a : LongInt);

{get initial values from the user}

begin
  repeat
Write('User Action:Pin data at altitude [150..100 050] m:');
    Readln(a);
  until (a >= 150) and (a <= 100050);
end; {GetUserValues}

{-----------------------***-------------------------}

function DivZeroError(value : Real; structure : String;
 position : Word) : Boolean;

{ determines if a division by zero error is likely to }
{ occur and gives }
{its location before exiting the program if true }

begin
  if value = 0
    then begin
Writeln('Calc Error: Division by zero error in
         ' + structure  + ' ', position);
           Halt(1); {exit program}
         end {then}
    else DivZeroError := False;
end; {DivZeroError}

{-----------------------***-------------------------}
```

```
begin
  GetUserValues(Alt);        {get initial values}
  rAlt := Alt;               {store for report}

Index  := Round(Alt/150);
 {convert altitude to an array index}

  rIndex := Index;           {store for report}

if not DivZeroError(theDensity[Index], 'Density', Index)
    then begin
  K  := (expCounts[Index] * Alt * Alt) / theDensity[Index];
       rK := K; {report}
         end; {then}

  for i := 1 to Size do
    begin
      Alt2 := theAltitude[i] * theAltitude[i];
      if not DivZeroError(Alt2, 'Rayleigh (Altitude)', i)
        then Rayleigh[i] := (theDensity[i] * K) / Alt2;
    end; {for}

  for j := 1 to Size do
    begin
if not DivZeroError(Rayleigh[j], 'ScatterRate (Rayleigh)',j)
       then ScatterRate[j] := expCounts[j] / Rayleigh[j];
    end; {for}
end; {Calculate}

{-----------------***-------------------------}

procedure SaveScatterData;

{ saves the raw temperature data to a file together }
{ with altitudes }

var
```

```
  ScatterFile       : Text;
  FileError         : Boolean;
  i                 : Word;

begin
  Assign(ScatterFile, ScatterFileName);
  {$I-} Rewrite(ScatterFile); {$I+}
  FileError := (IOResult <> 0);
  if FileError
then Writeln('File Error: Unable to open file :
   ' + ScatterFileName)
    else begin
     Writeln(ScatterFile, Size, '  ', 2); {rows, columns}
        for i := 1 to Size do
Writeln(ScatterFile, expAltitude[i]:0:0, '   ',
 ScatterRate[i]:0:5);
        Close(ScatterFile);
       end; {then}
end; {SaveScatterData}

{--------------------***-------------------------}

procedure Smooth(BigArray : Range);

{averages the five values around every sixth value }
{ in BigArray and writes to a file together with   }
{ altitude at six'th value }

var
  average    : Real;
  sum        : Real;
  i, j       : Word;    {loop indexes}
  NewSize    : Word;    {number of rows in new file}
  SmoothFile : Text;
  FileError  : Boolean;

begin
  Assign(SmoothFile, SmoothFileName);
```

```
  {$I-} Rewrite(SmoothFile); {$I+}
  FileError := (IOResult <> 0);
  if FileError
    then Writeln('File Error: Unable to open file :
' + SmoothFileName)
    else begin
           {calculate dimensions of new file}
           NewSize := Round(Size/6);
      if (NewSize mod 6) <> 0 then NewSize := NewSize+1;
      if (NewSize*6)+2 > Size then NewSize := NewSize-1;
     Writeln(SmoothFile, NewSize, ' ', 2);
     {write dimensions header}
           j := 0;
           repeat
       j := j + 6;   {select every six'th original value}
       sum := 0;                    {reset counter}
            for i := j-2 to j+2 do
      sum := sum + BigArray[i];
     {sum on either side of selected value}
            average := sum / 5;
   Writeln(SmoothFile, theAltitude[j]:0:0, '   ',
      average:0:5);
           until j+2 >= Size; {not enough values left}
           Close(SmoothFile);
         end; {else}
end; {Smooth}

{------------***--------------------}

procedure Report;

{generate a screen report of important data not written }
{ to file(s) }

begin
 Writeln('Report');
 Writeln('Data pinned at altitude: ', rAlt:0:5);
 Writeln('Avg of last ', offset, ' bins   : ', rAvg:0:5);
```

```
 Writeln('Altitude[',rIndex,']: ', theAltitude[rIndex]:0:5);
 Writeln('Counts[',rIndex,']  : ', expCounts[rIndex]:0:5);
 Writeln('Density[',rIndex,'] : ', theDensity[rIndex]:0:5);
 Writeln('K ratio              : ', rK:0:5);
 Writeln('Scatter Rate Filename: ', ScatterFilename);
 Writeln('Smooth Filename      : ', SmoothFilename);
end; {Report}

{----------------------***-----------------------}

begin
  Initialise;
  ReadFiles;
  SubtractNoise;
  Calculate;
  SaveScatterData;
  Smooth(ScatterRate);
  Report;
end. {main}

{------------------***----------------------------}
```

Appendix C

Programme listing of Lidar0.pas

```
{-----------------------------------***-------------------}
{ Program      : Lidar0.pas                                 }
{ Language     : Turbo Pascal v7.0                          }
{ Function     : Simple interface for Lidar Extinction      }
{ Coefficient programme                                     }
{-----------------------------------***-------------------}

{-------------------------------------------------}
{memory directives default values                 }
{-------------------------------------------------}

{$M 16384,0,655360} {StackSize, HeapMin, HeapMax}

{-------------------------------------------------}
{compiler directives optimised for speed not memory}
{-------------------------------------------------}

{$F+} {Force far calls  ON}
{$O+} {Overlays allowed ON}
{$A+} {Word align data  ON}
{$G+} {286 instructions ON}
{$R-} {Range checking   OFF}     {switch ON when debugging}
```

```
{$S-} {Stack checking   OFF}     {switch ON when debugging}
{$I+} {I/O checking     ON}      {IOResult used}

{$V-} {Strict var-strings OFF}   {switch ON when debugging}
{$B-} {Complete Boolean   OFF}   {switch ON when debugging}
{$X+} {Extended syntax    ON}    {required by MessageBox}

{$N+} {Numeric processing 8087/80287 ON}
{$E+} {Numeric processing Emulation  ON}

{$D-} {Debug information   OFF}  {switch ON when debugging}
{$L-} {Debug local symbols OFF}  {switch ON when debugging}

program Lidar0;

uses
  Dos, Crt, Extinct;

var
  e               : Extinct.TExtinct;
  p               : Extinct.ParameterRecord;
  Error, i        : Word;
  InFile, OutFile : String;

begin
  ClrScr;
  Writeln('             LIDAR EXTINCTION COEFFICIENTS');
  Writeln;
  Write('Input file               : ');
  Readln(InFile);
  Write('Output file              : ');
  Readln(OutFile);
  Writeln('Integration Method:');
  Writeln('  SummationMethod  [1]');
  Writeln('  Simpson1_3Method [2]');
  Writeln('  Simpson3_8Method [3]');
  Write('Enter [1] [2] [3]        : ');
  Readln(i);
```

```
 case i of
   1    : p.Integrate := SummationMethod;
   2    : p.Integrate := Simpson1_3Method;
   3    : p.Integrate := Simpson3_8Method;
   else   p.Integrate := Simpson3_8Method;
 end; {case}

 e.Init;
 e.ReadCounts(InFile);

 repeat
   Write('k                          : ');
   Readln(p.k);
   Write('r0 (km) [-1 = use peaks] : ');
   Readln(p.r0);
   Write('rm (km) [-1 = use last ] : ');
   Readln(p.rm);
   p.UsePeak := (p.r0 = -1);
   p.UseLast := (p.rm = -1);
   Error := e.SetParameters(p);
   case Error of
NoError       : Writeln;
Not150Step : Writeln('Altitude must be in steps of 150 m');
RmLtR0    : Writeln('Altitude rm must be greater then r0');
NegativePower : Writeln('Negative powers are not allowed');
R0OutOfRange  : Writeln('Altitude r0 is out of range');
RmOutOfRange  : Writeln('Altitude rm is out of range');
NoCountsAtR0  : Writeln('Altitude r0 has zero counts');
NoCountsAtRm  : Writeln('Altitude rm has zero counts');
  CmIs0         : Writeln('Divisor Cm evaluates to zero');
     else            Writeln('Unknown error');
   end; {case}
 until Error = NoError;

 e.CalcCoefficients;
 e.SaveCoefficients(OutFile);
 e.SetDisplay;
 e.PlotDisplay(Crt.LightGreen, Crt.Yellow);
```

```
  repeat
    {null}
  until KeyPressed;
  e.ClearDisplay;
  e.Done;
  Writeln('Lidar done');
end. {Lidar0}
```

```
{-------------------------------------***-------------------}
{ Unit         : Extinct.pas                                 }
{ Compiler     : Borland Turbo Pascal v7.0                   }
{ Function     : Calculates Extinction Coefficients for      }
{ Lidar Return Counts (taken as Power) at different          }
{ Altitudes                                                  }
{-------------------------------------***-------------------}

{-------------------------------------------------}
{memory directives default values                  }
{-------------------------------------------------}

{$M 16384,0,655360} {StackSize, HeapMin, HeapMax}

{-------------------------------------------------}
{compiler directives optimised for speed not memory}
{-------------------------------------------------}

{$F+} {Force far calls  ON}
{$O+} {Overlays allowed ON}
{$A+} {Word align data  ON}
{$G+} {286 instructions ON}
{$R-} {Range checking   OFF}     {switch ON when debugging}
{$S-} {Stack checking   OFF}     {switch ON when debugging}
{$I+} {I/O checking     ON}                  {IOResult used}
```

```
{$V-} {Strict var-strings OFF}   {switch ON when debugging}
{$B-} {Complete Boolean   OFF}   {switch ON when debugging}
{$X+} {Extended syntax    ON}      {required by MessageBox}

{$N+} {Numeric processing 8087/80287 ON}
{$E+} {Numeric processing Emulation  ON}

{$D-} {Debug information   OFF}   {switch ON when debugging}
{$L-} {Debug local symbols OFF}   {switch ON when debugging}

unit Extinct;

interface

uses
  Dos, Crt, Objects, Graph, StdHdr, WorldDr, SEGraph;


const
  NoError       = 0;
  Not150Step    = 1;
  RmLtR0        = 2;
  NegativePower = 3;
  R0OutOfRange  = 4;
  RmOutOfRange  = 5;
  NoCountsAtR0  = 6;
  NoCountsAtRm  = 7;
  CmIs0         = 8;

type
  Vector = array[0..1500] of Double;

  Integration = (SummationMethod, Simpson1_3Method,
   Simpson3_8Method);

  PExtinct = ^TExtinct;
```

```
  ParameterRecord = record
    k          : Double;
    r0         : Double;
    rm         : Double;
    Integrate  : Integration;
    UsePeak    : Boolean;
    UseLast    : Boolean;
  end; {record}

  TExtinct = object(TObject)
    Coefficients : Vector;
    Counts       : Vector;
    Curve        : Vector;
    Length       : Word;
    constructor Init;
    destructor  Done; virtual;
procedure   ReadCounts(Filename : PathStr); virtual;
procedure   SaveCoefficients(Filename : PathStr); virtual;
function    SetParameters(Parms : ParameterRecord) : Word;
 virtual;
procedure   GetParameters(var Parms : ParameterRecord);
 virtual;
procedure   CalcCoefficients; virtual;
procedure   PlotCoefficients(Colour : Word); virtual;
procedure   PlotCounts(Colour : Word); virtual;
procedure   PlotDisplay(Colour1, Colour2 : Word); virtual;
procedure   SetDisplay; virtual;
procedure   ClearDisplay; virtual;
private
    k            : Double;
    r0           : Double;
    rm           : Double;
    Integrate    : Integration;
    UsePeak      : Boolean;
    UseLast      : Boolean;
    GraphicsMode : Boolean;
    CountsFile   : Text;
    CoeffsFile   : Text;
```

```
    Fm_Cm        : Double;
    function     F(r : Double) : Double; virtual;
    function     P(r : Double) : Double; virtual;
    function     Power(Base, Exponent : Double) : Double;
     virtual;
    function     Simpson1_3(a, b, h : Double) : Double;
     virtual;
    function     Summation(a, b : Double) : Double; virtual;
    function     Simpson3_8(y : Vector; a, b : LongInt; h :
     Double) : Double; virtual;
  end; {object}


implementation

const
  Screen      = 1;
  CountScreen = 1;
  CoeffScreen = 2;
  Step        = 150.0/1000.0;

{------------------------***-------------------------------}

constructor TExtinct.Init;

var
  i : Word;

begin
  Length       := 0;
  k            := 1.0;
  r0           := 0.0;
  rm           := 0.0;
  Fm_Cm        := 0.0;
  UsePeak      := True;
  UseLast      := True;
  Integrate    := Simpson3_8Method;
  GraphicsMode := False;
```

```
  for i := 0 to 1500 do begin
    Counts[i]       := 0.0;
    Coefficients[i] := 0.0;
    Curve[i]        := 0.0;
  end; {for}
end; {TExtinct.Init}

{-------------------------------------***-------------------}

destructor TExtinct.Done;

begin
  TObject.Done;
end; {TExtinct.Done}

{-------------------------------------***-------------------}

procedure TExtinct.ReadCounts(FileName : PathStr);

var
  i, Columns : Word;
  Altitude   : Double;

begin
  Assign(CountsFile, FileName);
  {$I-}
  Reset(CountsFile);
  {$I+}
  if IOResult = 0 then begin
    Readln(CountsFile, Length, Columns);
    for i := 0 to Length - 1 do begin
      Readln(CountsFile, Altitude, Counts[i]);
    end; {for}
    Close(CountsFile);
  end; {then}
end; {TExtinct.ReadCounts}

{-------------------------------------***-------------------}
```

```
procedure TExtinct.SaveCoefficients(Filename : PathStr);

var
  i : Word;

begin
  Assign(CoeffsFile, FileName);
  {$I-}
  Rewrite(CoeffsFile);
  {$I+}
  if IOResult = 0 then begin
    Writeln( CoeffsFile, Length, ' 2' );
    for i := 0 to Length - 1 do begin
      Writeln( CoeffsFile, i*Step*1000:15:0,
       Coefficients[i]:15:6);

    end; {for}
    Close(CoeffsFile);
  end; {then}
end; {TExtinct.SaveCoefficients}

{----------------------***--------------------------------}

function TExtinct.SetParameters(Parms : ParameterRecord) :
 Word;

var
  S0, Sm, Cm, peak : Double;
  i, Error         : Word;
  Low, High        : LongInt;

begin
  Error     := NoError;
  Integrate := Parms.Integrate;
  k         := Parms.k;
  UsePeak   := Parms.UsePeak;
  UseLast   := Parms.UseLast;
```

```
if UsePeak then begin
  peak := 0.0;
  for i := 0 to Length - 1 do begin
    if Counts[i] > peak then begin
      peak := Counts[i];
      r0   := i*Step;
    end; {if}
    Curve[i] := F(i*Step);
  end; {for}
end {then}
else begin
  r0 := Parms.r0;
end; {else}

if UseLast then begin
  rm := (Length-1)*Step;
end {then}
else begin
  rm := Parms.rm;
end; {else}

{-------------------}
{Some error checking}
{-------------------}
if k < 0.0 then begin
  Error := NegativePower;
end; {if}

if rm <= r0 then begin
  Error := RmLtR0;
end; {if}

if ((r0 <= 0) or (r0 > (Length-1)*Step)) then begin
  Error := R0OutOfRange;
end; {if}

if ((rm <= 0) or (rm > ((Length-1)*Step)+1)) then begin
```

```
  Error := RmOutOfRange;
end; {if}


Low := Round(r0*1000) mod Round(Step*1000);
High := Round(rm*1000) mod Round(Step*1000);
if ((Low <> 0) or (High <> 0)) then begin
  Error := Not150Step;
end; {if}

if P(r0) = 0 then begin
  Error := NoCountsAtR0;
end; {if}

if P(rm) = 0 then begin
  Error := NoCountsAtRm;
end; {if}


if Error = NoError then begin
  {--------------------------------------}
  {Initialise the curve array            }
  {We can call F now that we have set k  }
  {--------------------------------------}
  for i := 0 to Length - 1 do begin
    Curve[i] := F(i*Step);
  end; {for}

  {-----------------------------------------------------}
  {Calculate some intermediate variables                }
  {abs is used as S0-Sm sometimes returns negative values}
  {-----------------------------------------------------}
  S0    := ln(r0*r0*P(r0));
  Sm    := ln(rm*rm*P(rm));
  Cm    := 0.5*abs(S0-Sm)/(rm-r0);
  if Cm = 0 then begin
    Error := CmIs0;
  end {then}
```

```
    else begin
      Fm_Cm := F(rm)/Cm;
    end; {if}
  end; {if}

  SetParameters := Error;
end; {TExtinct.SetParameters}

{-------------------------------------***--------------------}

procedure TExtinct.GetParameters(var Parms :
 ParameterRecord);

begin
  Parms.k         := k;
  Parms.r0        := r0;
  Parms.rm        := rm;
  Parms.Integrate := Integrate;
  Parms.UseLast   := UseLast;
  Parms.UsePeak   := UsePeak;
end; {TExtinct.GetParameters}

{-------------------------------------***--------------------}

procedure TExtinct.CalcCoefficients;

var
  i, b : Word;
  r    : Double;

begin
  case Integrate of
    SummationMethod  : begin
      for i := Round(r0/Step) to Round(rm/Step) do begin
        r := Step*i;
   Coefficients[i] := F(r) / (Fm_Cm + (2/k)*Summation(r,rm));
      end; {for}
    end; {SummationMethod}
```

```
    Simpson1_3Method : begin
      for i := Round(r0/Step) to Round(rm/Step) do begin
        r := Step*i;
Coefficients[i] := F(r) / (Fm_Cm + (2/k)*Simpson1_3(r,rm,Step));
      end; {for}
    end; {simpson1_3Method}
    Simpson3_8Method : begin
      b := Round(rm/Step);
      for i := Round(r0/Step) to Round(rm/Step) do begin
        r := Step*i;
Coefficients[i] := F(r) / (Fm_Cm + (2/k)*Simpson3_8(Curve,i
 ,b,Step));
      end; {for}
    end; {Simpson3_8Method}
  end; {case}
end; {TExtinct.CalcCoefficients}

{-------------------------------------***-------------------}

function TExtinct.F(r : Double) : Double;

begin
  F := Power((P(r)), 1/k);
end; {TExtinct.F}

{-------------------------------------***-------------------}

function TExtinct.P(r : Double) : Double;

begin
  {-----------------------------------------------------}
  {The relationship of Power to Counts requires the *r*r}
  {-----------------------------------------------------}
  P := Counts[Round(r/Step)]*r*r;
end; {TExtinct.P}

{-------------------------------------***-------------------}
```

```
function TExtinct.Power(Base, Exponent : Double) : Double;

begin
  if Base = 0.0 then begin
    Power := 1.0
  end {then}
  else begin
    Power := Exp(Exponent * Ln(Base))
  end; {else}
end; {TExtinct.Power}

{-------------------------------------***--------------------}

function TExtinct.Summation(a, b : Double) : Double;

var
  Sum, r : Double;

begin
  Sum    := 0.0;
  r      := a;
  repeat
    Sum := Sum + F(r);
    r   := r + Step;
  until r >= b;
  Summation := Sum;
end; {TExtinct.Summation}

{-------------------------------------***--------------------}

function TExtinct.Simpson1_3(a, b, h : Double) : Double;

var
  i, n        : Word;
  evens, odds : Double;
  cc, ans     : Double;
  sign        : Integer;
```

```
begin
  if a > b then begin
    cc   := a;
    a    := b;
    b    := cc;
    sign := -1;
  end {else}
  else begin
    sign := 1;
  end; {else}

  i := 1;
  evens := 0.0;
  odds  := 0.0;
  cc := a+step;
  repeat
    if Odd(i)
      then odds  := odds  + F(a + cc)
      else evens := evens + F(a + cc);
    cc := cc+step;
    i  := i + 1;
  until cc >= b-step;

  ans := sign*(F(a) +4*odds + 2*evens + F(b))*h/3;
  if ans < 0.0 then begin
    ans := ans * -1;
  end; {if}
  Simpson1_3 := ans;
end; {TExtinct.Simpson1_3}

{-------------------------------------***--------------------}

function TExtinct.Simpson3_8(y : Vector; a, b : LongInt;
 h : Double) : Double;

var
  n, x0, xn    : LongInt;
  area1, area2 : Double;
```

```
begin
  {-----------------}
  {initialisations  }
  {-----------------}
  n     := b-a;
  x0    := a;
  xn    := b;
  area1 := 0.0;
  area2 := 0.0 ;

  {-----------------}
  {simpsons 3/8 rule}
  {-----------------}
  if Odd(n) then begin
 area1 := 3/8*h*(y[xn-3] + 3*y[xn-2] + 3*y[xn-1] + y[xn]);
     xn    := xn-3;
  end; {if}

  {-----------------}
  {simpsons 1/3 rule}
  {-----------------}
  if n <> 3 then begin
    repeat
      area2 := area2 + 1/3*h*(y[x0] + 4*y[x0+1] + y[x0+2]);
      x0    := x0+2;
    until ((x0 >= xn) or (x0>1500));
  end; {if}

  Simpson3_8 := area1 + area2;
end;

{-----------------------------------***-------------------}

procedure TExtinct.SetDisplay;

begin
  SEGraph.InitSEGraphics('');
```

```
end; {TExtinct.SetDisplay}

{-----------------------------------***-------------------}

procedure TExtinct.PlotCoefficients(Colour : Word);

const
  SolidLine  : Integer = 0;
  Resolution : Integer = 2;

var
  i          : Word;
  x, y       : StdHdr.VeryLongVector;
  DataPoints : Word;
  kStr, r0Str, rmStr : String;

begin
  DataPoints := Length div Resolution;
  for i := 0 to DataPoints-1 do begin
    x[i] := i*Resolution*Step;
    y[i] := Coefficients[i*Resolution];
  end; {for}

  Str(k  :7 :3, kStr);
  Str(r0 :7 :3, r0Str);
  Str(rm :7 :3, rmStr);

  SEGraph.DefGraphWindow(0, 0, 639, 479, CoeffScreen);
  SEGraph.SetCurrentWindow(CoeffScreen);
  SEGraph.SetViewBackGround(Crt.LightGray);
  Graph.SetColor(Crt.White);
  SEGraph.BorderCurrentWindow(Crt.White);
  SEGraph.SetPlotBackground(Crt.Black);
  SEGraph.ClearGraph;
  SEGraph.SetAxesType(0, 0);
  SEGraph.AutoAxes(x,y,DataPoints,1);
  Graph.SetColor(Colour);
  SEGraph.TitleXAxis('altitude (km)');
```

```
  SEGraph.TitleYAxis('extinction coefficient (1/km)');
  SEGraph.TitleWindow('LIDAR');
  SEGraph.LabelGraphWindow(500, 900,
  'k: '+kStr+'  r0: '+r0Str+'km'+'rm: '+rmStr+'km', 1, 1);
  Graph.SetColor(Crt.White);
  SetLineStyleXX(DottedLn, 0, NormWidth);
  SEGraph.DrawGridX(10);
  SEGraph.DrawGridY(5);
  SetLineStyleXX(SolidLn, 0, NormWidth);
  Graph.SetColor(Crt.White);
  SEGraph.SetCurrentWindow(CoeffScreen);
  SEGraph.LinePlotData(x, y, DataPoints, Colour, SolidLine);
end; {TExtinct.PlotCoefficients}

{-----------------------------------***--------------------}

procedure TExtinct.PlotCounts(Colour : Word);

const
  SolidLine  : Integer = 0;
  Resolution : Integer = 2;

var
  x, y               : StdHdr.VeryLongVector;
  i, DataPoints      : Word;

begin
  DataPoints := Length div Resolution;
  for i := 0 to DataPoints-1 do begin
    x[i] := i*Resolution*Step;
    y[i] := Counts[i*Resolution];
  end; {for}

  SEGraph.DefGraphWindow(0, 0, 639, 479, CountScreen);
  SEGraph.SetCurrentWindow(CountScreen);
  SEGraph.SetViewBackGround(Crt.LightGray);
  Graph.SetColor(Crt.White);
  SEGraph.BorderCurrentWindow(Crt.White);
```

```
  SEGraph.SetPlotBackground(Crt.Black);
  SEGraph.ClearGraph;
  SEGraph.SetAxesType(0, 0);
  SEGraph.AutoAxes(x,y,DataPoints,1);
  Graph.SetColor(Colour);
  SEGraph.TitleXAxis('altitude (km)');
  SEGraph.TitleYAxis('counts');
  SEGraph.TitleWindow('LIDAR');
  Graph.SetColor(Crt.White);
  SetLineStyleXX(DottedLn, 0, NormWidth);
  SEGraph.DrawGridX(10);
  SEGraph.DrawGridY(5);
  SetLineStyleXX(SolidLn, 0, NormWidth);
  Graph.SetColor(Crt.White);
  SEGraph.SetCurrentWindow(CountScreen);
  SEGraph.LinePlotData(x, y, DataPoints, Colour, SolidLine);
end; {TExtinct.PlotCounts}

{-----------------------------------***-------------------}

procedure TExtinct.PlotDisplay(Colour1, Colour2 : Word);

const
  SolidLine  : Integer = 0;
  Resolution : Integer = 2;

var
  i          : Word;
  x, y       : StdHdr.VeryLongVector;
  DataPoints : Word;
  kStr, r0Str, rmStr : String;

begin
  DataPoints := Length div Resolution;
  for i := 0 to DataPoints-1 do begin
    x[i] := i*Resolution*Step;
    y[i] := Coefficients[i*Resolution];
  end; {for}
```

```
Str(k  :7 :3, kStr);
Str(r0 :7 :3, r0Str);
Str(rm :7 :3, rmStr);

SEGraph.DefGraphWindow(0, 239, 639, 479, CoeffScreen);
SEGraph.SetCurrentWindow(CoeffScreen);
SEGraph.SetViewBackGround(Crt.LightGray);
Graph.SetColor(Crt.White);
SEGraph.BorderCurrentWindow(Crt.White);
SEGraph.SetPlotBackground(Crt.Black);
SEGraph.ClearGraph;
SEGraph.SetAxesType(0, 0);
SEGraph.AutoAxes(x,y,DataPoints,1);
Graph.SetColor(Colour1);
SEGraph.TitleXAxis('altitude (km)');
SEGraph.TitleYAxis('extinction coefficient (1/km)');
SEGraph.TitleWindow('LIDAR');
SEGraph.LabelGraphWindow(500, 900,
                         'k: '+kStr+'  r0: '+r0Str+'km'+'
                          rm: '+rmStr+'km', 1, 1);
Graph.SetColor(Crt.White);
SetLineStyleXX(DottedLn, 0, NormWidth);
SEGraph.DrawGridX(10);
SEGraph.DrawGridY(5);
SetLineStyleXX(SolidLn, 0, NormWidth);
Graph.SetColor(Crt.White);
SEGraph.SetCurrentWindow(CoeffScreen);
SEGraph.LinePlotData(x, y, DataPoints, Colour1, SolidLine);

DataPoints := Length div Resolution;
for i := 0 to DataPoints-1 do begin
  x[i] := i*Resolution*Step;
  y[i] := Counts[i*Resolution];
end; {for}

SEGraph.DefGraphWindow(0, 0, 639, 239, CountScreen);
SEGraph.SetCurrentWindow(CountScreen);
```

```
  SEGraph.SetViewBackGround(Crt.LightGray);
  Graph.SetColor(Crt.White);
  SEGraph.BorderCurrentWindow(Crt.White);
  SEGraph.SetPlotBackground(Crt.Black);
  SEGraph.ClearGraph;
  SEGraph.SetAxesType(0, 0);
  SEGraph.AutoAxes(x,y,DataPoints,1);
  Graph.SetColor(Colour2);
  SEGraph.TitleXAxis('altitude (km)');
  SEGraph.TitleYAxis('counts');
  SEGraph.TitleWindow('LIDAR');
  Graph.SetColor(Crt.White);
  SetLineStyleXX(DottedLn, 0, NormWidth);
  SEGraph.DrawGridX(10);
  SEGraph.DrawGridY(5);
  SetLineStyleXX(SolidLn, 0, NormWidth);
  Graph.SetColor(Crt.White);
  SEGraph.SetCurrentWindow(CountScreen);
  SEGraph.LinePlotData(x, y, DataPoints, Colour2, SolidLine);
end; {TExtinct.PlotDisplay}

{-----------------------------------***-------------------}

procedure TExtinct.ClearDisplay;

begin
  SEGraph.CloseSEGraphics;
end; {TExtinct.ClearDisplay}

{-----------------------------------***-------------------}

  {null}
end.

{-----------------------------------***-------------------}
```

Laser and Particle Beams (1994), *vol.* 12, *no.* 3, *pp.* 531–538
Printed in the United States of America

Applications of the colliding shock lens

By M.M. MICHAELIS, N. LISI, R. KUPPEN, R. BUCCELLATO, AND A. PRAUSE
Department of Physics, University of Natal, Durban, South Africa

(Received 10 January 1994; accepted 19 January 1994)

The colliding shock lens is described briefly. Possible applications, industrial drilling and cutting, laser Q-switching and spatial filtering, ultrahigh-power applications, and "all gas lasers" are proposed. The time evolution, scaleability, and repetition rate operation are investigated.

1. Introduction

At a previous ECLIM, we described work with continuous gas lenses (Michaelis *et al.* 1991a). A novel pulsed gas lens has now been developed relying on the interaction of converging shocks in air. Here we report on the initial studies of the parameters of this lens undertaken to see which applications, if any, show promise. The article is divided into four parts: a brief description of the colliding shock lens (CSL); a list of potential applications suitable for the CSL; a study of the performance of various CSL designs; and concluding remarks.

2. The colliding shock lens

Gas lenses invented at Bell Labs in the early 1960s were soon discarded as bulky devices with a narrow field of view. A slight renewal of interest has resulted from a demonstration that they are able to focus laser light to drill holes (Notcutt *et al.* 1988; Michaelis *et al.* 1991a) or to generate laser-produced plasmas (Waltham *et al.* 1990). We have shown that they have sufficiently good optical quality to serve as objective lenses in telescopy (Michaelis *et al.* 1991b). We have also proposed that large aperture pulsed gas lenses could play an important part as the final focusing element in a laser-driven fusion reactor (Buccellato *et al.* 1993a). More recently (Buccellato *et al.* 1993b) we have described a different type of pulsed gas lens, the CSL.

The simplest CSL consists of 16 needles disposed in opposition on the arc of a circle (figure 1a). Eight electric arcs are struck between opposing points and generate eight shock waves that converge at the center. A cigar-shaped region of high gas density gradient results. If a pulsed laser is synchronized soon (500 ns) after the shock collision and directed through the center, it can produce a focus. Figures 1b and 1c show other CSL designs with different number of arcs and different diameters. We distinguish between the "electrical diameter," that of the circle of arcs, and the optical aperture, that of the effective lens. The optical aperture turns out to be an order of magnitude smaller than the electrical diameter. It is not yet clear whether the optical aperture will scale with the system geometry or with the typical shock width dimensions. The former would mean that the f-number could remain more or less constant with increasing optical aperture; the latter, that it does not scale at all. A first attempt at scaling up the first 1.2-cm electrical diameter device to 3 cm

 0263-0346/94 $5.00 + .00

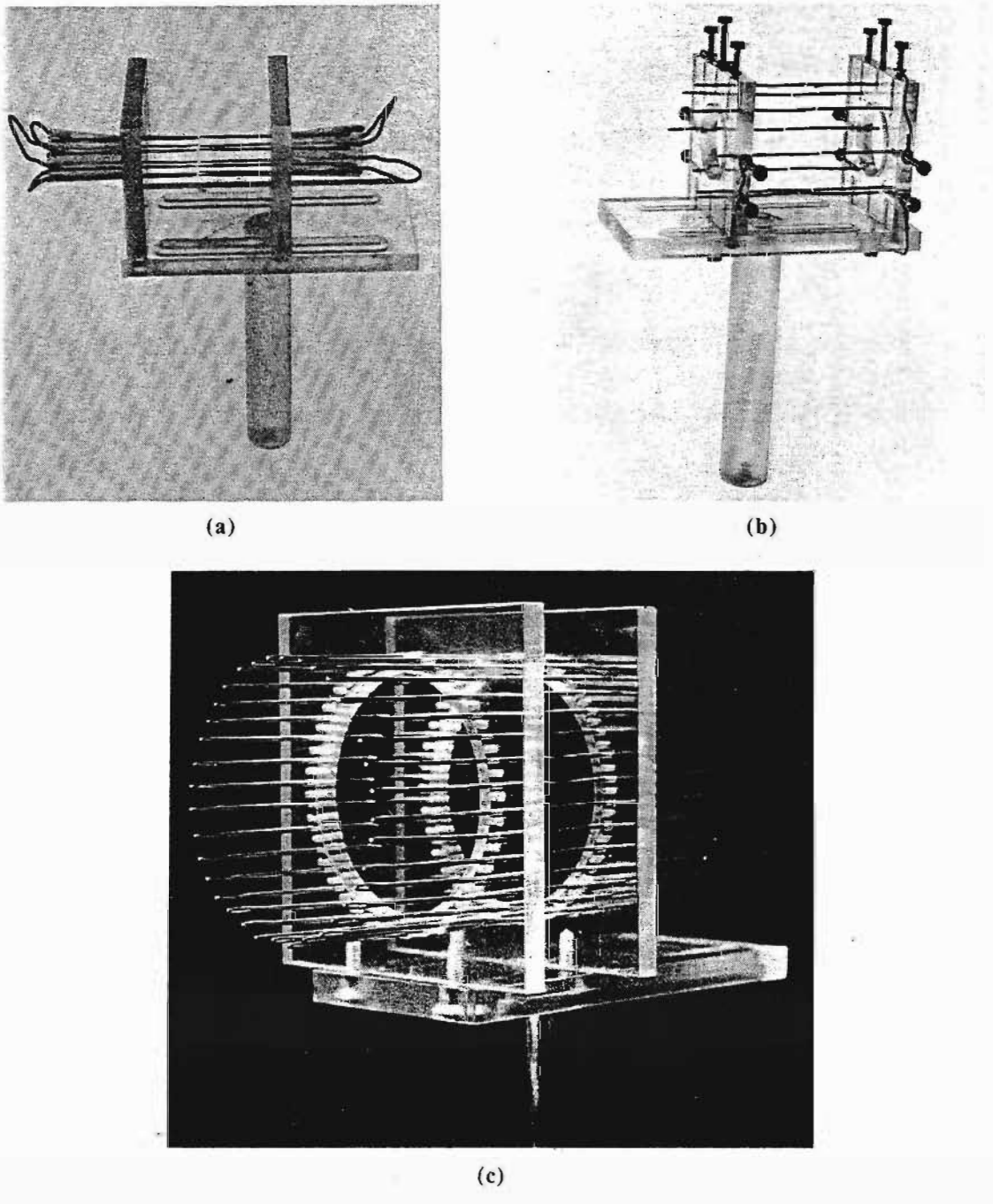

FIGURE 1. Colliding shock lenses. (a) 16-pin, 8-arc device. Electric diameter 1.2 cm. Optical aperture 2 mm. (b) 3-cm electric diameter device. Optical aperture approximately 3 mm. (c) 36-pin, 3-cm electric diameter device.

(figure 1b) indicates that the truth lies somewhere in between. Increasing the number of pins (figure 1c) did not have any obvious effect.

Depending on the time at which the pulsed laser is fired with respect to the arcs, a variety of illumination patterns results; figure 2 shows a sequence obtained with an eight-arc device. The frames are taken directly with a lensless television camera disposed 40 cm away from the center of the lens. The first three frames show the shock waves propagating almost undisturbed through one another. The detailed illumination pattern (i.e., dark and bright rings, coarse and fine fringes) is best understood by referring to articles on refractive fringe diagnostics (Bacon *et al.* 1989; Michaelis *et al.* 1991c). The next frames show nonlinear interaction between the shock waves resulting in noncylindrically symmetric illumination pat-

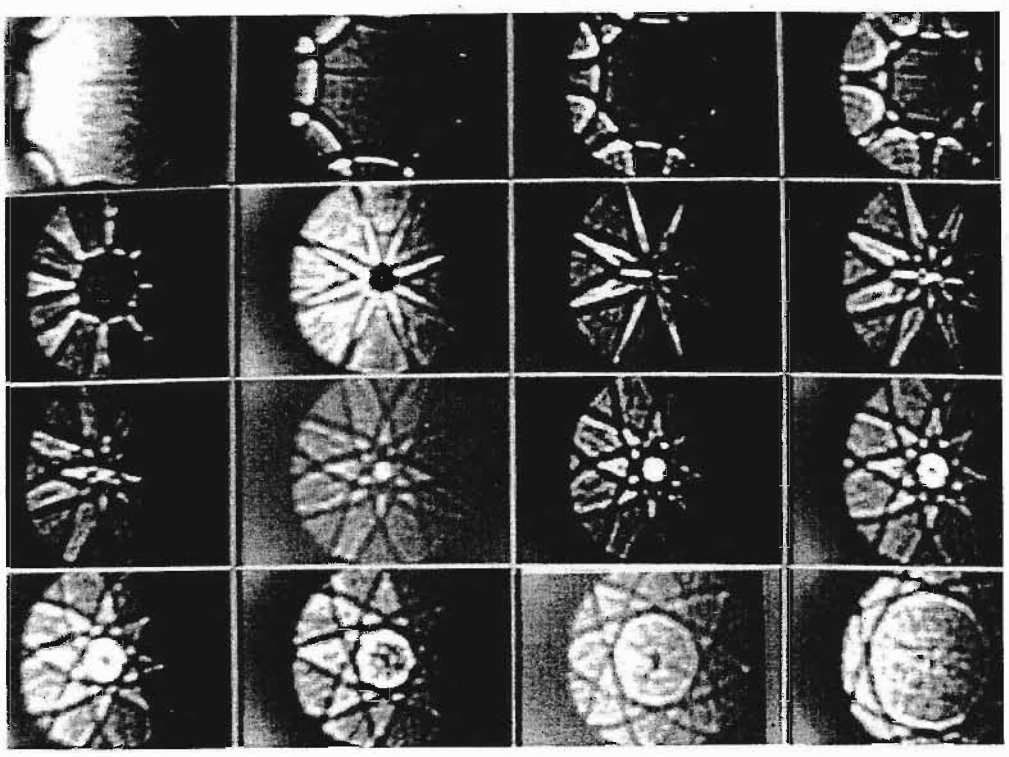

FIGURE 2. Illumination patterns 40 cm from the lens of figure 1a, at various times after the arcs: 3.2, 5, 6, 6.9, 8, 10, 10.4, 10.9, 11.3, 11.6, 11.8, 12.2, 12.4, 13.1, 14, 15.6 μs.

terns. The interesting point is that after the shocks have collided at the center, there is a cylindrically symmetric core. The shocks have forgotten where they originated. A sharp focus is seen in the seventh frame. An enlargement of the focal region (figure 3) shows an interesting set of Airy ring-like patterns centered on the strongly saturated focus.

3. Potential applications

3.1. *Drilling, cutting, and welding*

A good reason why lasers have not penetrated every industrial workshop is that their output windows and lenses are expensive and sensitive devices. We have already shown that CO_2 lasers coupled to gas lenses are capable of drilling through thick steel sheets (Michaelis *et al.* 1991a). However, the lenses we used were unwieldy CW devices with very long focal lengths (of the order of 80 cm.) The "dream" gas lens for this purpose would be a short focal length device (10 cm) capable of being "rep-rated" (100 Hz), with an optical aperture of at least 1 cm and minimal power consumption and weight.

3.2. *Q-switching and spatial filtering*

The combination of a CSL and a pinhole within the laser resonator could in principle serve to simultaneously Q-switch and spatially filter a laser oscillator. The pinhole would need to be under vacuum or, if the pulse is short enough, in helium gas to prevent breakdown. But Q-switching requires opening times of about 10–100 ns (Siegman 1986). For engineering applications, the focal length should not vary too quickly; whereas for Q-switching and beam handling (e.g., isolator) functions, fast switching is essential.

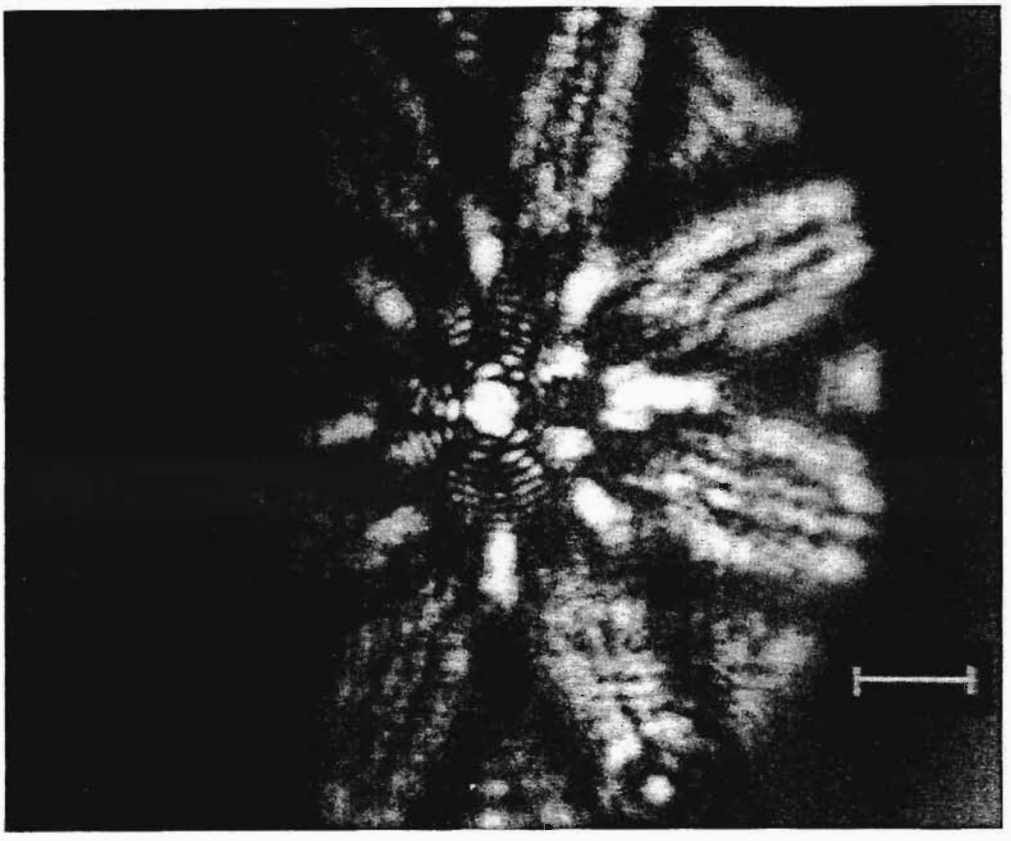

FIGURE 3. Magnified central region of 11.3-μs frame. (Bar = 1 mm)

3.3. *Ultrahigh-power and "all gas" lasers*

It is well known that even under clean room conditions lenses operating for pulse lengths of tens of nanoseconds start to fail at intensities in the GW/cm^2 range. Also, multiphoton processes at ultrahigh intensities render conventionally transmitting materials opaque or absorbing. We have previously pointed out that gas lenses could help alleviate these problems (Michaelis *et al.* 1991a). We foresee, without having the means to observe it, that very high powers may heat the gas and change the characteristics of the lens, just as in atmospheric "thermal blooming" (Barnard 1989). But for intermediate powers, the CSL could fill the present gap.

The final application we envisage is that of an "all gas" (or nearly all gas) system. Conventional pulsed gas laser systems are designed with beam diameters corresponding to the breakdown thresholds of solid optical components. A combination of aerodynamic windows and diverging and converging gas lenses could give gas laser design a new degree of freedom.

4. Performance of the CSL

All the applications listed above pose the following questions:

a. How good is the focus? Is it near diffraction limited?
b. How short is the focal length?
c. How quickly do CSLs switch, and how long do they last?
d. How large is the aperture, and is any light lost?
e. Can they be "rep-rated"? How much power do they consume?

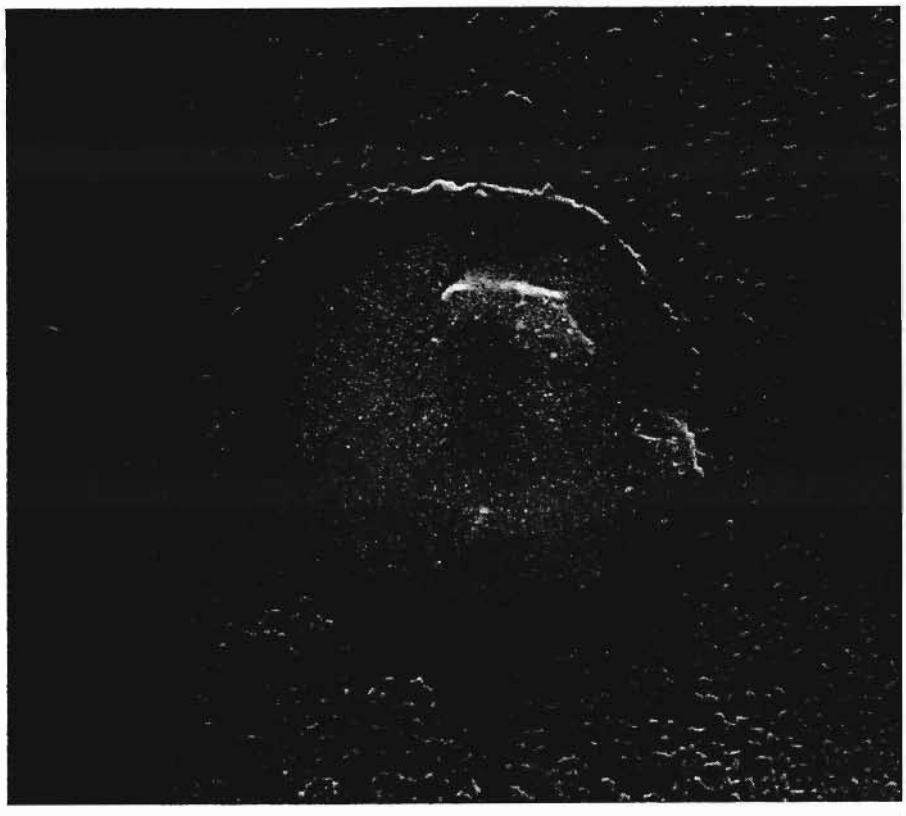

FIGURE 4. 130-μm burn pattern in aluminum foil obtained with lens of figure 1b.

a. From the very first experiments, we realized that this was somewhat surprisingly, given the limited number of arcs, an excellent lens. Figure 4 shows a burn pattern in aluminum foil obtained with an eight-arc lens. The optical aperture of the lens was 3 mm and the focal length 40 cm, so the diffraction limit would give a 130-μm hole. The central hole is approximately 130 μm.

b. The shortest focal length for an eight-arc device is about 20 cm. This is too long for many applications. We have already begun testing a double-ring device, and there is no apparent reason why several rings should not reduce the focal length to the 10-cm range.

c. For this purpose we have measured the switching ability. Our experimental apparatus is very simple and consists of a 10-mW HeNe laser followed by the CSL and a receiving photodiode at a distance L with a pinhole of diameter Φ immediately in front of it. We vary the distance L, the diameter Φ, and also the energy delivered to the shocks by changing the discharge capacitor. Figure 5 shows a typical switching time curve. In figure 6 we show how the switching rise time and the maximum signal vary with the pinhole size Φ at a fixed distance L, and in figure 7 we show how the same quantities vary with the focal length L for fixed Φ. As can be seen from switching curves like those in figure 5, the fall time of the signal is always comparable with the rise time (to within, say 50%), the latter being the critical quantity for Q-switching. The signals have been normalized to the signal produced by a 3-mm aperture, 50-cm focal length, spherical glass lens on the same photodiode and a pinhole $\Phi = 250$ μm. Figure 8 is like figure 6, but for a capacitor value of 1 μF. We believe that by increasing the shock energy we can make the switching faster.

The present CSL is thus a little too slow for Q-switching. But we have a concept for speeding it up that involves a multiple lens. Another problem in using this device for Q-switching is that it requires the presence of a pinhole in the cavity and the concomitant possibility of too high a radiation flux through it. Our idea is that this system could be worthwhile for cheaply Q-switching a small laser system.

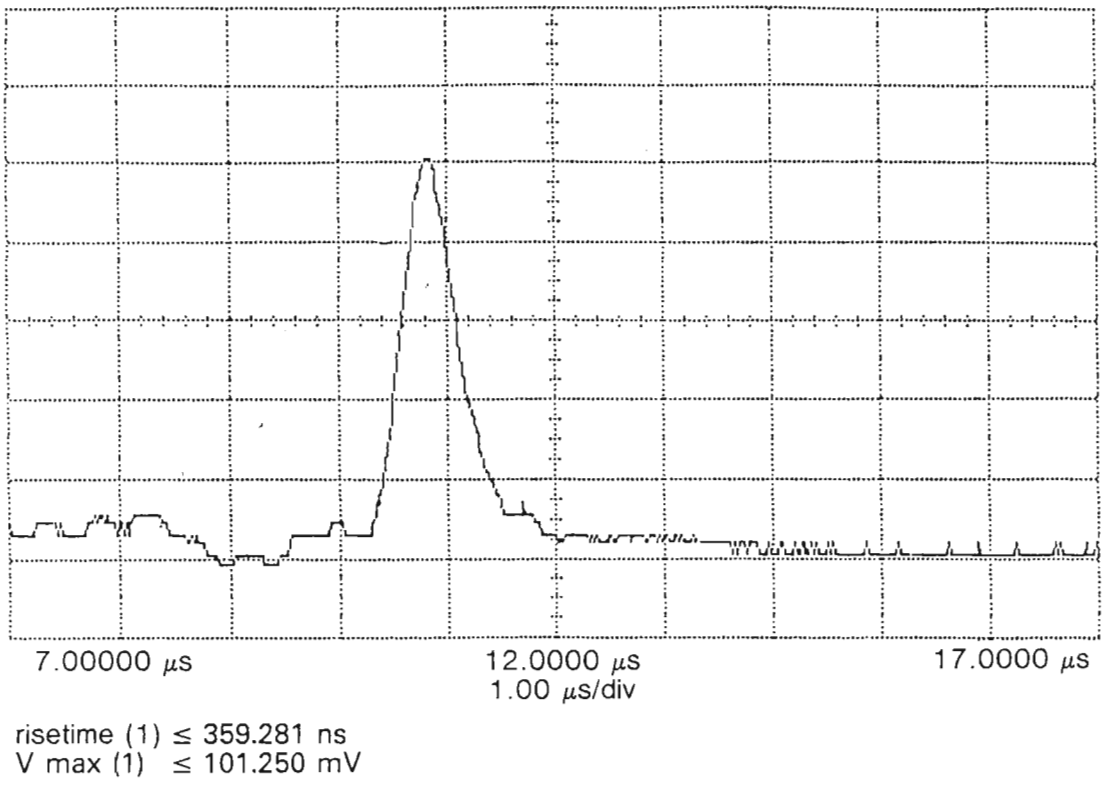

FIGURE 5. Switching curve. $L = 40$ cm, $\Phi = 300$ μm, $C = 5$ nF.

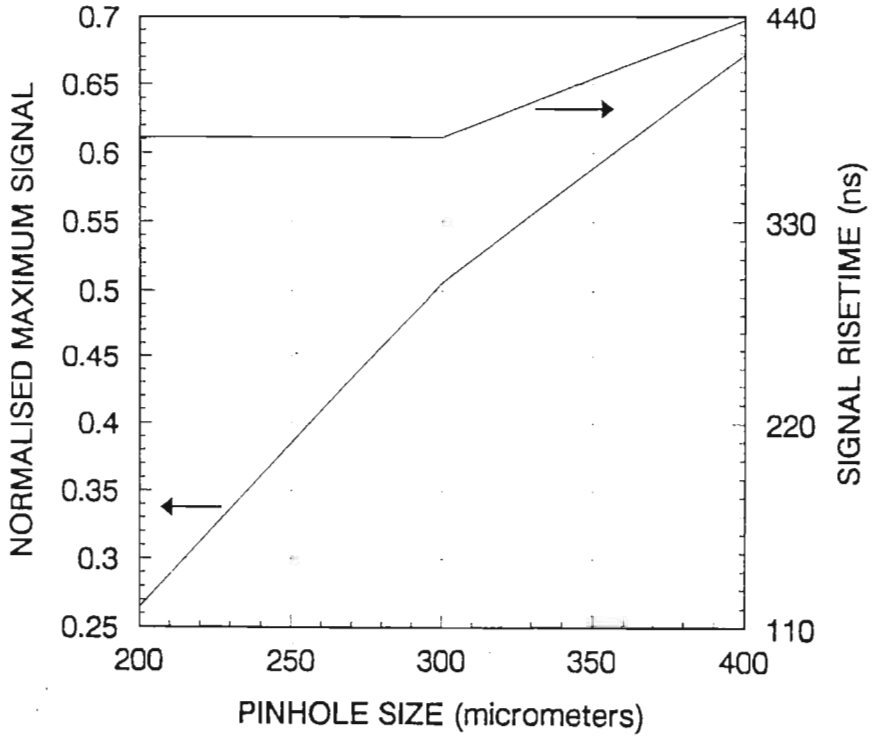

FIGURE 6. Switching rise time and maximum normalized signal versus pinhole size for $L = 40$ cm, $C = 5$ nF.

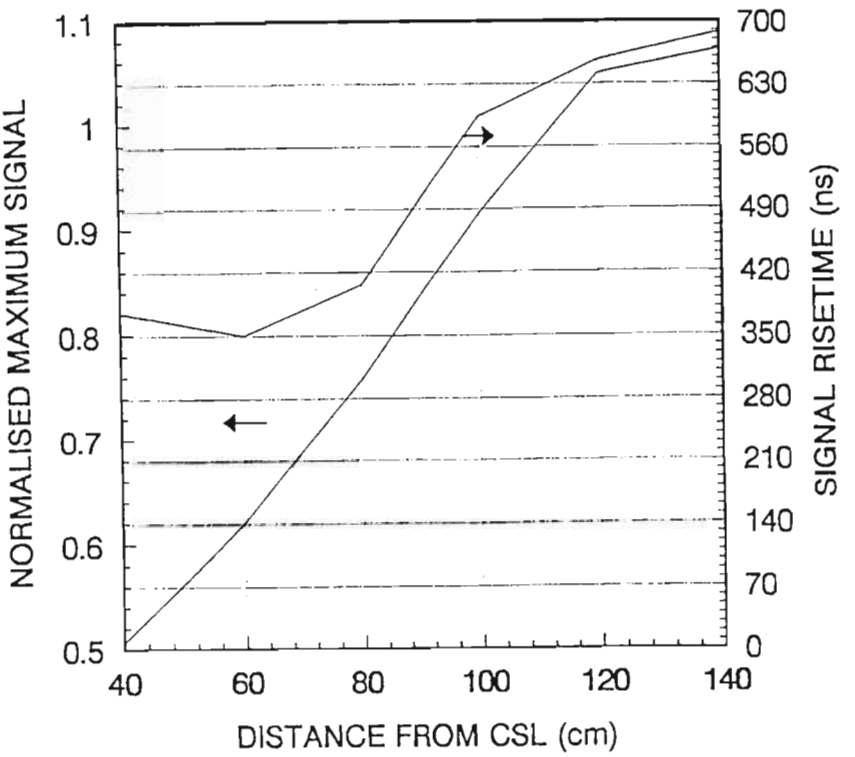

FIGURE 7. Switching rise time and maximum normalized signal versus distance from the CSL for $\Phi = 300\ \mu$m.

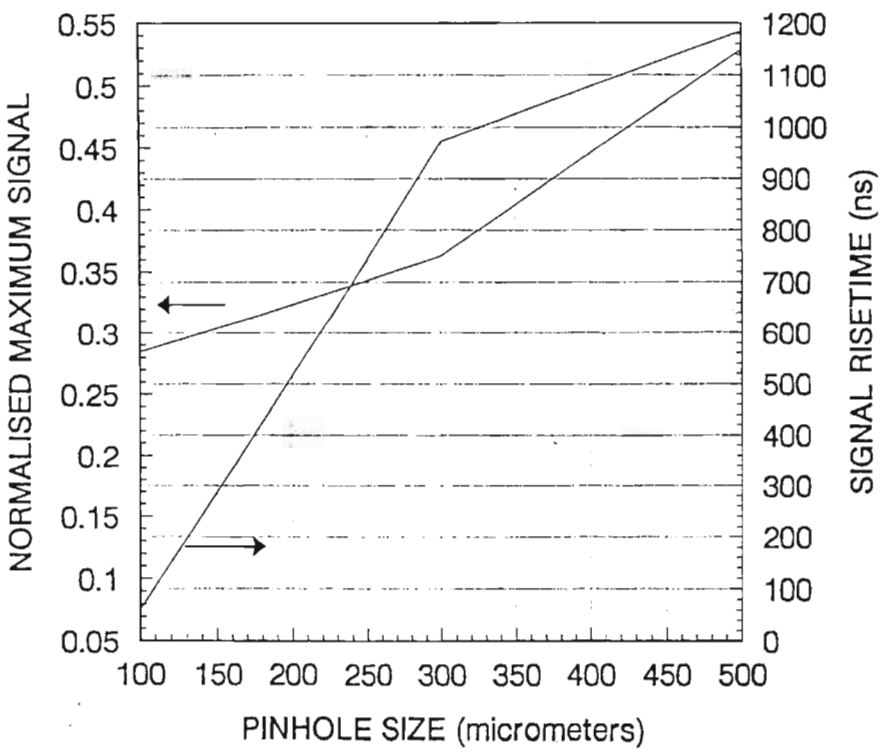

FIGURE 8. Switching rise time and maximum normalized signal versus pinhole size for $L = 40$ cm, $C = 1$ nF.

d. Possibly the worst feature of CSLs is the large electro-optic aspect ratio. The largest aperture obtained so far was only 4 mm. We plan to test a 10-cm electrical diameter lens in the hope of obtaining an 8-mm optical aperture. Another worrying feature of these lenses is that they are lossy. This, we believe, is inherent to their shock wave structure. The rear of the reflected shock refracts some light "in the wrong direction." This is to be expected from refractive fringe studies of shocks (Michaelis *et al.* 1991c). Orientatively we estimate the loss to be about 10%, slightly larger than that due to reflection in conventional lenses.

e. The question of "rep-rating" the lens has only been partially answered experimentally for want of a suitable high-voltage power supply. Operation at 10 Hz confirmed our expectations that the lens could run at moderate frequencies without degradation of the focus. At this repetition rate a typical switching curve such as that in figure 5 remains virtually unaltered. Based on dimension and speed of sound arguments, we would expect the limiting period to be of the order

$$\frac{\text{electrical diameter}}{\text{sound speed}} \approx 1 \text{ ms}.$$

The corresponding "rep-rate" would be 1 kHz, a useful frequency for industrial applications. The final question is that of power consumption. At a rep rate of $f = 1$ kHz, our present eight-pin lens would consume

$$W = f \cdot 1/2 \cdot CV^2 = 1 \text{ kW} \qquad (C = 5 \text{ nF}, V = 20 \text{ kV}).$$

This is a considerable amount of pulsed power. To reduce this we tested an enclosed CSL that confines the arcs to two rather than three dimensions. An order of magnitude reduction in energy consumption occurs. However, that may be counteracted by the necessity of increasing the electrical diameter.

5. Conclusion

The novel CSL appears to be on the borderline of becoming a promising optical component. The focus is good, but the lens is slightly lossy. The lens focuses quickly, but not quite quickly enough for efficient Q-switching. The aperture is disappointingly small but might be scaleable. The lens may be rep-rated but consumes appreciable electrical power and could be incredibly noisy.

Acknowledgments

This work was supported in part by the Plasma Physics Research Institute (P.P.R.I.) and the Laser Applications Research Institute (L.A.R.I.S.A.).

REFERENCES

BARNARD, J.J. 1989 *Appl. Opt.* **28**, 438.
BACON, M. *et al.* 1989 *J. Appl. Phys.* **66(3)**, 1075.
BUCCELLATO, R. *et al.* 1993a *Opt. Laser Technol.* **25**, 247.
BUCCELLATO, R. *et al.* 1993b *Opt. Commun.* **101**, 350.
MICHAELIS, M.M. *et al.* 1991a *Laser Part. Beams* **9**, 641.
MICHAELIS, M.M. *et al.* 1991b *Nature* **353**, 547.
MICHAELIS, M.M. *et al.* 1991c *Opt. Laser Technol.* **23**, 283.
NOTCUTT, M. *et al.* 1988 *Opt. Laser Technol.* **20(5)**, 243.
SIEGMAN, A.E. 1986 *Lasers* (University Science Books, Mill Valley, California).
WALTHAM, J.A. *et al.* 1990 *Laser Particle Beams* **8(1)**, 361.

a reprint from Applied Optics

Colliding shock lens as an intracavity Q-switch element

N. Lisi, M. M. Michaelis, R. Buccellato, M. Kuppen, and A. Prause

We show how a varifocal pulsed gas lens, the colliding shock lens, can be used as an intracavity element to Q switch a ruby laser. By placement of the shock lens in tandem with a second lens, a giant pulse is obtained. The second lens may be a conventional glass lens or a continuous-wave gas lens.

The quality factor or Q switching of lasers is an important method of enhancing the power of pulsed lasers.[1] Mechanical Q switches and dye cell switches have generally been discarded in favor of triggerable opto-electronic devices based on rotation of polarization by the use of the Kerr or Pockels effect. In this paper we discuss another form of triggerable Q switching that makes use of a new kind of gas lens. This lens, the colliding shock lens (CSL),[2] was developed in our laboratory, in step with the recent revival of interest in gas-lens optics.[3,4]

The principle of colliding shock Q switching (CS-QS) relies on the insertion of a steady-state converging lens and of the rapidly varying CSL in a laser cavity. The CSL focal length and lens diameter increase with time over a few microseconds. When the CSL is switched off, the steady-state lens renders the cavity unstable. Only when the CSL is switched on and while the focal regions of the two lenses overlap does the laser cavity become stable and the losses low. If this condition is achieved when the population inversion is at its peak in the active medium, lasing occurs in the form of a giant pulse.

In the experiment designed to test the CS-QS concept, a commercial ruby laser (1975 Korad Model K1) was modified to incorporate additional Q-switching components. Figure 1(a) is a schematic of the experiment. The laser consists of a ruby head, full reflector R1, and output coupler R2. The Q-switching components are CSL L2, continuous lens L1, and fluorescence-sensing photodiode PD1.

The authors are with the Plasma Physics Research Institute, University of Natal, Durban, South Africa 4001.

Received 21 March 1994; revised manuscript received 9 September 1994.

0003-6935/95/060942-04$06.00/0.

The CSL consists of eight arc discharges, struck simultaneously between pairs of opposing points located on the arc of a circle as illustrated in Fig. 1(b). Each point explosion produces an expanding spherical shock wave. After the eight shock waves collide at the center of the circle, a cigar-shaped, high-density, axially symmetric core expands outward. Focusing is due to the radially symmetric density gradients within the expanding region. As the lens diameter increases, the density diminishes and the focal length increases as depicted in Fig. 2. The CSL used for these experiments was specially chosen for its fast switching and large optical aperture. It consists of a 5.0-cm-diameter cylinder closed at both ends. The end plates that carry the 16 pins that form the eight gaps are 1.0 cm apart. The gaps are set to 1.5 mm, and the diameter of the circle of pins is 3.0 cm. The central apertures are 1.0 cm in diameter. A 100-nF capacitor, charged to 17 kV, is connected to the eight gaps in series by a triggerable spark gap. This series connection ensures simultaneous arcing.

Lens L1 can be either a conventional solid-state device or a continuous-wave gas lens. The spinning-pipe gas lens[5] used in some experiments, consists of a 1.0-m-long, 2.0-cm-diameter heated tube, spun at 30 Hz. The rotation centrifuges warm air out of the two ends and causes cold air to be aspired along the axis. The resulting density and refractive-index gradient produces a long-focal-length lens, the quality of which fluctuates.[6] One can vary the focal length from 1.5 m to several meters (as measured from the center of the pipe) by changing the pipe temperature and rotation speed. The two flat end mirrors are a full reflector, $R_1 = 96\%$, and an output coupler, $R_2 = 45\%$.

The operation sequence for all CS-QS experiments is the following: First the ruby flash lamp is fired and the PD1 photodiode detects the fluorescence signal from the active medium. This signal is elec-

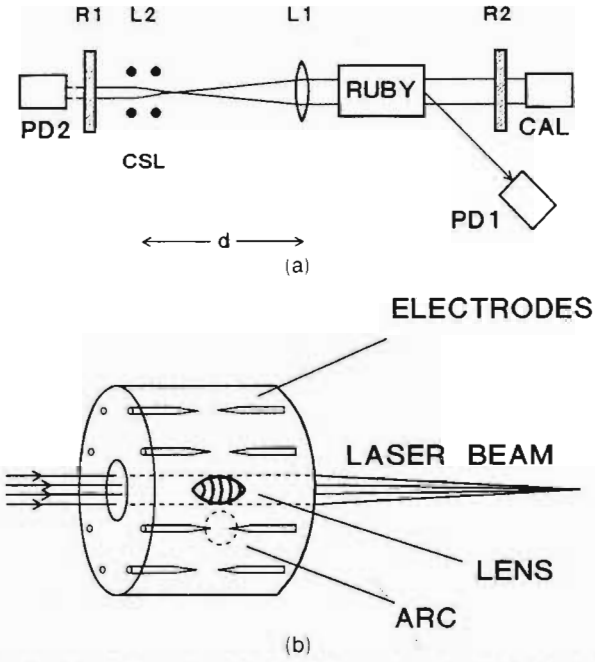

Fig. 1. (a) Schematic of the CS-QS experiment: PD's, photodiodes; CAL, calorimeter. (b) CSL geometry.

tronically delayed and used as a trigger for the CSL master spark-gap circuit. The signal from photodiode PD2, placed behind full reflector R_1, is read by a storage oscilloscope and yields the laser-pulse waveform. The laser-beam energy is measured with a calorimeter. A burn pattern of the attenuated beam at the focus of a lens can be used to measure the divergence of the beam.

The cavity is operated in three different modes described below in detail. Mode a maximizes the output energy and beam diameter. Mode b minimizes the Q-switched laser-pulse duration. Mode c explores the feasibility of a cavity with intracavity beam-expansion optics consisting entirely of gas.

The stability of the laser resonator can be determined in terms of the complex parameter m, which, in the formalism of the ray matrix optics, is half the trace of the round-trip resonator matrix.[7] For an unstable resonator, $abs(m) > 1$. In this case we define the magnification M as

$$M = \begin{cases} m + (m^2 - 1)^{1/2} & \text{if } m > 1 \text{ (positive branch)} \\ m - (m^2 - 1)^{1/2} & \text{if } m < -1 \text{ (negative branch),} \end{cases} \quad (1)$$

where M is the amplification of the beam cross section per round trip and can be related to the cavity losses. When $abs(m) < 1$, the cavity is stable, while $abs(m) = 1$ for a plane-parallel configuration, which corresponds to the confocal situation of the intracavity telescope.

In mode a, L1 is a 200-cm focal-length glass lens. The lens separation d is 250 cm. The condition $abs(m) = 1$ is achieved when $f_{CSL} = 50$ cm. The CSL lens aperture (d_{CSL}) is 3.0 mm (see Fig. 1), and the beam fills the ruby rod (10 mm). At slightly later times, the resonator becomes stable, and we expect lasing to occur. A drawback of this operating condition is that the cavity is long (3.0 m), as is consequently the rise time of the laser pulse. In this case the initial magnification of the resonator (before the CSL is operated) is low, $M = 2.8$. We must therefore operate the flash lamp below 4.3 kV to avoid free-running lasing. A 2.0-J laser pulse of a duration of 360 ns (FWHM) is observed 5 μs after the shock collision. Figure 3 shows the pulse waveform.

In mode b, L1 is a 50-cm focal-length glass lens ($d = 100$ cm). Again $m = 1$ is achieved when $f_l = 50$ cm, $d_{CSL} = 3.0$ mm, and the beam diameter on the output coupler is expected to be 3.0 mm. The initial magnification M is now 4.4, and free running is inhibited at any flash-lamp voltage. We operated the flash lamp at 4.5 kV. In this case we expect shorter

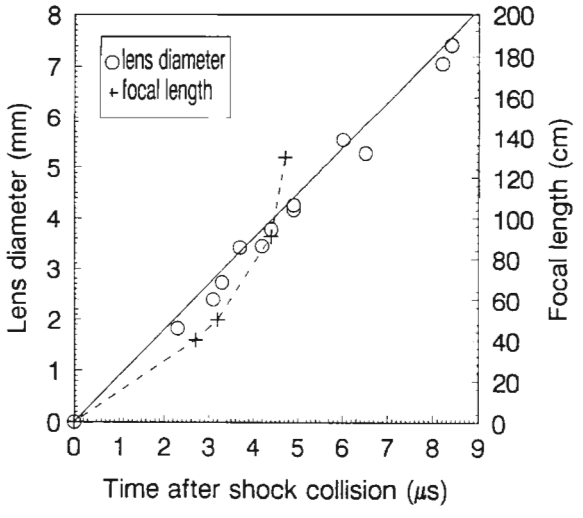

Fig. 2. CSL characteristics: Evolution of focal length and effective diameter after the shock collision.

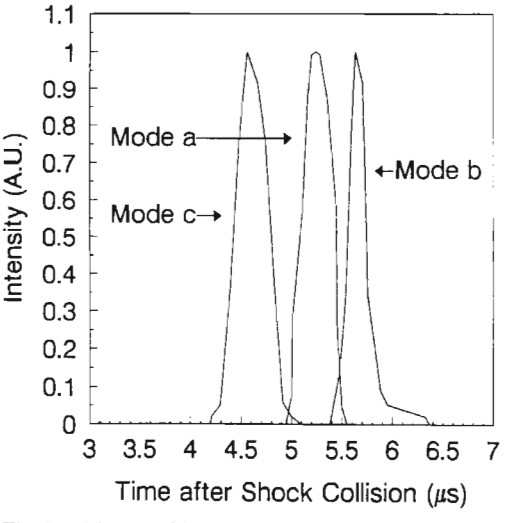

Fig. 3. Measured laser-pulse-intensity waveforms.

pulses and a very narrow beam together with lower energy. A 100-mJ pulse of a duration of 175 ns (FWHM) is observed 5.5 μs after the shock collision (see Fig. 3). On a few occasions when the CSL alignment appeared to be optimized, a pulse length of approximately 50 ns was observed.

In mode c, L1 is a spinning-pipe gas lens operated at a 200-cm focal length. For this all-gas Q switch, we expected similar performance to mode a. Figure 3 shows a 375-ns (FWHM) pulse 4.5 μs after the shock collision. However, the energy for this mode is now slightly higher (3.0 J). The absence of reflective losses in the cavity appears to outweigh the effect of spinning-pipe gas-lens aberrations.

In Table 1 we summarize the results of the experiment. The energy values reported in this paper are the maximum values obtained over a large number of experiments. Although the fluctuations are large, especially for mode c, which in this case is due to the unstable behavior of the spinning-pipe gas lens,[5] we noted that the operations do not critically depend on the cavity alignment and the gas-lens aberrations.

We now examine in greater detail the evolution of the cavity geometry after the CSL shocks have collided and how this affects the cavity losses. The losses can be split into two terms. The first term is constant and takes into account diffraction, surface reflections from lens L1, and the ruby-rod surface imperfections.

The second term depends on the cavity geometry and will vary explicitly with time. If no apertures are present in the cavity, the losses depend on only the parameter m and can be calculated according to the loss formula[1]

$$L = \begin{cases} 1 - 1/M^2 & \text{if } abs(m) > 1 \\ 0 & \text{if } abs(m) \le 1, \end{cases} \tag{2}$$

where L is the fractional intensity loss of an input beam that is entering the output coupler and whose linear magnification over one round trip is M. The evolution of M and the corresponding L is shown in Fig. 4 for mode a.

A simple model of the laser system was developed.[8] Because of the presence of apertures in the cavity, such as the ruby-rod external diameter and the CSL aperture, the expression for the loss term is more complex than that given by Eq. (2) and depends on the input beam cross section. The expression for the loss term coincides with Eq. (2) only for light that is traveling close to the optical axis. This was taken into account in the calculation of the losses as a function of the distance from the optical axis, which was carried out with the formalism of matrix optics. The laser beam was subdivided into a collection of annular beams. The laser rate equations were solved for each annulus, using the fourth-order Runge Kutta numerical method with variable step size. Independently an approximate computation of the beam divergence is performed for the resonator geometry that exists when lasing is at its peak. We generate a uniform planar distribution of rays at the position of the ruby rod, and we follow the path of each of the rays for a given number of round trips, recording the values of their angle at the output coupler. These values are used to calculate the beam divergence.

Figure 5 shows the computed laser-beam-intensity waveform in the center of the beam for modes a, b, and c. The computed values of the laser energy, pulse length, beam diameter, and divergence are summarized in Table 2. The discrepancy between the measured and the computed pulse lengths can be

Table 1. Summary of the Results of the CS-QS Experiment[a]

Mode	E_{max} (J)	t_p (ns)	d (mm)	div (mrad)
a	2.0	360	8.0	1.0
b	0.1	175	2.0	3.3
c	3.0	375	8.0	1.4

[a] E_{max}, maximum recorded value of the output energy in the three different resonator geometries; t_p, typical pulse duration (FWHM); d, laser spot diameter; div, divergence.

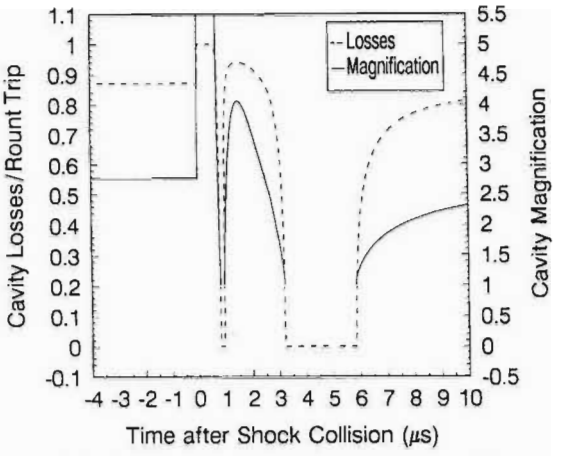

Fig. 4. Evolution of the cavity magnification M and losses L for the paraxial rays (mode a).

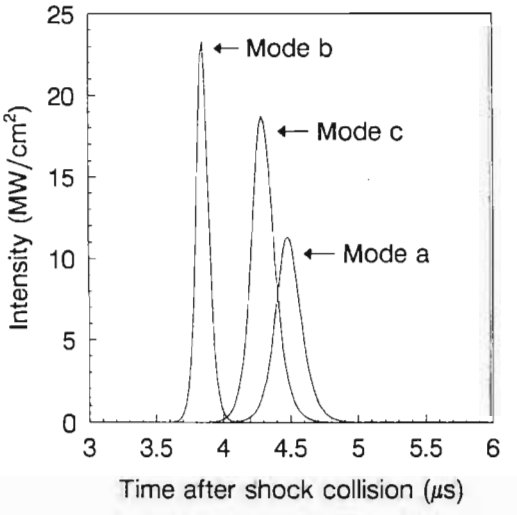

Fig. 5. Computed laser-pulse intensities in the center of the beam.

Table 2. Summary of the Computational Results of the CS-QS

Mode	E_{max} (J)	t_p (ns)	d (mm)	div (mrad)
a	2.0	225	10.0	1.0
b	0.13	105	2.8	4.0
c	3.0	200	10.0	0.9

attributed to the aberrations of the gas lenses, which are not included in the model.

In conclusion, we have demonstrated a novel Q-switching configuration that can use gas optics only. The advantages of the method are no damage threshold, both for high peak power and average power, and the absence of polarization and a polarizer. A major disadvantage is the necessity of having a long cavity, which results in a long laser pulse. Improvements in CSL design and performance may correct this problem.

We thank W. de Beer and D. Davies for unflagging technical support, P. Di Lazzaro, M. A. Hellberg, and M. H. Key for discussions, and the Foundation for Research and Development and the Laser Applications Research Institute of South Africa for financial support.

References

1. W. Koechner, *Solid-State Laser Engineering*, 2nd ed. (Springer-Verlag, Berlin, 1988), Chap. 8, p. 410.
2. R. Buccellato, N. Lisi, and M. M. Michaelis, "Colliding shock lens," Opt. Commun. **101,** 350–355 (1993).
3. M. M. Michaelis, C. A. Dempers, M. Kosch, A. Prause, M. Notcutt, P. F. Cunningham, and J. A. Waltham, "A gas telescope," Nature (London) **353,** 547–548 (1991).
4. B. L. Xie, S. J. Xia, and Q. T. Chow, "Gas varifocal lens," Chin. Phys. Lett. **2,** 509–512 (1985).
5. M. Notcutt, M. M. Michaelis, P. F. Cunningham, and J. A. Waltham, "Spinning pipe gas lens," Opt. Laser Technol. **20,** 243–250 (1988).
6. N. Lisi, R. Buccellato, and M. M. Michaelis, "Optical quality and temperature of a spinning pipe gas lens," Opt. Laser Technol. **26,** 25–27 (1994).
7. A. E. Siegman, *Lasers*, 2nd ed. (University Science, Mill Valley, Calif., 1986), Chap. 15, p. 599.
8. N. Lisi, "C.S.L. Q switch," Internal rep. (Department of Physics, University of Natal, Durban, South Africa, 4001, February 1993).

Scaling up the colliding shock lens

M. Kuppen, M. M. Michaelis, R. Buccellato, and N. Lisi
Plasma Physics Research Institute, University of Natal, Durban, South Africa

(Received 16 March 1995; accepted for publication 14 June 1995)

In this paper we characterize the behavior of a new pulsed gas lens, the colliding shock lens. We show how input energy, electrical diameter, number of discharge electrodes, and enclosing the discharges, affect its optical aperture and focal length. Experimental results are presented for three different lenses and for a 1 cm aperture lens with a focal length of 1.5 m. We derive a simple colliding shock lens scaling law. © *1995 American Institute of Physics.*

I. INTRODUCTION

With the ever-increasing power of pulsed lasers, breakdown-induced damage to solid state optics is becoming a growing concern. The use of gas rather than solid lenses extends the breakdown threshold by three orders of magnitude. For 20 ns pulses of visible light for example, the threshold intensity for uncoated glass optics lies in the 1 GW/cm^2 range, an intensity easily reached at the output window of table top systems. Breakdown in air at STP, for the same pulse length occurs at just below the terawatt/cm^2 level.

Recently, our group developed a novel pulsed gas lens, the colliding shock lens or CSL, (1) Fig. 1(a). This is a spin off from our study of the refractive fringe diagnostic of shocks in air reported in this journal (2) and of the plasma lens/isolator invented by Rumsby and Michaelis. (3) In the latter device four converging laser-produced plasmas were used either to focus or to interrupt a laser beam. The first CSL was very similar. Four electric arcs are stuck in air on the circumference of a circle to generate four converging shock waves. These shocks create a cigar-shaped region of high density air at the center of the circle which acts as a graded index or GRIN lens. By adjusting the time delay between convergence and the arrival of the pulsed laser beam, the aperture and focal length of the lens can be varied. Typical parameters for the first lens are an optical aperture of 1 mm for a focal length of 50 cm. The focus [Fig. 1(b)] is near-diffraction limited and the diameter of the circle of arcs is 1 cm. In this form it is unlikely to be a useful device.

Converging shocks have been extensively studied from the early 1940s primarily because of their ability to produce extremely high pressures and temperatures on convergence. This property also made them very attractive for use in laser fusion schemes. The theoretical treatment by Guderley[4] of a converging strong cylindrical or spherical shock wave has served as the basis for much of this work.

The method of converging shock creation ranged from the experiment of Perry and Kantrowitz[5] which involved the use of a tear-drop-shaped body placed in the center of a shock tube to force a planar incident shock wave to implode; to cylindrically imploding shocks created by detonating cylindrical explosive shells (Matsuo and Fujiwara).[6] Some experimenters[7] used multiple detonations to create what was initially a polygonal-shaped converging structure. This polygon was found to produce a circular (or cylindrical) converging shock wave prior to implosion.

Other methods involved the rupturing of two glass spheres each containing gases at different pressures, to study the behavior of the collision of two shock waves[8].

Experimental evidence has shown that for moderately strong shocks ($M \leq 2.4$), converging cylindrical shock waves are stable. Knystautas, Lee, and Lee[7] showed that when a number of planar detonation waves converge towards a center, Mach reflections result in a smooth cylindrical converging shock wave provided the obtuse included angle between the intersecting wave fronts is of the order of 100° or greater.

Since most of the work involving converging shocks was directed towards understanding the creation of the high temperature and pressure region at the point of convergence, much attention was given to the implosion stage of the process. Very little attention was paid experimentally to the expanding stage.

Also, although much work was done on shocks generated by electric arcs in air,[9,10] to the best of the authors' knowledge, they have not been used before for the production of converging shock waves. Our first refractograms[1] of the converging shocks indicated that a Mach addition of more than four shocks, would make the lens more effective. The first prototype was improved by providing it with eight pairs of opposing electrodes. The optical aperture increased to 2 mm for the same 50 cm focal length.

II. THE CSL AND THE SCALING QUESTION

As mentioned above, the first CSL had too small an aperture to be useful, although its optical quality seemed promising. But it did serve to pose the following question: could the CSL be scaled up? Two contradictory arguments were put forward.

According to the pessimist's view, refraction towards the focus is caused only by the narrow shock front gradient. This view is supported by our own refractive fringe study of shocks[2,10] and is illustrated by Fig. 1(c) in which the weak shocks have passed through each other, virtually undisturbed. According to this view, the lens would only work so long as the separating shock fronts are not too far apart, which explains why the first lens has a millimetric aperture. The aperture of the CSL would not scale up beyond a small geometric factor times the shock front thickness.

The optimistic counterargument runs as follows. The

 0034-6748/95/66(10)/5037/8/$6.00

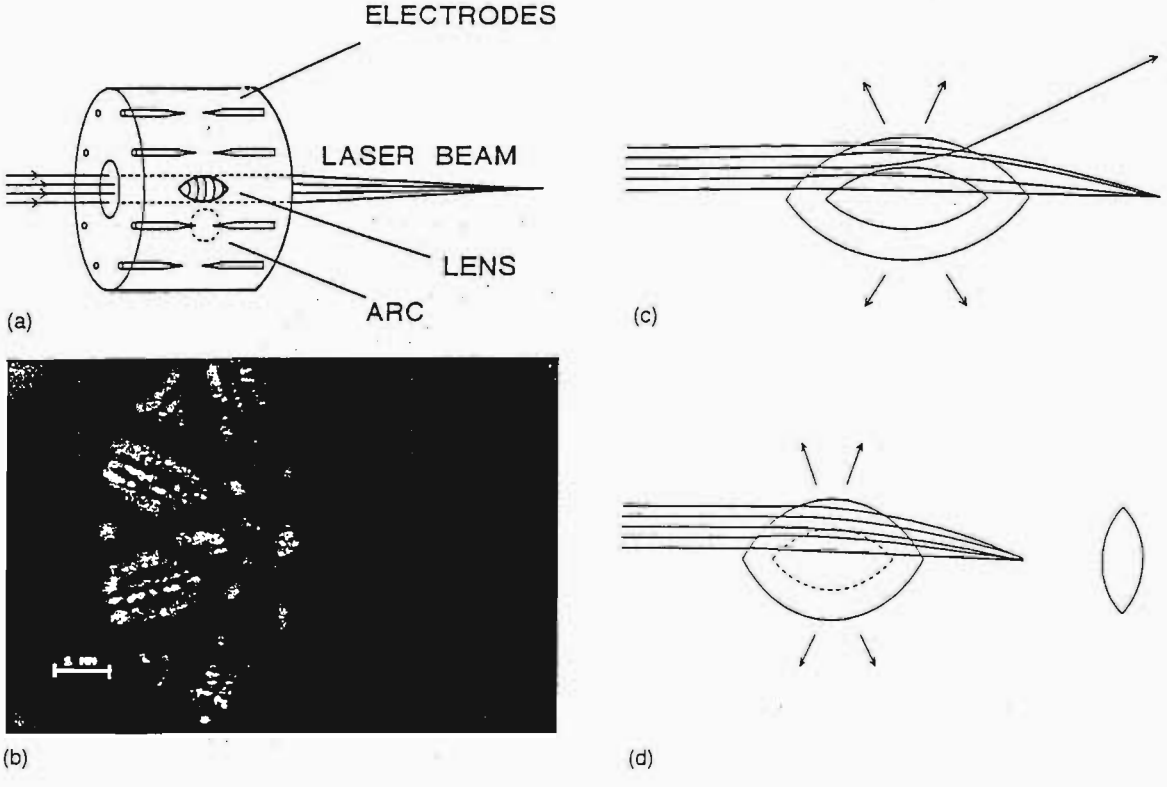

FIG. 1. (a) Schematic representation of the CSL. (b) Focus obtained with the first CSL at a focal length of 50 cm. (c) Schematic showing the lensing properties of weak shocks after collision. (d) Schematic showing the lensing properties of strong shocks after collision.

central collision of converging shocks produces a region of high density in which all "memory" of the early shocks is erased by nonlinear effects. This view is supported by the post-collision frames of Ref. 1 which show a circular rather than polygonal expansion front. This front may have a weaker gradient than the initial shocks and is therefore broader. The angular deflection of a ray being low, it is permissible to integrate the density along the ray, assuming that the ray's radial position does not change inside the lens. Integration of the hollow cigar gives the familiar lenticular shape: Figs. 1(d) and 3(b). Although it is true that only the front refracts light "inwards," the gradient of the shock rear is not strong enough to cancel the effect of the front. Gas inside the cigar plays a compensatory role which cannot be forgotten as in the first argument.

A millimetric gas lens is useless. A centimetric CSL would have many industrial applications. A decimetric pulsed gas lens could serve as the final focusing element for a laser fusion reactor.[11] Not being able to resolve the above discussion computationally, we decided it experimentally. In this paper we report how various factors (input electrical energy, electrical diameter, lens geometry) affect the optical aperture and focal length. With the successful operation of a 1.5 cm aperture CSL, we now believe the more complex second scenario.

II. EXPERIMENTAL APPARATUS

The experimental apparatus used for the following set of experiments was the same as that used by Buccellato *et al.*[1] Figure 2 is a schematic representation of the circuit in which C refers to the charging capacitor which is discharged through the electrodes of the CSL.

The CSL consists of two 5-mm-thick plexiglass plates which support eight or sixteen pairs of opposing electrodes: Fig. 1. (The plates can be either square as in Fig. 2, or circular as in Fig. 1). The separation between the plates can be adjusted from 1 to 4 cm.

The electrodes used in this experiment are constructed from 0.5-, 1-, 2-mm-diam stainless steel pins depending on the maximum energy to be stored in the capacitor. The electrode separation was always set at 0.5 mm. The electrodes are connected in series to ensure that the gaps break down simultaneously. A circular window is cut out of each of the

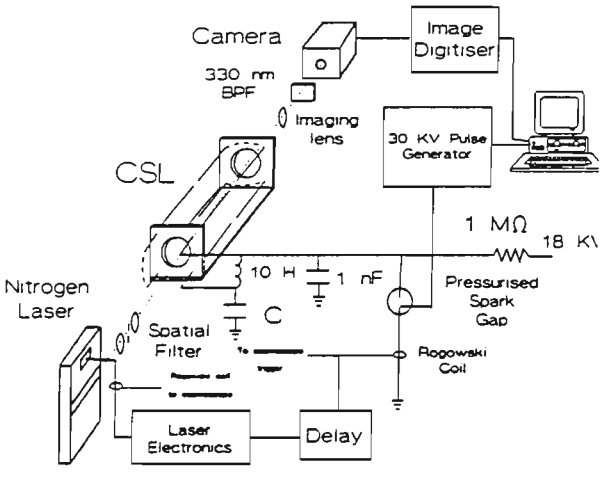

FIG. 2. Schematic representation of the CSL experimental setup. C refers to the charging capacitor.

plexiglass plates to allow a nitrogen laser beam (337 nm) to be shone through. It is with this beam that the properties of the CSL are studied.

The charging capacitor (C) is initially charged to 18 kV through a 10 H inductor by means of a high voltage dc power supply. A 5 V computer signal triggers the pulse generator resulting in a 30 kV pulse of 1 μs duration being sent to the extra electrode of the pressurized spark gap. This causes the spark gap to break down, pulling one side of the CSL to ground. The 1 nF capacitor provides the initial energy to break down the spark gap. The potential difference across the CSL produces the ring of simultaneous arc discharges. Each of these arcs generates an expanding spherical shock wave. The expanding shock waves collide at the center of the CSL and a high pressure, temperature, and density region is created. We call this the "implosion stage." A short time (of the order of microseconds) after collision, the expansion of this high density region results in the axisymmetric "cigar"-shaped density distribution which forms the graded index lens.

The detection circuit for this experiment is capable of detecting either the shock structure at various times or the focal spot for different focal lengths. This is accomplished in the following way: a Rogowsky coil in the CSL discharge circuit sends a signal to a delay box when the CSL "fires." This signal is then delayed and used to trigger the spatially filtered and expanded nitrogen laser beam. The beam then passes through the windows of the CSL before falling on the face plate of a charge-coupled device camera and is digitized by means of an Oculus 200 frame grabber. A 330 nm interference filter with a bandwidth of 10 nm is placed in front of the camera to select out the nitrogen beam from the light generated by the arcs. To study the behavior of the shock waves, a convex lens is used to image in the shock plane (Fig. 2). By varying the delay of the nitrogen laser one obtains a sequence of shadowgrams for the shock waves, from convergence to collision and finally divergence. This enables us to calculate the size of the lensing region formed by the cigar.

By removing the imaging lens and allowing the laser beam to fall directly on the face plate of the camera, the quality and size of the focal spot can be evaluated for different focal lengths. To avoid confusion in the terminology, we henceforth refer to the maximum diameter of the cigar-shaped lensing region as the "optical aperture" of the lens, to the plexiglass structure incorporating the electrodes as the CSL, and to the diameter of the circle of electrodes as the "electrical diameter."

IV. CHOICE OF VARIOUS CSL DESIGNS

To characterize the CSL one must determine the extent to which the various parameters (energy, electrical diameter, number of electrodes, wall geometry) affect the optical aperture, the focal length, and the quality of the focus. To this end the following parameters were varied.

A. Shock strength

The first question that needs to be answered is how the shock strength affects the lensing region. In our experiments, the shock strength is varied by changing the capacitance of the charging capacitor while keeping the voltage constant.

B. Electrical diameter

The electrical diameter is increased by using different CSLs. Some half-dozen CSLs were constructed to gain experience with these devices.

C. Number of electrodes

By increasing (or decreasing) the number of pairs of electrodes on the CSL, we can change the shape of the imploding shock structure and hence the shape of the lensing region.

D. Enclosure

We experiment with enclosed and unenclosed CSLs to determine whether confinement of the shocks affects the quality of the lensing. The CSL is enclosed by encasing it in a Plexiglass tube and reducing the separation of the vertical walls.

We now present a summary of the physical characteristics of the four CSLs constructed to test these concepts. The CSLs will be labeled CSL 1–4.

CSL1 : This is the original CSL (see Buccellato *et al.*).[1] It has eight pairs of electrodes arranged on a circle of diameter 11 mm. The diameter of the windows is 7.5 mm. CSL1 is unenclosed.

CSL2 : This CSL has an electrical diameter of 33.5 mm and a window diameter of 11 mm. This second unenclosed CSL has eight pairs of electrodes.

CSL3 : To see how enclosing the CSL would affect its lensing properties, we constructed a CSL with the same electrical diameter and windows as the preceding one but enclosed it in a plexiglass cylinder of diameter of 40 mm. This CSL like the preceding two is also fitted with eight pairs of electrodes. The wall separation was reduced from 40 to 10 mm.

CSL4 : The final CSL has an electrical diameter of 80 mm and a window diameter of 50 mm. The distance between the end plates is 21.5 mm and the diameter of the plexiglass tube is 120 mm. This lens can be fitted either with eight or sixteen pairs of electrodes.

V. RESULTS AND DISCUSSION

In order to better understand the scaling results we first briefly reexamine the process of GRIN lens formation.

When the pressurized spark gap in the CSL power supply breaks down, the electrical discharges between opposing pairs of electrodes in the CSL act as point sources for spherically expanding shock waves. As mentioned before, these shock waves collide at the center of the CSL. On collision of two or more shock waves, a high density, pressure, and temperature region forms. In our experiments where $M \approx 1.5$, we do not expect the region to become turbulent, except for higher energies, as explained below. This region then expands to form the cigar-shaped region already described. Figure 3(a) is a computed density profile that results during

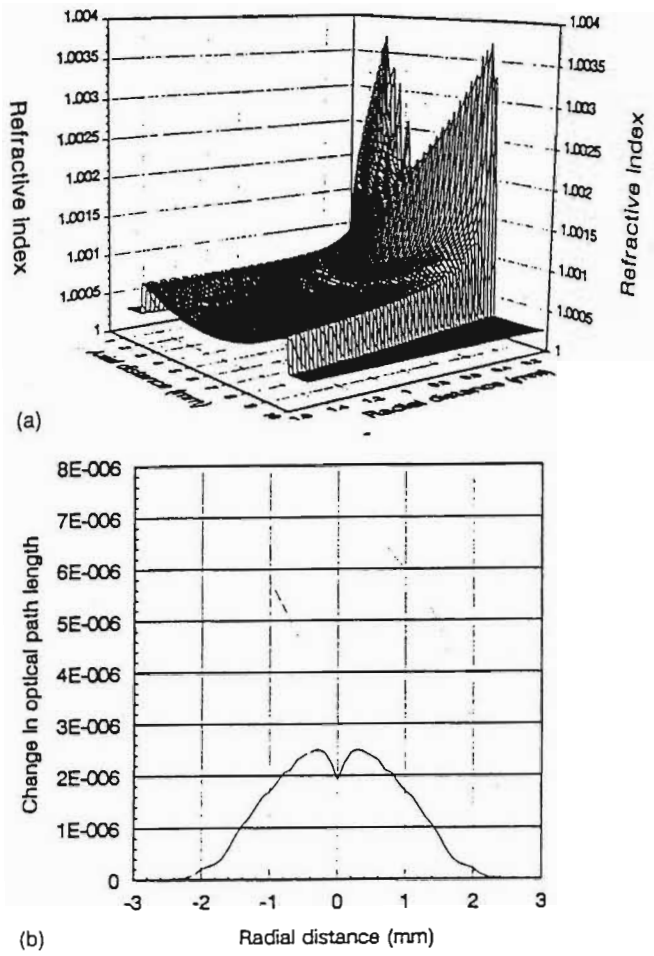

FIG. 3. Computed refractive index field of the CSL 1 μs after initial shock wave reflection. Inset below: integrated optical path length difference.

the expansion phase.[12] Only half the lensing region or "cigar" is shown. The refractive index increases sharply near the edges of the cigar and a depression is visible in the center.

Although this profile looks extraordinarily complicated, its computation allows one to verify the following statement, which simplifies the ray optics. There are virtually no radial deviations within the lens. This is because the refractive index differs from unity by less than one percent and the refractive index gradients and the angular deflections are small. (Less than 5 degrees).

To calculate the latter it suffices to integrate the density along the path of each fixed radius paraxial ray. The complicated profile then reduces to the familiar lenticular shape: Fig. 3(b) (The central "hole" may be computational).

We now compare the performance of various lenses. Typical parameters reported for the first eight arc colliding shock lens[1] were an optical aperture of 2 mm for a focal length of 52 cm and an input energy of 0.8 J. (C=5 nF). The focal spot size was near-diffraction limited.

A. Increasing the electrical aperture (unenclosed CSL)

By using CSL2 and keeping the same charging capacitor, we are able to determine the effect an increase in electrical diameter has on the focal length and optical aperture for the unenclosed CSLs. We would expect that since the energy falls off with shock radius R, the larger CSL (CSL2) should produce a weaker converging shock wave, since the shocks travel a greater distance before colliding. Hence, CSL1 should have a shorter focal length than CSL2 for the same optical aperture (or conversely a larger optical aperture for the same focal length).

Figure 4(a) shows a plot of optical aperture versus time after collision for CSL2. This is obtained by imaging in the shock plane of the CSL. We can see that the optical aperture increases with time. The focal length also shows the same trend [Fig. 4(b)]. Combining these two results, we obtain a plot of focal length versus optical aperture [Fig. 4(c)]. To compare CSL2 with CSL1, we read off the optical aperture for a known focal length, i.e., 52 cm. The lens diameter for this length is 0.5 mm (2 mm for CSL1). It is clear that the strength of the shocks on implosion is greater for CSL1 than for CSL2. For the same optical aperture, CSL1 has a shorter focal length than CSL2.

We can conclude that for the unenclosed case, increasing the electrical aperture must be accompanied by a corresponding increase in input energy to maintain and in fact improve the performance of the CSL.

B. Enclosing the CSL

Intuitively it would seem that by enclosing a CSL, reducing the loss of energy, and confining the shock waves to two dimensions rather than three, we should be able to produce stronger shock waves and hence better focusing (i.e., shorter focal lengths and larger optical apertures than with the unenclosed lens). We therefore constructed CSL3 which is an enclosed version of CSL2.

Figure 5(a) shows the focal length versus optical aperture for CSL2 and CSL3. The capacitor used was the same for both (5 nF), hence the input energy was the same as well (0.81 J). We also plot f number versus focal length for CSL2 and CSL3 [Fig. 5(b)].

The difference in the behavior of the two CSLs is striking. CSL3 has an optical aperture of 2.2 mm at 0.9 m focal length while CSL2 has an aperture of 0.7 mm for the same focal length. The f number of CSL3 is better than that of CSL2 by a factor of ≈ 3.

A quantitative assessment of how different types of enclosure strengthen the shocks, will require further investigation. But clearly, this is a promising feature of colliding shock lenses.

C. Varying the energy

Having established that the enclosed lens works well, we now adopt it for the energy dependence studies.

Three different capacitor sizes are used with CSL3. They are 5, 21, and 100 nF. These corresponded to energies of 0.8, 3, and 16 J, respectively. The energy increases by up to a factor of 20.

Figure 6(a)shows the focal length versus optical aperture for CSL3 at the different energies. We achieve an optical aperture of 4 mm at a focal length of 1.3 m for 100 nF.

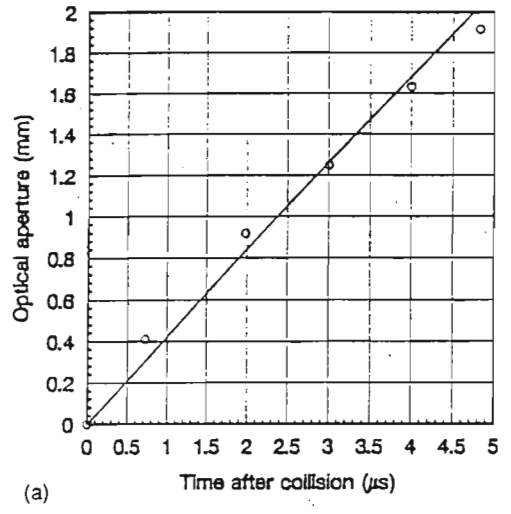

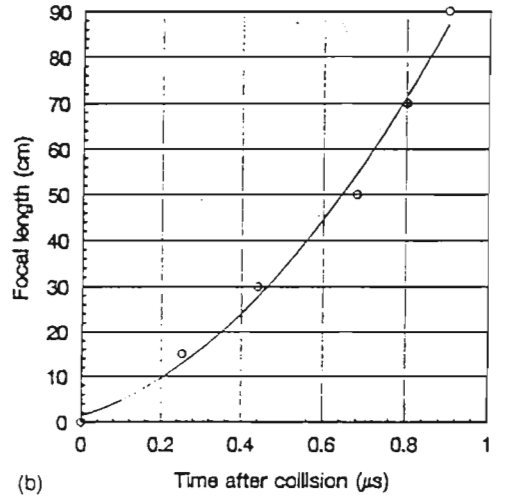

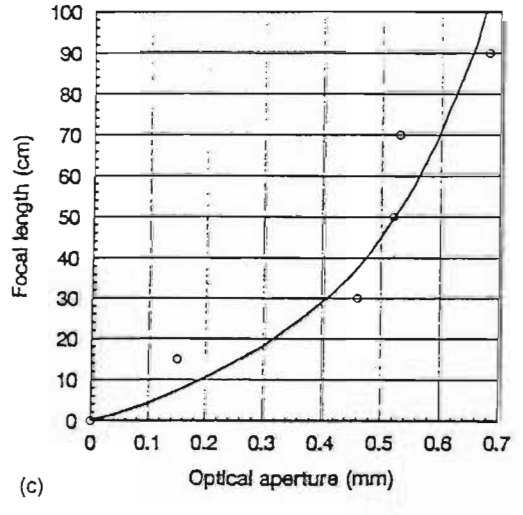

FIG. 4. (a) Plot of optical aperture vs time after collision for CSL2 using a 5 nF charging capacitor. (b) Focal length vs time after collision for the CSL2 - 5nF charging capacitor. (c) Optical aperture vs focal length for the CSL2 - 5nF charging capacitor.

Plotting the f number versus focal length [Fig. 6(b)] we see an improvement in the f number for 100 nF as compared to the 5 and 21 nF.

An attempt to use a 250 nF capacitor to increase the input energy by a factor of 2.5, was not successful. Although a cigar-shaped core did form, the quality of the focus was

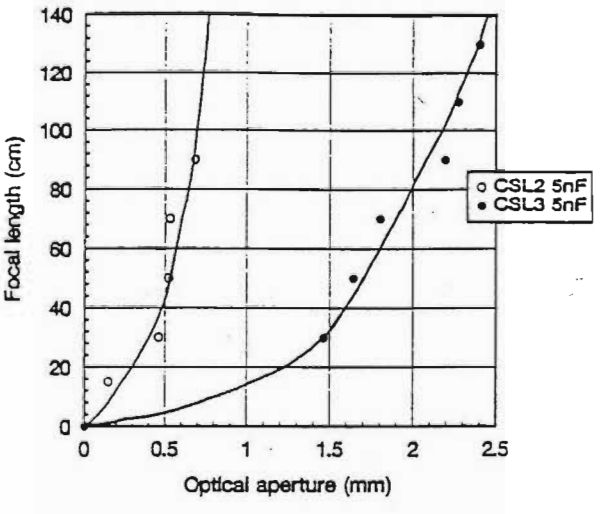

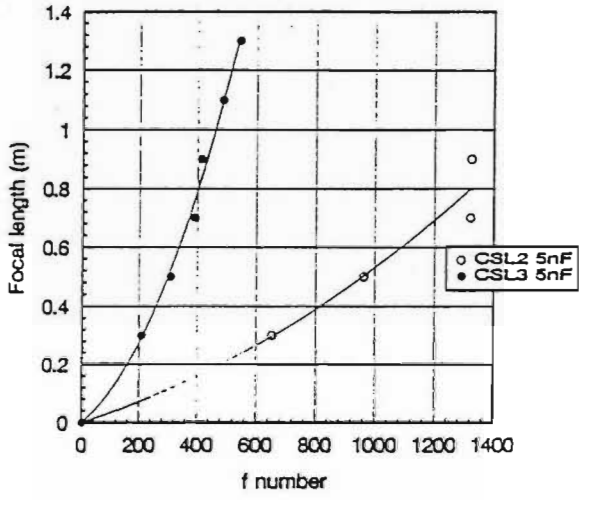

FIG. 5. (a) Comparative focal length vs optical aperture for the CSL2- and CSL3 - 5nF charging capacitor. (b) f number vs focal length for CSL2- and CSL3-5nF charging capacitor.

very poor indeed. We attribute this to the onset of turbulence, known to occur when strong shocks collide.

D. Increasing the electrical diameter (enclosed CSL)

Increasing the electrical diameter alone will not result in a larger optical aperture for similar focal lengths. This increase must also be accompanied by an increase in the input energy. There are two reasons for this. The first is that Mach addition requires large included angles. The second is that addition only occurs for strong shocks.

A larger electrical diameter results in weaker shock waves colliding near the center. Circular symmetry may then not be attained. We tried CSL4 with an eight electrode pair configuration. As expected this does not form a good lens since circular symmetry of the cigar is not achieved. Figure 7(a) shows the polygonal shock structure created by the collisions in this configuration. Circular symmetry has not been obtained.

E. Changing the number of electrodes

To regain circular symmetry in CSL4, eight more pairs of electrodes were inserted converting it into a sixteen pair

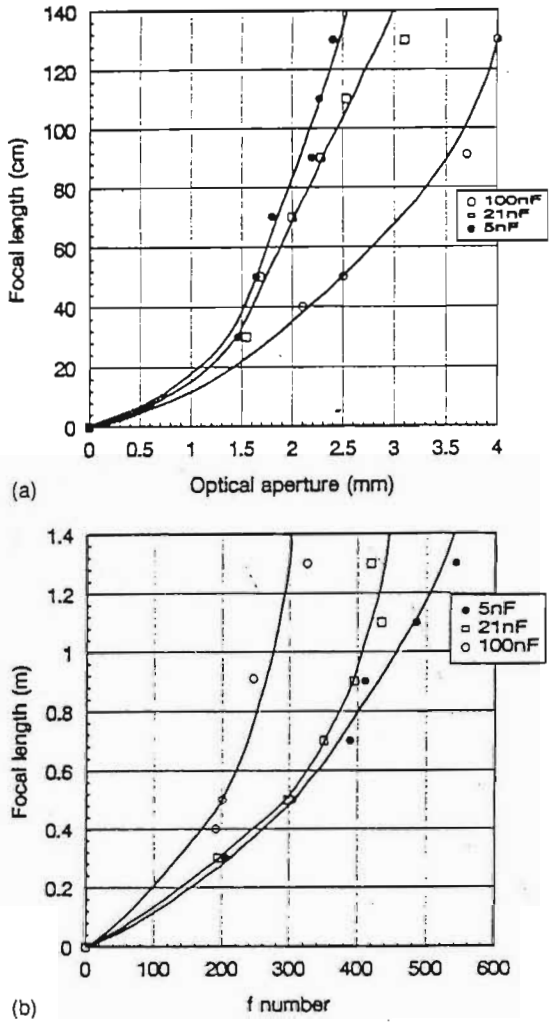

FIG. 6. (a) Focal length vs optical aperture for CSL3 using 5, 21, and 100 nF charging capacitors. (b) f number vs focal length for CSL3 using 5, 21, and 100 nF charging capacitors.

electrode CSL. The imploding shock waves achieve symmetry early. This can be seen from the sequence of four pictures showing the shocks after collision [Fig. 7(b)]. The circularly symmetric nature of the shock structure is evident. So adding more shocks was necessary for this large diameter CSL to symmetrize and to form a lens.

Figure 8 shows the focal length versus optical aperture for three different capacitor sizes viz. 21, 100, and 250 nF. Since we now have larger radii shock waves forming an axisymmetric cigar, we can expect a larger optical aperture. But since the density gradients for the same input energy may be weaker, we would expect to see an increase in the focal length (see Fig. 9).

It is interesting to note that CSL3 becomes turbulent at 250 nF. If we could increase the input energy into this CSL, it would perform better than CSL4. However every CSL has an upper limit for input energy. CSL4 with sixteen pairs of electrodes was very stable for the 250 nF capacitor. From Fig. 8 we see that CSL4 at 250 nF has an optical aperture of 3.2 mm for a focal length of 1.3m. The focal spot at this distance is shown in Fig. 10. It has a full width at half-maximum of 200 μm. By gas lens standards, this is close to diffraction limited.

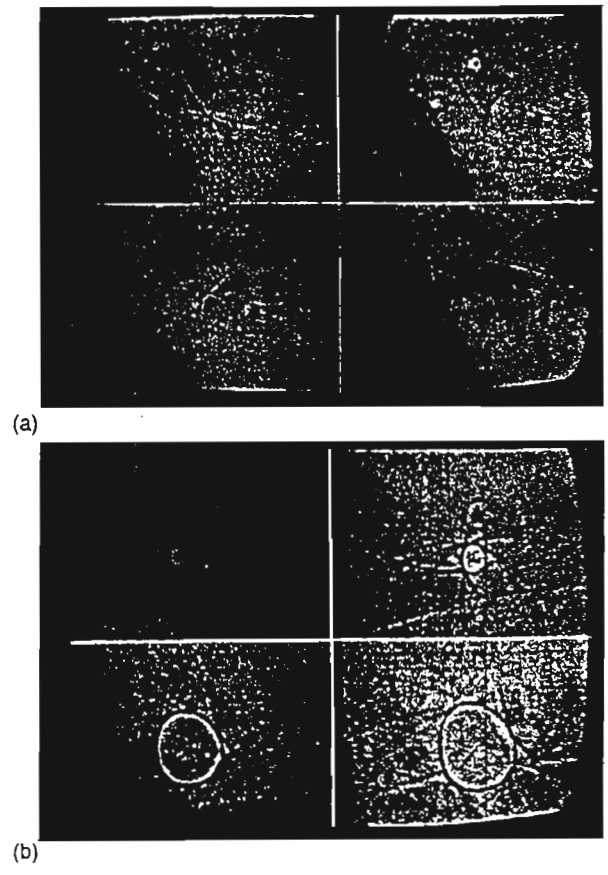

FIG. 7. (a) Sequence of colliding shock images [(a) implosion; (b) 6.2 μs; (c) 7.4 μs, and (d) 14 μs after implosion] taken using CSL4 having an eight pair electrode pair configuration and a charging capacitor of 100 nF. Magnification=0.33. (b) Sequence of colliding shock images [(a) 0.3 μs; (b) 1.5 μs; (c) 3.9 μs, and (d) 4.3 μs after implosion] taken using CSL4 with a sixteen electrode pair configuration and a charging capacitor of 100 nF. Magnification=0.5.

VI. CSL SCALING THEORY

An approximate scaling theory for CSLs can be derived with the help of the following assumptions.

(i) All the electrical energy stored in the charging capacitor is transferred to the shock waves by the arcs.

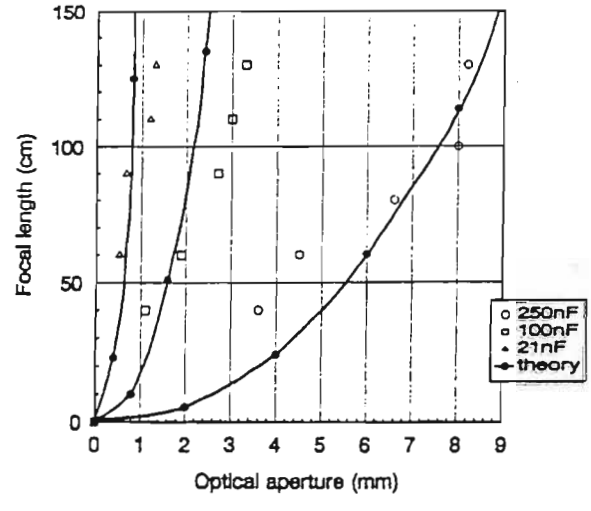

FIG. 8. Focal length vs optical aperture for CSL4 (sixteen electrode pairs) using 21, 100, and 250 nF charging capacitors.

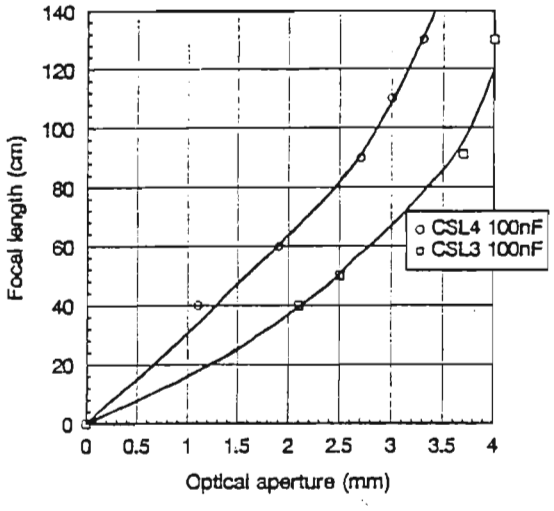

FIG. 9. Focal length vs optical aperture for CSL3 and CSL4 using a 100 nF capacitor.

(ii) A certain fraction of this energy is contained in the gas forming the lens. This fraction is represented by the product of a "geometric energy factor" G and a "shock weakness factor" G'.

(iii) For the purpose of calculating refraction, the actual density profile, however complex, can be approximated by a cigar-shaped, high density region with a constant refractive index gradient.

(iv) A simple order of magnitude focal length calculation is acceptable.

Clearly, all these assumptions can be examined and refined in great depth. But at this stage of development, we find the following simple calculation useful.

Only a fraction $W=G\,G'(1/2CV^2)$ of the total energy in the shocks is contained in the compressed gas of the lensing region, where

$$G^2=\frac{1}{20}\left(\frac{r}{R}\right)^3$$

and G' is a fitted parameter. G is the areal cross section that the lens offers up to the spherically expanding shock front. It is obtained by assimilating the cigar to two cones, each of height l and base radius r. Simple trignometry shows that the half-length of the cigar is

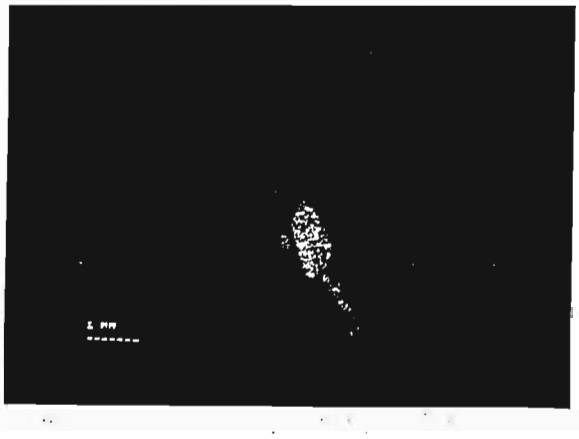

FIG. 10. Focal spot at 1.3 m away from CSL4 (250 nF charging capacitor).

$$l=\sqrt{2rR},$$

where R is the radius of two intersecting shocks.

G' represents the fraction of shock wave energy contained in the supersonic front as opposed to that which has been dissipated in forming the long shock rear and the shock tail. No figures are available for this factor, but simple visual examination of typical density and temperature curves,[13,14] show that it can vary from unity (all the energy is in the strong shock) to a few percent (very little energy is left in the shock itself which now resembles a sound wave). G' is also made to contain the small geometric errors, deliberately made in the rough calculation of G and that following for the focal length f.

In order to calculate the density of the gas in the lens, we now assume that the lens is formed adiabatically, so that

$$W=\frac{1}{\gamma-1}(p_fV_f-p_oV_o),$$

where the symbols have their usual meaning. The known quantities in this expression are the volume of the lens V_f and the initial pressure: p_o. The volume of the lens is approximated to that of two cones:

$$V_f=\frac{2}{3}\pi r^2 l.$$

Taking $\gamma=1.4$ and writing

$$p_oV_o^\gamma=p_fV_f^\gamma$$

one obtains

$$\frac{p_f}{p_o}-\left(\frac{p_f}{p_o}\right)^{1/\gamma}=\frac{0.4W}{p_oV_f}.$$

The right-hand side is known and p_f/p_o may be obtained graphically.

Knowing the average density $\rho_f=(V_o/V_f)\rho_o$ in the lens, the refractive index gradient may be calculated very approximately as follows.

The refractive index of air is roughly $n=1+3\times10^{-4}\rho$. The uniform refractive index gradient is therefore $(n-n_o)/r$ and a median ray traversing the lens $r/2$ mm away from the axis, is refracted by an angle

$$\theta=l(n-n_o)/r$$

and comes to a focus a distance $f=(r/2)/\theta$ away. (n_o is the refractive index of undisturbed air).

A little algebra yields the convenient formula

$$f^2=\frac{1.4r^3}{(\rho-1)^2R},$$

where f is in meters and r and R in millimeters.

We now attempt to model our large lens, CSL4. This has an electrical diameter of 8 cm, which yields an 8 mm GRIN lens with a focal length of the order of one meter. If G' is taken as unity, then the calculated focal length is too small.

This example and others, show that predicted focal lengths are a little short for strong shocks and far too short for weak. This was the reason for introducing the G' correction factor. If we take G' as $\frac{1}{2}$ for the strong 250 nF shocks,

$\frac{1}{30}$ for the weaker 100 nF, and $\frac{1}{100}$ for the very weak 21 nF, we obtain rough agreement. (See the calculated curves for Fig. 8). This simple theory and the scaling experiments described in earlier sections lead us to construct a final enclosed CSL with an electrical diameter of 26 cm powered by a half μF capacitor charged to 17 kV. Our first experiments with this lens showed it to be capable of generating a 1.5 cm aperture lens with a focal length of 1.5 m.

In this attempt to determine whether the aperture of the CSL can be scaled up, we find the following.

(1) Enclosing the lens improves its performance.
(2) Increasing the input energy also increases the aperture and decreases the focal length. However there is an upper limit to the amount of energy one can put into the shocks. The small lens (CSL3) with eight pairs of electrodes becomes unstable with the 250 nF capacitor whereas with more electrodes and a larger electrical aperture, CSL4 (sixteen electrode pairs) is very stable.
(3) Simply scaling up the electrical diameter does not necessarily increase the lens aperture. There has to be an accompanying increase in energy and perhaps more important, enough shocks for circular symmetry to be attained before implosion. The smaller CSLs (2 and 3) worked with eight sets of electrodes whereas the large CSL (CSL4) needs more electrodes to achieve symmetry.

In conclusion, we have shown that the colliding shock lens can be scaled up to useful apertures and how to do so. We have derived a simple CSL scaling law.

ACKNOWLEDGMENTS

The authors wish to thank the workshop staff of the Physics Dept. of the University of Natal. This work was partly supported by the Foundation for Research and Development.

[1] R. Buccellato, N. Lisi, and M. M. Michaelis, Opt. Commun. **101**, 350 (1993).
[2] M. Bacon, R. N. Campbell, P. F. Cunningham, and M. M. Michaelis, J. Appl. Phys. **66**, 1075 (1989).
[3] P. T. Rumsby and M. M. Michaelis, Opt. Commun. **21**, 337 (1977).
[4] G. Guderley, Luftfahrt-forsch **19**, 302 (1942).
[5] R. W. Perry and A. Kantrowitz, J. Appl. Phys. **22** 878 (1951).
[6] H. Matsuo and K. Fujiwara, Phys. Fluids A **2**, 266 (1992).
[7] R. Knystautas, B. H. Lee, and J. H. S. Lee, Shock Tube Symposium, Phys. Fluids Suppl. I, 1969 (unpublished).
[8] I. I. Glass and L. E. Heuckroth, Phys. Fluids **2**, 542 (1959).
[9] K. Muraoka, M. Hamamato, and M. Akazaki, Jpn. J. Appl. Phys. **19**, 293 (1980); M. Hamamoto, K. Muraoka, and M. Akazaki, *ibid.* **20**, 443 (1981).
[10] M. M. Michaelis, J. A. Waltham, and P. F. Cunningham, Opt. Laser Technol. **23**, 283 (1991).
[11] M. M. Michaelis, P. F. Cunningham, M. Notcutt, and J. A. Waltham, Laser Particle Beams **9**, 641 (1991).
[12] R. Buccellato, University of Natal Doctoral thesis, 1994.
[13] L. I. Sedov, *Methods of Similarity and Dimensional Analysis in Mechanics*, 3rd ed. (Academic, New York, 1959).
[14] Y. B. Zeldovich and Y. P. Raizer, *Physics of Shock Waves and High Temperature Hydrodynamic Phenomena* (Academic, New York, 1966), Vol I.